THE UNIVERSITY of ADELAIDE

Atomic Level Insights for Photocatalytic CO_2 Reduction

Yanzhao Zhang

School of Chemical Engineering and Advanced Materials

Faculty of Science, Engineering, and Technology

A thesis submitted for the degree of Doctor of Philosophy

The University of Adelaide

Feb 2023

Contents

Abstract

As the concentration of greenhouse gases in the atmosphere continues to rise, so does average global temperature. This process is irreversible over a short time. The development of renewable clean energy is important therefore to survival and sustainability. As a potential practical method of solar energy utilization, photocatalysis can convert CO_2 into high-value-added fossil fuels and assist to obviate global temperature and solve energy shortage. Photocatalytic CO_2 reduction (PCRR) is an artificial photosynthesis, that includes three steps: 1) Light absorption, 2) Charge separation and transfer, and 3) Surface redox reaction. However, high C=O double bond energy and the symmetrical molecular structure of CO_2 molecules make it necessary to overcome a significantly high energy barrier for adsorption and activation. Therefore, a simple, environmentally friendly and universal method is urgent to be developed to activate the catalyst surface and significantly boost affinity for CO_2 molecules. Additionally, photocatalytic CO_2 reduction reaction involves complex, multi-electron transfer paths, leading to complex catalytic products and reaction kinetics. However, the construction of photocatalytic reaction systems that exhibit excellent performance, stability and low cost and are environmentally benign is a significant practical challenge. This Thesis aim is to determine the fundamentals of the atomic level and to design novel nanostructured photocatalysts for CO_2 reduction reactions. Importantly, this involves detailed investigations on structure and performance, especially for charge transfer and surface reactions that can be reliably used to guide design of catalysts.

The significance, context and scope of this Thesis is presented in Chapter 1. A critical review of research progress for CO_2 photoreduction from atomic level understanding is provided in Chapter 2. This chapter critically evaluates the challenges and discusses atomic level active sites for PCRR, including defects, single atoms, functional groups and frustrated Lewis pairs and relationships between reactive sites and PCRR performance and impacts on selectivity, stability, efficiency and reactivity.

Chapter 3 focuses on synthesizing reactive sites on the surface of transition metal dichalcogenides (TMDs) to alter the inert surface. A heterojunction between CdS nanoparticles and ultra-thin ReS_2 nanosheets (6 nm thickness) is synthesized and the mechanism for CO_2 photoreduction is determined for this catalytic system. Photoelectrons separation and transfer

and *in situ* formed defects on the surface of ReS_2 are confirmed to act as reactive sites to boost photocatalytic performance.

Carbon contaminations have a significant influence on photocatalytic performance because carbon-contained products generated *via* CO_2 conversion remain at a low level. In Chapter 4, a targeted series of experiments are described to identify carbon impurities and to establish the influence of carbon impurities on subsequent performance tests. Based on findings from these, reliable experimental protocols to obviate potential carbon contamination effect are proposed in detail.

In Chapter 5, a straightforward strategy is developed for synthesis of surface defective bismuth oxide nanosheets. The (010) surface of nanosheets are actively regulated *via* oxygen vacancies. The surface-regulated Bi_2MoO_6 nanosheets exhibit practically promising PCRR performance. Findings from judiciously combined theoretical computations, kinetics analyses and *in situ* infrared spectroscopy are used to confirm that surface unsaturated metal atoms serve as the active sites, and that the hydrogenation of $*OCH_3$ for CH_4 formation is the rate-limiting step. Findings are shown to increase fundamemtal understanding of the regulated surface, and to form a basis for large-scale application.

In the concluding experimental chapter, Chapter 6, dual single atoms for efficient CO_2 conversion to value-added chemicals are explored. *In situ* characterizations and simulations evidence complex surface reaction and free energy diagram. Charge transfer is determined *via in situ* X-ray Photon Spectra (XPS) to demonstrate that the photogenerated electrons transfer direction is reversed in dual single atoms system compared with single-atom system. Findings are shown to develop understanding of the charge transfer between dual single atoms and single-atom research and mechanism.

The conclusions available from findings from this research on CO_2 photoreduction, togther with a perspective are presented in Chapter 7.

Declaration

I certify that this work contains no material which has been accepted for the award of any other degree or diploma in my name, in any university or other tertiary institution and, to the best of my knowledge and belief, contains no material previously published or written by another person, except where due reference has been made in the text. In addition, I certify that no part of this work will, in the future, be used in a submission in my name, for any other degree or diploma in any university or other tertiary institution without the prior approval of the University of Adelaide and where applicable, any partner institution responsible for the joint-award of this degree.

I acknowledge that the copyright of published works contained within this thesis resides with the copyright holder(s) of those works.

I also give permission for the digital version of my thesis to be made available on the web, via the University's digital research repository, the Library Search and also through web search engines, unless permission has been granted by the University to restrict access for a period of time.

I acknowledge the support I have received for my research through the provision of an Australian Government Research Training (RTP) program.

Signed: …… Date: 23/02/2023

Acknowledgments

First and foremost, I owe my deepest gratitude to my principal supervisor, Prof. Shi-Zhang Qiao. He sets a good example for me as a hardworking, professional and rigorous researcher. His patience, enthusiasm and instruction supported me a lot throughout my Ph.D. study. I will benefit from his training as a researcher in my future career. I also thank Dr. Jingrun Ran for his suggestions and continuous guidance during my Ph.D. study. I sincerely appreciate Associate Professor Yan Jiao for her guidance and help on theoretical simulations.

I am also grateful to all group members of Professor Qiao's group who give me support and assistance both in study and life. Special thanks go to Dr. Dazhi Yao, Dr. Anthony Vasileff, Dr. Xing Zhi, Dr. Fangxi Xie, Dr. Huanyu Jin, Dr. Cheng Tang, Dr. Bingquan Xia, Dr. Yongqiang Zhao, Dr. Chaochen Xu, Dr. Xuesi Wang, Dr. Laiquan Li and Mr. Ling Chen for their helpful support and valuable suggestions in my research program. I would also extend my thanks to Associate Professor Yao Zheng, Dr. Chao Ye, Dr. Pentang Wang, Dr. Jieqiong Shan and Mr. Chun-Chuan Kao for their encouragement and friendship. I cherished all my time working alongside the intelligent and hard-working people in Prof. Qiao's group.

I sincerely appreciate many academic and technical staff who assisted me in materials characterization and data processing. My deepest appreciation goes to Dr. Qiuhong Hu for her generous assistance in the lab facilities, Dr. Roy Lehmann, Dr. Ay Ching Hee, Tom Wilson and Jason Peak for their exceptional technical skills and general support, Dr. Ashley Slattery and Christopher Leigh for their TEM imaging, Ken Neubauer for his support with SEM characterization. Many thanks go to Prof. Haolan Xu, Dr. Huimin Yu and Dr. Ting Gao for the XPS testing at the University of South Australia, Prof. Youhong Tang for AFM measurement at Flinders University and Associate Professor Jeffrey R. Harmer for the EPR testing at the University of Queensland. I am grateful to Associate Professor Kenneth Davey at the University of Adelaide and Prof. Mietek Jaroniec at Kent State University for their assistance in paper drafting and polishing. My special gratitude goes to the professional staff, Dr. Bernt Johannessen and Dr. Bruce Cowie for their generous help and professional guidance on the application of synchrotron beamline, testing and data analysis. I appreciate Prof. Shaobin Wang and his research group for helping me with the OER performance tests. To the staff in the School of Chemical Engineering and Advanced Materials, I would like to thank them all for creating a such helpful and friendly environment.

I would also like to acknowledge the Australian Government, The University of Adelaide and Australia Research Council (ARC) for their financial support, Adelaide Microscopy, Phoenix High-Performance Computing (HPC), National Computational Infrastructure (NCI) and Australian Synchrotron (ANSTO) for technical support.

Finally, I forever appreciate all my family and friends for their encouragement and support throughout my life. Thanks to my Mum, Dad, Yanru, Di and grandparents for their forever love and support. Without their continued trust and love, I could not have completed my Ph.D. I am grateful to all my friends in China and Australia for their support and encouragement. Thank you all for cheering me up in those tough times.

Chapter 1

Introduction

1.1 Project Significance

Global energy demand is estimated to increase with some 80% of current demands that need to be satisfied by consuming fossil fuels.[1] This releases significant CO_2 that leads to increasing greenhouse effects, together with attendant changes including precipitation, atmospheric warming and rising sea levels.[2] It is important therefore to develop approaches to 'fix' carbon and to explore renewable energy sources. Solar energy is 'free', abundant and clean. The conversion of solar energy and carbon fixation can be realized by photocatalytic CO_2 reduction simultaneously.[3]

Photosynthesis inspires us how to use solar energy, which is to create artificial photosynthesis *via* CO_2 and water conversion to produce hydrocarbon. Moreover, photocatalysts are the key point in artificial photosynthesis as photocatalysts adsorb the solar light and convert the photon energy into chemical energy which is conserved in the hydrocarbon such as carbon monoxide and methane. Since Honda and Fujishima first reported the photocatalytic effect in 1972,[4] many researchers have made great efforts in photocatalysis to promote the development of this field. Various nanostructured materials were synthesized to enhance photocatalytic efficiency because of special nanostructures and physical and chemical properties.[5-11]

There are various approaches to improve the performance of photocatalysts including constructing semiconductor heterojunctions,[12-14] doping[15,16] and loading noble metals.[17-19] These methods have different merits in physicochemical properties for boosting photocatalytic performance.[20,21] Fabricating new active sites can boost the CO_2 chemisorption and lower the energy barrier for CO_2 photoreduction. Heterojunctions can also promote the separation and immigration of photogenerated charges. Doping is a very simple method to change the electronic structure of the photocatalysts resulting in the reduction of their band gaps which enhances their visible light harvest.[22] The research based on the atomic level understanding enables researchers to design and synthesize new materials more efficiently.[23]

1.2 Research Objectives

The highly efficient photocatalysts with desired nanostructure and physical/chemical properties will be prepared. In order to solve the problems above, this project will focus on four aspects as follows:

1. This Thesis will develop new high-performance photocatalysts which can adsorb visible light which makes up about 43% of solar lights.
2. To investigate the effect of cocatatlysts on the recombination and separation of photogenerated electrons and holes during the construction of nanostructures and nonocomposite material system.
3. The reactants can adsorb on the surface active sites of the photocatalysts. More active sites should be introduced which are usually the crystal defects such as oxygen vacancy in crystal lattice on the surface of the photocatalysts. These active sites can act as not only the adsorption sites but also the photocatalytic reaction sites, which will be beneficial to photocatalytic efficiency enhancement.
4. The relationship between composition and photocatalytic performance will be revealed and the process of the photocatalytic test will be detected.

1.3 Thesis Outline

This Thesis presents the outcomes of my Ph.D. research and is presented as a sequence of journal publications. The Chapters of this Thesis are presented as follows:

Chapter 1 summarizes the background of the Thesis and outlines the project scope and key contributions to solar energy utilization and CO_2 conversion.

Chapter 2 introduces the recent reports based on the semiconductor photocatalysts and the understanding of the structure-performance relationship from the atomic level.

Chapter 3 constructs the heterojunction between CdS nanoparticles and ReS_2 nanosheets and investigates the *in situ* formed reactive sites on nanosheets.

Chapter 4 identifies and eliminates the carbon contamination in the CO_2 photoreduction system and proposes rigorous experimental protocols.

Chapter 5 presents a novel and simple approach for fabricating the oxygen vacancies on specific facets of bismuth-based nanosheets and explores their applications in PCRR.

Chapter 6 unravels dual single atoms on the CdS nanoparticles and investigates the photogenerated electrons transfer and accumulation process and related mechanisms for the boosted performance of CO_2 photoreduction.

Chapter 7 presents the conclusions and perspectives for future work on the research of CO_2 photoreduction.

1.4 References

[1] N. S. Lewis, D. G. Nocera, **Proc. Natl. Acad. Sci. USA**, 2006, *103*, 15729.

[2] J. Ran, M. Jaroniec, S. Z. Qiao, **Adv. Mater.**, 2018, *30*, 1704649.

[3] Y. Zhang, B. Xia, J. Ran, K. Davey, S.Z. Qiao, **Adv. Energy Mater.**, 2020, *10*, 1903879.

[4] A. Fujishima, and K. Honda, **Nature**, 1972, *38*, 37–38.

[5] A. J. Bard, **Science**, 1980, *207*, 139–144.

[6] I. S. Cho, C. H. Lee, Y. Feng, M. Logar, P. M. Rao, L. Cai, D. R. Kim, R. Sinclair and X. Zheng, **Nat. Comm.,** 2013, *4*, 1723.

[7] M. Law, L. E. Greene, J. C. Johnson, R. Saykally, and P. D. Yang , **Nat. Mater.**, 2005, *4*, 455–459.

[8] S.-m. Chang and W.-s. Liu, **Appl. Catal. B Environ.**, 2011, *101*, 333-342.

[9] I. Gur, N. A. Fromer, M. L. Geier, and A. P. Alivisatos, **Science**, 2005, 310, 462–465.

[10] N. S. Lewis, **Science**, 2007, *315*, 798–801.

[11] H. Zhao, F. Huang, J. Hou, Z. Liu, Q. Wu, H. Cao, Q. Jing, S. Peng and G. Cao, **ACS Appl. Mater. Inter.**, 2016, *8*, 26675-26682.

[12] C. Y. Su, C. C. Wang, Y. C. Hsueh, V. Gurylev, C. C. Keic and T. P. Perng, **Nanoscale**, 2015, *7*, 19222-19230.

[13] L. Wang, S. Liu, Z. Wang, Y. Zhou, Y. Qin and Z. L. Wang, **ACS Nano**, 2016, *10*, 2636-2643.

[14] Y. J. Yuan, Z.-J. Ye, H.-W. Lu, B. Hu, Y. H. Li, D.-Q. Chen, J.-S. Zhong, Z.-T. Yu and Z.-G. Zou, **ACS Catal.,** 2016, *6*, 532-541.

[15] Y. Wang, Y.-Y. Zhang, J. Tang, H. Wu, M. Xu, Z. Peng, X.-G. Gong and G. Zheng, **ACS Nano**, 2013, *7*, 9375-9383.

[16] L. Kong, Z. Jiang, C. Wang, F. Wan, Y. Li, L. Wu, J.-F. Zhi, X. Zhang, S. Chen and Y. Liu, **ACS Appl. Mater. Interfaces**, 2015, *7*, 7752-7758.

[17] K. Lee, R. Hahn, M. Altomare, E. Selli and P. Schmuki, **Adv. Mater.**, 2013, 25, 6133-6137.

[18] J. Fei and J. Li, **Adv. Mater.**, 2015, *27*, 314-319.

[19] R. Dong, Q. Zhang, W. Gao, A. Pei and B. Ren, **ACS Nano**, 2016, *10*, 839-844.

[20] T. J. Athauda, J. G. Neff, L. Sutherlin, U. Butt and R. R. Ozer, **ACS Appl. Mater. Interfaces**, 2012, *4*, 6916-6925.

[21] X. Chen, J. Wei, R. Hou, Y. Liang, Z. Xie, Y. Zhu, X. Zhang and H. Wang, **Appl. Catal. B Environ.**, 2016, 188, 342-350.

[22] L. Liu, Y. Jiang, H. Zhao, J. Chen, J. Cheng, K. Yang and Y. Li, **ACS Catal.**, 2016, 6, 1097-1108.

[23] K. Awazu, M. Fujimaki, C. Rockstuhl, J. Tominaga, H. Murakami, Y. Ohki, N. Yoshida and T. Watanabe, **J. Am. Chem. Soc.**, 2008, *130*, 1676-1680.

Chapter 2

Literature Review: Atomic-Level Reactive Sites for Semiconductor-Based Photocatalytic CO_2 Reduction

2.1 Introduction and Significance

CO_2 photoreduction is a promising edge-cutting technology for achieving carbon neutrality and alleviating the green-house effect. Semiconductors-based nanomaterials can serve as excellent photocatalysts for converting solar energy to chemical energy as they have unique physical/chemical properties to adsorb solar energy and transfer CO_2 and water to hydrocarbons. The high-performance based on these catalysts originates from the reasonable designed active sites. However, a summary and critical evaluation of the reactive sites from the atomic level is still missing in the published reports, while they always concentrated on the features and functions of materials. The fundamentals of these active sites are basic for the further development of this field. Significant accomplishments have been made in an in-depth understanding of the mechanism and process of photocatalytic CO_2 reduction.

In this chapter, we critically assess different strategies to fabricate various forms of atomic-level reactive sites on the photocatalyst and explore the atomic-level understanding of the structure-performance relationships. Particularly, the contents are discussed according the following two aspects: (1) Different strategies to fabricate atomic-level reactive sites including vacancy engineering, single atoms, surface modification and frustrated Lewis pairs; and (2) Relationships between the reactive sites and photocatalytic CO_2 reduction performance and their impacts on the selectivity, stability, efficiency and reactivity. Additionally, we give some perspectives on this research field which enable the researchers to design and fabricate more efficient photocatalysts.

2.2 Atomic-Level Reactive Sites for Semiconductor-Based Photocatalytic CO_2 Reduction

This Chapter includes work published in the journal article ***Adv. Energy Mater.*** 2020, 10, 1903879. It presents a review of recent literature covering the active sites for CO_2 photoreduction and critically assesses the challenges of this field. Perspectives are also provided for the atomic-level design and fabrication of active sites.

Statement of Authorship

Title of Paper	Yanzhao Zhang, Bingquan Xia, Jingrun Ran, Kenneth Davey, Shi Zhang Qiao
Publication Status	☑ Published ☐ Accepted for Publication ☐ Submitted for Publication ☐ Unpublished and Unsubmitted w ork w ritten in manuscript style
Publication Details	Zhang, Y., Xia, B., Ran, J., Davey, K., Qiao, S. Z., Atomic-Level Reactive Sites for Semiconductor-Based Photocatalytic CO2 Reduction. Adv. Energy Mater. 2020, 10, 1903879.

Principal Author

Name of Principal Author (Candidate)	Yanzhao Zhang		
Contribution to the Paper	Design and conducted the experiments, analysed the data, wrote the manuscript.		
Overall percentage (%)	70%		
Certification:	This paper reports on original research I conducted during the period of my Higher Degree by Research candidature and is not subject to any obligations or contractual agreements with a third party that would constrain its inclusion in this thesis. I am the primary author of this paper.		
Signature		Date	06/12/2022

Co-Author Contributions

By signing the Statement of Authorship, each author certifies that:

i. the candidate's stated contribution to the publication is accurate (as detailed above);

ii. permission is granted for the candidate in include the publication in the thesis; and

iii. the sum of all co-author contributions is equal to 100% less the candidate's stated contribution.

Name of Co-Author	Bingquan Xia		
Contribution to the Paper	Discussion and revision of the manuscript		
Signature		Date	06/12/2022

Name of Co-Author	Jingrun Ran		
Contribution to the Paper	Assisted in experimental design and setup, sample characterization and data analysis. Provided review and comments on the manuscript.		
Signature		Date	24/1/23

Name of Co-Author	Kenneth Davey		
Contribution to the Paper	Discussion and revision of manuscript		
Signature		Date	6/12/2022

Name of Co-Author	Shi-Zhang Qiao		
Contribution to the Paper	Supervision of the work, discussion and conceptualization of this manuscript and manuscript evaluation and revision.		
Signature		Date	25/01/23

Atomic-Level Reactive Sites for Semiconductor-Based Photocatalytic CO_2 Reduction

Yanzhao Zhang, Bingquan Xia, Jingrun Ran, Kenneth Davey and Shi Zhang Qiao**

Y. Zhang, B. Xia, Dr. J. Ran, Dr. K. Davey, Prof. S.Z. Qiao

School of Chemical Engineering & Advanced Materials, The University of Adelaide, Adelaide, SA 5005, Australia.

E-mail: s.qiao@adelaide.edu.au; jingrun.ran@adelaide.edu.au

Abstract

Photocatalytic CO_2 reduction is an effective means to generate renewable energy. It involves redox reaction reduction of CO_2 and oxidation of water that leads to the production of solar fuel. Significant research effort has therefore been made to develop inexpensive and practically sustainable semiconductor-based photocatalysts. The exploration of atomic-level active sites on the surface of semiconductors can result in an improved understanding of the mechanism of CO_2 photoreduction. This can be applied to design and synthesis of efficient photocatalysts. In this review atomic-level reactive sites are classified into four types: vacancies, single atoms, surface functional groups, and frustrated Lewis-pairs (FLPs). These different photocatalytic reactive sites are shown to have varied affinity to reactants, intermediates and products. This changes pathways for CO_2 reduction and significantly impacts catalytic activity and selectivity. The design of a photocatalyst from an atomic-level perspective can therefore be used to maximize atomic utilization efficiency and lead to a high selectivity. The prospects for fabrication of effective photocatalyst based on in-depth understanding are highlighted.

1. Introduction

Since the industrial revolution, there has been a significant increase in global economies and populations, and a growing interdependence of these on technology. This dependence however requires ever increasing energy. Global energy demand is estimated to reach at a 2-fold increase by the mid-century relative to the present.[1] Fossil fuels including coal, oil and natural gas, account for more than 80 % of current energy demand.[1, 2] However, at least two significant problems will emerge if there is an uncontrolled and continuing reliance on these: fossil fuels-greenhouse impacts, and resource depletion.

Uncontrolled emission of carbon dioxide (CO_2) will lead to environmental green-house impacts such as changes in precipitation, atmospheric warming, and sea-level rises. Worryingly, these are irreversible in short-term.[1-5] It is estimated that if atmospheric CO_2 exceeds 600 ppm, the sea-level will increase by ~ 0.4 m. Consequences could be catastrophic.[3,4] Significantly, fossil fuel resources are not renewable, and will therefore ultimately be depleted.[1] To address these problems, a sustainable, environmentally-friendly and low-cost energy source is urgently needed globally. Solar energy is seen as promising. This is because it provides more energy in one-hour than the annual energy consumption by all humans.[1, 2] The promise is to be able to convert solar energy into chemical energy as hydrocarbons, such as through photocatalytic CO_2 reduction. This is attractive because it artificially mimics natural photosynthesis.[6-8] The potential of artificial photosynthesis is that it could simultaneously reduce global CO_2 accumulation and provide a sustainable fuel to meet growing global energy demand.[9-19] Since Halmann[20] in 1978 reported a single crystal gallium phosphide that transferred CO_2 into HCOOH, HCHO and CH_4 under ultraviolet (UV) light irradiation, photocatalytic CO_2 reduction, based on semiconductors, has had potential for artificial photosynthesis. In general, photocatalytic CO_2 reduction by semiconductor-based catalysts is complex and involves three essential steps, namely: 1) light absorption by semiconductors, 2) motivated electron-holes separation and transfer, and; 3) redox reaction between photogenerated charges and reactants absorbed on the surface of semiconductors. The first two have been widely studied and different strategies have been developed to broaden light absorption and to promote separation of charge, such as defect engineering,[13-16, 21] morphology adjustment[22-27], and heterostructure fabrication.[28-31] Recently, research interest has been directed to the third essential step.

However, there remain three obstacles that limit the photocatalytic efficiency in terms of the redox reaction. First is the difficulty for gaseous CO_2 to be absorbed by solid photocatalysts.[32-35] This heterogeneous catalysis makes absorption and diffusion of reactant on the surface of photocatalysts complex. Second, CO_2 molecules are highly thermodynamically stable. The high bond energy of C=O (750 kJ mol^{-1}) means that the dissociation of CO_2 requires high energy by conventional methods.[7, 22] Third, the pathway of photocatalytic CO_2 reduction appears complicated. In most cases, water vapour provides hydrogen and consumes the photogenerated holes. The intermediate reactants can be various and the pathway of redox reaction can be influenced by the surface chemical environment of photocatalysts, and the reaction environment.[36-46]

Although a number of reviews have been published that summarize the effectiveness of these strategies,[2, 6-8, 22, 23] virtually none have reviewed the literature from the perspective of the impact of atomic-level reactive sites. This is important as these influence the adsorption and activation of CO_2 molecules and intermediate products thereby leading to different activity and selectivity. Xia et al.[6] reviewed atomically dispersed catalytic sites and outlined atomic-level catalytic sites. However, little detail was presented. A comprehensive review therefore is needed. Atomic-level reactive sites can be introduced into photocatalysts via a range of strategies such as: introducing vacancies in the crystal lattice,[9-19,32-67] doping single heterogeneous atoms[68-83], anchoring functional groups[84-102] and loading metal-complexes[103-110] on the surface, and fabricating FLPs.[111-120] With advances in characterization technologies and synthesis methods, researchers can design materials from atomic-level to reveal fundamental photocatalytic CO_2 reduction from spatial-and-time perspectives using, for e.g., High Resolution Transmission Electron Microscope (HRTEM), Scanning Transmission Electron Microscopy (STEM), and *in situ* technologies.

Vacancies in crystal lattices have received significant attention. For example, oxygen vacancy,[32-46, 48-62, 65-67] sulfur vacancy,[14, 47, 63] nitrogen vacancy,[11,64] carbon vacancy[10] and cation vacancies[12, 14, 16, 19], even dual vacancies[16, 18], have been investigated as high reactive sites for photocatalytic CO_2 reduction. These studies have shown that vacancies can improve performance of photocatalysts in at least three ways: 1) they can change the surrounding electron density, this benefits the affinity of CO_2 molecules, 2) introduce a defect energy level in the band gap that favours light adsorption, and 3) some vacancies can act as photogenerated electrons capture sites to promote charge separation. Reactive sites on the matrix can be introduced by doping heterogeneous single atoms, including: Cu,[68, 69, 77, 78] Ag,[73, 82] Co,[71, 75] Ni,[80] Mg[73, 82], and; Zr[70] single atoms. These act to maximize efficiency of catalysts. When these single atoms are doped into the crystal lattice, they change the physical/chemical properties because of a different ion radius, chemical valence and electron density. In most cases, heterogeneous atoms also act as reactive sites when they are exposed on the surface of photocatalysts. The different adsorption energies on these sites with reactants can change the redox reaction pathways to result in different final products.

The anchoring of functional groups and ions on the surface of photocatalysts is a means to construct reactive sites. Functionalized amine,[84, 86-89, 94, 99] hydrogenation[90-93] and other groups[95, 101, 102], show excellent affinity with molecules of CO_2 and therefore affect the redox reaction pathways. However, a problem with this means is the impeded charge transfer from

matrix to CO_2 molecules. The fabrication of a hybrid material with noble metal-complexes and semiconductors - a similar modification with functional groups - can provide reactive sites for photocatalytic CO_2 reduction.[105, 106, 109, 110] Nevertheless, they are always expensive. Creating FLPs is a recent strategy to fabricate reactive sites. Stephan et al.[121, 122] reported FLPs in 2007. Lewis-acid sites and Lewis-base sites cannot combine with each other because of steric-hindrance. However, the bonding orbital, and antibonding orbital, of particular smaller molecules, such as H_2, N_2 and CO_2, is influenced, respectively, by the empty orbit of the Lewis-acid and lone-pair electrons of the Lewis-base. These smaller gas molecules however can be polarized, and result in dissociation and activation of these gas molecules. Stephan et al. developed FLPs based on homogeneous catalysis in which FLPs are unstable and un-recyclable. These are serious drawbacks that restrain fabrication and use of FLPs. Importantly, Geoffrey et al.[117, 118] fabricated FLPs on the surface of $In_2O_{3-x}(OH)_y$ for the first time to demonstrate significant CO_2 capture, and excellent photocatalytic rates. Fabrication of FLPs, in particular hydroxides and oxides, is more readily done than with other materials because unsaturated metal ions, due to the oxygen vacancies and the adjacent hydroxyls, can be FLPs.[111, 112, 114, 115, 118, 120] These findings have increased insight into utilization of FLPs for CO_2 absorption and activation and have been important for developments in this field. However, a comprehensive overview and comparative summary is missing.

Here, the design of a photocatalyst from atomic-level perspective is presented and an understanding is developed to maximize atomic utilization efficiency and high selectivity, which will provide practical guidance for the design and synthesis of significantly effective photocatalysts. In addition, we critically assess and comprehensively review various reactive sites for photocatalytic CO_2 reduction, together with characterization methods, functions and mechanisms. Prospects for fabrication of effective photocatalysts based on in-depth understanding are highlighted. Some new strategies and methods to prepare polynary reactive sites, such as dual vacancies, different components of reactive sites, and FLPs, are outlined. CO_2 photoreduction pathways and key influence factors are reviewed for different materials, together with related discussion for design of highly selective materials.

2. Fundamentals of Semiconductors for Photocatalytic CO_2 Reduction

2.1 Functions of Reactive Sites in Photocatalytic CO_2 Reduction

In photocatalytic CO_2 reduction, semiconductors act as photocatalysts because they generate electrons and holes under light irradiation that react with reactants absorbed on the surface of

photocatalysts, or particular co-catalysts. The reactive sites on the surface of photocatalysts have four different roles in enhancing photocatalytic CO_2 reduction: 1) CO_2 molecules can be adsorbed on these sites that have special affinity for CO_2; 2) reactive sites can lower the activation energy or overpotential for CO_2 reduction; 3) reactive sites can act as photogenerated electrons capture sites that promote charge separation, and; 4) they can change absorption and desorption energies of the intermediates and thereby improve selectivity.

2.2 CO_2 Reduction Pathways

CO_2 reduction is complex and various final products can be obtained from different reduction pathways e.g. CO, HCOOH, HCHO, CH_3OH and CH_4. However, these products require different reduction potentials (E_0 V *vs*. NHE at pH 7), namely:

$$CO_2 + e^- \rightarrow CO_2^- \quad E_0 = -1.90 \text{ V} \tag{1}$$

$$CO_2 + 2H^+ + 2e^- \rightarrow HCOOH \quad E_0 = -0.61 \text{ V} \tag{2}$$

$$CO_2 + 2H^+ + 2e^- \rightarrow CO + H_2O \quad E_0 = -0.53 \text{ V} \tag{3}$$

$$CO_2 + 4H^+ + 4e^- \rightarrow HCHO + H_2O \quad E_0 = -0.48 \text{ V} \tag{4}$$

$$CO_2 + 6H^+ + 6e^- \rightarrow CH_3OH + H_2O \quad E_0 = -0.38 \text{ V} \tag{5}$$

$$CO_2 + 8H^+ + 8e^- \rightarrow CH_4 + H_2O \quad E_0 = -0.24 \text{ V} \tag{6}$$

$$2H^+ + 2e^- \rightarrow H_2 \quad E_0 = -0.41 \text{ V} \tag{7}$$

From these, the strongest redox potential is seen to be - 1.90 V (Equation 1) in which the CO_2 molecule accepts the first electron. This potential is due to the high energy barrier that must be overcome for the linear CO_2 molecule to be curved on the surface of photocatalysts. This is regarded as the limiting-step in many photocatalytic CO_2 reduction systems. It is worth noting that water splitting is the competitive reaction to photocatalytic CO_2 reduction. The reductive reaction in photocatalysis is CO_2 reduced by photogenerated electrons, at the same time, the other half-reaction requires oxidative agents such as triethanolamine[105-107] (TEOA) or triethylamine (TEA).[95] However, water is the most widely used oxidative agent.

These agents can consume photogenerated holes and provide final products with hydrogen atoms. In this way, by-passing the side-reaction of water splitting is important in the approach to improve photocatalytic performance. Because all redox reactions occur on surface reactive sites of photocatalysts, it is instructive to summarize the functions of different reactive sites.

3. Vacancy Engineering

In crystal lattice, introducing vacancies is an effective means to improve catalytic performance. This has received therefore significant attention from researchers. Different vacancies are fabricated in crystals including oxygen vacancy[33, 36, 37, 41, 43, 49, 51-53, 55, 56, 60, 124], sulfur vacancy[9, 47, 63], nitrogen vacancy[11, 64] and, some cation vacancies.[14, 123] Some researchers introduce dual vacancies[18] in the same material. This can however change the neighbouring electronic structure and cause lattice distortion and lead to different properties.

3.1 Oxygen Vacancy (O_v)

3.1.1 TiO_2 Based Photocatalyst

Titania has a number of advantages as a photocatalyst such as: environmentally friendly, inexpensive, and good physical/chemical properties.[125-130] However, its band gap is too large to absorb visible light and poor surface reactive sites limit its utilization for photocatalysis. Introducing oxygen vacancies into the lattice is an effective strategy to broaden the light response. The surface oxygen vacancy can serve as reactive sites for CO_2 adsorption and activation, thereby promoting the overall reaction. Oxygen vacancy has been widely researched since black titanium dioxide was prepared in 2011 by Chen et al.[131] in photocatalysts based on titanium dioxide. Hydrogenated titanium dioxide has significant oxygen vacancies. The two electrons introduced by oxygen vacancy preferably occupy the Ti 3d orbit on the nearest neighbouring Ti ions of the oxygen vacancy, leading to the formation of Ti^{3+}. These defects can introduce tail-states in the forbidden-band gap thereby broadening the light absorption profile. Initially, black titanium dioxide was utilized for water splitting. After which, some researchers investigated it in photocatalytic CO_2 reduction. For example, Yin et al.[32] reported that CO_2 molecules are more likely to bond with the oxygen atoms near the oxygen vacancy site to form carbonate species. These are regarded as the important intermediate towards final hydrocarbon products such as CH_4 and CO. The length and angle of the C=O bond in CO_2 can be changed following absorption on these sites. This is because the reactive site can accept photogenerated electrons from matrix materials, and the C=O bond is affected by electrons and thereby weakened. Therefore, activation in these reactive sites is rapid.

However, the fabrication of black titania is complex and relatively energy demanding, and the formation of oxygen vacancy is affected by a number of factors. For example, Liu et al.[40] fabricated mixed anatase and rutile titanium dioxide with the oxygen vacancy and co-exposed (001) and (101) facets. These authors reported that the formation energy of O_v in the exposed

(101) facet is 4.46 eV which is lower than that in the (001) facets of 5.98 eV. These oxygen vacancies and Ti^{3+} can facilitate adsorption of CO_2 and form new intermediate (c-CO_3^{2-}). This can be verified by *in situ* diffuse reflectance infrared Fourier transform spectroscopy (*in situ* DRIFTS). At the same time, different coordinated Ti atoms on different facets can react as reactive sites. Density is important when these defective sites act as active sites. Excessive Ti^{3+} can act as a charge recombination centre thereby decreasing photocatalytic efficiency. Similarly, the low coordinated surface oxygen can influence photocatalytic performance of titania.[42] The oxygen vacancy formation energies on different facets with different TiO_2 morphologies are computed via density functional theory (DFT). An ordering of these values is (001) < (010) < (101) with energies of 3.5, 3.8 and 4.8 eV, respectively. These lower coordinated oxygen atoms and oxygen vacancies increase the basicity of facets, which is beneficial for CO_2 adsorption. Temperature-programmed desorption (TPD) tests show that disks of TiO_2 exposed with (001) and (101) facets have the greatest CO_2 capture capacity of 5.81 μmol m^{-2}.

Nevertheless, not all of the absorbed CO_2 can be activated by the photogenerated charges. This is because the physically absorbed CO_2 species can readily desorb from the TiO_2 surface, for example, particular carbonate species b-CO_3^{2-} and m-CO_3^{2-}.[51] The different exposed defective facets of titania may influence the pathway of CO_2 photoreduction. Ji et al.[46] gave two possible pathways in terms of defective anatase (101) surface, namely: fast hydrogenation (FH) path, and fast deoxygenation (FdO) path. These authors studied these two pathways via first-principles computations. Although the actual photocatalytic reaction proceeds via both pathways, final products are decided by one. They found that the oxygen vacancy is more active than Ti5c on a perfect surface along the FH pathway via lowering its energy barriers, whilst, the FdO pathway is difficult despite either a defective or perfect surface. In fact, mixed pathways are the preferable reaction during overall artificial photocatalysis. In these two pathways, the two electrons around the oxygen vacancy can prevent the absorbed intermediates from oxidizing by the photogenerated holes. This means that the oxygen vacancy influences the selectivity of photocatalysts.

A defective shell is fabricated on TiO_2 (001) facets.[49] The distribution of oxygen vacancies and Ti^{3+} was depicted by electron energy-loss spectroscopy (EELS) that showed that these defects exist mainly on the surface shell. Therefore, it enables these reactive sites to be exposed to the reactant, rather than act as a photogenerated charge recombination centre. Different titania crystal forms have different formation energy of oxygen vacancy. Brookite

for example has a lower formation energy (5.52 eV) than both rutile (5.82 eV) and anatase (5.58 eV). Liu et al. [69] prepared defective brookite under helium pre-treatment at a moderate temperature (300 ℃). These different crystals may have different pathways in terms of CO_2 photoreduction because from the *in situ* DRIFTS, CO_2^-, HCO_3^- and b-CO_3^{2-} are the main intermediates on the defective anatase surface, whilst CO_2^-, HCO_3^- and HCOOH are the primary intermediates on the defective brookite surface. The curved CO_2^- is the initial, key step in CO_2 photoreduction. The CO_2^- on defective brookite surface is more likely to react with H^+.

It is worth noting that another initial reactant, H_2O is affected by the oxygen vacancy on the brookite surface. The adsorption for CO_2 and H_2O is competitive whilst H_2 is not generated. The reason might be lack of noble metal co-catalysts, and that the intermediate for water splitting, such as protons, are consumed rapidly by the carbon species on the surface of photocatalysts. Yin et al.[33] fabricated hydrogenated TiO_2 by a Li-dissolved ethanediamine solvothermal method. It is known that the overpotential for CO_2 accepting the first electron from matrix materials is the greatest (*see* section 2.2). Therefore, it is usually the rate-determining step in photocatalytic CO_2 reduction. The first single electron reduction of CO_2 is facilitated by the defective surface of titania. The doped H and introduced defects on the surface of titania safeguard adsorption and activation of molecules of CO_2. The introduction of other co-catalysts can introduce oxygen vacancies and Ti^{3+} at the same time. These co-catalysts may have synergistic effects with these defects toward photocatalytic CO_2 reduction. For example, black titania was modified by Ni cluster and introduced with dual active-sites to improve selectivity.[43] The oxygen vacancy and Ni were composed of dual reactive sites. The synergistic effect of the dual reactive site can lower the energy barrier of the cleavage of C=O bonds (0.08 eV). In this adsorption structure, the carbon atom in CO_2 can bond with Ni and one of oxygen atoms in CO_2 can bond with the Ti5c (five-coordinated surface Ti atoms) near the oxygen vacancy (Ni-C(O)O-Ti[V_o]). This is energetically the most favourable adsorption structure. The bond length of C=O increased from 1.16 Å to 1.37 Å. The other two adsorption structures (Ni-C(O)O-Ni(a) and OC-Ni(a); O-Ni[V_o]) have energy barriers, respectively, of 0.59 ~~eV~~ and 0.85 eV.

In addition, Cu clusters can introduce oxygen vacancies on titania. Photo-deposited Cu clusters on the surface of TiO_2 can introduce oxygen vacancies under simulated solar light irradiation.[65] *In situ* electron paramagnetic resonance (EPR) shows that the intensity of oxygen vacancy signals decrease in CO_2 atmosphere because of filling by oxygen atoms of CO_2 molecules. The oxygen vacancy can serve as the reactive sites for the formation of CO_2^-.

Moreover, following CO_2^- desorption from oxygen vacancies, the oxygen vacancy can be formed again under light irradiation. The introduction of Cu clusters can improve the selectivity of CH_4.[34] The synergistic effect of oxygen vacancy and Cu has been studied.[69] Under light irradiation, CO_2 molecule can form Cu^+-CO and it is converted to CO according to the DRIFTS. Oxygen vacancies are filled by the O atom of CO_2, however, it can be regenerated under light irradiation and release oxygen gas at the same time thereby maintaining photocatalytic sustainability.

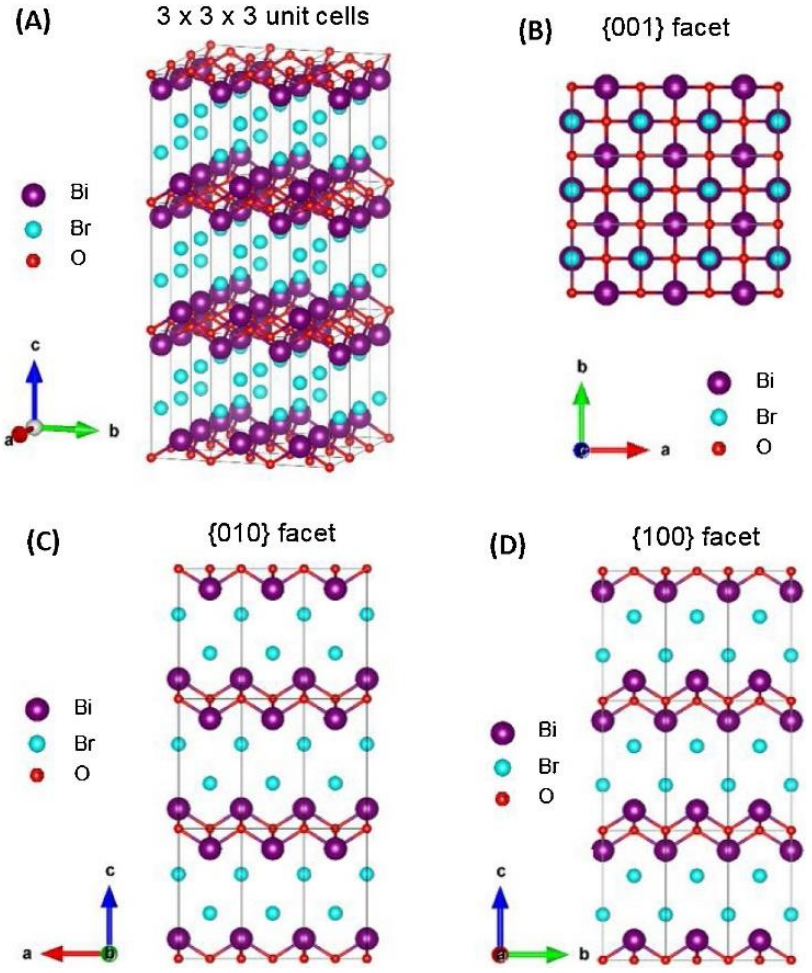

Figure 1. Schematic of BiOBr crystals, showing: a) 3D projection, b) {001} facet, c) {010} facet and d) {100} facet simulated by VESTA. Reproduced with permission.[61] Copyright 2018, Elsevier Inc.

3.1.2 Bismuth-based Photocatalyst

Recently, bismuth-based materials including bismuth oxide and bismuth oxyhalides (BiOX, where X represents halogen elements) have received significant global attention because of both environmental friendliness and abundant reserves.[132-137] Different BiOX morphologies are fabricated such as nanosheets,[54, 57, 59, 61] atomic layers[37] and nanotubes.[41] Oxygen atoms

readily leave the crystal lattice of BiOX so that oxygen vacancies can be introduced into the crystal, especially in nanotubes and ultrathin nanosheets.[59] The crystal structure of BiOX can be used to understand the principle of oxygen vacancies formation. Take for example, BiOBr, **Figure 1**. The structure of BiOBr is composed of $[Bi_2O_2]^{2+}$ slabs formed by strong covalent bonds, and two slabs of Br atoms stacked in the [001] direction. The $[Bi_2O_2]^{2+}$ slabs combine Br slabs with the weak Van der Waals interaction.[61] Self-built internal, static electric fields along the layer are therefore formed. This favours charge separation which is beneficial to overall, photocatalytic CO_2 reduction.[57] The BiOX exposed with (001) facets has a high density of oxygen atoms and small formation energy. This means oxygen vacancies can be readily formed on this surface.

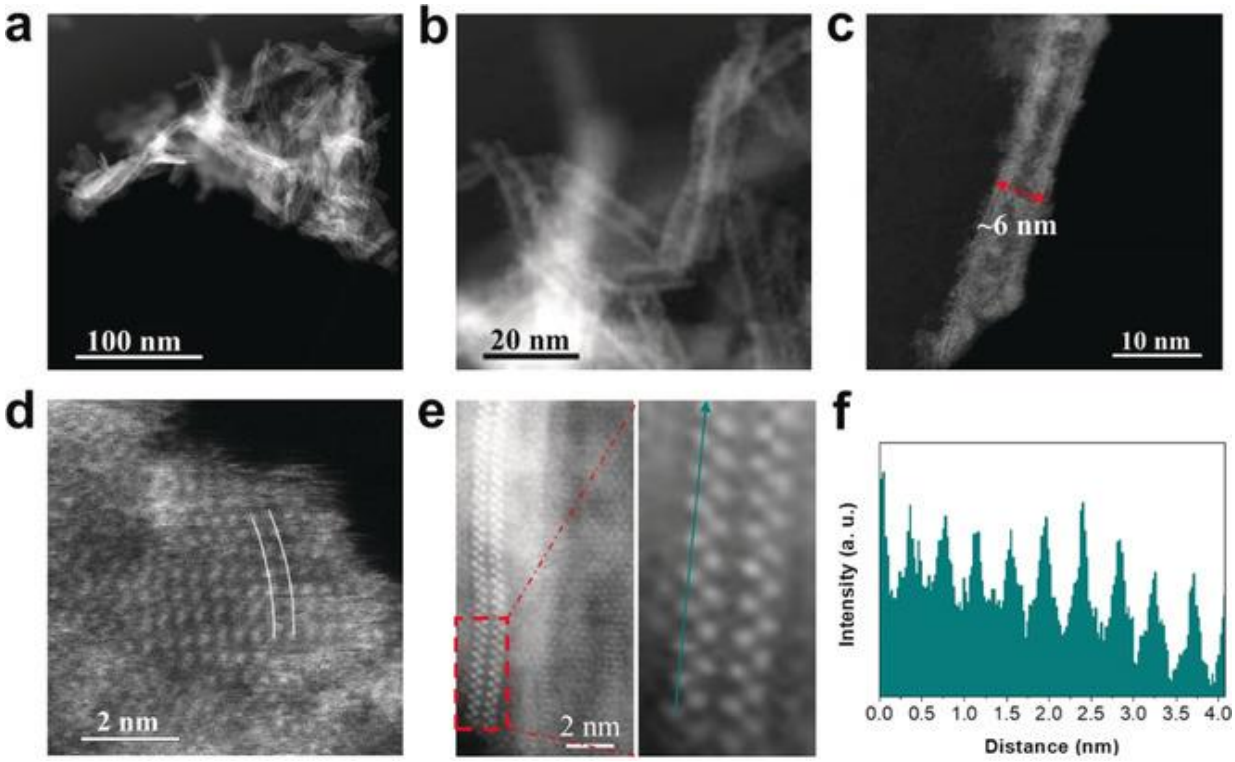

Figure 2. a)-e) Aberration-corrected HAADF-STEM images of $Bi_{12}O_{17}Cl_2$ nanotubes. f) Intensity profile corresponding to the dark cyan arrow in (e). Reproduced with permission.[41] Copyright 2018, WILEY-VCH Verlag GmbH & Co. KGaA, Weinheim.

Similarly with the hydrogenated titania, different methods of introducing the oxygen vacancy have been developed, including: annealing under inert atmosphere, introducing heterogeneous atoms, and UV light irradiation. These methods are effective approaches to produce oxygen vacancy in other material systems. For example, Wu et al.[37] fabricated defect-engineered BiOBr atomic layers under UV light irradiation. The ultrathin-layers promoted separation and transfer of photogenerated electrons and holes. This was demonstrated by time-

resolved fluorescence emission decay spectra and surface photovoltage. Moreover, the exposed (001) facets made it possible to form oxygen vacancies on the surface of atomic layers under high energy UV light. DFT computations showed that oxygen vacancies can introduce a new defect level in the forbidden-band gap, thereby increasing the visible light adsorption profile. According to *in situ* FTIR, the reduction pathway includes three steps, namely: 1) CO_2 is absorbed on the surface and H_2O is dissociated into hydroxy and hydrogenation ions, 2) CO_2* interacts with protons and generates COOH* which is the intermediate in the reduction of CO_2 to CO, and 3) COOH* is converted to CO*. Although the perfect and defective surface of BiOBr undergo the same pathways, greater production of COOH* on the defective surface means that the oxygen vacancy promotes activation of CO_2 and increases output of CO. Based on this, it can be readily know that the oxygen vacancy can be formed on the active facets (001) of BiOBr during photocatalytic CO_2 reduction.

Kong et al.[57] studied this. They found that oxygen vacancies can act as adsorption sites where CO_2 accepts one photogenerated electron and is activated into $\cdot CO_2^-$. This is the rate-determining step in CO_2 photoreduction. Generally, one oxygen atom from dissociation of CO_2 fills in the vacancy, resulting in sluggish photocatalytic performance. However, oxygen vacancies can be regenerated which leads to long-term stability and activity of BiOBr nanosheets. Apart from the photo-induced oxygen vacancy in BiOBr, the *in situ* method can introduce oxygen vacancies in BiOBr by a solvothermal method with ethylene glycol (EG). EG plays a requisite role in the formation of oxygen vacancy. It can be oxidized by the oxygen atom of BiOBr thereby forming a vacancy. Similarly, BiOCl can be applied to photocatalytic CO_2 reduction. Because of similar crystal forms with BiOBr and low bond energy, and long bond length of Bi-O bond, BiOCl can be readily doped with oxygen vacancies under light irradiation.[59] Because Bi atoms in BiOCl are exposed on the outside, whilst O atoms are buried on inside in crystal, Bi atoms readily escape from the crystal leading to Bi vacancy. However, Bi vacancy has not been studied in terms of photocatalytic CO_2 reduction. As for the oxygen vacancy, it is always filled by oxygen atoms from CO_2 and regenerated during subsequent photocatalysis under light irradiation. $Bi_{12}O_{17}Cl_2$ nanotubes can introduce a distorted lattice because of the curved structure, **Figure 2**. This is verified by measured exterior bismuth interatomic distance of 0.408 nm, a value much greater than that of 0.389 nm for bulk $Bi_{12}O_{17}Cl_2$.[41] This curved structure inevitably introduces more dangling bonds in the lattice. Generally, these dangling bonds at the material steps, corners, and edges, are disposed to be active sites for photocatalysis. These active sites enable the $Bi_{12}O_{17}Cl_2$ nanotubes to adsorb

CO_2 molecules with around 3.4 times greater CO_2 adsorption than that for bulk $Bi_{12}O_{17}Cl_2$. Because of abundant active sites on the surface of nanotubes, it shows better photocatalytic performance with 48.6 μmol g^{-1} h^{-1} generation rate of CO. This is 16.8 times greater than that for bulk $Bi_{12}O_{17}Cl_2$ of 2.9 μmol g^{-1} h^{-1}. Moreover, *in situ* method to form oxygen vacancy in BiOX materials is developed. Ma et al.[54] fabricated defective BiOCl ultrathin nanosheets by solvothermal method. They observed the redox reaction pathways. A portion of CO comes from the dissociation of HCOOH, which is an important intermediate. It can be readily converted into CO and some other intermediates on the defective surface, which is verified by DFT computations. The defective surface is more favourable for CO_2 to CO, with a rate determining barrier of 1.15 eV. The main pathway is along the hydrogenation with lower energy barrier. CH_4 is another final product. However, COOH* tends to dissociate into CO rather than further hydrogenate. This may be the reason that the final product is CO rather than CH_4. The CH_4 can be re-oxidized by photogenerated holes.

Bi-based photocatalysts include Bi_2O_3 and other oxides. For example, Chen et al.[55] prepared oxygen vacancy doped Bi_2O_3 atomic layers by oxidizing Bi metal directly. Moreover, the redox reaction occurred on the surface of oxygen vacancy rich Bi_2O_3 is different to photocatalytic CO_2 reduction. Methanol acts as photogenerated holes, sacrificial agents and CO_2 accepts photogenerated electrons from photocatalysts. The oxygen vacancy improves performance mainly from two perspectives: it can serve as the adsorption and activation sites for CO_2, by lowering adsorption energy and generate $\cdot CO_2^-$ that is regarded as the rate-determining step, and it can provide abundant localized electrons. The final product is dimethyl carbonate with nearly 100 % selectivity. Doping heterogeneous elements can also introduce oxygen vacancy.[62]

3.1.3 Other

Some other oxides are introduced into oxygen vacancy that can serve as active sites for CO_2 photocatalytic reduction, such as $Sr_2Bi_2Nb_2TiO_{12}$,[36] $LaTiO_2N$,[38] zinc germanate amorphous oxide,[39] ZnAl-layered double hydroxides (LDHs)[45], $In_2O_{3-x}(OH)_y$,[48, 50] WO_3,[52] $WO_3 \cdot 0.33H_2O$,[17] CeO_2,[53, 56], and Ga_2O_3.[58] For example, Zhao et al.[45] fabricated defect-rich ZnAl-LDH nanosheets and introduced oxygen vacancy by removing OH groups neighbouring Zn centres, thereby creating oxygen vacancy and under-coordinated Zn defect. The formation of oxygen vacancy is readily easier with decreasing LDH thickness. The photogenerated electrons can readily overcome the energy barrier for moving from oxygen vacancy to the adjacent Zn^{2+} centre that leads to formation of Zn^+. In this way, the oxygen

vacancy and Zn^+ complex are the reactive sites for CO_2 photoreduction. Its formation and stability are detected by EPR and X-ray adsorption near-edge structure (XANES) spectra. These defects can serve as the adsorption centres for CO_2 and water with adsorption energies, respectively, of 2.118 eV and 2.169 eV. These are greater than that for perfect ZnAl-LDH with 0.537 eV and 0.980 eV. Under light irradiation, the 4 s electron of the Zn^+ and oxygen vacancy complexes is excited to CO_2 and H_2O to promote overall photocatalytic CO_2 reduction.

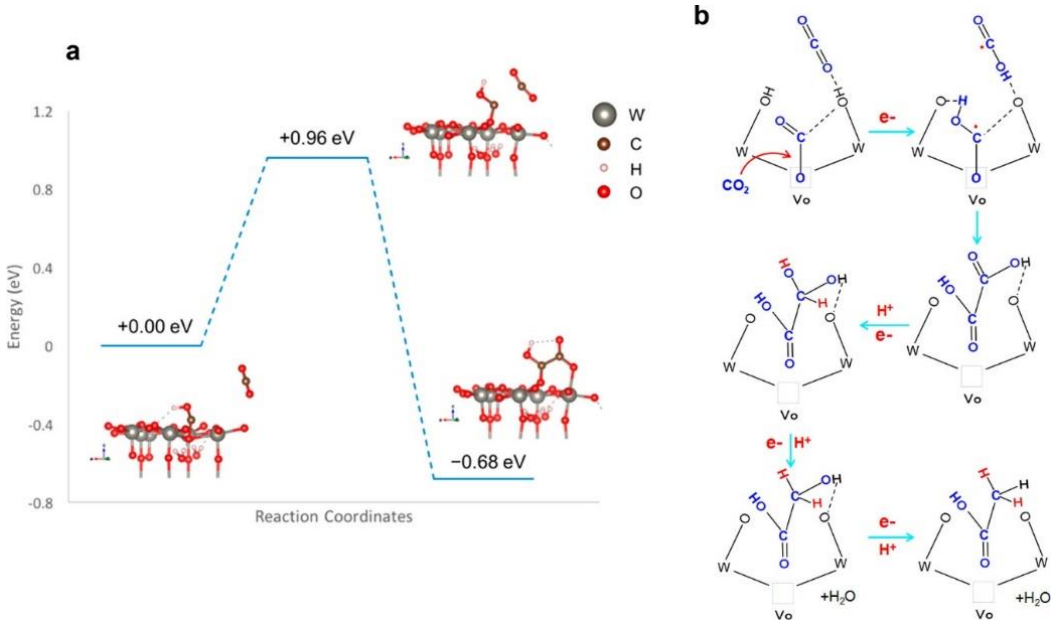

Figure 3. Possible CO_2 activation and hydrogenation on oxygen-deficient $WO_3 \cdot 0.33H_2O$ {001} surface. (a) Summary of the transition-state analysis and energy changes along the reaction pathways of C_2 product formation by DFT computation. The reference energy state is selected to be oxygen-defective $WO_3 \cdot 0.33H_2O$ {001} surface with one Vo-adsorbed CO_2 and one free CO_2. (b) Schematic of possible reaction pathway for CH_3COOH production. Reproduced with permission.[17] Copyright 2018, American Chemical Society.

Generally, some material systems introduce more than one reactive sites. Researchers can load another material that provides one reactive site on the matrix to provide another reactive site. For example, Lu et al.[38] modified $LaTiO_2N$ by loading La_2O_3 in which O_2^- served as basic sites for CO_2 chemisorption. In this basic site, the O-C-O bond angle is increased to 130.4° and the bond length is increased to 1.265 Å and 1.273 Å. The lowest unoccupied molecule orbit (LUMO) of CO_2 is decreased to promote injection of photogenerated electrons from the photocatalyst. However, the oxygen vacancy in $LaTiO_2N$ serves as the chemisorption site for H_2O. DFT computations show the adsorption model is favourable whilst this is different to many other material systems where the oxygen vacancy always captures CO_2 molecules and

gathers photogenerated electrons. For example, Wang et al.[39] prepared amorphous zinc germanate in which oxygen atoms can readily be oxidized by photogenerated holes and generate oxygen gas because of the weak lattice constraint. The oxygen vacancy captures oxygen atoms of CO_2 and both bond length and angle are increased. After the photogenerated electrons are injected into the activated CO_2, it is dissociated into CO and another oxygen atom cures defects which will be regenerated under light irradiation. In this way, the stability of oxygen vacancy is a significant challenge for defective oxides.

Sun et al.[17] prepared ultrathin nanotubes of $WO_3 \cdot 0.33H_2O$ with significant stable surface oxygen vacancies. These oxygen vacancies increase surface negative charge density to determine the adsorption and activation of CO_2. The O1 site in $WO_3 \cdot 0.33H_2O$ has the longer O-W bond. This means it is disposed to form the oxygen vacancy in lattice. The adsorption energy of CO_2 on this site is 1.32 eV, and the activated C=O bond length is increased from 1.169 to 1.459 Å. *In situ* DRIFT and TPD show that the oxygen vacancy adsorbed bicarbonate species can play a vital role in forming final CH_3COOH product. The bicarbonate species can be buried in the oxygen vacancy and form a hydrogen bond with an adjacent O atom. This leads to difficult desorption of HCO_3 from defective surface, **Figure 3a**. When another protonated CO_2 approaches the HCO_3, they will form a C_2-intermediate and the O atom in oxygen vacancy is released, making the oxygen vacancy stable. The pathway might readily be: $CO_2 \rightarrow \cdot COOH \rightarrow (COOH)_2 \rightarrow CH_3COOH$, **Figure 3b**. In this, the surface OH plays a vital role and can be regenerated under light irradiation. The synergetic-effect of two reactive sites leads to the formation of C_2 products and keeps the oxygen vacancy sustained. The doping of Cu atoms into CeO_2 can introduce stable oxygen vacancies and increase surface basicity that promotes CO_2 chemisorption and photocatalytic performance.[56] Oxides doped with oxygen vacancies have different mechanisms of CO_2 adsorption and activation. However, preparing ultrathin nanosheets modified with judiciously chosen co-catalysts and fabricating weaker metal oxygen bond materials, might be useful strategies for preparing and stabilizing defects. Moreover, the synergistic effect of defects and other reactive sites such as the adjacent coordinative unsaturated metal ions, hydroxyls and ions can enhance the photocatalytic performance. These useful explorations result in a deepening in understanding of the effect of oxygen vacancy and pave the way for designing defective photocatalysts.

Table 1. Vacancy engineering for photocatalytic CO_2 reduction.

Photocatalyst	Reactive sites	Reaction medium	Light source	Major product	Rate max.	Other products	Rate max.	Ref.
$CuIn_5S_8$	V_s	H_2O	>420 nm	CH_4	8.7 μmol g^{-1} h^{-1}	-	-	[9]
g-C_3N_4	V_C	H_2O vapour	300 W Xe lamp	CO	4.18 mmol g-1 h-1	-	-	[10]
g-C_3N_4	V_N	H_2O vapour	>420 nm	CO	6.21 μmol h^{-1}	-	-	[11]
NiAl-LDH	V_{Ni},V_{Al},V_{OH}	H_2O : CH_3CN : TEOA = 1 : 3 : 1	400-800 nm	CO	712 mmol g^{-1} h^{-1}	CH_4	168 mmol $g^{-1}h^{-1}$	[12]
$BiVO_4$	V_v	H_2O	300 W Xe lamp	CH_3OH	398.3 μmol g^{-1} h^{-1}	-	-	[13]
$ZnIn_2S_4$	V_{Zn}	H_2O	300 W Xe lamp	CO	33.2 μmol g^{-1} h^{-1}	-	-	[14]
ZnS	V_s	0.5MKHCO$_3$ and 0.5MK_2SO_3	300 W Xe lamp	HCOOH	427.5 μmol h^{-1}	CO	0.18 μmol h^{-1}	[15]
Bi_2MoO_6	V_{Bi}, V_o	H_2O	300 W Xe lamp	CO	3.62 μmol g^{-1} h^{-1}	-	-	[16]
$WO_3 \cdot 0.33H_2O$	V_o	H_2O	Solar simulator	CH_3COOH	9.4 μmol g^{-1} h^{-1}	CO HCOOH	Trace Trace	[17]
BiOCl	V_o, V_{Cl}	H_2O	>420nm	CO	3.94 μmol h^{-1} g^{-1}	CH_4	0.68 μmol h^{-1} g^{-1}	[18]
TiO_2	V_o	H_2O vapour	400-700 nm	CH_4	933 μmol h^{-1} g^{-1}	CO	588 μmol h^{-1} g^{-1}	[19]
TiO_2	V_o, Ti^{3+}	H_2O	400-780 nm	CH_4	1.4 μmol h^{-1} g^{-1}	CO	0.7 μmol h^{-1} g^{-1}	[32]
TiO_2	V_o	H_2O	400−780 nm	CH_4	2.7 μmol h^{-1} g^{-1}	CO	0.9 μmol h^{-1} g^{-1}	[33]
TiO_2	V_o	H_2O	300 W Xe lamp	CH_4	17.81 μmol h^{-1} g^{-1}	CO	4.23 μmol h^{-1} g^{-1}	[34]
TiO_2	V_o	H_2O vapour	>400nm	CH_4	3.3 μmol h^{-1} g^{-1}	-	-	[35]
$Sr_2Bi_2Nb_2TiO_{12}$	V_o	H_2O	300 W Xe lamp	CO	17.11 μmol h^{-1} g^{-1}	-	-	[36]
BiOBr	V_o	H_2O	>400nm	CO	87.4 μmol h^{-1} g^{-1}	-	-	[37]
La_2O_3 /$LaTiO_2N$	V_o-O^{2-}	H_2O	>420nm	CH_4	0.98 μmol g^{-1} h^{-1}	-	-	[38]
α-Zn-Ge-O	V_o	H_2O	300 W Xe lamp	CH_4	0.29 μmol	CO	0.28 μmol	[39]
TiO_2	V_o	H_2O vapour	400-700 nm	CO	~25 μmol g^{-1}	-	-	[40]
$Bi_{12}O_{17}Cl_2$	V_o	H_2O	300 W Xe lamp	CO	48.6 μmol g^{-1} h^{-1}	-	-	[41]
TiO_2/Ni	V_o-Ni	H_2O vapour	300 W halogen lamp	CH_3CHO	10 μmol g^{-1} h^{-1}	-	-	[43]
TiO_2	V_o	H_2O vapour	150 W solar simulator	CO	18.9 μmol g^{-1}	CH_4	Trace	[44]
ZnAl-LDH	V_o	H_2O	300 W Xe lamp	CO	7.6 μmol g^{-1} h^{-1}	-	-	[45]
ZnCdS	V_s	CH_3CN : H_2O : TEOA 3:1:1	420-780 nm	CO	0.39 μmol	CH_4	0.024 μmol	[47]
$In_2O_{3-x}(OH)_y$	V_o	H_2 150 °C	1000 W halide bulb	CO	~1.4 μmol g^{-1} h^{-1}	-	-	[48]
TiO_2	V_o	H_2O vapour	100 W mercury lamp	CH_4	2.49 μmol g^{-1} h^{-1}	-	-	[49]
In_2O_3	V_o	H_2 150 °C	1000 W halide bulb	CO	1.38 μmol g^{-1} h^{-1}	-	-	[50]
TiO_2/Au	V_o/Au	H_2O vapour	420-780 nm	CH_4	~5.5 μmol g^{-1} h^{-1}	CO	1 μmol g^{-1} h^{-1}	[51]
WO_3	V_o	H_2O	800-17000 nm	CO	~2.5 μmol g^{-1} h^{-1}	-	-	[52]
$Ce_{1-x}Zr_xO_2$	V_o	0.016M Na_2SO_3	300 W Xe lamp	CO	~8 μmol g^{-1} 6h	-	-	[53]

BiOCl	V_o	H_2O	>420nm	CO	8.66 μmol g^{-1} 4h	CH_4	Trace	[54]
Bi_2O_3	V_o	CH_3OH	300 W Xe lamp	dimethyl carbonate	Conversion 18%	-	-	[55]
CeO_2	V_o	H_2O vapour	300 W Xe lamp	CO	8.25 μmol g^{-1} 5h	-	-	[56]
BiOBr	V_o	H_2O vapour	>400nm	CH_4	4.86 μmol g^{-1}	-	-	[57]
Pt/Ga_2O_3	V_o	H_2O	300 W Xe lamp	CO	21 μmol g^{-1} h^{-1}	CH_4 CH_3OH HCHO HCOOH	Trace	[58]
BiOCl	V_o	H_2O	500 W Xe lamp	CO	8.1 μmol·g^{-1} 8h	CH_4	1.2 μmol·g^{-1} 8h	[59]
TiO_2	V_o	H_2O	300 W Xe lamp	CO	0.8 μmol·g^{-1} 4h	CH_4	0.7 μmol·g^{-1} 4h	[60]
BiOBr	V_o	H_2O vapour	>400 nm	CH_4	2.15 μmol g^{-1} h^{-1}	-	-	[61]
Bi_2WO_6	V_o	H_2O	>400 nm	CH_3OH	36 μmol g^{-1} h^{-1}	-	-	[62]
CdS	V_s	H_2O	>420 nm	CO	2.59 μmol g^{-1} h^{-1}	CH_4	0.33 μmol g^{-1} h^{-1}	[63]
g-C_3N_4	V_N	H_2O	300 W Xe lamp	CH_4	5.93 μmol g^{-1} 5h	CO	3.16 μmol g^{-1} 5h	[64]
TiO_2/Cu	V_o	H_2O	300 W Xe lamp	CH_4	8.68 μmol g^{-1} h^{-1}	-	-	[65]
TiO_2	V_o	H_2O vapour	400-700 nm	CH_4	880 μmol g^{-1} 6h	CO	550 μmol g^{-1} 6h	[67]
$ZnIn_2S_4$	V_{Zn}	Acetonitrile triethylamine	300 W Xe lamp	CO	276.7 μmol g^{-1} h^{-1}	-	-	[123]

3.2 Other Vacancies

3.2.1 Other Anion Vacancy

Sulfur vacancies have also been studied. For example, Li et al.[9] fabricated sulfur vacancy rich $CuIn_5S_8$ atomic layers that contained charge-enriched Cu-In dual sites and showed highly selective activity toward production of CH_4. DFT computations on $CuIn_5S_8$ showed charge enrichment around In and Cu atoms adjacent to sulfur vacancy. These dual sites can serve as active sites to strongly bond with C and O atoms to form the stable rate-limiting, COOH* intermediate. Moreover, another intermediate CHO* is prone to adsorption on the dual sites. The formation is exothermic and spontaneous, whilst CO* desorption is endothermic, and has to overcome a large energy barrier thereby leading to low production of CO. Additionally, the oxygen atom of the important intermediate CH_3O* radical that is the essential intermediate for CH_4 can bond with the charge-enriched In atoms, thereby weakening the C-O bond and promoting desorption of CH_4. These dual sites in the defective $CuIn_5S_8$ are coordinatively

unsaturated metal ions adjacent to sulfur vacancy and are more effective than the single In or Cu atoms.

The sulfur vacancy can also be introduced in ZnS crystal by doping with Ni[15] and Cd.[47] These sulfur vacancies can serve as CO_2 adsorption sites and photogenerated electrons trapping sites to facilitate charge separation and transfer.[63] 2D graphitic carbon nitride has received significant research attention. Nitrogen[11, 64] and carbon[10] vacancies are created in this material by annealing in an H_2 atmosphere, NH_3 atmosphere and *in situ* method. In nitrogen vacancy, abundant lone-pair electrons are captured to facilitate adsorption and activation of molecules of CO_2. The important intermediate CO_2^- is formed towards final CO. However, the excessive nitrogen vacancy has a negative impact on overall photocatalytic performance. This is because it can act as a charge recombination centre.[10] Co-doping K and B via thermal polymerization of dicyandiamide with KBH_4 can introduce nitrogen vacancy because KBH_4 can generate H_2 that reacts with $-NH_x$ to form gaseous NH_3 and leave nitrogen vacancy in C_3N_4. DFT computations show that the CO_2 adsorption site is an interstitial site for defective C_3N_4. The adsorption energy is nearly 4 times greater than that for pristine C_3N_4. *In situ* DRIFTS shows that defective C_3N_4 is favourable toward forming more CO_2^-. The electron-rich surface of C_3N_4 introduced by N vacancy facilitates the charge transfer to CO_2 and promotes reduction.[64] In addition, the carbon vacancy in C_3N_4 can serve as CO_2 adsorption sites. When a CO_2 molecule is adsorbed on the carbon vacancy of C_3N_4, the bond length in C=O is increased from 1.169 Å to 1.177 Å. This means that the carbon vacancy shows good CO_2 affinity and activation ability. This is confirmed by TPD test. The chemisorption and physical adsorption ability of the defective C_3N_4 are greater than that for pristine C_3N_4. [10] BiOCl with oxygen and chlorine dual vacancies has been fabricated.[18] The introduction of dual vacancies creates crystal distortion. This can be verified by X-ray absorption fine structure (XAFS). The dual vacancies not only change the band structure, but also act as reactive sites for CO_2 adsorption and activation.

3.2.2 Cation Vacancy

In addition to anion vacancies, cation vacancy has been studied to boost photocatalytic CO_2 reduction. For example, Jiao et al.[14] prepared zinc vacancy rich $ZnIn_2S_4$ one-unit-cell layers by solvothermal methods. Zinc vacancy in $ZnIn_2S_4$ results in dangling S bonds that capture photogenerated electrons. This can promote charge separation. The electron accumulation makes the defective $ZnIn_2S_4$ surface more negatively charged to improve adsorption of CO_2. He et al.[123] synthesised 3D hierarchical $ZnIn_2S_4$ nanosheets with rich Zn vacancies, and

explored surface adsorption of CO_2. CO_2 TPD indicated a stronger peak at 242.7 °C than that for bulk $ZnIn_2S_4$. This means alkaline sites on defective $ZnIn_2S_4$. These alkaline sites can serve as CO_2 adsorption sites. The *in situ* FTIR showed that the key intermediate CO_2^- could be more readily generated on the defective $ZnIn_2S_4$ surface. They also reported that the surface defects facilitate formation of surface hydroxyls. This is important as these appear to play a vital role in photocatalytic CO_2 reduction. However, sufficient confirming detail is not to hand. Gao et al.[13] introduced vanadium vacancy into $BiVO_4$ layers by the *in situ* method. They found that the greater vanadium vacancy density facilitates CO_2 adsorption on $BiVO_4$. Moreover, the surface adsorbed CO_2 and H_2O have polarization affects that strongly impact electron affinity and photocatalytic reaction. Di et al.[16] introduced Bi-O vacancy pairs in Bi_2MoO_6 nanosheets by ion exchange process with BiOBr ultrathin nanosheets as the template. CO_2 adsorption isotherms test showed that the defective Bi_2MoO_6 exhibits 7.4 times greater CO_2 adsorption than bulk samples, and that the key intermediate COOH* was observed from *in situ* FTIR. CO TPD showed that formed CO* can be readily desorbed from the surface at the lower CO onset desorption temperature. This indicates that the CO is the main, final product.

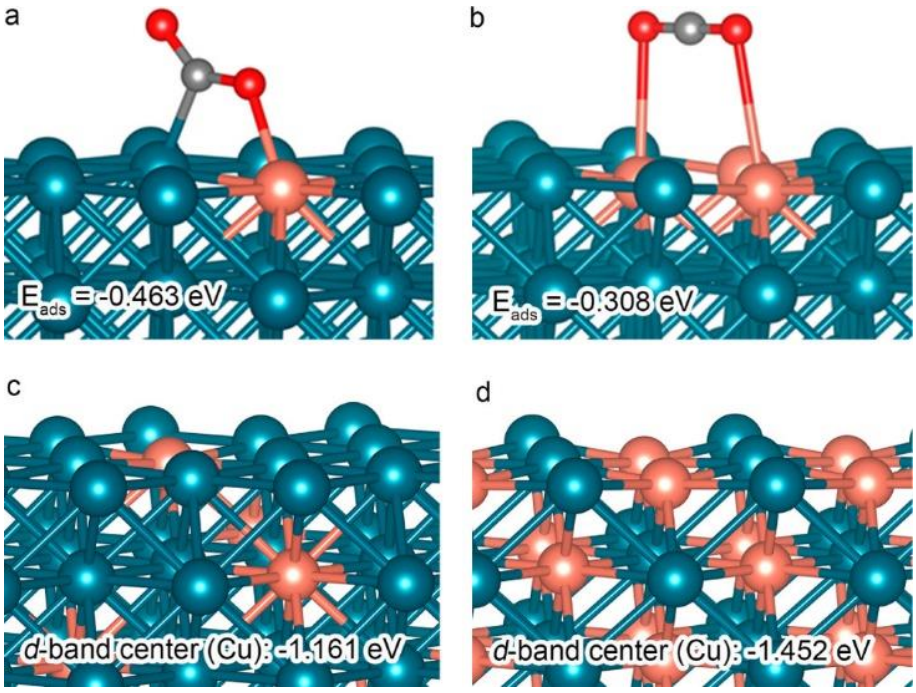

Figure 4. Most favourable configurations and adsorption energies of CO_2 at (a) an isolated Cu atom (i.e. a Cu-Pd pair), and (b) two neighboured Cu atoms (i.e. a Cu-Cu pair). The structural models and Cu d-band centres for ordered (c) Pd_7Cu_1 and (d) Pd_1Cu_1 lattices. All results are obtained from first-principles simulation. Reproduced with permission.[77] Copyright 2017, American Chemical Society.

The high selectivity of photocatalytic CO_2 reduction is always decided by desorption energy barrier of different intermediates. For example, surface hydroxyls on the nickel alumina layered double hydroxide (NiAl-LDH) can decrease the Gibbs free energy barrier of a vital, hydrogenation from CH_3* to CH_4 step.[12] Additionally, Ni and Al vacancies in NiAl-LDH can lower the energy barrier of CO_2 to CH_4 from 0.486 eV to 0.127 eV. The existence of metal vacancy and surface hydroxyls has a synergetic impact on selectivity of CO_2 photoreduction.

4. Single Atoms

Single atom catalysts have received significant attention because isolated single atoms on the surface of the matrix can maximize atom-utilization and catalytic efficiency. This is beneficial for reducing consumption of catalysts, especially for noble metals. In consequence, the isolated single atom as the heterogeneous co-catalyst has received research attention in photocatalytic CO_2 reduction.

4.1 Single Atom Doping

Because metal single atoms have affinity for CO_2 molecules, various single atoms are doped into matrix to form reactive sites for photocatalytic CO_2 reduction. Long et al.[77] fabricated isolated Cu atoms in Pd lattice. This reactive site showed a high selectivity of 96 % for CH_4 production. The authors loaded Pd nanoparticles doped with different, proportional Cu atoms onto TiO_2 nanosheets. The alloy metal nanocrystal integrated with TiO_2 nanosheets improved the charge separation and provided reactive sites for CO_2 reduction. Extended XAFS showed that Cu atoms are prone to bond with Pd atoms, and that isolated Cu atoms lead to high activity and selectivity. The optimal is Pd_7Cu_1. This exhibited a CH_4 production rate of 19.6 μmol g^{-1} h^{-1}. *In situ* DRIFTS showed that the Cu sites significantly enhance formation of three important intermediates species, namely: HCO_3^-, CO_2^- and $CO_3^=$. The different adsorption configurations, **Figure 4a and b,** have different adsorption energy determined from first-principles simulations. CO_2 optimal adsorption configuration is Cu-Pd pairs with an adsorption energy of - 0.463 eV. The d-band centre of Cu sites is elevated by surrounded Pd atoms, which is beneficial for catalytic performance, **Figure 4c and d**. Atomically dispersed Cu species is composed of different Cu with different chemical states.[78] Cu species are dispersed on the surface of $mTiO_2$. Under light irradiation the photogenerated electrons transfer from $mTiO_2$ to Cu species. The Cu (II) accepts the electrons and is reduced to Cu (I), and ultimately to Cu (0). Meantime, Cu (0) is oxidized to Cu (I) and then Cu (II) by photogenerated holes. This process is favourable for electron accumulation and to promote CO_2 reduction to CH_4. This consumes

eight electrons. The photogenerated electrons can be transferred from Cu species to CO_2 and the mixture of Cu (I)/Cu (0) species shows best photocatalytic performance. This is because Cu (0) with a low Fermi level is prone to accumulate electrons and Cu (I) is an active site to promote formation of CH_4. Interestingly, atomically dispersed Cu on the ultrathin nanosheets is processed by photodeposition methods[68] and Cu^0 is oxidized to Cu^+ with reducing CO_2 to CO.

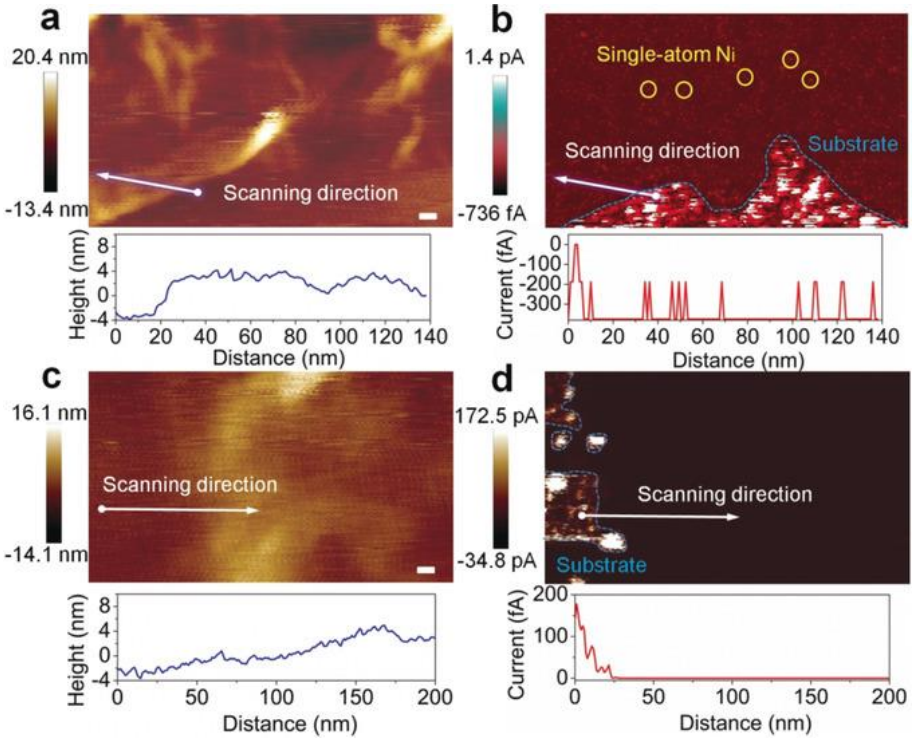

Figure 5. a) AFM topography and height profile of Ni-SNG catalyst (scale bar: 20 nm). b) Current-responsive image of Ni-SNG catalyst with corresponding line profiles of topography and current. c) AFM topography and height profile of Ni-SNG reference (scale bar: 20 nm). d) Current-responsive image of Ni-SNG reference with corresponding line profiles of topography and current. Reproduced with permission.[76] Copyright 2019, WILEY-VCH Verlag GmbH & Co. KGaA, Weinheim.

In addition to Cu, other single atoms have been reported for photocatalytic CO_2 reduction. For example, Gao et al.[79] investigated the effect of Pt and Pd single atoms loaded on graphitic carbon nitride by DFT. In the overall photocatalytic reaction, the graphitic carbon nitride provided hydrogen from the hydrogen evolution reaction, whilst isolated single atom Pt/Pd serve as reactive sites for CO_2 reduction. However, these two noble metal single atoms lead to different final products. Both Pt and Pd tend to be doped into the 6-fold cavity of graphitic carbon nitride with, respectively, a binding energy of -2.95 eV and -2.17 eV. The electron

density calculation results showed that the lone-pair electrons of the adjacent pyrudunic nitrogen atoms interact with metal atoms strongly, thereby preventing aggregation. The preferred final product of Pd/g-C_3N_4 is HCOOH with an energy barrier of 0.66 eV, whilst Pt/g-C_3N_4 is favourable to CH_4 with an energy barrier of 1.16 eV. The reason for these different final products might be because they have different affinities towards hydrocarbon reactants. Because of the two uncoupled electrons, Pt atoms interact with hydrocarbon intermediates more strongly, leading to a different energy barrier in the pathways, and different final products.

An additional important factor that impacts photocatalytic performance is electron accumulation on reactive sites. These atomically dispersed reactive sites accept photogenerated electrons from matrix materials, or photo-sensitizer, then transfer these to the adsorbed reactants such as CO_2, H_2O and intermediates, to promote the redox reaction until products desorb from the reactive sites. Photocatalytic CO_2 reduction always approaches complex pathways and the final product CH_4 is an eight-electron process, whilst CO requires just two electrons. Therefore, the different numbers of accumulated electrons on the reactive sites will lead to different pathways, and final products. Zhang et al.[76] investigated this factor of single Ni atoms and explored the collection and localization of electrons by electrochemical microscopy-atomic force microscopy (SECM-AFM). Results showed that the single nickel atom sites have a uniform capacity of electron storage, **Figure 5**. This research provided a novel perspective on photocatalytic performance of nickel single atoms for its special properties in electrons accumulation and the impacts on the photocatalytic performance.

Single atom silver manganese photocatalysts have also been developed.[73] Single silver atoms are formed in a single-atom chain in the lattice tunnels of the hollandite manganese dioxides by thermal migration of silver atoms. These lattice tunnels are made up of eight electron-rich oxygen atoms that serve as electron donors. The single-atom silver chain can also generate hot electrons due to the localized surface plasmon resonance. Under light irradiation, the single-atom silver chain can generate plasmon-excited electrons that are transferred to manganese dioxides via Ag-O-Mn link. This inhibits recombination of electron and holes and therefore boosts photocatalytic performance. The adsorbed CO_2 on the manganese dioxide will be reduced, at the same time the silver single atoms have affinity with H_2O which will be decomposed by the holes. The special lattice tunnels of manganese dioxides can effectively prevent aggregation of single silver atoms to maintain high photocatalytic performance.

Table 2. Single atoms for photocatalytic CO_2 reduction.

Photocatalyst	Reactive sites	Reaction medium	Light source	Major product	Rate max.	Other products	Rate max.	Ref.
TiO_2	Cu	H_2O	300 W Xe lamp	CO	3.2 μmol g^{-1} 2h	-	-	[68]
TiO_2	Cu/V_o	H_2O	150 W solar simulator	CO	4.3 μmol g^{-1} h^{-1}	-	-	[69]
ZrPP-1-Co	Co	Acetonitrile triethanolamine	>420 nm	CO	14 μmol g^{-1} h^{-1}	CH_4	0.5 μmol g^{-1} h^{-1}	[70]
PCN-222		Acetonitrile triethanolamine	>420 nm	$HCOO^-$	30 μmol	-	-	[71]
Zr-DMBD	Co^{II}	$[Ru(phen)_3](PF_6)_2$ CH_3CN/H_2O triethanolamine	= 450 nm	CO	3.33 μmol	-	-	[72]
MnO_2/Ag	Ag	H_2O vapour	>420 nm	CH_4	0.61 mol mol-1	-	-	[73]
TiO_2/Mg	Mg	Acetonitrile H_2O	UV light	CH_3OH	5910 μmol g^{-1} h^{-1}	CO CH_4	29.2 2.3	[74]
g-C_3N_4/Co^{2+}	Co	Acetonitrile triethanolamine	>420 nm	CO	0.128 μmol/mg	-	-	[75]
Ni-SNG	Ni	0.5 M $NaHCO_3$	Solar light	CO	216.094 mmol g^{-1}	-	-	[76]
TiO_2/Pd_xCu	Cu	H_2O	<400 nm	CH_4	19.6 μmol g^{-1} h^{-1}	CO	1.90 μmol g^{-1} h^{-1}	[77]
TiO_2/Cu	Cu	H_2O	300 W Xe lamp	CH_4	8.5 μmol g^{-1} h^{-1}	CO	3.5 μmol g^{-1} h^{-1}	[78]
MOF-525-Co	Co	Acetonitrile triethanolamine	400-800 nm	CO	200.6 μmol g^{-1} h^{-1}	CH_4	36.67 μmol g^{-1} h^{-1}	[80]
SnS_2	O	H_2O	>420 nm	CO	12.28 μmol g^{-1} h^{-1}	-	-	[81]
MnO_2/Ag	Ag	H_2	>420 nm	CH_4	6 μmol g^{-1} h^{-1}			[82]
$CsPbBr_3$/ZIF-67	Co	H_2O vapour	100 W Xe lamp	CH_4	10 μmol g^{-1} h^{-1}	CO	~2 μmol g^{-1} h^{-1}	[83]
InP/Ru complex	Ru	H_2O	>400 nm	HCOOH	4.71 μmol cm^{-1}	-	-	[103]
Dinuclear cobalt complex	Co	Acetonitrile H_2O	450 nm	CO	2.11 μmol	-	-	[104]
Eu-Ru(phen)$_3$-MOF	Eu	Acetonitrile triethylamine	420–800 nm	$HCOO^-$	45 μmol	-	-	[105]
Ru/g-C_3N_4	Ru	Acetonitrile triethylamine	>400 nm	HCOOH	19.345 μmol	CO	2.997 μmol	[106]
Co-complex/g-C_3N_4	Co	Acetonitrile triethylamine	400–800 nm	CO	17 μmol g^{-1} h^{-1}	CH_4	0.7 μmol g^{-1} h^{-1}	[107]
Ru-complex /g-C_3N_4	Ru	Acetonitrile triethylamine	>400 nm	HCOOH	1.854 μmol	-	-	[108]
Ru-complex /Ta_2O_5	Ru	Acetonitrile triethylamine	410–750 nm	HCOOH	3.5 μmol-h	-	-	[109]
Ru-complex /g-C_3N_4	Ru	N,N-dimethylacetamid triethanolamine	>400 nm	HCOOH	8.8 μmol	-	-	[110]
Ru-complex /g-C_3N_4	Ru	Acetonitrile triethanolamine	>400 nm	HCOOH	TON~170	-	-	[138]
Ru-complex/Ag /g-C_3N_4	Ru	EDTA • 2Na	>400 nm	HCOOH	TON>2000	-	-	[139]
Ru-complex /g-C_3N_4	Ru	EDTA • 2Na	>400 nm	HCOOH	TON=33000	-	-	[140]
Co-complex/ CdS	Co	$NaHCO_3$	>420 nm	CO	34.51 μmol			[141]
Co-complex/ g-C3N4	Co	Acetonitrile triethanolamine	>420 nm	CO	3.7 μmol	H_2	0.6 μmol	[142]
Ni-complex/ CdS	Ni	Acetonitrile	>400 nm	CO	1 μmol	H_2	trace	[144]
Fe-complex/ mpg-C3N4	Fe	Acetonitrile triethanolamine	>400 nm	CO	12.4 μmol	HCOOH H_2	0.7 μmol trace	[145]

Similar research with H_2 as the hole sacrificial agents has been reported with the same material system.[82] The utilization of the natural lattice channels of manganese dioxides to prevent the aggregation of single atoms and to maintain the single-atom chain surface plasmon resonance appears an ingenious method to stabilize single atoms and to improve photocatalytic performance. Non-metal single atom has been introduced into photocatalysts. Jiao et al.[81] fabricated SnS_2 atomic layers with partial oxidization. Compared with the oxides, the S 3p orbitals with more negative potentials occupy the valence bands of metal sulphides. This ensures that metal sufides have a narrower band gap than metal oxides. Pathways were investigated by *in situ* FTIR to show the adsorbed CO_2* reacts with the protons decomposed from water to form COOH*. This intermediate leads to the final product CO. The formation of COOH* is the rate-limiting step and requires a lower energy barrier on the surface of partially oxidized SnS_2 surface than that for perfect SnS_2 surface. This is attributed to the electron accumulation of O atoms around Sn atoms that enhance bonding between Sn and COOH*. Moreover, the desorption energy of CO* detected by CO TPD indicates that it is more readily desorbed from oxidized SnS_2 surface. The introduction of oxygen atom on the surface of metal sulfides can change the electron density around Sn atoms and thereby change the energy barrier for intermediate formation and desorption. Single atoms of transition metals are useful for adsorption and activation of CO_2 because their empty orbits can promote a bond with reactants. The coordinative number of single atoms is usually lower than that for surface atoms of bulk materials, which favours adsorption and activation of reactants. This is, additionally, a reason for higher catalytic performance. Moreover, d-band centre theory successfully describes this property. Generally, the more the d-band centre of the transition metal is close to the Fermi Level, the better the CO_2 activation according to the first-principle.[77-79]

4.2 Single Atoms Grafted in Metal Organic Framework (MOF)

To prevent single atom aggregation, these atoms are doped into metal organic frameworks (MOF). A judicious choice of different functional groups and metal single atoms can ensure improvement in photocatalytic performance. For example, Zhang et al.[80] developed a MOF with excellent performance in CO_2 capture, and visible light absorption, by unsaturated Co single atom incorporated with a porphyrin unit, **Figure 6a**. The incorporation of unsaturated Co atoms was verified by Co K-edge EXAFS and X-ray absorption near edge structure (XANES) spectroscopies, **Figure 6b, c and d**. These tests demonstrated the existence of Co-N bond without Co-Co and confirmed that Co atoms exit as mono-nuclear centres. Moreover, XANES confirmed unsaturated Co single atoms implanted in MOF-525-Co. These unsaturated

Co single atoms serve as adsorption affinity sites for reactants. The lone electron pairs in oxygen atoms of CO_2 bond with unoccupied Co orbits to improve CO_2 adsorption of photocatalysts. EPR test indicated that Co^{II} can trap the photogenerated electrons from the porphyrin unit and be transferred to Co^{I} under light irradiation without CO_2. Following introduction of CO_2 the signal for Co^{I} decreased. This showed that Co^{I} is oxidized back to Co^{II}, at the same time, CO_2 is activated by the electrons from Co^{II}. First-principles simulations revealed that the adsorption energy of CO_2 on the reactive sites is 2.189 eV. All of these tests illustrate that the coordinatively unsaturated Co sites linked with porphyrin units are the reactive sites for this hybrid material.

In addition to porphyrin units, other materials can serve as the light absorber. For example, Kong et al.[83] fabricated composite $CsPbBr_3$ and Co centres in ZIF-67. This composite material showed excellent charge separation performance and final product CH_4 selectivity. This can be attributed to the Co centres that are beneficial for electron accumulation and fabrication of interfaces between $CsPbBr_3$ and ZIF-67 that promote charge separation. Liu et al.[72] anchored Co centres into Zr-based MOF by incorporation of Co and freestanding -SH groups forming Co-S bonds. This research showed that Co-thiolate anchored in the MOF serves as the reactive sites. Zr clusters can be anchored in MOF and act as reactive sites for photocatalytic CO_2 reduction. Xu et al.[71] processed zirconium-porphyrin MOF, PCN-222. The mechanism of PCN-222 photocatalytic CO_2 reduction is similar to that for MOF-525-Co.

However, the tetrakis(4-carboxyphenyl)-porphyrin (H_2TCPP) units absorb light and generate photogenerated electrons and holes. Thereafter the electrons are transferred to Zr oxo clusters for generation of $HCOO^-$ when the TEOA acts as the hole-sacrificial agent. In addition, for metalation at the porphyrins centres to fabricate the reactive sites for CO_2 adsorption and activation, Chen et al.[70] developed a highly effective MOF, Zr-PP-1-Co. The metalation of porphyrins can provide pairs of positively charged anchors to bond with O atoms in CO_2 to enhance CO_2 adsorption. The photogenerated electrons are injected into the CO_2^+ and the metal ions are reduced to Co^0. Then, under TEOA as the hydrogen source and hole sacrificial agents, CO_2 is reduced and hydrogenated to CH_4. This MOF showed excellent selectivity of CH_4 production with 96.4 %. However, the exact factor for high selectivity remains unclear, although it is reckoned that the stability of CO_2^- adduct plays a vital role in this process.

Dual sites have also been introduced into MOFs. For example, Yan et al.[105] combined dinuclear $Eu(II)_2$ as connecting nodes and $Ru(phen)_3$-derived ligands as linkers to fabricate MOFs in photocatalytic CO_2 reduction. $Ru(phen)_3$-derived ligands often act as the photo-

sensitizer for photocatalytic CO_2 reduction, and the Eu(II) ion is effective in reduction conversion. $Eu(III)_2$ can accept electrons from the Ru complex and can be reduced to $Eu(II)_2$. The exposed $Eu(II)_2$ centre can adsorb CO_2 through Eu-O linkage with an adsorption energy -0.55 eV and bond length 2.745 Å. CO_2 can be activated by the electrons transferred from $Eu(II)_2$, something verified by charge density map from DFT computations. Following CO_2 injection with two electrons, $HCOO^-$ is formed and $Eu(III)_2$ is generated again. The charge transfer mechanism is demonstrated by an EPR test. MOFs are a promising material for the photocatalytic applications because of special structure and ready modification. However, significant drawbacks are instability and high cost. Therefore, it remains necessary to fabricate more effective MOFs for photocatalysis.

4.3 Metal-complexes

Metal-complexes can also act as reactive sites for photocatalytic CO_2 reduction. For example, Re or Ru metal-complexes often are used for selective formation of $COOH^-$ or CO. Different Ru complexes were investigated by Kuriki using C_3N_4 as the photo-sensitizer and TEOA as the holes sacrificial agents.[110] The photogenerated electrons transfer from C_3N_4 to the Ru complex. This charge transfer is impacted by the reduction potential of Ru metal-complex. RuP and RuH have similar reduction potential of -1.4 V *vs.* $Ag/AgNO_3$, which is a value more positive than the conduction band minimum for C_3N_4 of -1.65 V *vs.* $Ag/AgNO_3$. However, the lower reduction potential difference between Ru metal-complex (RuCP and RuMe) (-1.5 V *vs.* $Ag/AgNO_3$) and C_3N_4 leads to poor photocatalytic performance. The poor charge transfer properties are caused by the two $-CH_2-PO_3H_2$ (or $-CH_3$) groups. Therefore, the reduction potential of the Ru complex is crucial for charge transfer from C_3N_4 to Ru metal-complex, **Figure 7**. The possible linkage form of Ru complex and C_3N_4 might be hydrogen-bonding between $-NH_2$ groups on the edge of graphitic carbon nitride and phosphonate anchors in Ru complex.[108] In this hybrid material system, the adsorbed Ru metal-complex is verified by FTIR test and the loading amount of Ru metal-complex controls the rate of HCOOH production. The selectivity of HCOOH exceeds 80 %.[106] A similar result was also reported that the phosphonic acid groups are efficient in photocatalytic CO_2 reduction.[138] The binuclear ruthenium complex can bind robustly with carbon nitride in basic aqueous solution and form a Z-Scheme heterojunction.[139, 140] These two ruthenium metals have two different effects: one is the photosensitizing unit to form the Z-Scheme with carbon nitride; and the other is the catalytic unit to adsorb CO_2. The final product is HCOOH with more than 99 % selectivity because of the large overpotential for H_2 evolution.

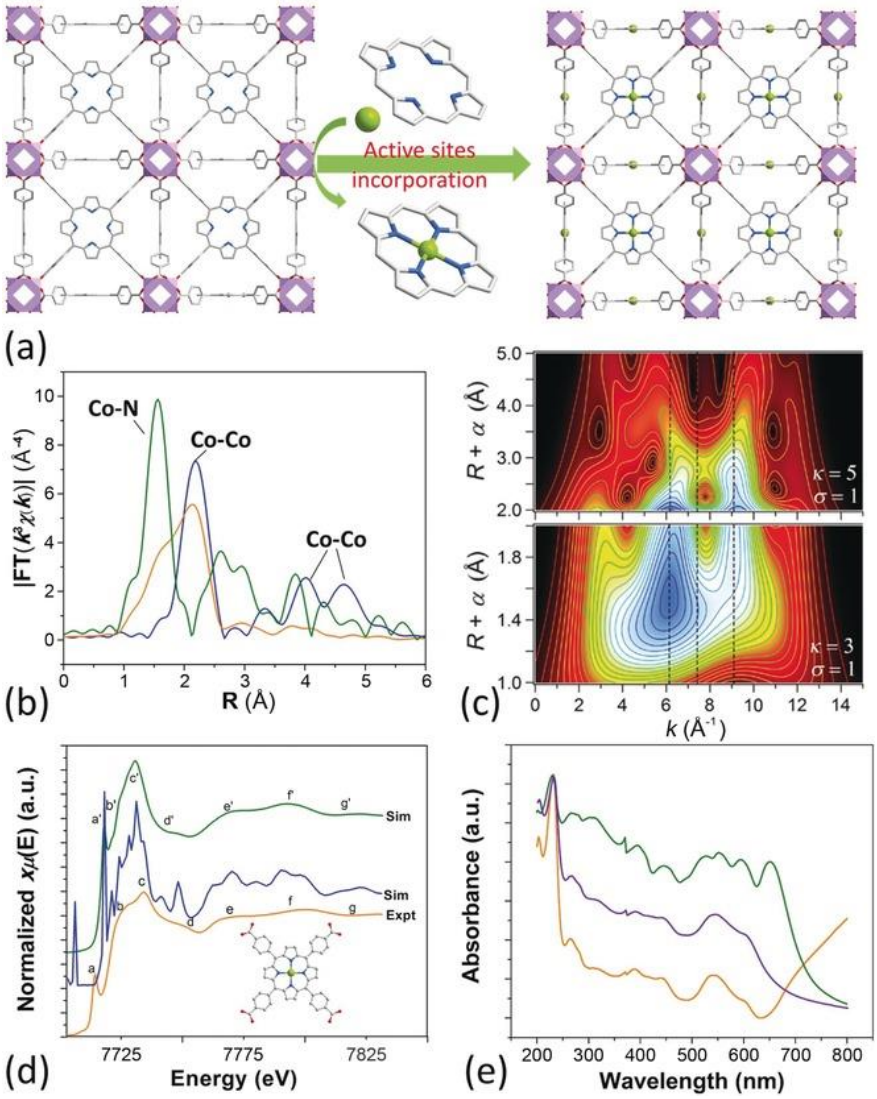

Figure 6. a) View of 3D network of MOF-525-Co featuring a highly porous-framework and incorporated active-sites. b) Fourier transform magnitudes of the experimental Co K-edge EXAFS spectra of samples (not corrected for phase shift). Key: Co foil (blue), Co@C (orange), MOF-525-Co (green). c) Wavelet transform for the k3-weighted EXAFS signal of MOF-525-Co, based on Morlet wavelets with optimum resolution at the first (lower panel) and higher (upper panel) coordination shells. Vertical dashed lines denoting k-space positions of the Co-N and Co-Co contributions are provided to guide the eye. d) Comparison between Co K-edge XANES experimental spectrum (orange) of MOF-525-Co and theoretical spectrum calculated with the depicted structure. For clarity, the non-convoluted theoretical spectrum is also shown. e) UV/Vis spectra of MOF-525 (green), MOF-525-Co (purple), and MOF-525-Zn (orange). Reproduced with permission.[80] Copyright 2016, WILEY-VCH Verlag GmbH & Co. KGaA, Weinheim.

In addition to graphitic carbon nitride, other particular semiconductors can act as photo-absorber, such as N-doped Ta_2O_5.[109] The charge transfer process is similar to that for the Ru metal-complex and C_3N_4 hybrids. However, the HCOOH selectivity is 75 %. It should be noted that the TEOA in the hybrid material system acts as both the electron donor and proton source. Because the valance band maximum of N-doped Ta_2O_5 is more negative than that for potential oxidation of H_2O to O_2, the N-doped Ta_2O_5 cannot oxidize the H_2O to O_2. However, if the N-doped Ta_2O_5 is replaced by other semiconductors in which the valance band maximum is more positive than the oxidation of H_2O to O_2, water can act in both these two roles in the hybrid materials, for example, InP/Ru complex hybrid photocatalyst.[103] This hybrid material shows 70 % selectivity to production of $HCOO^-$. Apart from Ru metal-complex, Co porphyrin can be loaded onto graphitic carbon nitride for photocatalytic CO_2 reduction.[141-143] Polymeric cobalt phthalocyanime (CoPPc) and Co ion coordinated with a bipyridine ligand were anchored on the surface of C_3N_4 as a cocatalyst. Zhao et al.[107] fabricated Co-porphyrin-oligomers of melems. FTIR test indicated the formation of Co-N coordination. The semiconductor graphitic carbon nitride generates electrons and holes under light irradiation. The photogenerated electrons can be readily trapped by Co^{II} sites to form Co^{I}, then the Co^{I} sites reduce the absorbed CO_2 to form CO. Some dinuclear metal-complex has been used as reactive sites in photocatalytic CO_2 reduction.[102,140, 141] Lu et al.[141] fabricated a negatively charged CdS to form an assembly with Co_2L by electrostatic interatcions that facilitate the electron transfer and photocatalytic performance. Ni complexes are used as anchoring groups on the surface of CdS.[144] The metal complexes are expensive and are used as cocatalysts in aqueous solution to favour H_2 evolution reaction. $[Ni(terpyS)_2]^{2+}$ is inexpensive and the anchored complex on the CdS quantum dots can suppress the H_2 evolution. Fe(qpy) was researched and is reported to show good selectivity (99 %) for CO.[145] It is concluded that researchers should pay increased attention to dinuclear and multinuclear metal-complex reactive sites based on the semiconductors for photocatalytic CO_2 reduction.

5. Surface Modification

Because photocatalytic CO_2 reduction occurs on the surface of photocatalysts, the surface chemical environment impacts directly photocatalytic performance. Therefore some researchers have attempted to modify the surface of the semiconductors by particular functional groups to improve CO_2 adsorption and activation. These functional groups mainly include metal ions and groups, $-NH_2$ and -OH. These functional groups can be grafted onto the surface

of photocatalysts to change the CO_2 adsorption configuration and lower the adsorption and activation energy barrier.

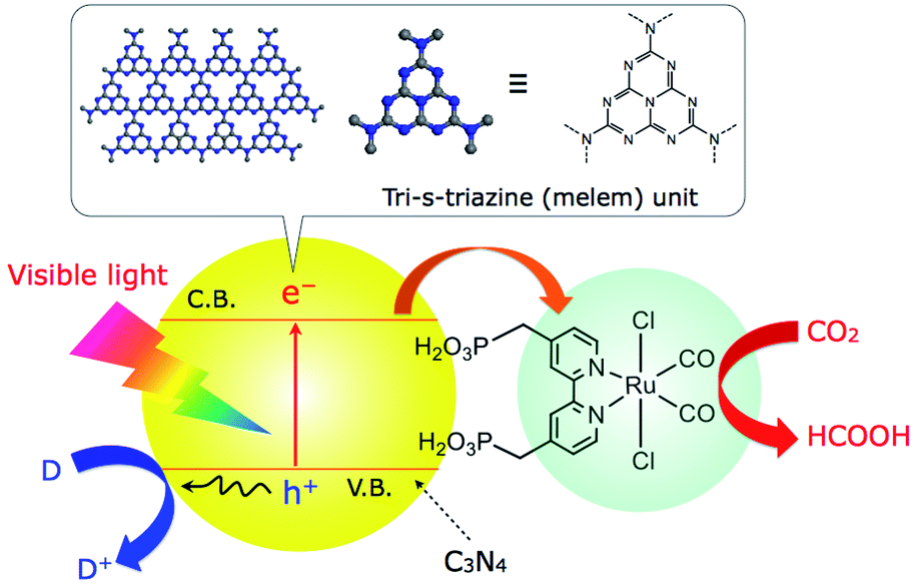

Figure 7. Schematic of photocatalytic CO_2 reduction on Ru/C_3N_4 composite under visible light illumination. Reproduced with permission.[108] Copyright 2014, The Royal Society of Chemistry.

5.1 Metal Ions and Groups

2D materials such as g-C_3N_4[146-148] are an ideal matrix for surface modification because they have a large specific area and short charge transport distance. These properties are favourable to light adsorption and charge transfer.

Zhang et al.[102] grafted atomically dispersed Mo atoms onto the surface of amorphous g-C_3N_4 by polycondensation of melamine and ammonium molybdate. X-ray diffraction patterns showed that the long-range order of g-C_3N_4 is broken with its typical peaks decreased significantly with increasing loading of Mo. However, the FTIR test illustrated that the short-range order of g-C_3N_4 remains unchanged, which indicates that the introduction of Mo atoms lead to amorphous change of g-C_3N_4. This is because the introduction of Mo atoms causes distortion of g-C_3N_4 and disordered amorphous atomic arrangement. The Mo 4 d orbit becomes the top of the valence band which narrows the band gap of g-C_3N_4 and broadens the light response profile. An additional factor is that the Mo will bond with C and N atoms. This will localize the electrons around Mo atoms. The new bonds will provide charge transport pathways decreasing recombination. The CO_2 adsorption and activation energy barrier will be decreased

on the Mo modified g-C_3N_4.[149] The bond length and angle of CO_2 will be changed to, respectively, 1.25 Å and 141.92°, significantly different to that for pristine g-C_3N_4 of 1.18 Å and 180°. The activation energy barrier is lowered by Mo modified g-C_3N_4 to 1.11 eV, compared with that of pristine g-C_3N_4 of 7.15 eV.

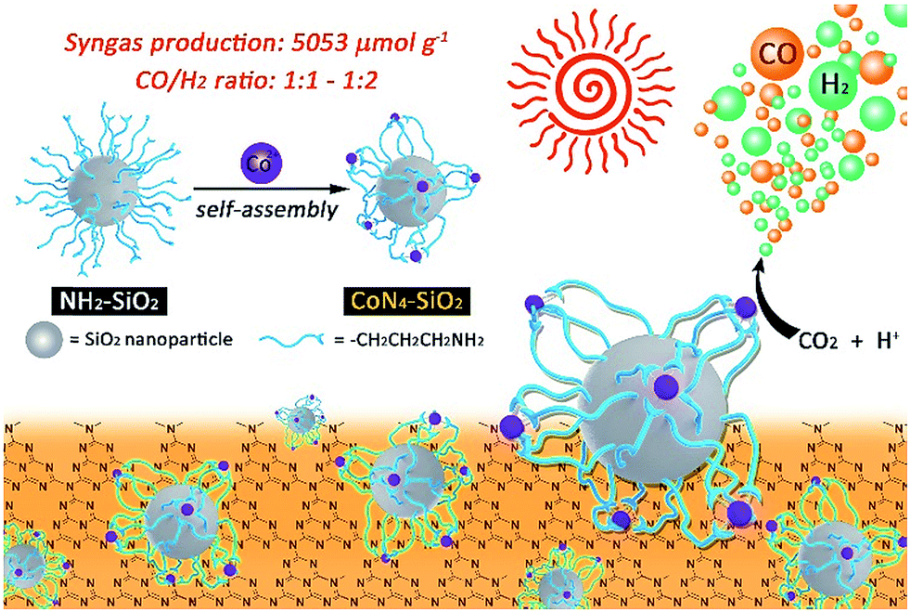

Figure 8. Schematic of the preparation of the CoN_4-SiO_2 nanoparticle and photocatalytic system. Reproduced with permission.[95] Copyright 2019, The Royal Society of Chemistry.

Hu et al.[95] fabricated CoN_4 active sites on SiO_2 based on g-C_3N_4 as a photo-sensitizer for photocatalytic CO_2 reduction. The Co-N_4 active site was formed by $CoCl_2$ and 3-(trimethooxysilyl)propan-1-amine (APTMS) on the SiO_2 surface based on strong coordination between CO_2^+ and amino groups, **Figure 8**. This hybrid material shows photocatalytic CO_2 reduction performance with the g-C_3N_4 as the photo-sensitizer and TEA as the electron donor in CO_2-saturated TEA/CH_3CN mixed solution. The $Co^{II}N_x$ species obtain one electron from excited g-C_3N_4 by light irradiation to form $Co^{I}N_x$ species. However, the CoN_4 reactive site is not sufficiently stable. It will decompose during photocatalysis. Huang et al.[75] dispersed single Co sites on the surface of g-C_3N_4. According to Co K-edge EXAFS, the Co coordination environment is similar to that for Co-cyclam without Co-O-Co. This indicates that the Co is dispersed as single sites on the surface of g-C_3N_4. However, with increasing Co load a Co-O bond occurs, whilst the cobalt oxides are inactive in photocatalytic CO_2 reduction. The hybrid material showed excellent selectivity for CO production of around 80 %.

Metal clusters can be loaded onto the surface of semiconductor photocatalysts. For example, Liu et al.[51] loaded Au cluster on the (001) facets of TiO_2 nanosheets with abundant

oxygen vacancies and Ti^{3+}. The nitrogen adsorption-desorption isotherms and CO_2 adsorption curves indicated that the decorated Au nanoparticles promoted chemical adsorption of CO_2 with an adsorption energy -1.87 eV, a value significantly greater than that without Au nanoparticles of -0.25 eV. The adsorbed hydrocarbons have different activities towards final products. For example, the surface HCO_3^-, CO_2^- and CO are active whilst the carbonate species including b-CO_3^{2-} and m-CO_3^{2-} are inactive. The Au-bound CO facilitates conversion of CO to produce CH_4. In addition, Bi ions are absorbed on the TiO_2 nanosheets for CO_2 photoreduction.[99] The isolated Bi ions facilitate the built-in electric field that promotes charge separation. The TiO_2-Bi is therefore preferable for production of CH_4.

5.2 Amine Functionalization

Amine-functionalized photocatalyst provides new reactive sites for adsorption of CO_2 and H_2O, especially on the surface of 2D materials exposed with abundant functional groups. Different matrix materials have been explored, such as graphitic carbon nitride, graphene, titania nanosheet, and MOFs. Huang et al.[86] prepared amine-functionalized g-C_3N_4 by monoethanolamine (MEA) solution. The condensed -NH_2 groups on the graphitic carbon nitride are potential CO_2 adsorption sites because of basic properties and the acidity of CO_2. However, the amount is too trace because g-C_3N_4 preparation is conducted under high temperature. Amino groups on the surface can promote CO_2 chemisorption, something verified by CO_2 adsorption curves and zeta potential tests. The CO_2 is adsorbed on the amine-functionalized g-C_3N_4 by coordinating with the amino groups. This process based on g-C_3N_4 can be realized with annealing under an ammonia atmosphere.[85] The optimal adsorption configurations on the surface of pristine g-C_3N_4 and amine-functionalized g-C_3N_4 have been explored through DFT with the result that adsorption energies are -0.99 and -1.37 eV, respectively. Beside the surface functional groups, the C_3N groups are exposed because NH_3 exfoliations are Lewis-base sites that can also act as CO_2 adsorption sites so the amine-functionalized g-C_3N_4 shows greater affinity for CO_2. Cho et al.[87] developed amine-functionalized reduced graphene oxide by an N,N'-dicyclohexylcarbodiimide coupling between the amine group of ethylenediamine and the carboxylic group of GO. The amine-functionalized graphene (AG) wraps-around the CdS nanoparticles to form the composite AG/CdS. The *in situ* FTIR test showed that the alkylammonium carbamate ion pairs, generated through interaction with two amine molecules and the isolated amine group, leads to the formation of carbamic acid. Results showed that the CO_2 adsorbed on the surface of AG/CdS can be activated. The CdS generates electrons under light irradiation and the graphene acts as

the transport pathways for the photogenerated charge. The activated CO_2 accepts the electrons from graphene and is reduced to CH_4, **Figure 9**.

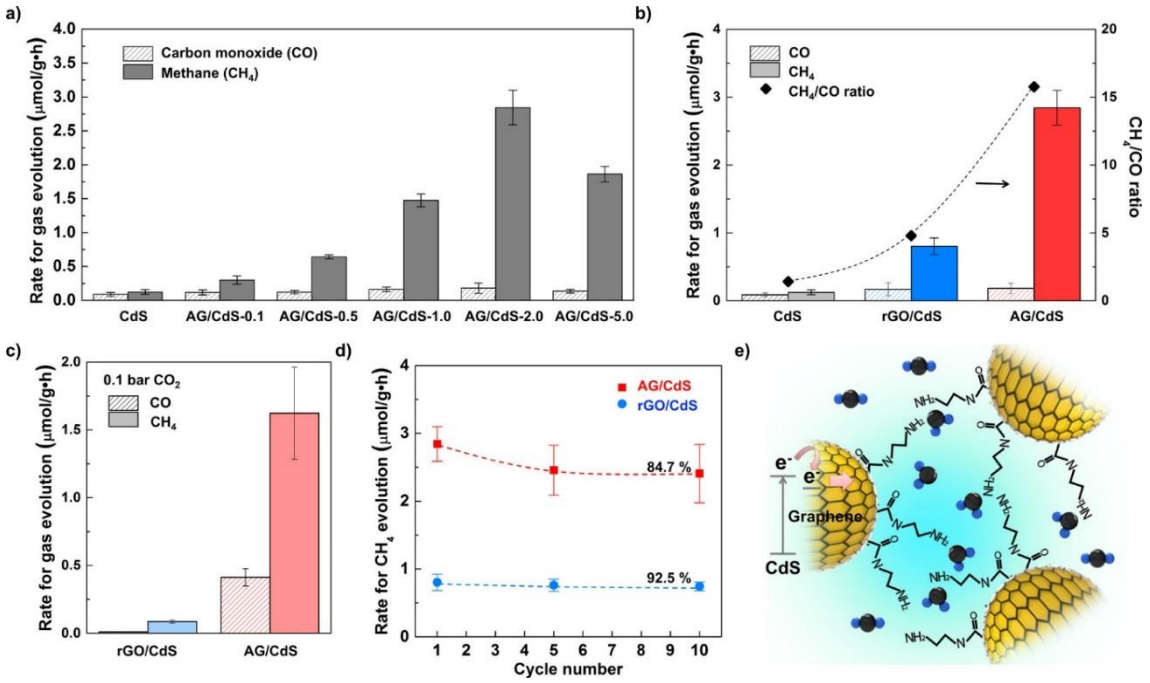

Figure 9. CO_2 photoreduction on CdS composites: (a) photoreduction of CO_2 (1 bar) on AG/CdS with varying graphene content under visible light (>420 nm); (b, c) CO_2 photoreduction and CH_4/CO ratio on CdS, G/CdS, and Ag/CdS (b) under CO_2 at 1 bar (40 °C) and (c) under low-pressure CO_2 (0.1 bar, 40 °C); (d) cyclic photoreduction of CO_2 on rGO/CdS and AG/CdS; (e) illustration of proposed mechanism of CO_2 photoreduction on AG/CdS. Reproduced with permission.[87] Copyright 2017, American Chemical Society.

Amino groups can be modified on the surface of titanate by the *in situ* method. For example, Liu et al.[88] prepared amine-functionalized titanate nanosheet-assembled yolk-shell microspheres for CO_2 photoreduction. The material was fabricated by solvothermal reaction using diethylenetriamime (DETA) as the morphology-control agent, because of the strong basicity of typical organic amine. Additionally, Sun et al.[100] developed K-incorporated amino-rich carbon nitride (K-AUCN) by treating g-C_3N_4 with KOH. The amino groups are formed by etching of KOH with the sacrifice of C and N species in g-C_3N_4 to introduce C and N vacancies in the g-C_3N_4 at the same time. The increase of amino groups was verified by XPS and FTIR. The result is the promotion of CO_2 adsorption and activation. The existence of K^+ incorporated with g-C_3N_4 in the layers, rather than on the surface, suppresses charge recombination. The vacancies broaden the light adsorption spectrum. These different reactive sites in g-C_3N_4 play different roles in photocatalytic CO_2 reduction to boost performance. MOFs, TiO_2 and ZnO

nanosheets can be grafted by -NH_2 groups. ZnO nanosheets[84] are prepared and modified by the one-step hydrothermal method using MEA to promote CO_2 chemisorption and to enhance performance of photocatalytic CO_2 reduction. NH_2-MIL-125(Ti) MOF is synthesised, and particular polar substituent groups such as -OH, -COOH and -NH_2, which have high affinity to CO_2, improve its adsorption capacity.[89, 94] Liao et al.[99] obtained amine-functionalized and hydroxyl-functionalized TiO_2 by using, respectively, MEA and ethylene glycol during the solvothermal reaction. The amine-functionalized TiO_2 (MEA-TiO_2) showed higher affinity toward CO_2 than hydroxyl-functionalized TiO_2 (EG-TiO_2). The amino groups incorporate with CO_2 molecules via the 'C-N' bond to form carbamate. This is more active than the linear CO_2. The carbamate accepts electrons from the surface titanium cations to implement reduction.

5.3 Additional functional groups

Other functional groups can also be grafted onto the surface of photocatalysts, such as the surface hydrogenation, cyano and carboxyl groups. The surface hydrogenation on some semiconductors can be developed to prepare high efficiency photocatalysts. Alkali-decorated graphitic carbon nitride can be obtained by treating the g-C_3N_4 in NaOH, or KOH, aqueous solution. The alkali-functionalized g-C_3N_4 does not show differences in terms of light adsorption, surface area, morphology and elemental states, except for CO_2 adsorption capacity and charge separation highlighted via CO_2 adsorption curves and photocurrent tests. From computation, pristine g-C_3N_4 (0.76 eV) and alkali-functionalized g-C_3N_4 (1.13 eV for KOH and 0.86 eV for NaOH) show different adsorption energies for H_2CO_3. This is the main form of CO_2 in photocatalysis. In this way, g-C_3N_4 treated with KOH exhibited 'best' photocatalytic CO_2 performance amongst the three types of g-C_3N_4.

Hydroxyl-group-enriched single TiO_2 crystal is fabricated by calcining hydrothermal production.[93] This work reported that surface hydroxyls have an affinity toward the Lewis-acidic CO_2 molecules and impact selectivity of CH_4 production. Commercial titania (P25) with alkalinized titanium carbide MXene also exhibited excellent CO_2 adsorption and provided abundant reactive sites for CO_2 photoreduction.[90] These authors conducted a range of experiments to investigate the role(s) of the surface OH groups in photocatalytic CO_2 reduction. Hybrids of alkalinized TiC with P25 (TC-OH/P25) exhibited both enhanced activity and selectivity for CH_4 when compared with pristine TiC/P25 and TiC/P25-OH. The energy barrier of CO_2 activation is decreased by distortion of the linear structure of CO_2 molecules because of the lowering of the energy level of LUMO. By DFT computation CO_2 adsorption energy on TC-OH is -0.44 eV – a value significantly less than that for TC-F of -0.13 eV.

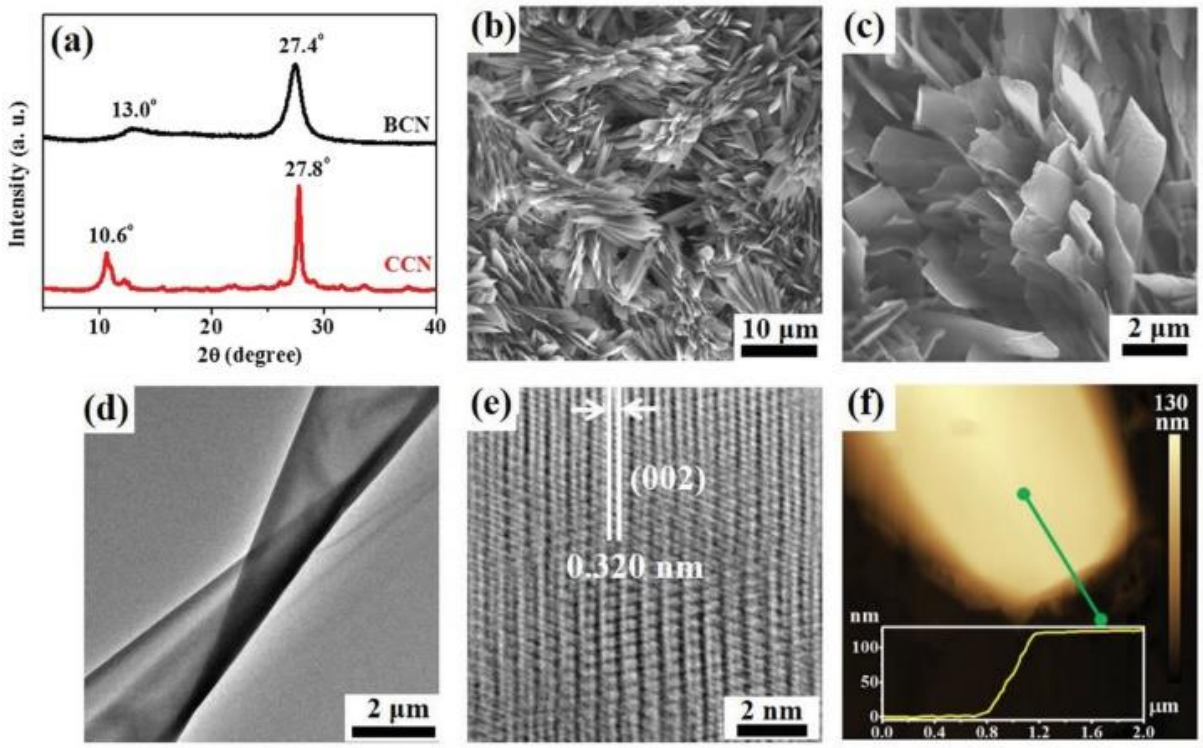

Figure 10. a) Powder XRD patterns of CCN and BCN. SEM b,c), TEM d), Fourier filtered Cs-corrected HRTEM e), and AFM f) images of CCN. Reproduced with permission.[98] Copyright 2019, Wiley-VCH Verlag GmbH &Co. KGaA, Weinheim.

The surface hydrogenation of photocatalysts has received research attention in related fields. However the role of surface hydroxyl groups and the strategies for introducing hydroxyls lacks a comprehensive study of photocatalytic CO_2 reduction. Xia et al.[98] developed crystalline carbon nitride with connecting cyano and carboxyl groups (CCN) on the surface using guanidine hydrochloride (GH) and dicyandiamide (DCD) as precursors in acetonitrile by solvothermal reactions. From XRD patterns, CCN samples have meaningfully different layer distances with ordinary g-C_3N_4 because of the interstitial functional groups, **Figure 10**. Interestingly, these functional groups not only provide CO_2 adsorption sites but also extend the light response profile, and improve charge transfer and storage on the surface. This in fact was verified by TPD, UV-Vis diffuse reflectance spectra and time-resolved photoluminescence. These impacts are different to those of other functional groups that often have a single impact on photocatalytic CO_2 reduction. Xie et al.[91] introduced different alkylamines (ethylenediamine (EN), diethylenetriamine (DETA) and triethylenetetramine (TETA)) into MIL-101-Cr MOFs by post-modification to investigate chemisorption properties toward CO_2 gas. Among these the EN modified MOF exhibited the greatest CO generation of 47.2 μmol g^{-1} h^{-1} with a 96.5 % selectivity. EN modification promoted CO_2 adsorption capacity with 3.57

mmol g^{-1}. Moreover, TPD tests showed that the anchored EN serves as chemisorption sites for CO_2. The electrochemical impedance spectroscopy, and PL tests, indicated that charge transfer and separation is promoted by the grafted EN. This is therefore beneficial for increased photocatalytic CO_2 reduction.

Table 3. Functional groups for photocatalytic CO_2 reduction.

Photocatalyst	Reactive sites	Reaction medium	Light source	Major product	Rate max.	Other products	Rate max.	Ref.
MEA-ZnO	$-NH_2$	H_2O	Xe lamp	CO	25.3 μmol g^{-1}	CH_4	4.4 μmol g^{-1}	[84]
NH_3-g-C_3N_4	$-NH_2$	H_2O vapour	300 W Xe lamp	CH_3OH	1.87 μmol g^{-1} h^{-1}	CH_4	1.39 μmol g^{-1} h^{-1}	[85]
MEA-g-C_3N_4	$-NH_2$	H_2O	300 W Xe lamp	CH_4	0.34 μmol g^{-1} h^{-1}	CH_3OH	0.28 μmol g^{-1} h^{-1}	[86]
AG/CdS	$-NH_2$	H_2O	>420 nm	CH_4	2.84 μmol g^{-1} h^{-1}	CO	Trace	[87]
titanate	$-NH_2$	H_2O	>400 nm	CH_3OH	2.1 μmol h^{-1} g^{-1}	-	-	[88]
NH_2-MIL-125(Ti	$-NH_2$	Acetonitrile triethanolamine	420-800 nm	HCOO-	8.14 μmol 10h	-	-	[89]
Ti_3C_2 MXene	-OH	H_2O	300 W Xe lamp	CH_4	16.61 μmol g^{-1} h^{-1}	CO	11.74 μmol g^{-1} h^{-1}	[90]
MIL-101-Cr	-OH	H_2O triethanolamine	xenon lamp	CO	47.2 μmol g^{-1} h^{-1}			[91]
TiO_2-OH	-OH	H_2O	300 W Xe lamp	CH_4	3.7 μmol 6h	-	-	[93]
NH_2-Uio-66(Zr)	$-NH_2$	Acetonitrile triethanolamine	420–800 nm	HCOO-	13.2 μmol 10h	-	-	[94]
g-C_3N_4-CoN_4-SiO_2	CoN_4	Acetonitrile triethylamine	450 nm	CO	398 μmol g^{-1}	-	-	[95]
g-C_3N_4-OH	-OH	H_2O	>420 nm	CO	~4.7 μmol g^{-1}	CH_3CHO CH_4	3.5 μmol g^{-1} Trace	[96]
CeO_2/TiO_2	Ce-Ti	H_2O vapour	300 W Xe lamp	CO	46.6 μmol g^{-1} 6h	CH_4	30.2 μmol g^{-1} 6h	[97]
g-C_3N_4	-COOH -CN	H_2O vapour	350 W Xe lamp	CH_4	~6 μmol g^{-1} h^{-1}	CO CH_3OH CH_3CH_2OH	1 4 2	[98]
MEA-TiO_2	$-NH_2$	H_2O	xenon lamp	CO	21.75 ppm h^{-1}	CH_4	2.75 ppm h^{-1}	[99]
g-C_3N_4	$-NH_x$	H_2O vapour	simulated sunlight	CO	50 μmol g^{-1} 5h	CH_4	1.6 μmol g^{-1}5h	[100]
Bi-TiO_2	-Bi	H_2O	300 W Xe lamp	CH_4	153.08 μmol g^{-1}	CO	6.38 μmol g^{-1}	[101]
Mo-g-C_3N_4	Mo	H_2O	>420 nm	CH_4	105 μmol g^{-1}	-	-	[102]

6. Frustrated Lewis-Pairs (FLPs)

It is widely accepted that the adsorption and activation of CO_2 molecules on the surface of photocatalysts is the limiting-step for CO_2 photoreduction. Because of this, research approaches have been developed to activate CO_2 molecules. Constructing FLPs on the surface is an effective means to achieve dissociation of C=O. As mentioned in the section 1, CO_2 molecules can be readily polarized by the interaction between the empty orbit of FLPs and the

bonding orbit of CO_2 as well as between lone electrons pairs of FLPs and anti-bonding orbit of CO_2. The bond length and angle of CO_2 molecules are extended and changed, leading to the activation of CO_2.

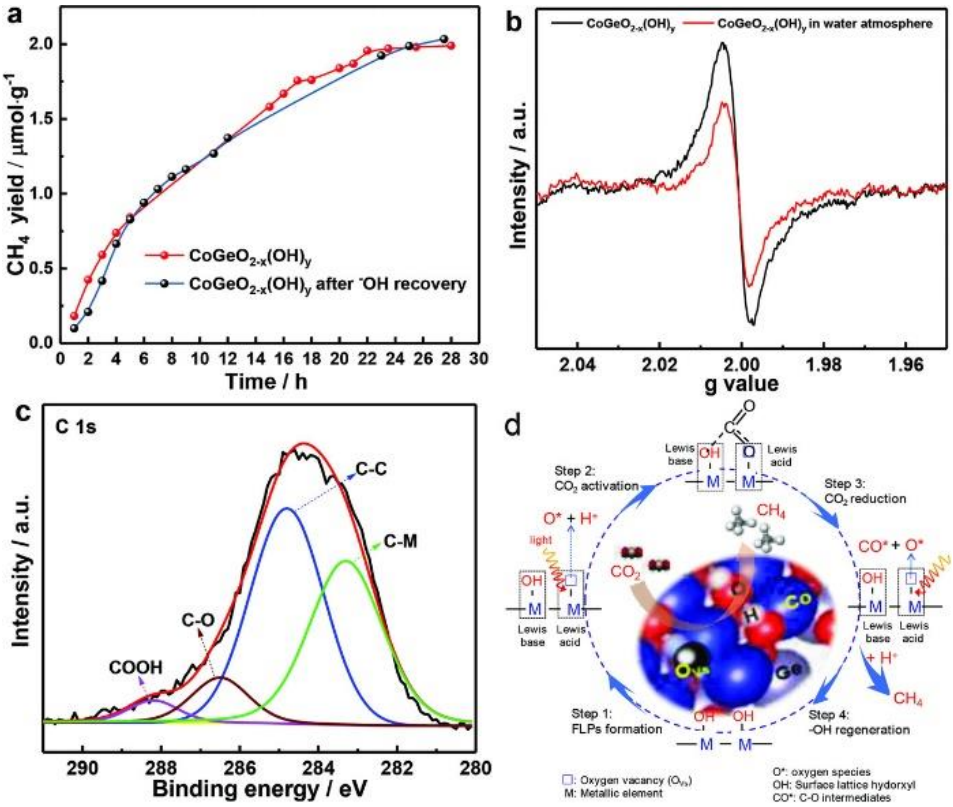

Figure 11. a) CH_4 yield over $CoGeO_{2-x}(OH)_y$ and $CoGeO_{2-x}(OH)_y$ with regenerated hydroxyls under long-term irradiation. b) Room-temperature EPR signals of $CoGeO_{2-x}(OH)_y$ before and after exposing to water-molecule containing atmosphere. c) C 1s XPS spectra for $CoGeO_{2-x}(OH)_y$ after 28 h irradiation under CO_2. d) Possible four-step CH_4 generation mechanism for using the surface lattice hydroxyl as solid-state proton source. Step 1: FLP formation by photogenerated holes oxidizing hydroxyls. Step 2: Activating CO_2 by FLPs' synergetic-effects. Step 3: Accelerating CH_4 generation by proton reduction released from surface hydroxyls with decreasing conversion kinetics of intermediates. Step 4: Regeneration of the consumed surface hydroxyls by exposing photocatalyst into water-molecule containing atmosphere. Reproduced with permission.[112] Copyright 2018, Wiley-VCH Verlag GmbH &Co. KGaA, Weinheim.

Hoch et al.[111] first designed $In_2O_{3-x}(OH)_y$ nanoparticles with FLPs on the surface for photocatalytic CO_2 reduction. They found that the activity of samples was associated with surface density of oxygen vacancy and hydroxides. Samples with different surface populations were prepared by annealing the precursor $In(OH)_3$ under different temperatures. The resulting

different density of surface defects affects CO_2 affinity significantly to impact photocatalytic performance. This research paved the way for the utilization of FLPs in photocatalytic CO_2 reduction. Fabricating FLPs in particular hydroxides, or oxides, is more readily done than with some other materials. This is because the unsaturated metal ions, due to oxygen vacancies and hydroxyls, can be FLPs. Therefore $In_2O_{3-x}(OH)_y$ has received research interest for construction of FLPs. However only at specific sites, in which there are Lewis-basic -OH and Lewis-acidic unsaturated In atoms, can small gas molecules like CO_2 be activated. For example, Dong et al.[117] doped bismuth into the lattice of $In_2O_{3-x}(OH)_y$ to promote efficiency in photoreduction of CO_2. The In^{3+} ions were substituted by Bi^{3+} ions of which the $6s^2$ electrons pairs hybridize with the oxygen of In-OH resulting in increasing the basicity of this Lewis-base. The substituted Bi^{3+} also acts as Lewis-base site. However, not all of the substituted Bi^{3+} strengthens activity of FLPs. The position of Bi^{3+} of which chemical bond length and Bader charges at certain value can increase the basicity and acidity of FLPs, leads to polarization and dissociation of H_2 and CO_2 molecules.

In this way, the configuration of Bi substitution influences acidity and basicity of Lewis-pairs. DFT computations indicate that when Bi substitutes the neighbouring In_3 site, both of the Lewis-basicity and -acidity is increased and results in boosted performance. However, with increasing amounts of Bi substitution, the In_2 site can be substituted and the Lewis-basicity and -acidity are reduced. This is consistent with experimental observation that CO_2 reduction activity decreased rapidly with increasing Bi substitution over 0.5 % (the nominal molar ratio), despite the fact that oxygen vacancy and surface hydroxides increase. Polymorph selection for constructing FLPs to increase basicity and acidity has been reported. Yan et al.[119] for example prepared different crystal pattern rhombohedral polymorph of indium sesquioxide that exhibited boosted photocatalytic performance because of the strengthened acidity and basicity of surface FLPs. Based on DFT computations the different crystal structures have different energy profiles for CO_2 hydrogenation via the formate pathway. More recently, different FLPs on various materials to promote adsorption and activation of small gas molecules to realize heterogeneous catalysis has been reported. For example, there is interest in CeO_2 because of its different oxidized states, Ce^{3+}/Ce^{4+} and abundant surface defects.[113] The Cu atoms of decorated Cu_2O act as Lewis-base to bond with C via the d electron of Cu. Oxygen vacancy reacts with the O atom. This adsorption configuration promotes CO_2 activation and dissociation. The dynamic of FLPs on ceria have been investigated by *ab initio* molecular dynamics simulations and DFT computations. Results illustrated that the formation of FLPs on

the surface of ceria depended on the number of oxygen vacancies. The most common FLPs in solid-catalysts is unsaturated metal ions caused by oxygen vacancies and neighbouring oxygen ions, and/or the surface hydroxyl groups. These FLPs can only be realized in metal oxides and hydroxides. In addition to $In(OH)_3$ and CeO_2, research has been used to investigate other materials in an attempt to broaden utilization of FLPs. For example, Wang et al.[112] fabricated FLPs on $CoGeO_2(OH)_2$ with abundant surface defects, **Figure 11**. The fabrication of FLPs was realized by UV light. The bridge oxygen-atoms are affected by the UV light so as to leave an oxygen vacancy in the lattice to form the FLPs. The surface functional groups impact the pathway for CO_2 reduction. The process of CO_2 activation by FLPs may be that an O atom of CO_2 is captured by oxygen vacancy (Lewis-acid) and a C atom is attracted by surface hydroxyls (Lewis-base). The dissociation of activated CO_2 generates intermediates towards final products. Some intermediates react with the surface OH groups to form COOH* which is a necessary intermediate toward CH_4. Consumed surface hydroxyl groups can regenerate when the material is exposed to a water-molecule containing-atmosphere. This property makes the photocatalyst sustainable.

The fabrication of FLPs on the surface of solid catalysts remains a significant practical challenge because it is an elaborate process, and because the stability and mechanism of activation, including dynamics, are unclear. The preparation of different materials at an atomic-level is practically difficult to control and realize. The result is a limited utilization of FLPs. It might however be effective in activation of gas molecules, such as N_2 and methane, and should therefore receive research attention. The distance of the Lewis-acid centre and Lewis-base centre can be adjusted to lead to different acidity and basicity. This is an approach for different activation and stability of FLPs.

Table 4. FLPs for photocatalytic CO_2 reduction.

Photocatalyst	Reactive sites	Reaction medium	Light source	Major product	Rate max.	Other products	Rate max.	Ref.
$In_2O_{3-x}(OH)_y$	V_o-OH	H_2 150 °C	300 W Xe lamp	CO	15 μmol g^{-1} h^{-1}	-	-	[111]
$CoGeO_{2-x}(OH)_2$	V_o-OH	H_2O	300 W Xe lamp	CH_4	6.6 μmol g^{-1}	CO	Trace	[112]
CeO_2/Cu_2O	V_o-Ce^{3+}	H_2O	300 W Xe lamp	CO	1.2 μmol g^{-1}	-	-	[113]
$In_2O_{3-x}(OH)_y$	V_o-OH	H_2 150 °C	1000 W halide bulb	CO	1.32 μmol g^{-1} h^{-1}	-	-	[117]
$In_2O_{3-x}(OH)_y$	V_o-OH	H_2 190 °C	300 W Xe lamp	CO	153 μmol g^{-1} h^{-1}	-	-	[118]
Rh-$In_2O_{3-x}(OH)_y$	V_o-OH	H_2 270 °C	300 W Xe lamp	CH_3OH	180 μmol g^{-1} h^{-1}	CO	2.4 mmol g^{-1} h^{-1}	[119]
Pt/MgAl-LDO/TiO_2	V_o-OH	H_2O vapour	300 W Xe lamp	CH_4	0.364 μmol	CO	0.246 μmol	[120]

7. Conclusions

An atomic-level perspective permits an increased understanding of photocatalysis and of photocatalytic CO_2 reduction. Of critical importance is the role reactive sites play in photocatalytic reaction. We conclude that there are four different strategies to fabricate atomic-level reactive sites on the surface of photocatalysts, including: vacancy engineering, doping with single atoms, surface modification with functional groups, and constructing frustrated Lewis-pairs (FLPs). These change pathways for CO_2 reduction and significantly impact catalytic activity and selectivity.

Vacancy engineering, usually caused via removal of atoms in the lattice, can serve as active sites on the surface of semiconductors. Activity not only derives from the vacancy caused by the removal of atoms, but also by the synergistic impact of the adjacent ion with unsaturated coordination like dangling bonds that have an affinity for CO_2. The vacancy can result in accumulation of photogenerated electrons. These electrons promote complicated CO_2 reduction pathways. Vacancies introduce a defect energy-level in the forbidden-band gap and narrow the band gap of semiconductors that broadens the light response profile. However, the stability and position of vacancies is important. Doping single atoms is a useful strategy for noble metal use with large-scale application. Single atoms can be dispersed in matrix and coordinatively unsaturated with adjacent atoms. Single metal atoms accumulate electrons by chemical valence states to provide sufficient electrons for CO_2 reduction. Heterogeneous single atom doping can change the band gap of semiconductors to broaden the light response profile. However the fabrication of single atom photocatalysts in large-scale remains a significant practical challenge because preparation is often complicated and is energy-consuming. Surface modification is a relatively simple means to fabricate reactive sites on photocatalysts, especially in anchoring organic functional groups. In most cases these functional groups bond with CO_2 molecules to improve chemisorption. Metal groups show high activity for photocatalytic CO_2 reduction. However organic functional groups show no effect on the light response, charge transfer and separation. Additionally, the complex structure can interfere with the electron transfer from matrix to CO_2 to reduce photocatalytic performance. However decomposition of metal groups anchored on the matrix constrains utilization. Therefore finding more effective functional groups to increase stability is a significant challenge for surface modification. Fabricating FLPs, in fact, produces dual sites for CO_2 adsorption and activation. Because Lewis- basic sites cannot combine with Lewis-acidic sites as a result of steric-hindrance, FLPs are effective in activating and dissociating CO_2 gas in heterogeneous catalysts.

However fabrication and utilization of FLPs is limited with the components of the basic-sites and acidic-sites being oxygen vacancy and surface hydroxyls. Fabrication of FLPs is an elaborate process, for example, the position of two sites is difficult to control in because they tend to bond with each other. Therefore research on FLPs for photocatalytic CO_2 reduction should concentrate on broadening utilization in different material systems.

Compared with single component active sites, dual sites can promote efficiency of single atoms, and a synergistic effect of heterogeneous atoms lowers further the energy barrier of CO_2 adsorption and activation. Dual sites can be heterogeneous single atoms, functional groups, dual sites of metal-complex and/or a combination of two types. Dual sites can be developed by different strategies, for example, introducing vacancies in binary metal compounds may expose dangling bonds of two heterogeneous metal atoms that can serve as reactive sites. It is concluded overall that the design of photocatalysts from an atomic-level perspective and understanding will result in maximal atomic utilization efficiency and lead to a high selectivity. Therefore future practical prospects are considered excellent for improved design and fabrication of photocatalysts based on a carefully articulated in-depth understanding.

Acknowledgements

This work was supported financially by the Australian Research Council (ARC) through Discovery Project and Linkage Project Programs (DP160104866, LP160100927, and FL170100154).

Conflict of Interest

The authors declare no conflict of interest.

Keywords

CO_2 photoreduction, atomic reactive sites, semiconductors

Received: Novermber 26, 2019

Revised: January 8, 2020

Published online: January 31, 2020

References

[1] N. S. Lewis, D. G. Nocera, *Proc. Natl. Acad. Sci.* **2006**, *103*, 15729.

[2] J. Ran, M. Jaroniec, S. Z. Qiao, *Adv. Mater.* **2018**, *30*, 1704649.

[3] S. Solomon, G. K. Plattner, R. Knutti, P. Friedlingstein, *Proc. Natl. Acad. Sci.* **2009**, *106*, 1704.

[4] M. Vermeer, S. Rahmstorf, *Proc. Natl. Acad. Sci.* **2009**, *106*, 21527.

[5] M. Meinshausen, N. Meinshausen, W. Hare, S. C. Raper, K. Frieler, R. Knutti, D. J. Frame, M. R. Allen, *Nature* **2009**, *458*, 1158.

[6] T. Xia, R. Long, C. Gao, Y. Xiong, *Nanoscale* **2019,** *11*, 11064.

[7] R. Shi, G. I. Waterhouse, T. Zhang, *Solar RRL* **2017**, *1*, 1700126.

[8] H. L. Wu, X. B. Li, C. H. Tung, L. Z. Wu, *Adv. Mater.* **2019**, *31*, 1900709.

[9] X. Li, Y. Sun, J. Xu, Y. Shao, J. Wu, X. Xu, Y. Pan, H. Ju, J. Zhu, Y. Xie, *Nat. Energy* **2019**, *4*, 690.

[10] M. Shen, L. Zhang, M. Wang, J. Tian, X. Jin, L. Guo, L. Wang, J. Shi, *J. Mater. Chem. A* **2019**, *7*, 1556.

[11] W. Tu, Y. Xu, J. Wang, B. Zhang, T. Zhou, S. Yin, S. Wu, C. Li, Y. Huang, Y. Zhou, *ACS Sustain. Chem. Eng.* **2017**, *5*, 7260.

[12] Y. F. Song, L. Tan, S. M. Xu, Z. Wang, Y. Xu, X. Wang, X. Hao, S. Bai, C. Ning, Y. Wang, *Angew. Chem. Int. Ed.* **2019,** *131*, 11986.

[13] S. Gao, B. Gu, X. Jiao, Y. Sun, X. Zu, F. Yang, W. Zhu, C. Wang, Z. Feng, B. Ye, *J. Am. Chem. Soc.* **2017**, *139*, 3438.

[14] X. C. Jiao, Z. W. Chen, X. D. Li, Y. F. Sun, S. Gao, W. S. Yan, C. M. Wang, Q. Zhang, Y. Lin, Y. Luo, Y. Xie, *J. Am. Chem. Soc.* **2017**, *139*, 7586.

[15] H. Pang, X. Meng, H. Song, W. Zhou, G. Yang, H. Zhang, Y. Izumi, T. Takei, W. Jewasuwan, N. Fukata, *Appl. Catal., B* **2019**, *244*, 1013.

[16] J. Di, X. Zhao, C. Lian, M. Ji, J. Xia, J. Xiong, W. Zhou, X. Cao, Y. She, H. Liu, *Nano Energy* **2019**, *61*, 54.

[17] S. Sun, M. Watanabe, J. Wu, Q. An, T. Ishihara, *J. Am. Chem. Soc.* **2018**, 140, 6474.

[18] M. Li, Y. Zhang, X. Li, Y. Wang, F. Dong, L. Ye, S. Yu, H. Huang, *ACS Sustain. Chem. Eng.* **2018**, *6*, 2395.

[19] T. D. Pham, B. K. Lee, *J. Catal.* **2017**, *345*, 87.

[20] M. Halmann, *Nature* **1978**, *275*, 115.

[21] O. K. Varghese, M. Paulose, T. J. LaTempa, C. A. Grimes, *Nano Lett.* **2009**, *9*, 731.

[22] N. N. Vu, S. Kaliaguine, T. O. Do, *Adv. Funct. Mater.* **2019**, *29*, 1901825.

[23] Y. Fang, X. Wang, *Chem. Commun.* **2018**, *54*, 5674.

[24] S. Lian, M. S. Kodaimati, D. S. Dolzhnikov, R. Calzada, E. A. Weiss, *J. Am. Chem. Soc.* **2017**, *139*, 8931.

[25] S. Lian, M. S. Kodaimati, E. A. Weiss, *ACS Nano* **2018**, *12*, 568.

[26] G. C. Xi, S. X. Ouyang, P. Li, J. H. Ye, Q. Ma, N. Su, H. Bai, C. Wang, *Angew. Chem. Int. Ed.* **2012**, *51*, 2395.

[27] P. Zhang, S. B. Wang, B. Y. Guan, X. W. Lou, *Energ. Environ. Sci.* **2019**, *12*, 164.

[28] S. B. Wang, B. Y. Guan, X. W. D. Lou, *J. Am. Chem. Soc.* **2018**, *140*, 5037.

[29] M. Zhou, S. Wang, P. Yang, C. Huang, X. Wang, *ACS Catal.* **2018**, *8*, 4928.

[30] H. Li, Y. Gao, Y. Zhou, F. Fan, Q. Han, Q. Xu, X. Wang, M. Xiao, C. Li, Z. Zou, *Nano Lett.* **2016**, *16*, 5547.

[31] J. Jin, J. G. Yu, D. P. Guo, C. Cui, W. K. Ho, *Small* **2015**, *11*, 5262.

[32] G. Yin, Q. Bi, W. Zhao, J. Xu, T. Lin, F. Huang, *ChemCatChem* **2017**, *9*, 4389.

[33] G. Yin, X. Huang, T. Chen, W. Zhao, Q. Bi, J. Xu, Y. Han, F. Huang, *ACS Catal.* **2018**, *8*, 1009.

[34] J. Jin, J. Luo, L. Zan, T. Peng, *ChemPhysChem* **2017**, *18*, 3230.

[35] Z. He, J. Tang, J. Shen, J. Chen, S. Song, *Appl. Surf. Sci.* **2016**, *364*, 416.

[36] H. J. Yu, J. Y. Li, Y. H. Zhang, S. Q. Yang, K. L. Han, F. Dong, T. Y. Ma, H. W. Huang, *Angew. Chem. Int. Ed.* **2019**, *58*, 3880.

[37] J. Wu, X. D. Li, W. Shi, P. Q. Ling, Y. F. Sun, X. C. Jiao, S. Gao, L. Liang, J. Q. Xu, W. S. Yan, C. M. Wang, Y. Xie, *Angew. Chem. Int. Ed.* **2018**, *57*, 8719.

[38] L. Lu, B. Wang, S. M. Wang, Z. Shi, S. C. Yan, Z. G. Zou, *Adv. Funct. Mater.* **2017**, *27*, 1702447.

[39] B. Wang, X. Wang, L. Lu, C. Zhou, Z. Xin, J. Wang, X. K. Ke, G. Sheng, S. Yan, Z. Zou, *ACS Catal.* **2017**, *8*, 516.

[40] L. Liu, Y. Jiang, H. Zhao, J. Chen, J. Cheng, K. Yang, Y. Li, *ACS Catal.* **2016**, *6*, 1097.

[41] J. Di, C. Zhu, M. X. Ji, M. L. Duan, R. Long, C. Yan, K. Z. Gu, J. Xiong, Y. B. She, J. X. Xia, H. M. Li, Z. Liu, *Angew. Chem. Int. Ed.* **2018**, *57*, 14847.

[42] U. Tumuluri, J. D. Howe, W. P. Mounfield, M. J. Li, M. F. Chi, Z. D. Hood, K. S. Walton, D. S. Sholl, S. Dai, Z. L. Wu, *ACS Sustain. Chem. Eng.* **2017**, *5*, 9295.

[43] T. Billo, F. Y. Fu, P. Raghunath, I. Shown, W. F. Chen, H. T. Lien, T. H. Shen, J. F. Lee, T. S. Chan, K. Y. Huang, C. I. Wu, M. C. Lin, J. S. Hwang, C. H. Lee, L. C. Chen, K. H. Chen, *Small* **2018**, *14*, 1702928.

[44] L. J. Liu, H. L. Zhao, J. M. Andino, Y. Li, *ACS Catal.* **2012**, *2*, 1817.

[45] Y. F. Zhao, G. B. Chen, T. Bian, C. Zhou, G. I. N. Waterhouse, L. Z. Wu, C. H. Tung, L. J. Smith, D. O'Hare, T. R. Zhang, *Adv. Mater.* **2015**, *27*, 7824.

[46] Y. F. Ji, Y. Luo, *J. Am. Chem. Soc.* **2016**, *138*, 15896.

[47] P. Li, X. Zhang, C. Hou, L. Lin, Y. Chen, T. He, *Phys. Chem. Chem. Phys.* **2018**, *20*, 16985.

[48] L. B. Hoch, P. Szymanski, K. K. Ghuman, L. He, K. Liao, Q. Qiao, L. M. Reyes, Y. Zhu, M. A. El Sayed, C. V. Singh, *Proc. Natl. Acad. Sci.* **2016**, *113*, E8011.

[49] R. Shi, Y. Chen, *ChemCatChem* **2019**, *11*, 2270.

[50] L. B. Hoch, L. He, Q. Qiao, K. Liao, L. M. Reyes, Y. Zhu, G. A. Ozin, *Chem. Mater.* **2016**, *28*, 4160.

[51] X. Liu, M. Ye, S. Zhang, G. Huang, C. Li, J. Yu, P. K. Wong, S. Liu, *J. Mater. Chem. A* **2018**, *6*, 24245.

[52] L. Liang, X. Li, Y. Sun, Y. Tan, X. Jiao, H. Ju, Z. Qi, J. Zhu, Y. Xie, *Joule* **2018**, *2*, 1004.

[53] L. Li, P. Li, Y. Wang, L. Lin, A. H. Shah, T. He, *Appl. Surf. Sci.* **2018**, *452*, 498.

[54] Z. Ma, P. Li, L. Ye, Y. Zhou, F. Su, C. Ding, H. Xie, Y. Bai, P. K. Wong, *J. Mater. Chem. A* **2017**, *5*, 24995.

[55] S. Chen, H. Wang, Z. Kang, S. Jin, X. Zhang, X. Zheng, Z. Qi, J. Zhu, B. Pan, Y. Xie, *Nat. Commun.* **2019**, *10*, 788.

[56] M. Wang, M. Shen, X. X. Jin, J. J. Tian, M. L. Li, Y. J. Zhou, L. X. Zhang, Y. S. Li, J. L. Shi, *ACS Catal.* **2019**, *9*, 4573.

[57] X. Y. Kong, W. P. C. Lee, W.-J. Ong, S.-P. Chai, A. R. Mohamed, *ChemCatChem* **2016**, *8*, 3074.

[58] Y. X. Pan, Z. Q. Sun, H. P. Cong, Y. L. Men, S. Xin, J. Song, S. H. Yu, *Nano Res.* **2016**, *9*, 1689.

[59] L. Zhang, W. Wang, D. Jiang, E. Gao, S. Sun, *Nano Res.* **2015**, *8*, 821.

[60] W. Fang, L. Khrouz, Y. Zhou, B. Shen, C. Dong, M. Xing, S. Mishra, S. p. Daniele, J. Zhang, *Phys. Chem. Chem. Phys.* **2017**, *19*, 13875.

[61] X. Y. Kong, B. J. Ng, K. H. Tan, X. Chen, H. Wang, A. R. Mohamed, S. P. Chai, *Catal. Today* **2018**, *314*, 20.

[62] J. Hou, S. Cao, Y. Wu, F. Liang, Y. Sun, Z. Lin, L. Sun, *Nano Energy* **2017**, *32*, 359.

[63] C. Bie, B. Zhu, F. Xu, L. Zhang, J. Yu, *Adv. Mater.* **2019**, *0*, 1902868.

[64] K. Wang, J. Fu, Y. Zheng, *Appl. Catal., B* **2019**, *254*, 270.

[65] S. Zhu, S. Liang, Y. Tong, X. An, J. Long, X. Fu, X. Wang, *Phys. Chem. Chem. Phys.* **2015**, *17*, 9761.

[66] J. Qiu, G. Zeng, M. A. Ha, B. Hou, M. Mecklenburg, H. Shi, A. N. Alexandrova, S. B. Cronin, *Chem. Mater.* **2015**, *27*, 7977.

[67] T. D. Pham, B. K. Lee, *Appl. Catal., A* **2017**, *529*, 40.

[68] Z. Jiang, W. Sun, W. Miao, Z. Yuan, G. Yang, F. Kong, T. Yan, J. Chen, B. Huang, C. An, *Adv. Sci.* **2019**, *6*, 1900289.

[69] L. J. Liu, C. Y. Zhao, Y. Li, *J. Phys. Chem. C* **2012**, *116*, 7904.

[70] E. X. Chen, M. Qiu, Y. F. Zhang, Y. S. Zhu, L. Y. Liu, Y. Y. Sun, X. H. Bu, J. Zhang, Q. P. Lin, *Adv. Mater.* **2018**, *30*, 1704388.

[71] H. Q. Xu, J. H. Hu, D. K. Wang, Z. H. Li, Q. Zhang, Y. Luo, S. H. Yu, H. L. Jiang, *J. Am. Chem. Soc.* **2015**, *137*, 13440.

[72] D. C. Liu, T. Ouyang, R. Xiao, W. J. Liu, D. C. Zhong, Z. T. Xu, T. B. Lu, *ChemSusChem* **2019**, *12*, 2166.

[73] J. Ding, X. F. Liu, M. G. Shi, T. Li, M. Y. Xia, X. W. Du, R. L. Shang, H. Gu, Q. Zhong, *Sol. Energ. Mat. Sol. C.* **2019**, *195*, 34.

[74] J. O. Olowoyo, M. Kumar, N. Singhal, S. L. Jain, J. O. Babalola, A. V. Vorontsov, U. Kumar, *Catal. Sci. Technol.* **2018**, *8*, 3686.

[75] P. P. Huang, J. H. Huang, S. A. Pantovich, A. D. Carl, T. G. Fenton, C. A. Caputo, R. L. Grimm, A. I. Frenkel, G. H. Li, *J. Am. Chem. Soc.* **2018**, *140*, 16042.

[76] H. W. Zhang, J. T. Ming, J. W. Zhao, Q. Gu, C. Xu, Z. X. Ding, R. S. Yuan, Z. Z. Zhang, H. X. Lin, X. X. Wang, J. L. Long, *Angew. Chem. Int. Ed.* **2019**, *58*, 7718.

[77] R. Long, Y. Li, Y. Liu, S. M. Chen, X. S. Zheng, C. Gao, C. H. He, N. S. Chen, Z. M. Qi, L. Song, J. Jiang, J. F. Zhu, Y. J. Xiong, *J. Am. Chem. Soc.* **2017**, *139*, 4486.

[78] L. Yuan, S. F. Hung, Z. R. Tang, H. M. Chen, Y. J. Xiong, Y. J. Xu, *ACS Catal.* **2019**, 9, 4824.

[79] G. P. Gao, Y. Jiao, E. R. Waclawik, A. J. Du, *J. Am. Chem. Soc.* **2016**, *138*, 6292.

[80] H. B. Zhang, J. Wei, J. C. Dong, G. G. Liu, L. Shi, P. F. An, G. X. Zhao, J. T. Kong, X. J. Wang, X. G. Meng, J. Zhang, J. H. Ye, *Angew. Chem. Int. Ed.* **2016**, *55*, 14308.

[81] X. C. Jiao, X. D. Li, X. Y. Jin, Y. F. Sun, J. Q. Xu, L. Liang, H. X. Ju, J. F. Zhu, Y. Pan, W. S. Yan, Y. Lin, Y. Xie, *J. Am. Chem. Soc.* **2017**, *139*, 18044.

[82] M. Y. Xia, J. Ding, X. W. Du, R. L. Shang, Q. Zhong, *J. Alloys Compd.* **2019**, *777*, 406.

[83] Z. C. Kong, J. F. Liao, Y. J. Dong, Y. F. Xu, H. Y. Chen, D. B. Kuang, C. Y. Su, *ACS Energy Lett.* **2018**, *3*, 2656.

[84] Y. S. Liao, Z. N. Hu, Q. Gu, C. Xue, *Molecules* **2015**, *20*, 18847.

[85] P. F. Xia, B. C. Zhu, J. G. Yu, S. W. Cao, M. Jaroniec, *J. Mater. Chem. A* **2017**, *5*, 3230.

[86] Q. Huang, J. G. Yu, S. W. Cao, C. Cui, B. Cheng, *Appl. Surf. Sci.* **2015**, *358*, 350.

[87] K. M. Cho, K. H. Kim, K. Park, C. Kim, S. Kim, A. Al Saggaf, I. Gereige, H. T. Jung, *ACS Catal.* **2017**, *7*, 7064.

[88] S. W. Liu, J. Q. Xia, J. G. Yu, *ACS Appl. Mater. Interfaces* **2015**, *7*, 8166.

[89] Y. H. Fu, D. R. Sun, Y. J. Chen, R. K. Huang, Z. X. Ding, X. Z. Fu, Z. H. Li, *Angew. Chem. Int. Ed.* **2012**, *51*, 3364.

[90] M. H. Ye, X. Wang, E. Z. Liu, J. H. Ye, D. F. Wang, *ChemSusChem* **2018**, *11*, 1606.

[91] Y. Xie, Z. B. Fang, L. Li, H. X. Yang, T. F. Liu, *ACS Appl. Mater. Interfaces* **2019**, *11*, 27017.

[92] M. W. Logan, J. D. Adamson, D. Le, F. J. Uribe Romo, *ACS Appl. Mater. Interfaces* **2017**, *9*, 44529.

[93] H. Yu, S. C. Yan, P. Zhou, Z. G. Zou, *Appl. Surf. Sci.* **2018**, *427*, 603.

[94] D. R. Sun, Y. H. Fu, W. J. Liu, L. Ye, D. K. Wang, L. Yang, X. Z. Fu, Z. H. Li, *Chem. Eur. J.* **2013**, *19*, 14279.

[95] J. C. Hu, M. X. Gui, W. Xia, J. Wu, Y. N. Zhou, N. D. Feng, J. W. Xiao, H. F. Liu, C. H. Tung, L. Z. Wu, F. Wang, *J. Mater. Chem. A* **2019**, *7*, 10475.

[96] Z. X. Sun, J. Fischer, Q. A. Li, J. Hu, Q. J. Tang, H. Q. Wang, Z. B. Wu, M. Hankel, D. J. Searles, L. Z. Wang, *Appl. Catal., B* **2017**, *216*, 146.

[97] Y. Wang, J. Zhao, T. F. Wang, Y. X. Li, X. Y. Li, J. Yin, C. Y. Wang, *J. Catal.* **2016**, *337*, 293.

[98] P. F. Xia, M. Antonietti, B. C. Zhu, T. Heil, J. G. Yu, S. W. Cao, *Adv. Funct. Mater.* **2019**, *29*, 1900093.

[99] Y. S. Liao, S. W. Cao, Y. P. Yuan, Q. Gu, Z. Y. Zhang, C. Xue, *Chem. Eur. J.* **2014**, *20*, 10220.

[100] Z. X. Sun, S. C. Wang, Q. Li, M. Q. Lyu, T. Butburee, B. Luo, H. Q. Wang, J. Fischer, C. Zhang, Z. B. Wu, L. Z. Wang, *Adv. Sustain.* **2017**, *1*, 1700003.

[101] X. G. Li, W. T. Bi, Z. Wang, W. G. Zhu, W. S. Chu, C. Z. Wu, Y. Xie, *Nano Res.* **2018**, *11*, 3362.

[102] R. Y. Zhang, P. H. Li, F. Wang, L. Q. Ye, A. Gaur, Z. A. Huang, Z. Y. Zhao, Y. Bai, Y. Zhou, *Appl. Catal. B* **2019**, *250*, 273.

[103] S. Sato, T. Arai, T. Morikawa, K. Uemura, T. M. Suzuki, H. Tanaka, T. Kajino, *J. Am. Chem. Soc.* **2011**, *133*, 15240.

[104] T. Ouyang, H. H. Huang, J. W. Wang, D. C. Zhong, T. B. Lu, *Angew. Chem. Int. Ed.* **2017**, *56*, 738.

[105] Z. H. Yan, M. H. Du, J. X. Liu, S. Y. Jin, C. Wang, G. L. Zhuang, X. J. Kong, L. S. Long, L. S. Zheng, *Nat. Commun.* **2018**, *9*, 3353.

[106] K. Maeda, K. Sekizawa, O. Ishitani, *Chem. Commun.* **2013**, *49*, 10127.

[107] G. X. Zhao, H. Pang, G. G. Liu, P. Li, H. M. Liu, H. B. Zhang, L. Shi, J. H. Ye, *Appl. Catal. B* **2017**, *200*, 141.

[108] K. Maeda, R. Kuriki, M. W. Zhang, X. C. Wang, O. Ishitani, *J. Mater. Chem. A* **2014**, *2*, 15146.

[109] S. Sato, T. Morikawa, S. Saeki, T. Kajino, T. Motohiro, *Angew. Chem. Int. Ed.* **2010**, *49*, 5101.

[110] R. Kuriki, K. Sekizawa, O. Ishitani, K. Maeda, *Angew. Chem. Int. Ed.* **2015**, *54*, 2406.

[111] L. B. Hoch, T. E. Wood, P. G. O'Brien, K. Liao, L. M. Reyes, C. A. Mims, G. A. Ozin, *Adv. Sci.* **2014**, *1*, 1400013.

[112] X. H. Wang, L. Lu, B. Wang, Z. Xu, Z. Y. Xin, S. C. Yan, Z. R. Geng, Z. G. Zou, *Adv. Funct. Mater.* **2018**, *28*, 1804191.

[113] Y. Pu, Y. D. Luo, X. Q. Wei, J. F. Sun, L. L. Li, W. X. Zou, L. Dong, *Appl. Catal., B* **2019**, *254*, 580.

[114] K. K. Ghuman, L. B. Hoch, T. E. Wood, C. Mims, C. V. Singh, G. A. Ozin, *ACS Catal.* **2016**, *6*, 5764.

[115] M. Ghoussoub, S. Yadav, K. K. Ghuman, G. A. Ozin, C. V. Singh, *ACS Catal.* **2016**, *6*, 7109.

[116] K. K. Ghuman, L. B. Hoch, P. Szymanski, J. Y. Y. Loh, N. P. Kherani, M. A. E Sayed, G. A. Ozin, C. V. Singh, *J. Am. Chem. Soc.* **2016**, *138*, 1206.

[117] Y. C. Dong, K. K. Ghuman, R. Popescu, P. N. Duchesne, W. J. Zhou, J. Y. Y. Loh, A. A. Jelle, J. Jia, D. Wang, X. K. Mu, C. Kubel, L. Wang, L. He, M. Ghoussoub, Q. Wang, T. E. Wood, L. M. Reyes, P. Zhang, N. P. Kherani, C. V. Singh, G. A. Ozin, *Adv. Sci.* **2018**, *5*, 1700732.

[118] K. K. Ghuman, T. E. Wood, L. B. Hoch, C. A. Mims, G. A. Ozin, C. V. Singh, *Phys. Chem. Chem. Phys.* **2015**, *17*, 14623.

[119] T. J. Yan, L. Wang, Y. Liang, M. Makaremi, T. E. Wood, Y. Dai, B. B. Huang, A. A. Jelle, Y. Dong, G. A. Ozin, *Nat. Commun.* **2019**, *10*, 2521.

[120] R. F. Chong, C. H. Su, Y. Q. Du, Y. Y. Fan, Z. Ling, Z. X. Chang, D. L. Li, *J. Catal.* **2018**, *363*, 92.

[121] J. S. J. McCahill, G. C. Welch, D. W. Stephan, *Angew. Chem. Int. Ed.* **2007**, *46*, 4968.

[122] G. C. Welch, R. R. S. Juan, J. D. Masuda, D. W. Stephan, *Science* **2006**, *314*, 1124.

[123] Y. He, H. Rao, K. Song, J. Li, Y. Yu, Y. Lou, C. Li, Y. Han, Z. Shi, S. Feng, *Adv. Funct. Mater.*, *0*, 1905153.

[124] S. Bai, N. Zhang, C. Gao, Y. Xiong, *Nano Energy* **2018**, *53*, 296.

[125] J. Low, L. Zhang, B. Zhu, Z. Liu, J. Yu, *ACS Sustain. Chem. Eng.* **2018**, *6*, 15653.

[126] A. Y. Meng, L. Y. Zhang, B. Cheng, J. G. Yu, *ACS Appl. Mater. Interfaces* **2019**, *11*, 5581.

[127] F. Xu, B. Zhu, B. Cheng, J. Yu, J. Xu, *Adv. Opt. Mater.* **2018**, *6*, 1800911.

[128] D. Gao, X. Wu, P. Wang, Y. Xu, H. Yu, J. Yu, *ACS Sustain. Chem. Eng.* **2019**, *7*, 10084.

[129] J. Low, B. Dai, T. Tong, C. Jiang, J. Yu, *Adv. Mater.* **2019**, *31*, 1802981.

[130] A. Meng, L. Zhang, B. Cheng, J. Yu, *Adv. Mater.* **2019**, *31*, 1807660.

[131] X. B. Chen, L. Liu, P. Y. Yu, S. S. Mao, *Science* **2011**, *331*, 746.

[132] H. Li, J. Li, Z. Ai, F. Jia, L. Zhang, *Angew. Chem. Int. Ed.* **2018**, *57*, 122.

[133] H. Li, F. Qin, Z. Yang, X. Cui, J. Wang, L. Zhang, *J. Am. Chem. Soc.* **2017**, *139*, 3513.

[134] L. Li, C. Tang, B. Xia, H. Jin, Y. Zheng, S.-Z. Qiao, *ACS Catal.* **2019**, *9*, 2902.

[135] H. Huang, K. Xiao, Y. He, T. Zhang, F. Dong, X. Du, Y. Zhang, *Appl. Catal. B.*, **2016**, *199*, 75.

[136] H. W. Huang, X. W. Li, J. J. Wang, F. Dong, P. K. Chu, T. R. Zhang, Y. H. Zhang, *ACS Catal.* **2015**, *5*, 4094.

[137] G. Xi, J. Ye, *Chem. Com.* **2010**, *46*, 1893.

[138] K. Maeda, R. Kuriki, O. Ishitani, *Chem. Lett.* **2016**, *45*, 182.

[139] R. Kuriki, M. Yamamoto, K. Higuchi, Y. Yamamoto, M. Akatsuka, D. Lu, S. Yagi, T. Yoshida, O. Ishitani, K. Maeda, *Angew. Chem. Int. Ed.* **2017**, *56*, 4867.

[140] R. Kuriki, H. Matsunaga, T. Nakashima, K. Wada, A. Yamakata, O. Ishitani, K. Maeda, *J. Am. Chem. Soc.* **2016**, *138*, 5159.

[141] Q. Q. Bi, J. W. Wang, J. X. Lv, J. Wang, W. Zhang, T. B. Lu, *ACS Catal.* **2018**, *8*, 11815.

[142] J. L. Lin, Z. M. Pan, X. C. Wang, *ACS Sustain. Chem. Eng.* **2014**, *2*, 353.

[143] S. Roy, E. Reisner, *Angew. Chem. Int. Ed.* **2019**, *58*, 12180.

[144] M. F. Kuehnel, K. L. Orchard, K. E. Dalle, E. Reisner, *J. Am. Chem. Soc.* **2017**, *139*, 7217.

[145] C. Cometto, R. Kuriki, L. J. Chen, K. Maeda, T. C. Lau, O. Ishitani, M. Robert, *J. Am. Chem. Soc.* **2018**, *140*, 7437.

[146] P. Yang, L. Wang, H. Zhuzhang, R. Wang, M.-M. Titirici, X. Wang, *Appl. Catal. B.*, **2019**, *256*, 117794.

[147] M. Zhu, S. Kim, L. Mao, M. Fujitsuka, J. Zhang, X. Wang, T. Majima, *J. Am. Chem. Soc.* **2017**, *139*, 13234.

[148] X. Wang, K. Maeda, A. Thomas, K. Takanabe, G. Xin, J. M. Carlsson, K. Domen, M. Antonietti, *Nat. Mater.* **2009**, *8*, 76.

[149] P. Li, F. Wang, S. Wei, X. Li, Y. Zhou, *Phys. Chem. Chem. Phys.* **2017**, *19*, 4405.

Chapter 3

ReS_2 Nanosheets with *In Situ* Formed Sulfur Vacancies for Efficient and Highly Selective Photocatalytic CO_2 Reduction

3.1 Introduction and Significance

Photocatalytic CO_2 reduction is a promising practical approach to utilization of solar energy and CO_2 conversion. However, the activity and selectivity of CO_2 photoreduction is significantly limited by the carrier charge recombination and large energy barrier for CO_2 activation. Amongst various photocatalysts, transition metal dichalcogenides (TMDs) have received widespread attentions because of their unique structure and physicochemical properties. Unfortunately, a drawback in the photocatalytic system based on TMDs is that the active sites are limited to the edge of the TMDs nanosheets, whilst the surface of the nanosheets remains inert.

To address these issues, we constructed a heterojunction between CdS nanoparticles and ultra-thin ReS_2 nanosheets (6 nm thickness), and studied the mechanism of CO_2 photoreduction in this catalytic system. We show that the photoelectrons separation and transfer process and the *in situ* formed defects on the surface of ReS_2 act as reactive sites to boost photocatalytic performance.

Highlights of this work include:

1. Ultrathin ReS_2 nanosheets with highly-efficient photocatalytic activity and selectivity. Ultra-thin ReS_2 nanosheets of around 6 nm thickness were synthesized from commercial bulk ReS_2 in water with ultra-sound. The heterojunction fabricated by the ReS_2 nanosheets and CdS nanoparticles was studied by advanced characterizations e.g. XANES, to determine charge separation and transfer. The composite showed 3 times activity and 93.4 % selectivity;

2. *In situ* formed sulfur vacancy of ReS_2 as the reactive sites for CO_2 adsorption and activation. The surface of ReS_2 nanosheets is shown to form defects under visible light. Density functional theory (DFT) computations show that these surface defects favor the chemisorption of CO_2 and, change the C-O bond length and angle to 1.398 Å and 117.9°;

3. Understanding of activity origin and photocatalytic CO_2 reduction mechanism with ReS_2 nanosheets. *In situ* characterizations highlight that the defects boost CO_2 conversion. The pathways for CO_2 photoreduction are postulated.

3.2 ReS_2 Nanosheets with *In Situ* Formed Sulfur Vacancies for Efficient and Highly Selective Photocatalytic CO_2 Reduction

This Chapter is included as it appears as a journal paper published by Yanzhao Zhang, Dazhi Yao, Bingquan Xia, Haolan Xu, Youhong Tang, Kenneth Davey, Jingrun Ran and Shi-Zhang Qiao. ReS_2 Nanosheets with *In Situ* Formed Sulfur Vacancies for Efficient and Highly Selective Photocatalytic CO_2 Reduction, ***Small Sci.*** 2021, 1, 2000052.

Statement of Authorship

Title of Paper	ReS2 Nanosheets with In Situ Formed Sulfur Vacancies for Efficient and Highly Selective Photocatalytic CO2 Reduction
Publication Status	☑ Published ☐ Accepted for Publication ☐ Submitted for Publication ☐ Unpublished and Unsubmitted w ork w ritten in manuscript style
Publication Details	Zhang, Y., Yao, D., Xia, B., Xu, H., Tang, Y., Davey, K., Ran, J. and Qiao, S., ReS2 Nanosheets with In Situ Formed Sulfur Vacancies for Efficient and Highly Selective Photocatalytic CO2 Reduction. Small Sci., 1: 2000052

Principal Author

Name of Principal Author (Candidate)	Yanzhao Zhang		
Contribution to the Paper	Design and conducted the experiments, analysed the data, wrote the manuscript.		
Overall percentage (%)	70%		
Certification:	This paper reports on original research I conducted during the period of my Higher Degree by Research candidature and is not subject to any obligations or contractual agreements with a third party that would constrain its inclusion in this thesis. I am the primary author of this paper.		
Signature		Date	06/12/2022

Co-Author Contributions

By signing the Statement of Authorship, each author certifies that:

i. the candidate's stated contribution to the publication is accurate (as detailed above);

ii. permission is granted for the candidate in include the publication in the thesis; and

iii. the sum of all co-author contributions is equal to 100% less the candidate's stated contribution.

Name of Co-Author	Dazhi Yao		
Contribution to the Paper	DFT simulation and revised the manuscript		
Signature		Date	06/12/2022

Name of Co-Author	Bingquan Xia		
Contribution to the Paper	Assisted in experimental design and setup. Provided review and comments on manuscript.		
Signature		Date	06/12/2022

Name of Co-Author	Haolan Xu		
Contribution to the Paper	XPS tests and data analysis		
Signature		Date	06/12/2022

Name of Co-Author	Youhong Tang		
Contribution to the Paper	AFM characterization and data analysis		
Signature		Date	06/12/2022

Name of Co-Author	Kenneth Davey		
Contribution to the Paper	Manuscript evaluation and revision.		
Signature		Date	6/12/2022
Name of Co-Author	Jingrun Ran		
Contribution to the Paper	Supervision of the work and manuscript evaluation and revision.		
Signature		Date	25/11/2023

Name of Co-Author	Shi-Zhang Qiao		
Contribution to the Paper	Supervision of the work, discussion and conceptualization of this manuscript and manuscript evaluation and revision.		
Signature		Date	25/01/23

ReS_2 Nanosheets with *in situ* Formed Sulfur Vacancies for Efficient and Highly-Selective Photocatalytic CO_2 Reduction

Yanzhao Zhang, Dazhi Yao, Bingquan Xia, Haolan Xu, Youhong Tang, Kenneth Davey, Jingrun Ran, and Shi-Zhang Qiao**

Y. Zhang, D. Yao, B. Xia, Dr. K. Davey, Dr. J. Ran, Prof. S. Z. Qiao
School of Chemical Engineering & Advanced Materials, The University of Adelaide, SA 5005, Australia.
E-mail: s.qiao@adelaide.edu.au; jingrun.ran@adelaide.edu.au
Prof. H. Xu
Future Industries Institute, University of South Australia, SA 5095, Australia.
Prof. Y. Tang
Center for Nanoscale Science and Technology, School of Computer Science, Engineering, and Mathematics, Flinders University, SA 5042, Australia.

Artificial photosynthesis can provide valuable fuels and positively impact greenhouse effects, via transforming carbon dioxide (CO_2) and water (H_2O) into hydrocarbons using semiconductor-based photocatalysts. However, the inefficient charge-carrier dissociation and transportation as well as the lack of surface active sites are two major drawbacks to boosting their activity and selectivity in photocatalytic CO_2 reduction. Recently, ReS_2 has received tremendous attention in photocatalysis area owing to its intriguing physicochemical properties. Nevertheless, the application of ReS_2 in photocatalytic CO_2 reduction is scarcely covered. In this study, we report a heterojunction formed between ReS_2 nanosheets and CdS nanoparticles, achieving an apparently-raised CO production of 7.1 μmol g^{-1} and high selectivity of 93.4%. The as-prepared ReS_2/CdS heterojunction exhibits the strengthened visible-light absorption, high-efficiency electron-hole pairs separation/transfer and increased adsorption/activation/reduction of CO_2 on *in situ* created sulfur vacancies of ReS_2, thus all favouring CO_2 photoreduction. These are corroborated by advanced characterization techniques, *e.g.,* synchrotron-based X-ray absorption near-edge structure, and density functional theory based computations. Our findings will be of a broad interest in practical design and fabrication of surface active sites and semiconductor heterojunctions for applications in catalysis, electronics and optoelectronics.

CO_2 emission leads to severe global greenhouse effect. Therefore, various strategies are developed to relieve this process including CO_2 fixation and cyclic utilization.[1-4] Meanwhile, the application of clean and renewable energy to fix CO_2 can not only promote the carbon cycle but also relieve the global energy crisis. Semiconductor-based photocatalytic carbon dioxide (CO_2) conversion represents a carbon-neutral and sustainable strategy to generate fuels and chemicals using renewable and clean solar energy.[1-5] This process is fundamentally impacted by three steps: i) light absorption to excite semiconductor-based photocatalysts, ii) photo-generated electron-hole pairs separation and transfer efficiency and; iii) redox reactions on the surface of the photocatalyst.[6, 7] To improve photocatalytic CO_2 reduction, researchers have generally focused on approaches including introducing defects in the crystal lattice,[8-13] loading metal cocatalysts,[14, 15] exposing highly active facets,[16, 17] and fabricating heterojunctions[7, 18]. Among these, forming heterojunctions in composites is deemed as an effective strategy due to efficient suppression of charge carrier recombination and highly-promoted migration efficiency.[19, 20] Some cocatalysts broaden the light absorption spectrum to utilize long-wavelength light.[21, 22] However, CO_2 molecules are highly thermodynamically stable with a bond energy of 750 kJ mol^{-1} for C=O.[6] This implies that the dissociation of CO_2 requires high energy via conventional methods.[6] The activation of CO_2 molecules on the surface of photocatalysts relies on various active sites, *e.g.* functional groups, frustrated Lewis pairs, single atoms and vacancies. These possess an affinity for CO_2 and water (H_2O) adsorption and activation. These are however rare on the perfect surfaces of photocatalysts. The deliberate creation of active sites on the surfaces of photocatalysts is therefore a major research approach to practically realize effective photocatalysis.[6]

Transition metal dichalcogenides (TMDs) have received significant attention in catalysis, rechargeable batteries and sensing devices.[23-28] For example, Zhou *et al.* reported that the FeS ultrathin nanosheets on the carbon fiber cloth achieved highly efficient hydrogen evolution due to the phase transition triggered by the illumination at room temperature.[29] Similarly, Fu *et al.* prepared $MoReS_3$ with a layered structure, a new type of TMDs, and it showed excellent hydrogen evolution in electrocatalysis.[30] As a new type of TMDs, ReS_2 has been studied in photocatalytic hydrogen evolution (PHE), both experimentally and theoretically.[31-38] Zhang *et al.*[34] reported that ReS_2 exhibited significant performance in PHE, a two-electron catalytic reaction. This is because free electrons are captured by tightly bound excitons to form trions that constrain recombination and thereby promote performance. The corresponding computation indicates that the adsorption energy of the H atoms exhibits a small absolute value

(-0.5 eV), revealing the highly efficient PHE performance. With a narrow band gap of 1.7 eV, ReS_2 possesses the strong absorption in visible-light range, thus benefiting photocatalytic activity. Additionally, ReS_2 exhibits an automatic transition of hydrophobicity-hydrophilicity, before and following, visible-light illumination.[35] This is because that defects on its surface change the adsorption configuration of H_2O and oxygen (O_2) to form hydroxyl groups leading to the transmission of hydrophilicity.[35] This adsorption configuration impacts adsorption of CO_2 and H_2O in CO_2 photoreduction. Zhou *et al*[36] reported that Re sites can absorb hydrogen as the intermediate for CO_2 hydrogenation. Findings suggest ReS_2 nanosheet (NS) is a potential photocatalyst for CO_2 reduction. A drawback however with most TMDs is that the reactive sites are located at the edge of the NS, because of the hanging-bond created by breakage of the bond between transmitting metal and sulfur. These limited active sites on the edge and, inert surface elsewhere, is a significant impediment to apply TMDs as photocatalysts. Therefore, the activation of the inert surface through the introduction of defects on ReS_2 NSs is regarded as an effective strategy to boost its photocatalytic performance.

Herein, we report a simple self-assembly approach to synthesize a heterojunction composed of ReS_2 NSs and CdS nanoparticles (NPs) for photocatalytic CO_2 reduction. The optimized ReS_2/CdS heterostructure exhibits a boosted photocatalytic CO_2-to-CO conversion activity of 7.1 μmol g^{-1} accompanied with a high selectivity of 93.4%. The enhanced performance is aroused by high-efficiency interfacial charge transfer between ReS_2 and CdS as well as *in situ* formed sulfur vacancies on the ReS_2 surface. Results from advanced characterizations, *e.g.* synchrotron-based X-ray absorption near-edge structure (XANES), together with X-ray photoelectron spectroscopy (XPS), confirm the strong electronic coupling between ReS_2 and CdS. Density functional theory (DFT) based computations highlight the adsorption and activation of CO_2 on the ReS_2 surface with *in situ* formed sulfur vacancies based on electron transfer and change in C-O bond length and angle. Our work will be of immediate practical interest to a wide range of researchers for the design and synthesis of nanostructured materials in energy conversion and storage field.

ReS_2 NSs were prepared by exfoliating commercial bulk ReS_2 under ultrasonication in deionized water; whilst CdS NPs were fabricated by a hydrothermal method. Then, the heterojunctions of ReS_2 and CdS were synthesized by physical mixing. The as-prepared samples were denoted as CdS, CR4, CR8 and CR12, respectively, according to the added volumes of ReS_2 NSs suspension (0, 4, 8 and 12 ml, respectively). The X-ray diffraction (XRD) patterns of all the as-prepared samples are presented in Figure S1 of supporting information.

The pattern displayed is ascribed to cubic-phase CdS (PDF #10-0454). A weak peak at 14.6° is attributed to the presence of ReS_2 NSs. The intensity of this peak is enhanced with increasing content of ReS_2 in the heterojunction. No apparent alteration of peak positions and intensities is observed for cubic-phase CdS after its combination with ReS_2, suggesting the weak interaction formed via physical mixing at room temperature doesn't change the crystal structure.

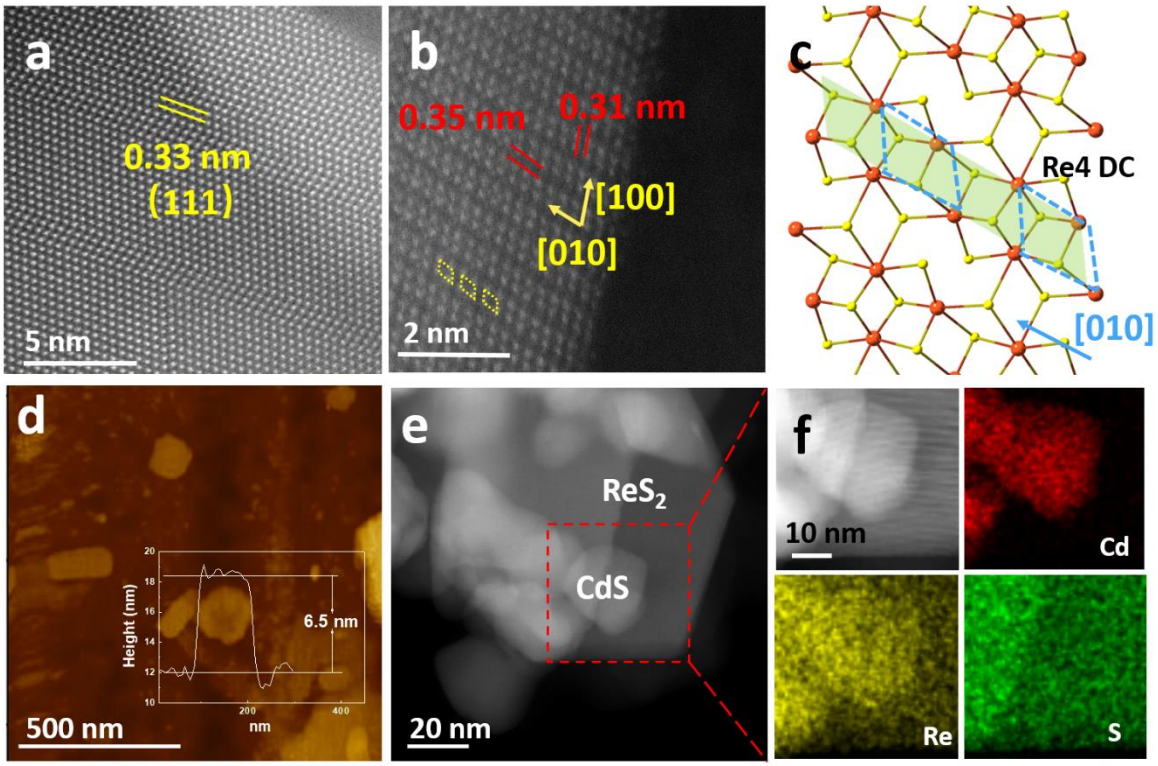

Figure 1. Aberration-corrected HAADF-STEM images of a) CdS NPs and b) ReS_2 NSs. c) Simulated model for ReS_2. The red and yellow colored spheres denote Re and S, respectively, and the blue-dot line denotes Re4 diamond chain. d) AFM image of ReS_2 nanosheet and measured thickness of ReS_2. e) TEM of ReS_2 nanosheets and CdS nanoparticles. f) EDX mapping of CR12 from red dotted rectangle of e).

Furthermore, the morphologies and microstructures of CdS NPs, ReS_2 NSs and CR12 are characterized by aberration-corrected high angle annular dark field scanning transmission electron microscopy (HAADF-STEM), transmission electron microscopy (TEM) and HAADF-STEM elemental mapping. The HAADF-STEM image of CdS NPs (**Figure 1**a) exhibits a lattice spacing value of 0.33 nm, ascribed to the (111) facet of cubic-phase CdS. In addition, the HAADF-STEM image of ReS_2 NS (**Figure 1**b) shows the typical Re4 diamond

chains (DC) structure (yellow dot line square). The spacing values between the Re4 diamond in the a [100] and b [010] directions are 0.35 and 0.31 nm, respectively (**Figure 1**b). This is also displayed in the simulated atomic structure of ReS_2 monolayer (**Figure 1**c). It is reported

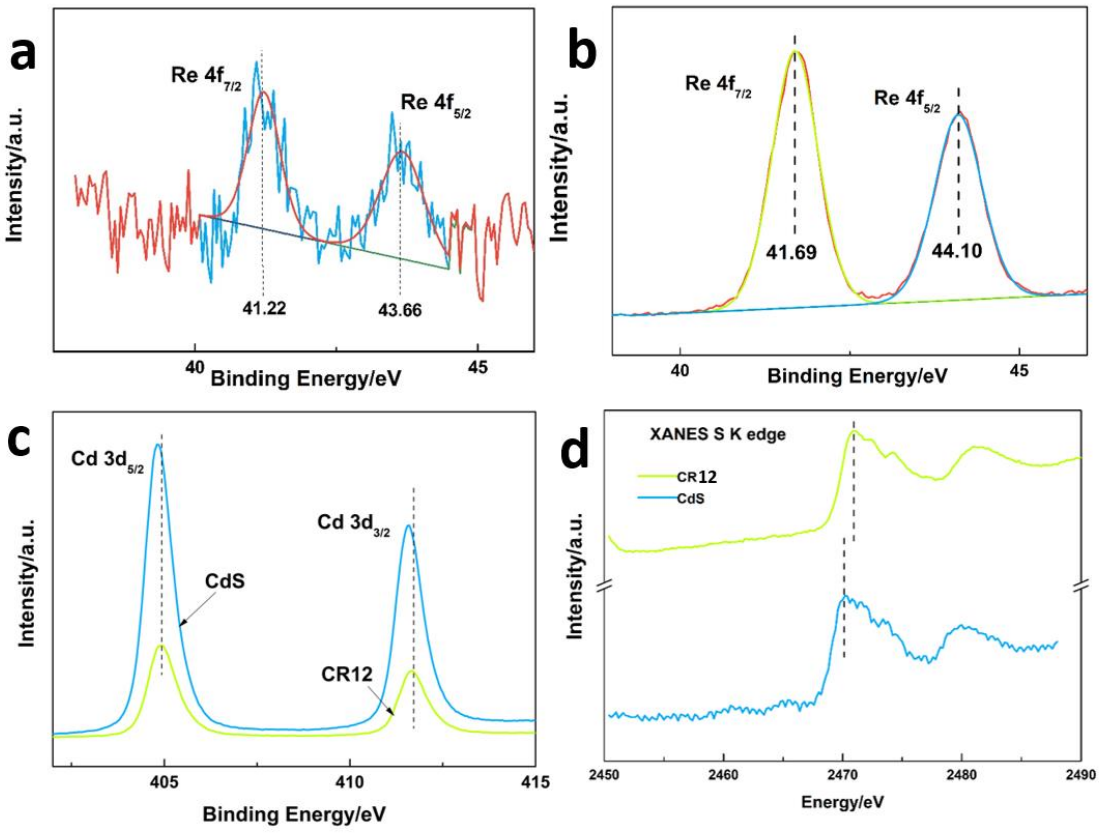

Figure 2. a) High-resolution XPS spectrum of Re 4f for CR12. b) High-resolution XPS spectrum of Re 4f for ReS_2. c) High-resolution XPS spectrum of Cd 3d for CdS and CR12. d) XANES S K edge of CdS and CR12.

that Re4 DC can act as reactive sites for water splitting. This is because these favor water adsorption and activation, and possibly assist proton transfer to participate in CO_2 photoreduction.[33, 34] The thickness of ReS_2 NS is further confirmed to be *ca.* 6.5 nm using atomic force microscopy (AFM; **Figure 1**d). The ultrathin thickness of ReS_2 NS not only endows it large surface area to form strong electronic coupling with other materials but also increases the number of exposed active sites towards catalytic reactions. The combination of ReS_2 NS and CdS NPs in CR 12 is shown in **Figure 1**e. Moreover, the HAADF-STEM image and the corresponding energy dispersive X-ray (EDX) elemental mapping images further corroborate the hybridization of ReS_2 NS and CdS NP (**Figure 1**f) in CR12. The colours of red,

yellow and green are shown in **Figure 1**f represent, respectively, the distribution of Cd, S and Re elements, in agreement with the HAADF-STEM image.

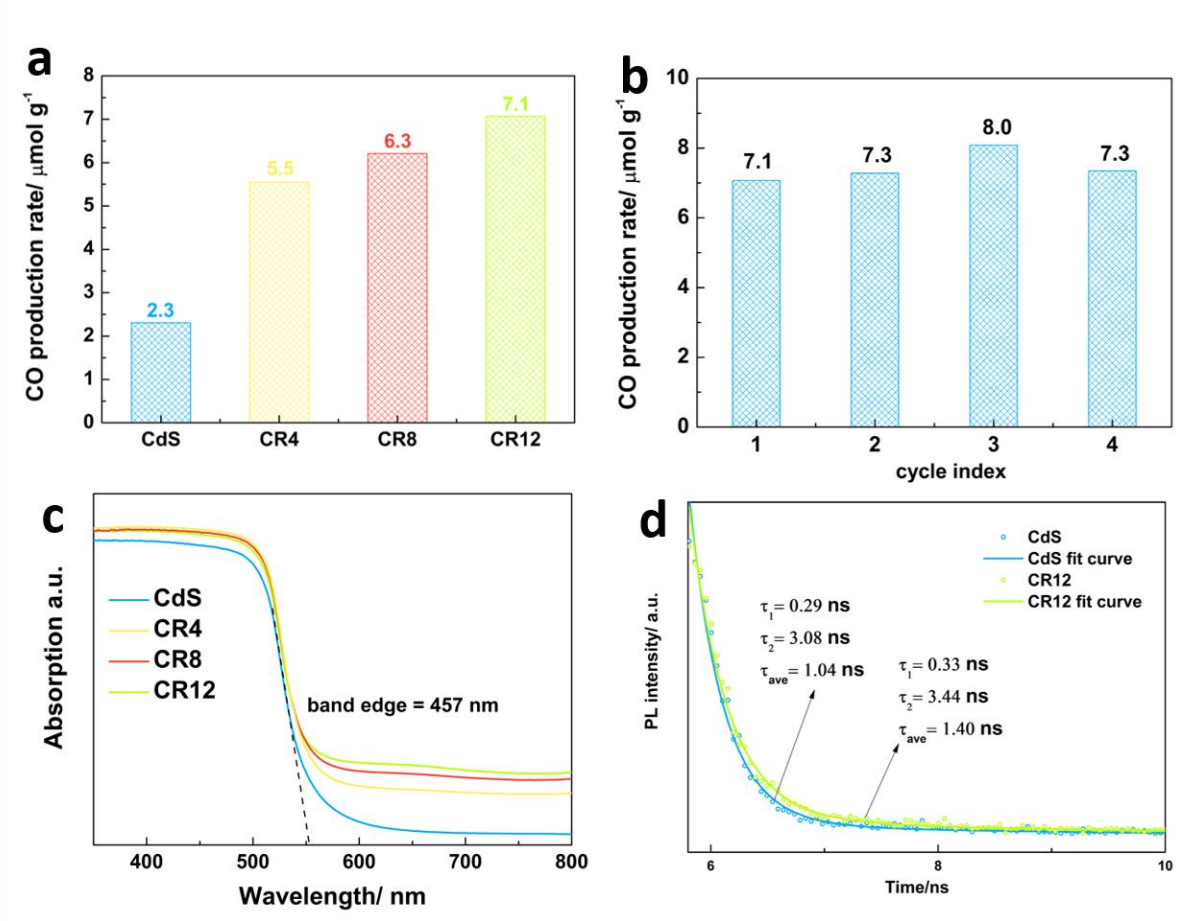

Figure 3. a) Photocatalytic CO_2 reduction activities of CdS, CR4, CR8 and CR12 under visible-light illumination ($\lambda \geq 420$ nm). b) Photocatalytic CO_2 reduction activity of CR12 recycle test with 7 h per cycle test. c) UV-vis diffuse reflectance spectroscopy and band edge for CdS, CR4, CR8, CR12. d) Transient-state photoluminescence (TSPL) spectra for CdS and CR12.

Moreover, both surface-sensitive X-ray photoelectron spectroscopy (XPS) and synchrotron-based XANES were conducted to disclose the interactions between CdS and ReS_2 in CR12. The high-resolution Re 4f XPS spectrum for CR12 (**Figure 2**a) showed a shift of *ca.* 0.5 eV towards the direction of lower binding energy compared with that for pure ReS_2 (**Figure 2**b), suggesting the electron transfer from CdS to ReS_2 in CR12. Besides, the high-resolution XPS spectrum of Cd 3d for CR12 shifts to the direction of higher binding energy (**Figure 2**c), also indicating the electron migration from CdS to ReS_2 in CR12. Furthermore, synchrotron-based XANES was performed (**Figure 2**d). The S K-edge XANES of CR12 indicates a shift towards

high photon energy direction, in comparison with that for CdS. This also supports the electron transfer from CdS to ReS_2 in CR12.

Solid-gas phase photocatalytic CO_2 reduction activities of the as-prepared samples were examined under visible-light irradiation ($\lambda \geq 420$ nm). As shown in **Figure 3**a, CdS shows a limited photocatalytic CO_2 reduction activity with CO and CH_4 production of 2.3 μmol g^{-1} and 1.1 μmol g^{-1} over 7 h (Figure S2, supporting information). The coupling of ReS_2 and CdS (CR4, CR8 and CR12) leads to apparent enhancement of both activity and selectivity in visible-light-driven CO_2-to-CO conversion (**Figure 3**a). In particular, CR12 shows the highest photocatalytic CO_2-to-CO conversion activity of 7.1 μmol g^{-1} and selectivity of 93.4%, *ca.* 309% and 138% times higher than those of CdS alone. This result for the first time demonstrates that the coupling with ReS_2 NS could significantly boost both activity and selectivity in photocatalytic CO_2-to-CO conversion. In addition, we conducted three blank experiments under the same conditions but purged with ultrahigh purity argon gas instead of CO_2, without visible-light illumination and without photocatalyst, respectively. These contrast experiments show no photocatalytic CO_2 conversion performance, suggesting that the products (CO and CH_4) are generated from photo-induced CO_2 conversion. Furthermore, the stability of CR12 was studied via 4 cycle-testing with 7 h per cycle (**Figure 3**b). No apparent deterioration in photocatalytic CO_2 reduction performance of CR12 is found over a 28-hour test. The TEM image and EDX spectrum (Figure S3, supporting information) of CR12 after photocatalytic CO_2 reduction exhibited no obvious difference with that before reaction. This finding suggests that no apparent change in morphology and chemical composition of CR12 occurs after the 28-hour photocatalytic reaction.

To further investigate the origin of the enhanced activity and selectivity, as well as the reaction mechanism in CR12 for photocatalytic CO_2 reduction, both experimental characterizations and density functional theory (DFT) based theoretical calculations are conducted. The light absorption capacity is studied by UV-vis diffuse reflectance spectroscopy. As shown in **Figure 3**c, increased absorption in the range of 460-800 nm is attributed to the presence of ReS_2 NSs. However, the adsorption edge of CR12 (457 nm) does not display any shift. This finding suggests that the bandgap (2.24 eV) is not changed following combination with the ReS_2 NSs. The bandgap of ReS_2 NSs is 1.7 eV (Figure S4, supporting information). This induces the 'bulge' at ~600-800 nm in the UV-vis spectrum of CR12. Such an improved visible-light absorption probably contributes to the raised activity in photocatalytic CO_2 reduction.

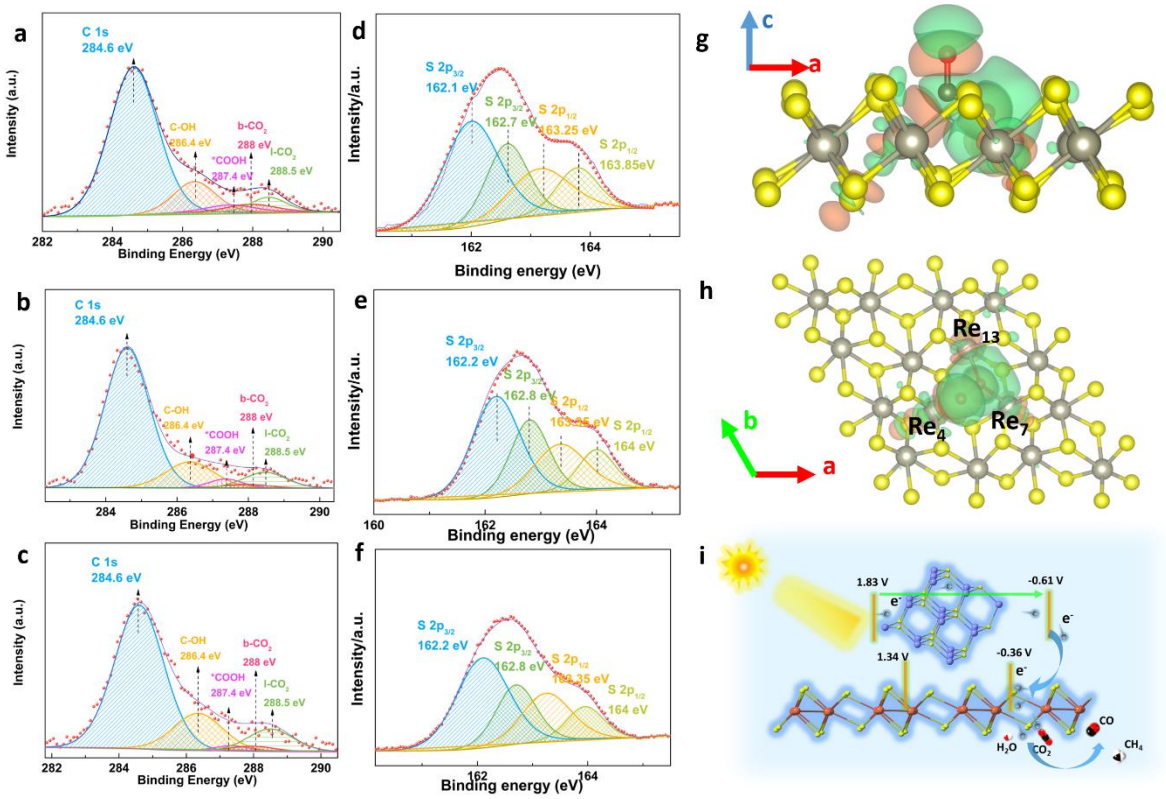

Figure 4. a) and d) High-resolution XPS spectrum for C 1s and S 2p for RS1. b) and e) High-resolution XPS spectrum for C 1s and S 2p for RS2. c) and f) High-resolution XPS spectrum for C 1s and S 2p for RS3. g) Side-view (elevation) and h) Top-view (plan) of the electron density distribution of absorbed CO_2 on V_s-ReS_2. The red, yellow, grey and brown colored spheres denote O, S, Re and C atoms, respectively. The iso-surface value is set to 0.002 e $Å^{-3}$. i) Schematic of photocatalytic CO_2 reduction in CR12 system under visible-light illumination ($\lambda \geq 420$ nm). The purple, red, yellow, orange, white and black colored spheres denote Cd, O, S, Re, H and C atoms, respectively.

A range of characterization methods, *e.g.*, steady-state photoluminescence (PL) spectroscopy, transient-state photoluminescence (TSPL) spectroscopy, electrochemical impedance spectroscopy (EIS), and transient photocurrent (TPC) density measurement, are executed to probe into the efficiency of charge carrier separation and transportation. The steady-state PL (Figure S5, supporting information) intensity of CR12 is significantly lower than that for CdS. This finding is attributed to the oppressed charge-carrier recombination after coupling with ReS_2 NS in CR12. After fitting of the TSPL curves in **Figure 3**d, elongated lifetimes of charge carriers (τ_1 = 0.33 ns; τ_2 = 3.44 ns; τ_{ave} = 1.40 ns) for CR12 are observed, in comparison with those for CdS (τ_1 = 0.29 ns; τ_2 = 3.08 ns; τ_{ave} = 1.04 ns). This also supports

the more effective dissociation and migration of photo-generated electrons and holes in CR12. Furthermore, the EIS spectra (Figure S6a, supporting information) exhibit a smaller semicircle radius for the Nyquist plot, together with a decreased charge-transfer resistance (R_t = 4672 Ω) for CR12 in contrast with that of CdS (R_t = 4830 Ω). This finding suggests a faster charge carrier migration rate in CR12. In addition, CR12 exhibits a greater TPC density over CdS (Figure S6b, supporting information). This also confirms the more efficient dissociation of light-induced excitons, in agreement with the above PL and EIS spectra results.

To investigate CO_2 adsorption, activation and reduction process, XPS and Raman characterizations were conducted for pristine ReS_2, RS1, RS2 and RS3 (see details in supporting information 1.5). The C 1s peaks in **Figure 4**a-c mainly consist of a peak located at 284.6 eV, ascribed to the contaminated carbon. All other peaks were calibrated using this peak. After deconvolution of the C 1s peaks in **Figure 4**a-c, four satellite peaks can be obtained and attributed to, C-OH, *COOH, b-CO_2 (chemisorbed and bent CO_2) and l-CO_2 (physisorbed and linear CO_2), respectively.[39] Among these adsorption configurations, *COOH is deemed as the precursor for CO, consistent with the major product (CO) of this work.[40, 41] The contents (mol%) acquired based on the areas of four satellite C 1s peaks are provided in Table S1 (see supporting information). RS1 shows the highest contents of C 1s peaks associated with *COOH and b-CO_2, in comparison to RS2 and RS3. This is because that the water vapor can facilitate the adsorption of CO_2.[42-44] The above results indicate that the adsorption of CO_2 on the surface of ReS_2 NS is obviously enhanced by visible-light illumination. To further study the key role of illumination on CO_2 adsorption, the high-resolution XPS spectra of S 2p for pristine ReS_2 NS, RS1, RS2 and RS3 are collected. ReS_2 NS exhibit two peaks located at 162.05 and 163.18 eV, ascribed to the S $2p_{3/2}$ and S $2p_{1/2}$ (Figure S7, supporting information). In comparison, after light illumination, satellites peak located at 162.7 and 163.85 eV appear (**Figure 4** d-f), attributed to the presence of sulfur vacancy induced by visible-light illumination. Moreover, the high-resolution Re 4f XPS spectrum (Figure S7, supporting information) of pristine ReS_2 NS only exhibits two peaks at 41.65 and 44.06 eV, attributed to the Re $4f_{7/2}$ and Re $4f_{5/2}$ peaks, respectively. In comparison, Re 4f satellites peaks located at lower binding energy positions are observed in the high-resolution Re 4f XPS spectra of RS1, RS2 and RS3 (Figure S8a-c, supporting information), also implying the presence of sulfur vacancies in ReS_2 after light illumination. Furthermore, the aberration-corrected HAADF-STEM images of RS1 and pristine ReS_2 are displayed in Figure S9a and b, respectively. In contrast with pristine ReS_2,

RS1 exhibits more defects, *e.g.*, vacancies and pores, on its surface after the light illumination. This finding is in agreement with the afore-mentioned XPS results.

These findings are further corroborated by the Raman spectroscopy characterization. Pristine ReS_2 displays a typical E_g-like peak at *ca.* 305 cm^{-1} (Figure S10, supporting information). In contrast, RS1, RS2 and RS3 all exhibit a blue shift of E_g-like peak. This might be caused by the presence of sulfur vacancy leading to the mass fluctuation at S position. Additionally, RS1, RS2 and RS3 all exhibit the peaks at *ca.* 1271 cm^{-1}, ascribed to *COOH (Figure S11). [40,41] In particular, the highest *COOH peak intensity is observed for RS1, compared to those of RS2 and RS3, in coincidence with the above XPS results (Table S1, supporting information). These findings were reinforced in the Fourier Transform Infrared Spectroscopy (FTIR) spectra (Figure S12, supporting information). The bands at 1620 cm^{-1} are attributed to *COOH and the bands at 1404 cm^{-1} to the symmetric (O-C-O) vibration, indicating the presence of adsorbed CO_2 molecules on the surface of the photocatalyst. These findings are consistent with those from the XPS results.

To verify the possible CO_2 activation on the ReS_2 with the sulfur vacancy (V_s-ReS_2), DFT based theoretical computation was carried out to determine the adsorption of CO_2 and local electronic structure. As shown in Figure S13 (Supporting Information), the atomic structures for V_s-ReS_2 were constructed and optimized. The adsorption behavior of CO_2 on the surface of V_s-ReS_2 was studied (**Figure 4**g, h). The adsorption energy (E_{ad}) of CO_2 on V_s-ReS_2 was found to be -0.82 eV. This value demonstrates that the chemisorption of CO_2 on V_s-ReS_2 is favorable.[45, 46] The CO_2 molecule loses linearity to change α(OCO) to 117.9°, and the two C-O_1 and C-O_2 bonds are lengthened to 1.209 and 1.398 Å, respectively, thereby denoting activation of the C=O bond on V_s-ReS_2.[46, 47]

Bader charge analysis (Figure S14, supporting information) was conducted to study the charge distribution on the CO_2 adsorbed V_s-ReS_2 and, to investigate the electronic impact. It was found that Re atoms and C atoms are electron deficient, whilst S atoms and O atoms are negatively charged (Figure S14a, supporting information). In particular, Re near a sulfur vacancy (Re_4, Re_7, and Re_{13}) changed more positively when CO_2 was absorbed onto V_s-ReS_2 (Figure S14b, supporting information).[38, 46, 47] Charge density difference was employed to visualize electron transfer behaviour. Findings showed that Re and carbon atoms donate charges to oxygen and that they are positively charged.[37, 46, 47] These findings confirm that V_s-ReS_2 favorably impacts chemisorption and activation of CO_2 and electron transfer between CO_2 and V_s-ReS_2.

Based on the findings from both the experimental studies and theoretical computations, a possible photocatalytic CO_2 reduction mechanism is proposed. The conduction band (CB) and valence band (VB) edge positions of CdS and ReS_2 are estimated via combining their Mott–Schottky plots (Figure S15, supporting information) and UV-vis diffuse reflectance spectrum (Figure S5, Supporting Information). As shown in **Figure 4**i, CdS and ReS_2 form a type I (straddling type) heterojunction. Under visible-light illumination ($\lambda \geqslant 420$ nm), the CdS NPs are photo-excited and the electrons transfer from the VB to the CB, while the photogenerated holes in the VB of CdS will migrate to the VB of ReS_2, where H_2O molecules are oxidized. Then, photogenerated electrons in the CB of CdS transfer to the CB of ReS_2. ReS_2 NS accommodates abundant active sites for the adsorption, activation and reduction of CO_2 and H_2O to evolve CO and CH_4 (equations 1-3). The most likely pathways for the CO_2 photoreduction on CdS/ReS_2 heterojunction are proposed as below:

$$* + CO_2 + e^- + H^+ \rightarrow COOH^* \quad (1)$$

$$COOH^* + e^- + H^+ \rightarrow CO^* + H_2O \quad (2)$$

$$CO^* \rightarrow * + CO \uparrow \quad (3)$$

The asterisks and vertical arrows, respectively, denote reactive sites and the release of gas.

The presence of ReS_2 NSs in CR12 leads to the apparent enhancement in the selectivity of photocatalytic CO_2-to-CO conversion. This is probably because that the electrons in ReS_2 can be captured by tightly-bound excitons to form trions consisting of two electrons and one hole, [34] which facilitates the two-electron reduction reaction of CO_2-to-CO conversion rather than the eight-electron reduction reaction of CH_4 production.

In summary, we have successfully prepared a heterojunction of ReS_2 nanosheets and CdS nanoparticles using a facile self-assembly method via physical mixing at room temperature. This nanocomposite exhibits a significantly boosted visible-light photocatalytic CO production of 7.1 μmol g^{-1} together with an increased CO_2-to-CO conversion selectivity of 93.4%. Such an improved photocatalytic performance originates from two factors: i) intimate electronic interaction advancing efficient photo-generated electron-hole separation and migration; ii) *in situ* generated sulfur vacancies serving as active sites for CO_2 adsorption, activation and reduction to CO. These are verified by both state-of-art characterizations, *e.g.*, synchrotron-based X-ray absorption near edge structure, and theoretical calculations. Our work demonstrates the promising potency of ReS_2 in light-driven CO_2 reduction and the intriguing

opportunities of applying *in-situ* generated anion vacancies of transitional metal dichalcogenides in catalysis, electronics and optoelectronics.

Supporting Information

Supporting information is available from the Wiley Online Library, or the author.

Acknowledgments

This work was supported financially by the Australian Research Council (ARC) through the Discovery Project Program (DP160104866, FL170100154 and DE200100629). The authors thank Dr. Ting Gao, University of South Australia, for the XPS testing and Dr. Ashley Slattery, Adelaide Microscopy, The University of Adelaide for technical assistance. Y.Z. acknowledges financial support from the Australian Government Research Training Program Scholarship (RTP). This research was undertaken on the X-ray absorption spectroscopy beamline at the Australian Synchrotron, part of ANSTO.

Conflict of Interest

The authors declare no conflict of interest.

Keywords

CO_2 photoreduction, sulfur vacancy, ReS_2, heterojunction, transition metal dichalcogenides

Received: November 15, 2020
Revised: November 30, 2020
Published online: January 15, 2021

References

[1] S. Solomon, G.K. Plattner, R. Knutti, P. Friedlingstein, *Proc. Natl. Acad. Sci. USA* **2009**, *106*, 1704.

[2] N. S. Lewis, D. G. Nocera, *Proc. Natl. Acad. Sci. USA* **2006**, *103*, 15729.

[3] M. Vermeer, S. Rahmstorf, *Proc. Natl. Acad. Sci. USA* **2009**, *106*, 21527.

[4] P. N. Pearson, M. R. Palmer, *Nature* **2000**, *406*, 695.

[5] M. Meinshausen, N. Meinshausen, W. Hare, S. C. Raper, K. Frieler, R. Knutti, D. J. Frame, M. R. Allen, *Nature* **2009**, *458*, 1158.

[6] Y. Zhang, B. Xia, J. Ran, K. Davey, S. Z. Qiao, *Adv. Energy Mater.* **2020**, *10*, 1903879.

[7] J. Ran, M. Jaroniec, S. Z. Qiao, *Adv. Mater.* **2018**, *30*, 1704649.

[8] Z. Jiang, W. Sun, W. Miao, Z. Yuan, G. Yang, F. Kong, T. Yan, J. Chen, B. Huang, C. An, *Adv. Sci.* **2019**, *6*, 1900289.

[9] S. Sato, T. Morikawa, S. Saeki, T. Kajino, T. Motohiro, *Angew. Chem., Int. Ed.* **2010**, *49*, 5101.

[10] Q. Zhang, T. Gao, J. M. Andino, Y. Li, *Appl. Catal., B* **2012**, *123*, 257.

[11] X. Li, Y. Sun, J. Xu, Y. Shao, J. Wu, X. Xu, Y. Pan, H. Ju, J. Zhu, Y. Xie, *Nat. Energy* **2019**, *4*, 690.

[12] M. Shen, L. Zhang, M. Wang, J. Tian, X. Jin, L. Guo, L. Wang, J. Shi, *J. Mater. Chem. A* **2019**, *7*, 1556.

[13] S. Gao, B. Gu, X. Jiao, Y. Sun, X. Zu, F. Yang, W. Zhu, C. Wang, Z. Feng, B. Ye, *J. Am. Chem. Soc.* **2017**, *139*, 3438.

[14] R. Long, Y. Li, Y. Liu, S. Chen, X. Zheng, C. Gao, C. He, N. Chen, Z. Qi, L. Song, *J. Am. Chem. Soc.* **2017**, *139*, 4486.

[15] X. Cheng, P. Dong, Z. Huang, Y. Zhang, Y. Chen, X. Nie, X. Zhang, *J. CO_2 Util.* **2017**, *20*, 200.

[16] Y. Zhang, X. Wang, P. Dong, Z. Huang, X. Nie, X. Zhang, *Green Chem.* **2018**, *20*, 2084.

[17] H. Xu, S. Ouyang, P. Li, T. Kako, J. Ye, *ACS Appl. Mate. Interfaces* **2013**, *5*, 1348.

[18] H. Shi, G. Chen, C. Zhang, Z. Zou, *ACS Catal.* **2014**, *4*, 3637.

[19] S.W. Cao, X.F. Liu, Y.P. Yuan, Z.Y. Zhang, Y.S. Liao, J. Fang, S. C. J. Loo, T. C. Sum, C. Xue, *Appl. Catal., B* **2014**, *147*, 940.

[20] J. Ran, W. Guo, H. Wang, B. Zhu, J. Yu, S.Z. Qiao, *Adv. Mater.* **2018**, *30*, 1800128.

[21] C. Zhao, A. Krall, H. Zhao, Q. Zhang, Y. Li, *Int. J. Hydrog. Energy* **2012**, *37*, 9967.

[22] T. Yui, A. Kan, C. Saitoh, K. Koike, T. Ibusuki, O. Ishitani, *ACS Appl. Mate. Interfaces* **2011**, *3*, 2594.

[23] Y.C. Lin, H.P. Komsa, C.H. Yeh, T. Bjorkman, Z.Y. Liang, C.H. Ho, Y.S. Huang, P.W. Chiu, A. V. Krasheninnikov, K. Suenaga, *ACS Nano* **2015**, *9*, 11249.

[24] Y. Yu, G.H. Nam, Q. He, X.J. Wu, K. Zhang, Z. Yang, J. Chen, Q. Ma, M. Zhao, Z. Liu, F.R. Ran, X. Wang, H. Li, X. Huang, B. Li, Q. Xiong, Q. Zhang, Z. Liu, L. Gu, Y. Du, W. Huang, H. Zhang, *Nat. Chem.* **2018**, *6*, 638.

[25] M. Samadi, N. Sarikhani, M. Zirak, H. Zhang, H.L. Zhang, A. Z. Moshfegh, *Nanoscale Horiz.* **2018**, *3*, 90.

[26] C. Martella, C. Mennucci, A. Lamperti, E. Cappelluti, F. B. de Mongeot, A. Molle, *Adv. Mater.* **2018**, *30*, 1705615.

[27] Q. Yun, Q. Lu, X. Zhang, C. Tan, H. Zhang, *Angew. Chem., Int. Ed.* **2018**, *57*, 626.

[28] X. Wang, G. Li, M. H. Seo, F. M. Hassan, M. A. Hoque, Z. Chen, *Adv. Energy Mater.* **2015**, *5*, 1501106.

[29] G. Zhou, Y. Shan, L. Wang, Y. Hu, J. Guo, F. Hu, J. Shen, Y. Gu, J. Cui, L. Liu, X. Wu, *Nat. Commun.* **2019**, *10*, 399.

[30] Y. Fu, Y. Shan, G. Zhou, L. Long, L. Wang, K. Yin, J. Guo, J. Shen, L. Liu, X. Wu, *Joule* **2019**, *3*, 2955.

[31] K. Keyshar, Y. Gong, G. Ye, G. Brunetto, W. Zhou, D. P. Cole, K. Hackenberg, Y. He, L. Machado, M. Kabbani, A. H. C. Hart, B. Li, D. S. Galvao, A. George, R. Vajtai, C. S. Tiwary, P. M. Ajayan, *Adv. Mater.* **2015**, *27*, 4640.

[32] S. Tongay, H. Sahin, C. Ko, A. Luce, W. Fan, K. Liu, J. Zhou, Y.S. Huang, C.H. Ho, J. Yan, D. Ogletree, S. Aloni, J. Ji, S. Li, J. Li, F. M. Peeters, J. Wu, *Nat. Commun.* **2014**, *5*, 3252.

[33] Q. Zhang, W. Wang, J. Zhang, X. Zhu, L. Fu, *Adv. Mater.* **2018**, *30*, 1704585.

[34] Q. Zhang, W. Wang, J. Zhang, X. Zhu, Q. Zhang, Y. Zhang, Z. Ren, S. Song, J. Wang, Z. Ying, R. Wang, X. Qiu, T. Peng, L. Fu, *Adv. Mater.* **2018**, *30*, 1707123.

[35] W. Wang, J. Zhang, Q. Zhang, S. Wan, X. Zhu, Q. Zhang, W. Wang, Y. Zhang, Y. Liu, L. Fu, *Adv. Mater.* **2018**, *30*, 1804559.

[36] Y. Zhou, E. Song, J. Zhou, J. Lin, R. Ma, Y. Wang, W. Qiu, R. Shen, K. Suenaga, Q. Liu, J. Wang, Z. Liu, J. Liu, *ACS Nano* **2018**, *12*, 4486.

[37] B. Chen, H. Li, H. Liu, X. Wang, F. Xie, Y. Deng, W. Hu, K. Davey, N. Zhao, S.Z. Qiao, *Adv. Energy Mater.* **2019**, *30*, 1970117.

[38] J. Pan, X. Zhou, J. Zhong, J. Hu, *Phys. Lett. A*, **2019**, *31*, 125883.

[39] M. Favaro, H. Xiao, T. Cheng, W. A. Goddard, J. Yano, E. J. Crumlin, *Proc. Natl. Acad. Sci. USA* **2017**, *114*, 6706.

[40] A. Vasileff, X. Zhi, C. Xu, L. Ge, Y. Jiao, Y. Zheng, S.Z. Qiao, *ACS Catal.* **2019**, *9*, 9411.

[41] N. J. Firet, W. A. Smith, *ACS Catal.* **2017**, *7*, 606.

[42] A. O. Yazaydin, A. I. Benin, S. A. Faheem, P. Jakubczak, J. J. Low, R. R. Willis, R. Q. Snurr, *Chem. Mater.* **2009**, *21*, 1425.

[43] M. B. Yue, L. B. Sun, Y. Cao, Z. J. Wang, Y. Wang, Q. Yu, J. H. Zhu, *Microporous Mesoporous Mater.* **2008**, *114*, 74.

[44] B. Zhao, Y.X. Pan, C.J. Liu, *Catal. Today* **2012**, *194*, 60.

[45] X. Zhi, Y. Jiao, Y. Zheng, S. Qiao, *Small*, **2019**, *15*, 1804224.

[46] R. Khaledialidusti, A. K. Mishra, A. Barnoush, *ACS Omega* **2019**, *4*, 15935.

[47] H. Li, J. Shang, Z. Ai, L. Zhang, *J. Am. Chem. Soc.* **2015**, *137*, 6393.

Supporting information

ReS_2 Nanosheets with *in situ* Formed Sulfur Vacancies for Efficient and Highly-Selective Photocatalytic CO_2 Reduction

Yanzhao Zhang, Dazhi Yao, Bingquan Xia, Haolan Xu, Youhong Tang, Kenneth Davey, Jingrun Ran, and Shi-Zhang Qiao**

Y. Zhang, D. Yao, B. Xia, Dr. K. Davey, Dr. J. Ran, Prof. S. Z. Qiao

School of Chemical Engineering & Advanced Materials, The University of Adelaide, SA 5005, Australia.

E-mail: s.qiao@adelaide.edu.au; jingrun.ran@adelaide.edu.au

Prof. H. Xu

Future Industries Institute, University of South Australia, SA 5095, Australia.

Prof. Y. Tang

Center for Nanoscale Science and Technology, School of Computer Science, Engineering, and Mathematics, Flinders University, SA 5042, Australia.

Part I: Experimental Section

1.1 Materials and fabrication

Fabrication of ultra-thin nanosheets of ReS_2: All reagents were analytic grade and used without further purification. Bulk ReS_2 was purchased from Alfa Aesar. ReS_2 nanosheets were prepared by a liquid-phase exfoliation using an ultrasonic probe followed by ice-bath sonication in deionized water. Bulk ReS_2 (50 mg) was dispersed in deionized water for 2 h. The ultrasonic probe was operated 2 s and stopped for 4 s. Subsequently, the dispersion was centrifuged at 8000 rpm for 2 mins to collect supernatant. The concentration of the supernatant was determined to be 50 μg mL^{-1}. This was confirmed by inductively coupled plasma mass spectrometry using a Perkin Elmer Nexion 350 D.

Fabrication of CdS nanoparticles: Nanoparticles were prepared by a precipitation-hydrothermal method. 3.424g $Cd(NO_3)_2 \cdot 4H_2O$ was added into 87 mL deionized water followed by stirring for 60 min. Subsequently, 20 mL 0.9 M Na_2S aqueous solution was added dropwise into the solution, followed by stirring for 1 h. The suspension was transferred to a 200 mL Teflon-lined autoclave and kept at 180 °C for 12 h. The final products were washed by deionized water and ethanol twice and dried at 60 °C for 5 h.

Fabrication of CdS/ReS_2 heterojunction: ReS_2 coupled CdS was fabricated by mechanically mixing the ReS_2 suspension with *as-fabricated* CdS in an agate-mortar. 50 mg of *as-fabricated* CdS was added to the agate mortar, followed by the addition of volume of ReS_2 suspension. The suspension was mechanically ground for 15 mins. Water was evaporated naturally, and the remaining solid ground into powders as final product. The volume of ReS_2 suspension was 0, 4, 8 and 12 mL and the resulting samples were labeled as CdS, CR4, CR8 and CR12, respectively.

1.2 Physicochemical characterization

X-ray diffraction (XRD) patterns were recorded on a powder X-ray diffractometer (Miniflex, Rigaku) using Cu Kα radiation. Transmission electron microscopy under STEM mode (FEI Titan Thermis, 200 kV) was utilized to obtain HRTEM EDX mapping. XPS measurement was performed on a VGESCALAB 210 XPS spectrometer with Mg Kα source. The binding energies were referenced to the C 1s peak at 284.8 eV. The XANES measurements were performed in an ultra-high vacuum chamber of the undulator soft X-ray spectroscopy beamline at the Australian Synchrotron. Samples were dispersed in deionized water and loaded and dried

on Au-plates. The raw XANES data were normalized to the photoelectron current of the photon beam, measured on an Au-grid. UV S4 Visible diffuse reflectance spectra were obtained on a UV-Vis spectrophotometer (UV2600, Shimadzu, Japan). An RF-5301PC spectrofluorophotometer (Shimadzu, Japan) was employed to obtain steady-state photoluminescence (PL) spectra at room temperature (25 ℃). The transient-state PL decay curves were obtained on an FLS1000 fluorescence lifetime spectrophotometer (Edinburgh Instruments, UK). Raman spectra were acquired by an iHR550 Raman microscope (HORIBA Scientific) with a charge-coupled device (CCD) detector and, a confocal microscope. Fourier Transform Infrared Spectroscopy was collected from the Nicolet 6700.

1.3 Photocatalytic CO_2 reduction test

The photocatalytic CO_2 reduction experiments were conducted in a 287 mL home-made reactor, sealed with silicone-rubber septa at ambient conditions. A 300 W Xenon arc lamp equipped with a UV-cutoff filter ($\lambda \geq 420$ nm) was employed as the light source to trigger the photocatalytic reaction. In a typical test 50 mg photocatalyst was dispersed in 10 mL deionized water and sonicated for 2 h. The photocatalyst was coated on the bottom of the reactor after the water was dried under infrared light. Before illumination the reactor was purged by ultra-pure wet CO_2 gas bubbled from deionized water at flow rate of 40 mL for 1 h. Three blank experiments were conducted by the same process as that for CR12 but purged with ultrahigh purity argon instead of CO_2, without visible-light illumination and without photocatalyst, respectively. The product was collected from the reactor and examined by a gas chromatograph (GC, 7890B, Agilent). The GC was fitted with Plot-Q and a 5Å sieve columns (Agilent) in series, TCD and methanizer/FID detectors, and UHP Ar (BOC) as the carrier gas.

1.4 Electrochemical and photoelectrochemical test

Mott-Schottky plots were obtained on an electrochemical analyser (CHI760D instruments) using 0.5 M Na_2SO_4 aqueous solution. The test was conducted in a standard, three-electrode system with the *as-fabricated* samples as the working electrode, a Pt wire as the counter electrode, and Ag/AgCl (saturated KCl) as a reference electrode. The alternating current (AC) frequency applied was 1200 Hz. In the identical three-electrode system the EIS measurement was carried out in the range from 1 to 2 x 10^5 Hz with an AC amplitude of 20 mV. 0.5 M Na_2SO_4 was employed as the electrolyte. The polarization curves were acquired in the three-electrode system. The bias sweep range was -1.5 to -0.8 V *vs.* Ag/AgCl with a step size of 5 mV. 0.5 M Na_2SO_4 was applied as the electrolyte. In the same three-electrode system the TPC

response measurement was carried out. A 300 W Xenon light with a UV-cutoff filter ($\lambda \geq 420$ nm) was utilized as the light source. 0.5 M Na_2SO_4 aqueous solution was applied as the electrolyte. The working electrodes were prepared as follows: 10 mg sample, 15 mg polyethylene glycol (PEG; molecular weight: 20000), and 1.0 mL ethanol were ground together to make a slurry. A doctor-blade method was used to coat the slurry onto a 2 x 1.5, cm FTO glass electrode. Under flowing N_2 the acquired electrode was dried and heated at 350 °C for 0.5 h.

1.5 XPS and Raman testing of CO_2 adsorbed ReS_2

To investigate the adsorption of CO_2 on the ReS_2 surface three samples were prepared under different conditions that employed XPS and Raman to study surface chemical composition of the ReS_2. ReS_2 nanosheets were loaded on the sealed reactor. Ultra-high purity argon was purged into the reactor for 40 min. The reactor was under Xenon lamp illumination (with a UV cut off filter, $\lambda \geq 420$ nm) for 14 h. Following Xenon lamp illumination ultra-high purity CO_2 gas with water vapor was purged into the reactor for 5 h to reach the adsorption equilibrium. ReS_2 was collected and denoted as RS1. The second sample was prepared by the same process as that for RS1 but purged with CO_2 without water vapor. It is denoted as RS2. The third sample was prepared with the same process as the RS2 with the Xenon lamp illumination lasting for 28 h. It is labeled as RS3.

Part II: Computation Section

1.1 Computational parameters and models

Computational models for ReS_2 and sulfur vacancy containing ReS_2 (V_s-ReS_2) were built according to the characterization results and reports in literature.[1, 2] The Vienna *ab initio* Simulation Package (VASP) was used in DFT computations. The projector augmented wave (PAW) method with generalized gradient approximation (GGA) proposed by Perdew, Burke, and Ernzerh (PBE) was performed. The ReS_2 monolayer with 4 x 4 supercell and CO_2 adsorbed V_s-ReS_2 contained 16 Re and 31 S, 1 C atom, and 2 O atoms (shown in Figure S11 supporting information). The vacuum layer in the perpendicular direction was set as 20 Å.[1] The cut-off energy for plane wave expansion was set at 450 eV. The convergence criterion for electronic structure iteration was set at 10^{-5} eV. For geometry optimization the structures were relaxed to forces on all atoms smaller than 0.02 eV/Å. A Gaussian smearing of 0.20 eV was applied during the geometry optimization and for total energy computations. For the energy

computations the Brillouin zone was sampled using Gamma centered-grids for all structures and K-points set at 2 x 2 x 1. The DFT-D2 method of Grimme was employed in all computations to address van der Waals (vdW) interactions between atoms.[3] Adsorption energy (E_{ad}) is equal to, $E_{ad} = E_{total} - E\mathrm{CO_2} - E_{substrate}$, where E_{total} for the total energy of V_s-ReS_2 with one CO_2 molecule adsorbed, $E\mathrm{CO_2}$ for thermodynamic energy of CO_2 gaseous molecule and the $E_{substrate}$ for the energy of the initial system (V_s-ReS_2).[1] Charge difference (ρ_{diff}) was computed according to $\rho_{diff} = \rho_{total} - \rho\mathrm{CO_{2*}} - \rho_{substrate}$, where ρ_{total} for total charge density of V_s-ReS_2 with one CO_2 molecule adsorbed, $\rho\mathrm{CO_{2*}}$ and $\rho_{substrate}$ for charge density of CO_2 gaseous molecule and the initial system (V_s-ReS_2) respectively.[4]

Part III: Supplementary Results

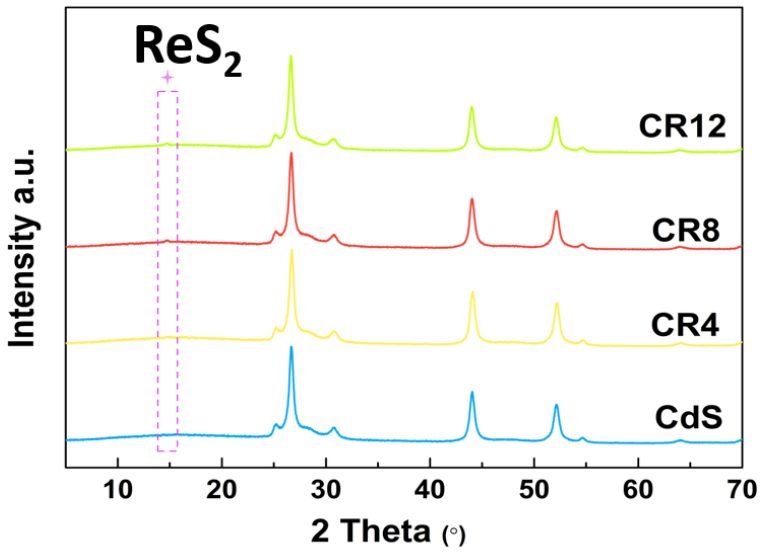

Figure S1. XRD patterns for CdS, CR4, CR8 and CR12. The pink-colored cross and purple circle, denote peaks of ReS_2 and cubic CdS, respectively.

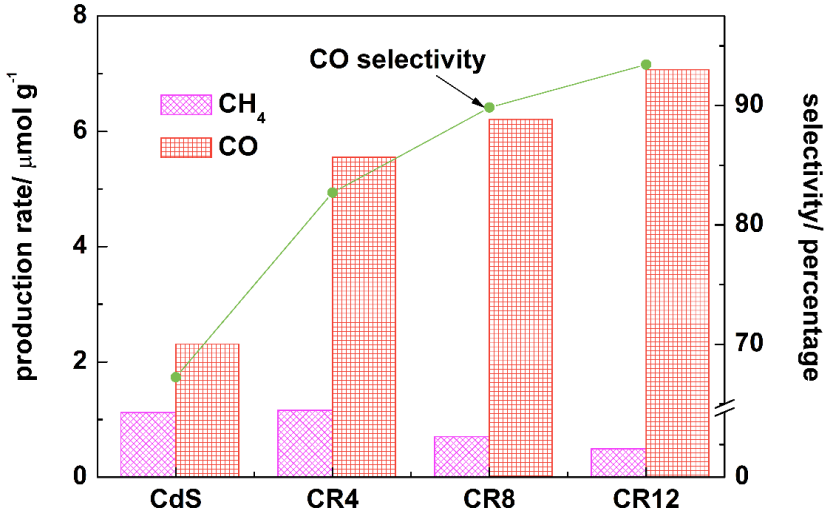

Figure S2. CO and CH_4 production of photocatalytic CO_2 reduction of CdS, CR4, CR8 and CR12 under visible-light illumination ($\lambda > 420$ nm) and corresponding CO selectivity.

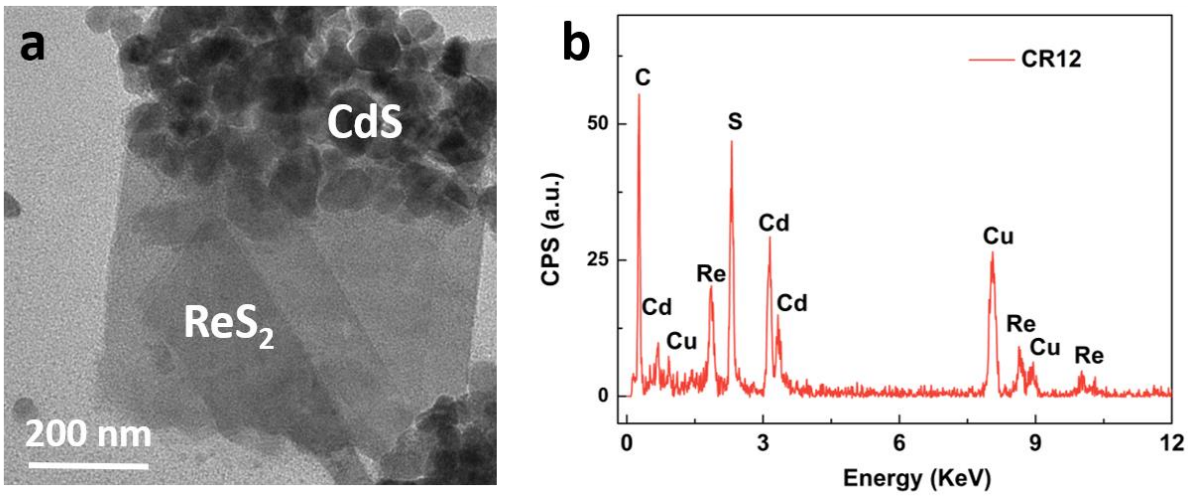

Figure S3. a) TEM image of CR12 after photocatalytic CO_2 reduction testing and b) corresponding EDX spectrum.

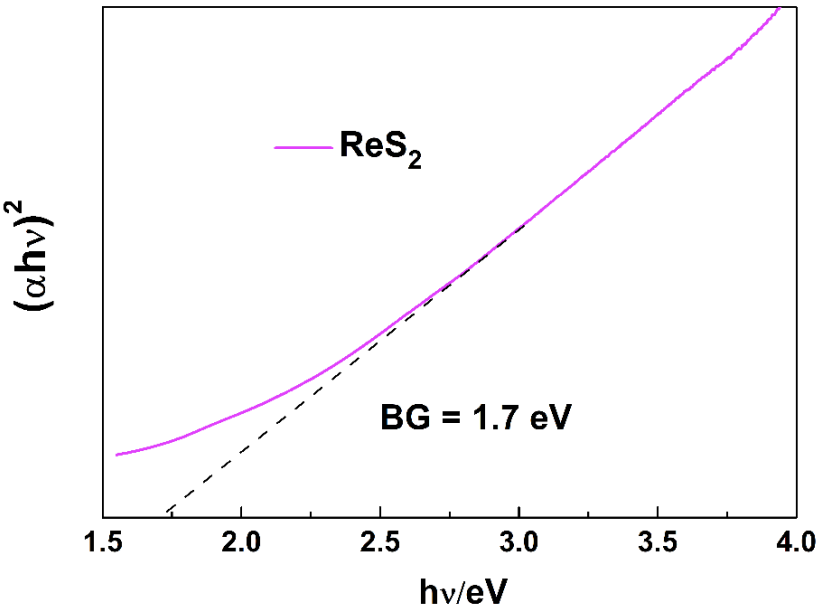

Figure S4. Tauc plot of ReS_2 NSs and bandgap.

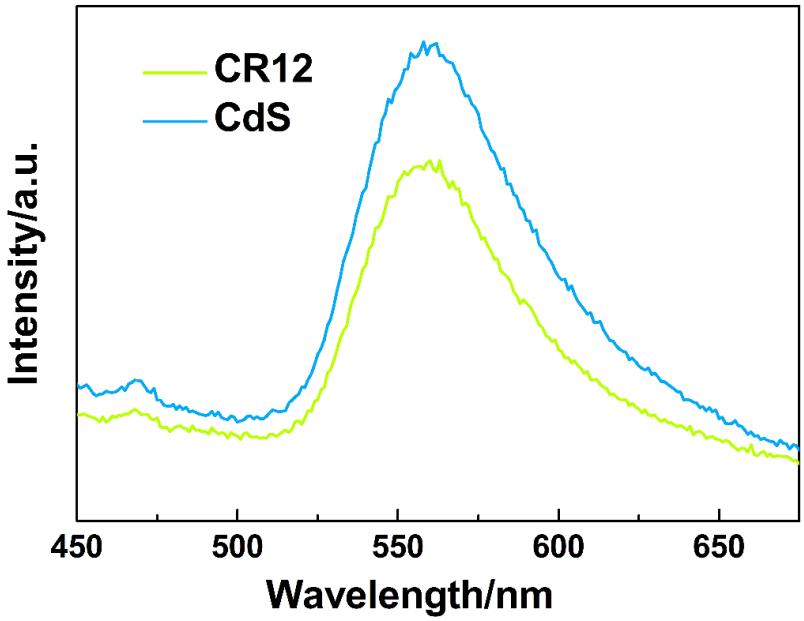

Figure S5. Steady-state photoluminescence (PL) spectra for CdS and CR12.

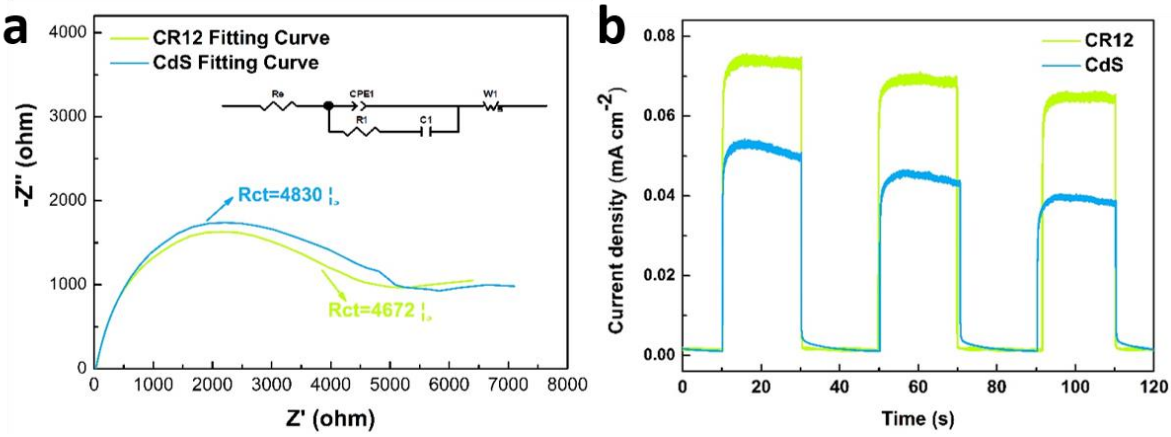

Figure S6. a) EIS Nyquist plots of CdS and CR12 in 0.5 M Na_2SO_4 aqueous solution. b) Transient photocurrent density measurement for CdS and CR12 in 0.5 M Na_2SO_4 aqueous solution.

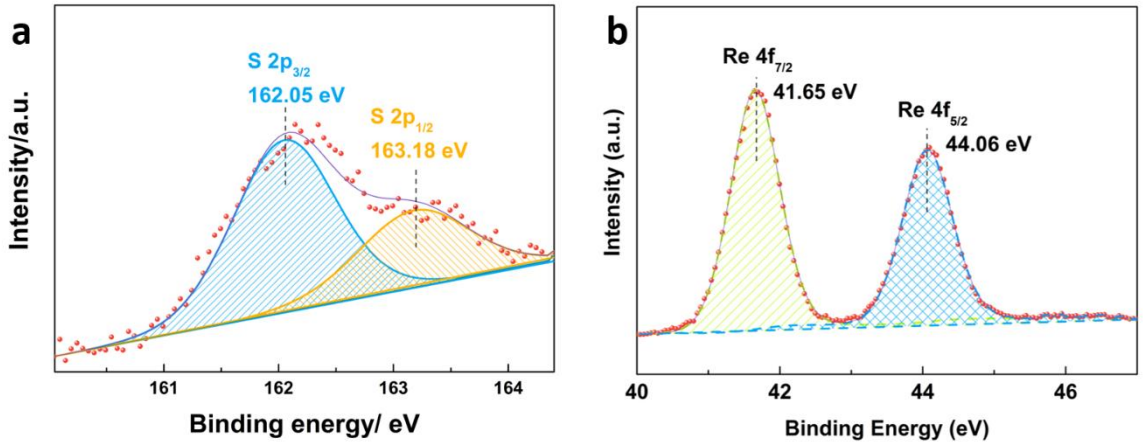

Figure S7. High-resolution Re 4f and S 2p XPS spectrum of ReS_2.

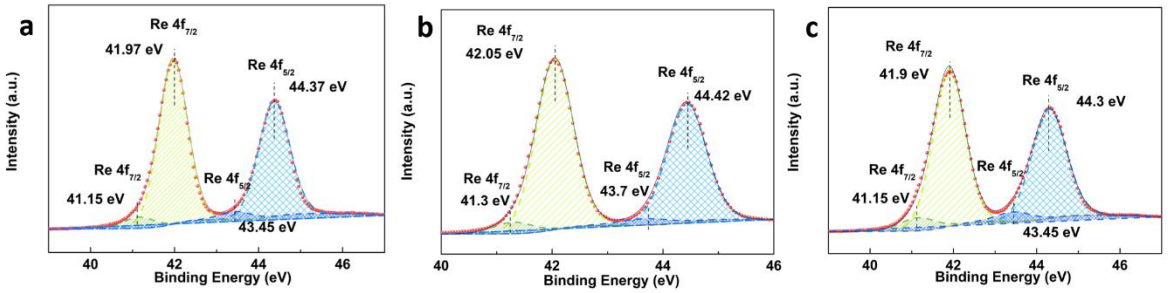

Figure S8. High-resolution Re 4f XPS spectrum of RS1, RS2 and RS3.

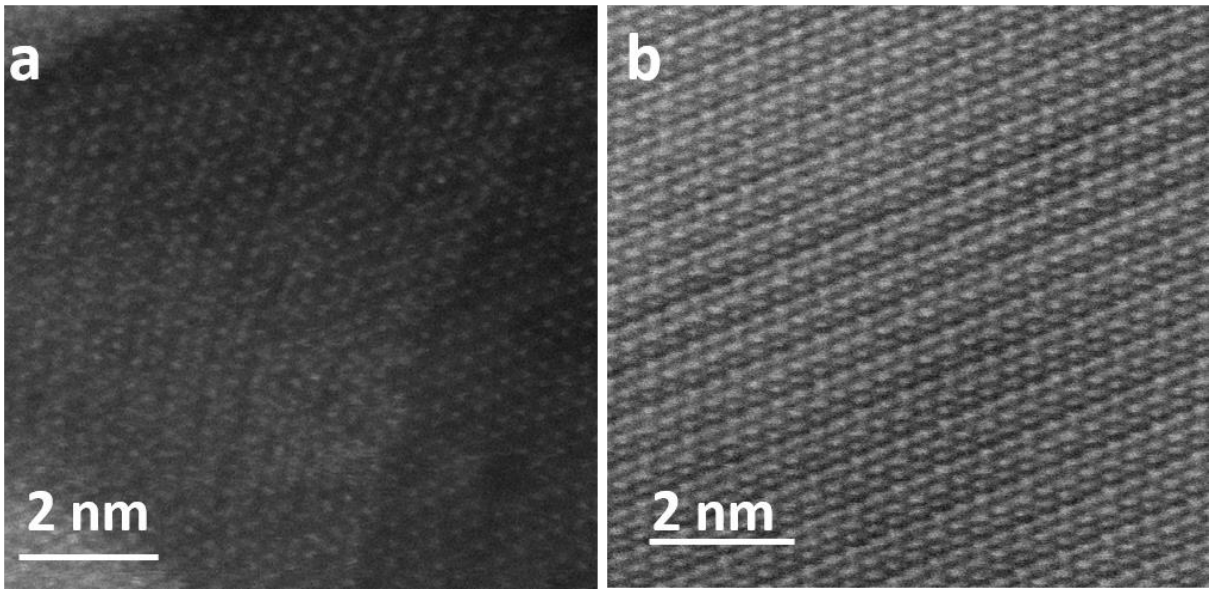

Figure S9. HRTEM for RS1 (a) and ReS_2 (b).

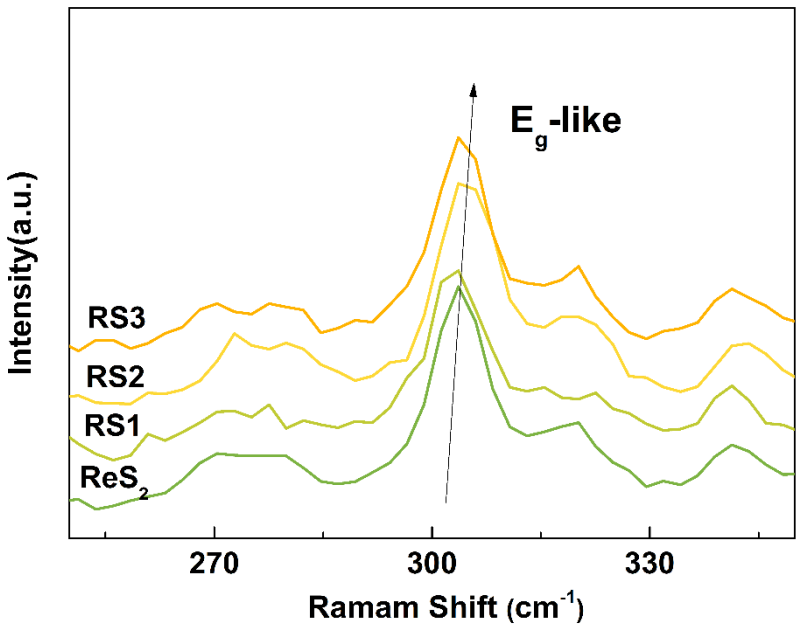

Figure S10. Raman spectra for E_g-like peaks of pristine ReS_2, RS1, RS2 and RS3.

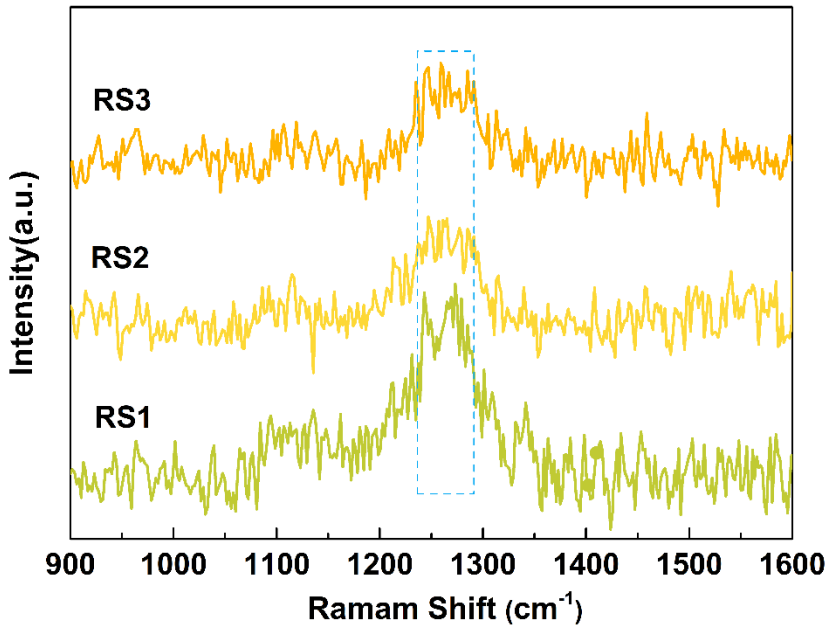

Figure S11. Raman spectra for RS1, RS2 and RS3 with CO_2 adsorption.

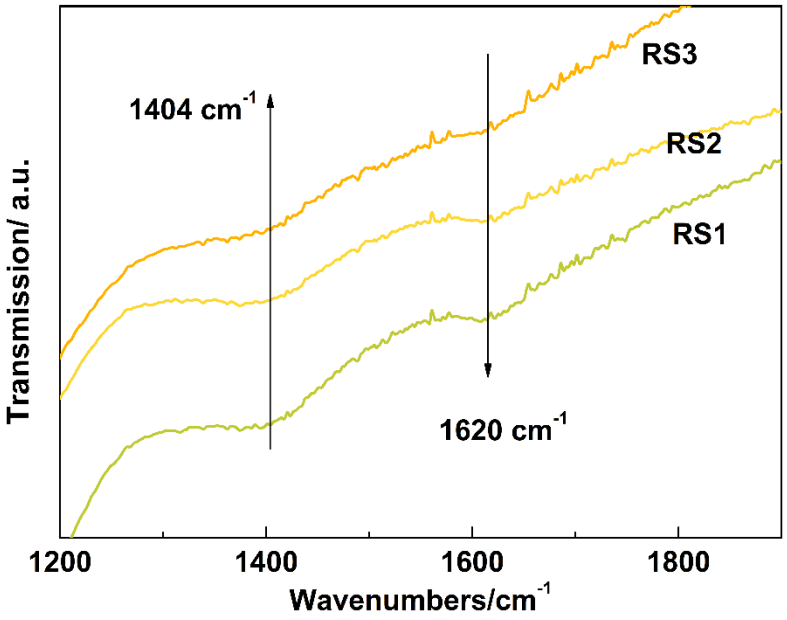

Figure S12. FTIR spectra for RS1, RS2 and RS3 with CO_2 adsorption.

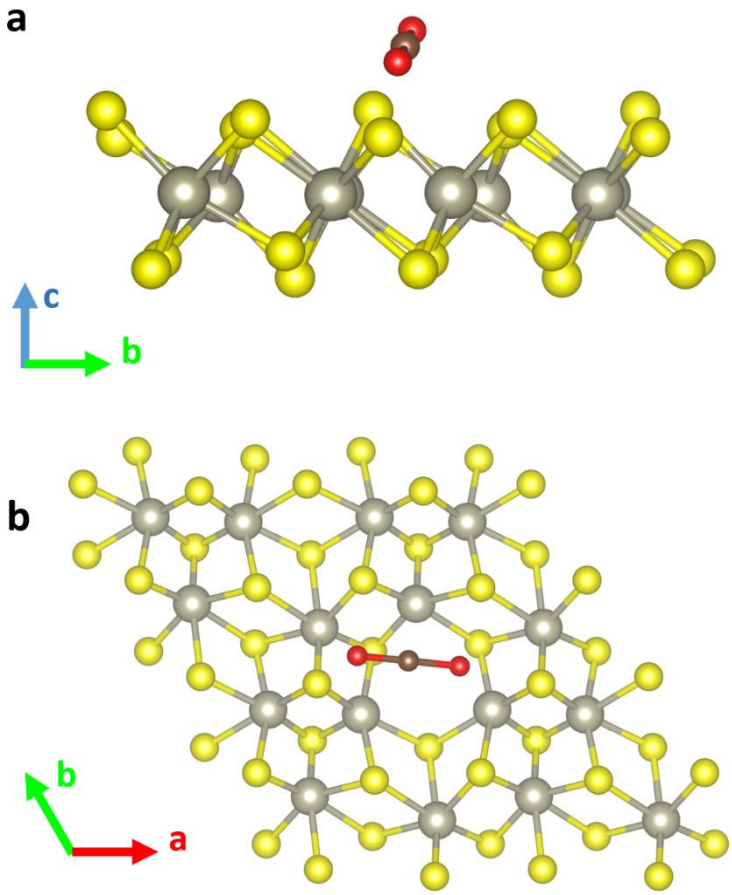

Figure S13. a) Side-view (elevation) and h) Top-view (plan) of CO_2 molecule and atomic structures of Vs-ReS_2. The red, yellow, grey and brown colored-spheres denote O, S, Re and C atoms, respectively.

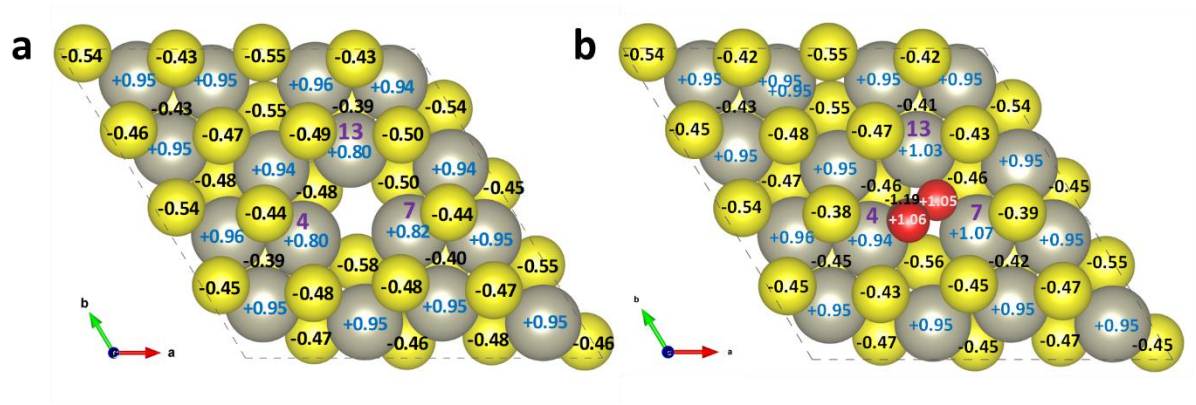

Figure S14. Bader charge analysis of a) V_s-ReS_2 and b) CO_2 adsorbed on V_s-ReS_2. The yellow, grey, red and brown color-spheres represent Re, S, O and C atoms, respectively. All data are shown as two digits after the decimal. The positive and negative signs in the figure stand for, respectively, electron loss and accumulation that has a meaning similar to valency.

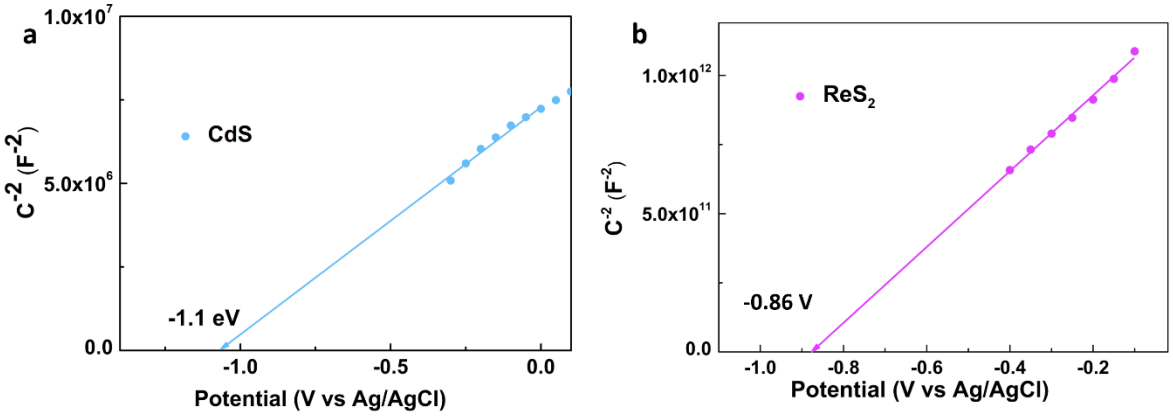

Figure S15. a) Mott-Schottky plot for CdS and b) ReS_2 electrode in 0.5 M Na_2SO_4 aqueous solution. The plot suggests that the flat band potential for CdS (ReS_2) is -1.1 V (-0.86 V) *vs.*Ag/AgCl, corresponding to -0.51 V (-0.26 V) *vs.* standard hydrogen electrode (SHE). The conduction band (CB) edge position of CdS (ReS_2) is estimated therefore to be -0.61 V (-0.36 V) *vs.* SHE.

Table S1. Contents of surface carbon groups in ReS_2, RS1, RS2 and RS3

Sample	**Contents of carbon group from C 1s XPS (mol%)**			
	C-OH	*COOH	b-CO_2	l-CO_2
RS1	13.38	3.68	3.99	5.45
RS2	14.46	3.49	1.94	7.79
RS3	16.74	3.35	2.18	8.7

Part IV: Supplementary References

[1] B. Chen, H. Li, H. Liu, X. Wang, F. Xie, Y. Deng, W. Hu, K. Davey, N. Zhao, S.Z. Qiao, *Adv. Energy Mater*. **2019**, *30*, 1970117.

[2] J. Pan, X. Zhou, J. Zhong, J. Hu, *Phys. Lett. A* **2019**, *31*, 125883.

[3] S. Grimme, *J. Comput. Chem.* **2004**, *25*, 1463.

[4] Y. Jiao, Y. Zheng, P. Chen, M. Jaroniec, S.Z. Qiao, *J. Am. Chem. Soc.* **2017**, *139*, 18093.

Chapter 4

Photocatalytic CO_2 Reduction: Identification and Elimination of False-Positive Results

4.1 Introduction and Significance

Photocatalytic CO_2 reduction is a promising approach to reaching the carbon neutrality goal by utilizing solar energy and promoting CO_2 conversion, which is evidenced by a growing number of research works. Nevertheless, carbon contaminations have a significant influence on the photocatalytic performance evaluation, since the carbon-contained products generated by CO_2 conversion are still at a very low level. Additionally, there are no uniform and rigorous experimental protocols to exclude carbon contaminations, which renders the influence unclear and reduces the reliability of performance evaluation. Although this is an important topic in CO_2 photoreduction, no systematic works are available on this issue in the past decades. To address this issue, we designed a series of rigorous experiments to identify the carbon impurities and evaluate the influence of carbon impurities on the subsequent performance test. Based on these results, we proposed reliable experimental protocols to eliminate/exclude the potential carbon contamination effect.

This is a new, comprehensive and systematic research perspective on the reliability of photocatalytic CO_2 reduction. The sources of carbon contamination are identified. All carbon contaminations can be classified into two groups: the out-system and intrasystem contaminations. The out-system contaminations are mainly from the reactor, gas, and shared lab facilities, which can be excluded by rigorous operation. The intrasystem ones originate from the process of preparation and washing of photocatalysts. These carbon contaminants can be identified by Raman and FTIR spectroscopy. *In situ* DRIFTS spectra confirm the decomposition of carbon contaminants on the surface of photocatalysts under illumination.

Approaches to eliminate carbon contaminations are proposed. High-temperature annealing and plasma cleaning are two effective ways to remove surface carbon contaminants. However, the high-temperature annealing might lead to the crystal structure and morphology change of nanomaterials. Therefore, plasma cleaning, a mild method, is proposed. The effects and limitations of these two approaches are compared and some suggestions are given for their applicability.

A rigorous experimental protocol is proposed. Based on the above research and previous reports, a series of rigorous experimental protocols is proposed. The proposed protocol includes the identification, elimination and evaluation of carbon contaminations to promote the reliability and credibility of the research results. This protocol may provide some

suggestions to improve the reliability of other catalytic processes such as photocatalytic nitrogen fixation.

4.2 Photocatalytic CO_2 Reduction: Identification and Elimination of False-Positive Results

This Chapter is included as it appears as a journal paper published by Yanzhao Zhang, Dazhi Yao, Bingquan Xia, Mietek Jaroniec, Jingrun Ran and Shi-Zhang Qiao. Photocatalytic CO_2 Reduction: Identification and Elimination of False-Positive Results. ***ACS Energy Lett.*** 2022, 7, 1611-1617.

Statement of Authorship

Title of Paper	Photocatalytic CO2 Reduction: Identification and Elimination of False-Positive Results
Publication Status	☑ Published ☐ Accepted for Publication ☐ Submitted for Publication ☐ Unpublished and Unsubmitted w ork w ritten in manuscript style
Publication Details	Yanzhao Zhang, Dazhi Yao, Bingquan Xia, Mietek Jaroniec, Jingrun Ran, Shi-Zhang Qiao, ACS Energy Lett. 2022, 7, 5, 1611–1617

Principal Author

Name of Principal Author (Candidate)	Yanzhao Zhang		
Contribution to the Paper	Design and conducted the experiments, analysed the data, wrote the manuscript.		
Overall percentage (%)	70%		
Certification:	This paper reports on original research I conducted during the period of my Higher Degree by Research candidature and is not subject to any obligations or contractual agreements with a third party that would constrain its inclusion in this thesis. I am the primary author of this paper.		
Signature		Date	06/12/2022

Co-Author Contributions

By signing the Statement of Authorship, each author certifies that:

i. the candidate's stated contribution to the publication is accurate (as detailed above);
ii. permission is granted for the candidate in include the publication in the thesis; and
iii. the sum of all co-author contributions is equal to 100% less the candidate's stated contribution.

Name of Co-Author	Dazhi Yao		
Contribution to the Paper	Helped data analysis, and revised the manuscript		
Signature		Date	06/12/2022

Name of Co-Author	Bingquan Xia		
Contribution to the Paper	Review and comments on the manuscript.		
Signature		Date	06/12/2022

Name of Co-Author	Mietek Jaroniec		
Contribution to the Paper	Discussion and revision of manuscript		
Signature		Date	Dec, 6, 2022

Name of Co-Author	Jingrun Ran		
Contribution to the Paper	Discussion and revision of manuscript		
Signature		Date	28/11/2023

Name of Co-Author	Shi-Zhang Qiao		
Contribution to the Paper	Supervision of the work, discussion and conceptualization of this manuscript and manuscript evaluation and revision.		
Signature		Date	25/01/2023

Photocatalytic CO_2 Reduction: Identification and Elimination of False-Positive Results

Yanzhao Zhang,[†] Dazhi Yao, [†] Bingquan Xia, [†] Mietek Jaroniec, [§] Jingrun Ran[,†], and Shi-Zhang Qiao*[,†]*

[†]School of Chemical Engineering & Advanced Materials, The University of Adelaide, Adelaide, SA 5005, Australia.

[§]Department of Chemistry and Biochemistry & Advanced Materials and Liquid Crystal Institute, Kent State University, Kent, OH 44242, USA.

E-mail: s.qiao@adelaide.edu.au; jingrun.ran@adelaide.edu.au

The massive consumption of fossil fuels can lead to the global energy shortage and severe greenhouse effect. Therefore, it is a great urgency to develop alternative energy resources and reduce the emission of carbon dioxide (CO_2). Photocatalytic CO_2 reduction is a highly promising approach to scale up renewable energy generation and promote carbon neutrality under mild conditions.[1-4] However, the efficiency and product yield of photocatalytic CO_2 reduction are far from satisfactory.[5-7] Furthermore, synthetic procedures of photocatalysts can affect the product yield thus causing falsely positive results (**Scheme 1**). Therefore, it is of great significance to identify and eliminate carbon contaminants in the experiment.

To make sure that the product is from the conversion of CO_2 rather than the carbon contaminants, the key point is to identify and remove all the contaminant sources as thoroughly as possible. Although this is a very important topic in CO_2 photoreduction, to the best of our knowledge, no work has studied and discussed this issue systematically in the past. Here, we propose a series of rigorous experiment protocols to study CO_2 photoreduction with a thorough discussion of various experimental conditions. The carbon contamination sources can be classified into three groups: out-system, intrasystem and carbon-based photocatalysts.[3, 8-10] The out-system contamination mainly originate from gas, shared ovens/furnaces and the organic parts/sealing oil of photocatalytic reactors.[8] By rigorous and careful operation, this out-system contamination can be excluded rationally and does not cause any substantial influence. Additionally, the intrasystem contamination (e.g., the capping agent and organic solvent) used

in the preparation/cleaning of photocatalyst is indeterminate, which usually results in a significant impact on CO_2 photoreduction.[9] Some of carbon-based materials can experience self-decomposition under illumination. They may release some products during the decomposition process. However, up till now, there is no systematic work on this source of carbon contamination.

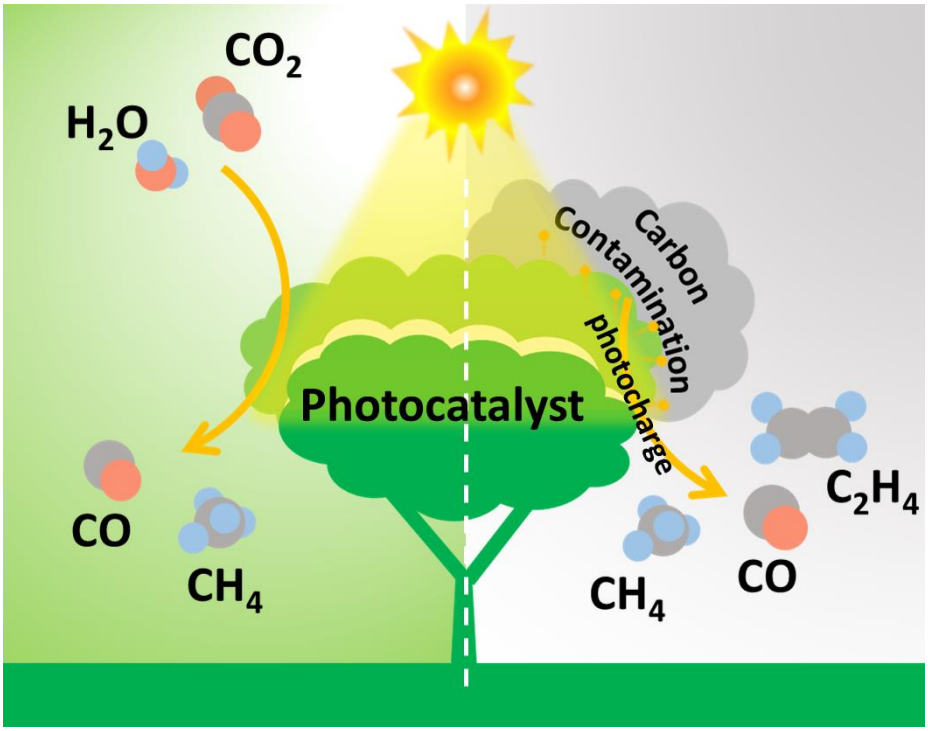

Scheme 1. Schematic illustration of artificial photosynthesis showing the CO_2 reduction on photocatalysts to yield carbon monoxide (CO) and methane (CH_4) (left side) and the conversion of absorbed carbon contaminations by the photogenerated charges on photocatalysts to yield CO and hydrocarbon products (right side). Hydrogen, oxygen, photogenerated charges and carbon atoms are denoted as blue, red, yellow and grey balls, respectively.

In this work, surface capping agent and organic solvent used in the process of preparation and the subsequential cleaning cannot be removed by the ordinary method, such as washing by water and drying in vacuum oven. Significant carbon product yield with excellent reproducibility was observed using the four most widely applied photocatalysts[2, 11-14] (i.e., C_3N_4, TiO_2, CdS and Bi_2WO_6) in pure Argon (Ar) atmosphere. The decomposition of carbon-based photocatalysts can be identified easily by blank experiments. As regards the elimination of intrasystem contaminations, some effective approaches, such as high-temperature annealing and plasma cleaning, have been studied. Based on the above research, we propose a series of

rigorous experimental protocols to identify and eliminate the falsely positive results in photocatalytic CO_2 reduction.

Most of the extraneous (out-system) carbon contaminants causing false-positive results can be easily removed via rigorous operation. However, the intrasystem carbon contaminants (e.g., organic capping agent and solvent) used to control crystal growth and develop specific morphologies are difficult to be thoroughly removed. For instance, ethylenediamine and hexadecyltrimethylammonium bromide (CTAB) are usually applied to synthesize CdS nanorods and Bi_2WO_6 nanosheets, respectively.[14-16] These two organic molecules cannot be thoroughly removed through washing with deionized water and ethanol, thus becoming the carbon contaminants in the subsequential photocatalytic performance test.

"Excellent performance" from the carbon contamination. Due to the extremely low carbon product yield and non-negligible influence of carbon contamination in the experiment, the catalytic performance of the specific catalyst for CO_2 photoreduction always suffers from fluctuation and poor reproducibility. We observed excellent reproducibility and desirable cumulative effect in four hours by using three typically contaminated materials in the Ar atmosphere. Ar is an inert gas that cannot react with these three photocatalysts under illumination. Therefore, the products detected from the system should be converted from the "carbon contaminants" on the photocatalyst surface. These contaminants usually come from three sources: the capping agent, organic solvent in solvothermal reaction and ethanol from the washing process. For example, CTAB was used as a capping agent for the preparation of Bi_2WO_6 nanosheets. Without any washing, the remaining CTAB can cause severe contaminations as shown in the blank (Ar+BWO+illumination) photocatalytic test (see **Figure S1**; the following notation is used in this paper: BWO - Bi_2WO_6 nanosheets, W - water washing after preparation, E - ethanol washing after preparation, A - high-temperature annealing after ethanol washing, P - plasma cleaning after ethanol washing). The CO, CH_4 and C_2H_4 were detected and reached 968.2, 120.0, 12.2 μmol/g, respectively. Furthermore, after hydrothermal reaction and washing with deionized water, CTAB cannot be removed thoroughly. As shown in **Figure 1a**, the yield of CO and CH_4 on BWO-W reached 360.1 and 91.1 μmol/g in a four-hour test and a few products C_2H_4 and H_2 were detected at 7.9 and 27.2 μmol/g levels, respectively (**Figure S2**). In this CO_2-free reaction system, these carbon-based products originate from the conversion/decomposition of CTAB. In the case of CdS nanorods, this carbon contaminant can lead to different products. Namely, without any washing of CdS, the products CO, CH_4 and H_2 were detected and reached 34.0, 3.3 and 46.2 μmol/g, respectively (**Figure S3**). The CdS-W nanorods were prepared by solvothermal reaction in ethylenediamine

and washed with deionized water. In **Figure 1b**, H_2 and CO are the main products with the yield of 41.0 and 30.1 μmol/g, respectively. Moreover, 1.3 μmol/g of CH_4 was also detected after four hours. As for the P25-W, it shows trace products (**Figure 1c**) because it was not polluted by any organic moiety. These results show that the organic molecules used in the preparation of photocatalysts can cause serious contaminations in subsequential photocatalytic performance tests and water washing cannot remove them thoroughly. In many circumstances, ethanol is a widely used washing agent to remove the as-mentioned surface absorbed organic compounds. As shown in **Figure 1d** for BWO-E washed with ethanol, the smaller yield of CO

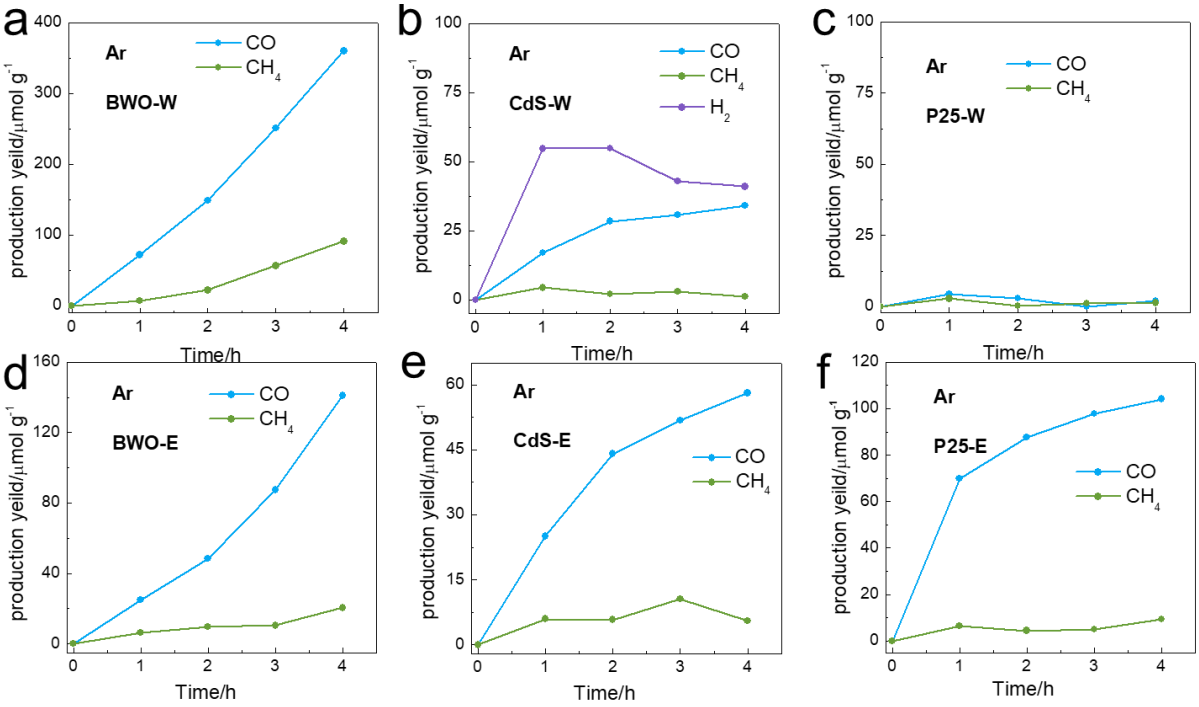

Figure 1. Production yields on different samples in Ar under four-hour irradiation. 20 mg samples were loaded on the glass fiber filter in the reactor. The reactor was purged by Argon bubbling through deionized water for 1 hour. Then the illumination was started. The products were collected per hour and analyzed. (a) BWO-W, (b) CdS-W, (c) P25-W, (d) BWO-E, (e) CdS-E and (f) P25-E.

and CH_4 was achieved in comparison to that on BWO-W, but still reached 141.1 and 20.4 μmol/g, respectively. As regards to C_2H_4, its yield reached 8.6 μmol/g (**Figure S4**). This shows that ethanol can partially remove CTAB on Bi_2WO_6 nanosheets. Nevertheless, ethanol washing may cause unaware side-effect for photocatalysts. As shown in **Figure 1e**, ethanol-washed CdS (CdS-E) exhibits higher CO and CH_4 yields of 58.1 and 5.4 μmol/g respectively, compared with those on CdS-W. Similarly, the ethanol-washed P25 (P25-E) yielded 104.1 and 9.4 μmol/g

of CO and CH_4, respectively under illumination (**Figure 1f**), indicating that adsorbed ethanol cannot be removed thoroughly even after drying in vacuum oven. More importantly, the recycling tests in Ar atmosphere revealed that the carbon contaminations can still exist in the system even after several times of recycling (**Figure S5**), which denotes that the carbon contaminations can influence the "photocatalyst stability" evaluation. It is noticeable that the generation of C_2H_4 can be detected from BWO-W and BWO-E. C_2 products are high-valued chemicals in CO_2 photoreduction and are still generated on very few photocatalysts. These results remind us that in the pursuit of high-value products (e.g., C_2 and even C_3), the falsely positive results from the carbon contaminations must be excluded. All of the above results verified that ethanol can not only be carbon contamination but also can significantly influence the performance and stability tests.

Identification of carbon contamination. In many cases, the introduction of surface adsorbed carbon species is inevitable during the catalyst's preparation. These carbon species can be degraded, thus releasing carbon products under irradiation according to previous reports.[17] Therefore, we examined the presence of the surface adsorbed carbon species using Raman spectroscopy in which the intensity is proportional to their concentration. As shown in **Figure S6a** and **d**, a shift in the Raman peak around 2930 cm^{-1}, ascribed to alkyl group, can be observed for P25-E. The residue of ethanol is likely to cause its high intensity as compared to P25-W.[18-19] Moreover, the typical Raman peaks of CTAB are visible on the spectra of both BWO-W and BWO-E (**Figure S6b** and **e**). For example, the peaks at 1273-1440 cm^{-1} and 2854-2890 cm^{-1} can be attributed to the CH_2 group and those at 2932-3025 cm^{-1} to the CH_3 group (**Table S1**).[20] In addition, in the case of BWO-E, a new peak at 2963 cm^{-1} can be attributed to the CH_3 vibration from ethanol. The OH stretch at 3150-3600 cm^{-1} could be attributed to ethanol on BWO-E. However, no corresponding stretch is observed in the case of BWO-W. This rationalizes the aforementioned conclusion that ethanol can also be a contamination source. The CdS-W and CdS-E exhibit almost the same Raman spectra while bands around 2850 and 3000 cm^{-1} originate from CH_2 vibration and a band at 3170 and 3300 cm^{-1} can be attributed to NH_2, which may stem from ethylenediamine after the solvothermal reaction (**Figure S6c** and **f**).[21-22] Samples without any washing were also investigated (**Figure S7**). Compared with the water/ethanol-washed samples, they all show similar but much stronger Raman peaks. This illustrates that the washing process can remove part of the organic moieties. However, all of the above results confirm that the organic solvent used in the preparation of these photocatalysts cannot be removed thoroughly by ethanol washing and the washing with ethanol can lead to an additional contamination.

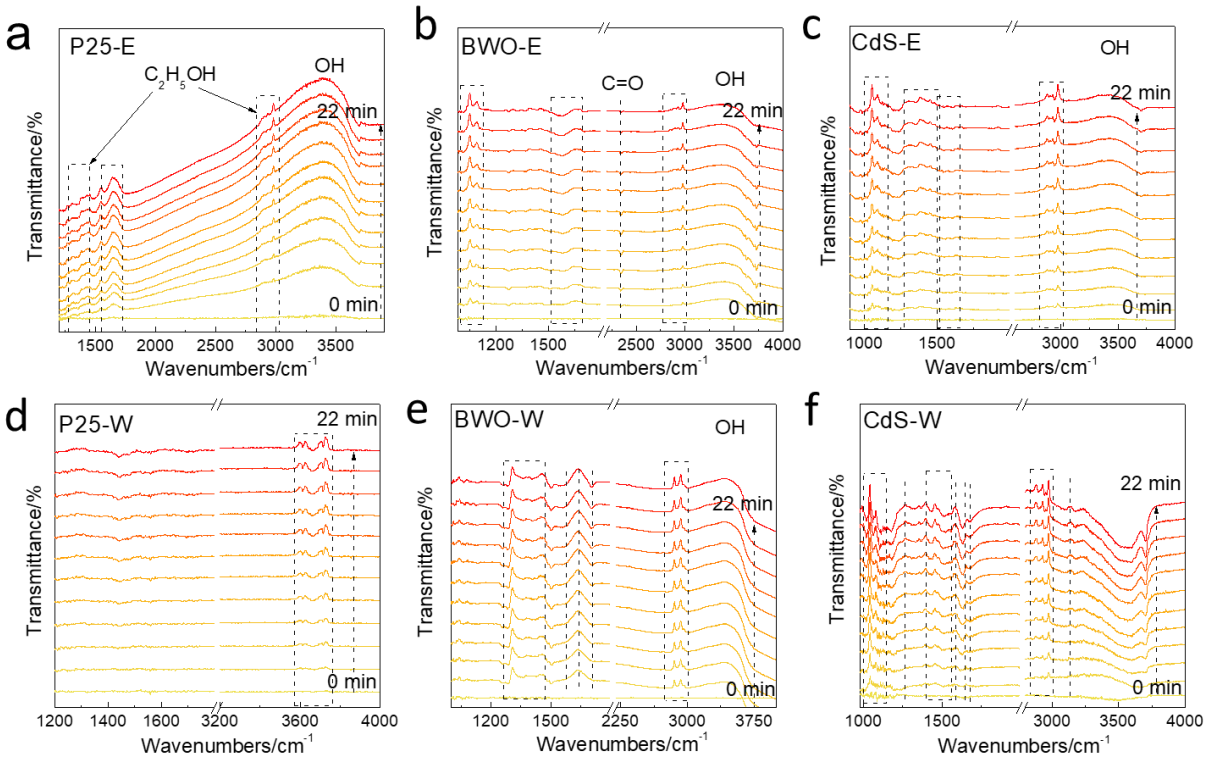

Figure 2. ***In situ*** **DRIFTS of various carbon contaminations on different samples under illumination in Ar. 0 min spectrum is collected after background and the illumination started meantime. Then, the remaining spectra are collected every two minutes until 22 min. Argon is bubblingthrough the deionized water. (a) P25-E, (b) BWO-E, (c) CdS-E, (d) P25-W, (e) BWO-W and (f) CdS-W.**

To detect the influence of these carbon contaminations on the subsequential photocatalytic performance test, we conducted the *in situ* Diffuse Reflectance Infrared Fourier Transform Spectroscopy (DRIFTS) in Ar atmosphere and/or under illumination (**Figure 2**). In **Figure 2a-e**, the positive peaks around 1500-1750 and 3000-3600 cm^{-1} can be ascribed to the OH stretch vibration from water. It is noticeable that some characteristic peaks for ethanol increasingly emerged around 1300-1500 and 2900-3000 cm^{-1} (**Table S2**).[17] These results illustrate that the ethanol was adsorbed on the surface of photocatalysts and converted to the carbon-containing intermediates under illumination. However, for P25-W, there are almost no peaks under illumination while the peaks at 3600-3800 cm^{-1} can be assigned to the OH of water and surface hydroxyl groups (**Figure 2d**).[17] In **Figure 2e**, BWO-W shows a much stronger and more complex spectrum compared with BWO-E. The peak around 2850-2950 cm^{-1} is due to the asymmetric and symmetric CH stretching groups of the alkyl chain of CTAB. The peak at 1630 cm^{-1} and the broadband around 3400 cm^{-1} can be attributed to the surface OH moieties, while

that at 1300-1480 cm^{-1} refers to carbonate species.[23-29] All of these peaks indicate that the CTAB absorbed on BWO-W was decomposed under illumination, whereas two small peaks at 1715 and 1550 cm^{-1} are negatively increasing. These two growing peaks are assigned to the C=O band of acetaldehyde from intermediates of ethylene[17], indicating that the CTAB cannot be removed by water washing and is converted to hydrocarbons in the subsequential photocatalytic tests. In addition, for CdS-W (**Figure 2f**), the presence of NH_2 at 1267, 1586 and 3134 cm^{-1} along with the CH_2 stretching band (2800-3000 cm^{-1}) demonstrates that the adsorbed carbon species may stem from residue ethylenediamine after solvothermal reaction. The peaks at 1630 and 3200-3700 cm^{-1} can be assigned to the surface hydroxyl groups, which may indicate the decomposition of carbon contaminations or water toward hydrogen production. The negative peaks around 1366-1560 cm^{-1} are ascribed to the production of intermediates CO or CH_4.[25] The peaks at 1000-1100 cm^{-1} are attributed to C-O that may come from the carbon-containing products after ethylenediamine solvothermal reaction.[17] It is the intermediate of CO in photocatalytic CO_2 reduction. In contrast, fewer contaminants could be observed on CdS-E the peaks of which are almost the same as those of CdS-W while much reduced. All of these results are consistent with the Raman spectra above and illustrate that ethanol/water washing cannot fully remove the carbon contaminants, and these contaminants would make the performance evaluation far from accurate.

To confirm the degradation of these carbon contaminations on photocatalysts, the role of CTAB/ethanol was examined by conducting the experiment without photocatalyst in the same Ar atmosphere under illumination as the blank test. There are no products detected, which indicates that these compounds are stable under illumination. According to previous reports,[17, 29] the surface absorbed organic moieties can be degraded by the photogenerated holes or reactive oxygen species. We observed the degradation of carbon impurities by using *in situ* DRIFTS. The degradation of organic moieties may follow various pathways leading to different products. For instance, the carbon impurity can be oxidized and converted to acetaldehyde. Next, decarbonylation of acetaldehyde can lead to CO and CH_4. Acetaldehyde is also an intermediate towards ethylene.

Stability of carbon-based semicondutors photocatalysts. For some of the carbon-based nanomaterials, a partial decomposition of photocatalysts under illumination may also result in the same products as those formed during CO_2 photoreduction. Carbon nitride received much attention as photocatalyst for CO_2 reduciton. In our experiment no products were detected after four-hour illumination in Ar as evidenced by similar both the XRD patterns and FTIR spectra (**Figure S8**) recorded before and after illumination, which reveals that C_3N_4 is stable under

illumination. Besides, other carbon-based materials such as metal-organic frameworks and graphene are widely used for photocatalytic CO_2 reduction while their partial decomposition is not studied enough. To exclude the secondary contamination towards the falsely positive results, further research is needed.

Elimination of carbon contamination from the surface of photocatalysts. It is known that the surface carbon contaminants can be decomposed at high temperature whereas metal oxides or sulfides are relatively stable at high temperature in air or nitrogen. According to thermogravimetric analysis (TGA) results (**Figure S9**) and previous reports,[10, 30] ethanol, CTAB and ethylenediamine can be decomposed under 400, 660 and 400 ℃, respectively. Therefore, to eliminate the surface carbon species, we annealed P25-E, BWO-E and CdS-E at 400 (air), 660 (air) and 400 ℃ (nitrogen) for 4 hours and denoted the resulting samples as P25-A, BWO-A and CdS-A, respectively. As shown in **Figure S10a**, all the annealed samples show much smaller product yield in CO_2 photoreduction, compared with the ethanol-washed samples (**Figure S10b**) and water-washed samples (**Figure S10c**). BWO-A, P25-A and CdS-A show the yields of CO and CH_4 as 4.3 and 0.1 μmol/g, 2.2 and 3.9 μmol/g as well as 4.5 and 0.5 μmol/g, respectively (**Figure S10a**). Moreover, the X-ray diffraction patterns (XRD) (**Figure S11**) of the as-annealed samples show that the crystal can keep its original structure while the diffraction peaks have smaller full width at half maximum (FWHM). This shows the higher crystallinity of the as-annealed samples, which would benefit the subsequent photocatalytic reactions. Besides, the morphologies of nanomaterials are also changed after high-temperature treatment. In **Figure S12-13**, the sizes of TiO_2 nanoparticles and CdS nanorods are not apparently altered after annealing. However, the Bi_2WO_6 nanosheets grow up with the thickness increasing from 6 nm to around 15 nm (**Figure S14-15**). Also, a significant enlargement in the lateral size of Bi_2WO_6 nanosheets can be observed. In **Figure S16**, the lateral size distribution of BWO-E and BWO-P is similar, namely around 30-40 nm. However, the lateral size of BWO-A increases up to 150-200 nm. The increased sizes of nanomaterials can prominently reduce the specific surface area, which may decrease the photocatalytic performance.[5, 12, 27] Based on the above results, we conclude that high-temperature annealing can effectively eliminate carbon species; however, it can influence the crystallinity and size of some nanomaterials.[31] Therefore, it is critical to select an appropriate temperature and atmosphere for annealing.

Given the above side effects of high-temperature annealing, we also developed a plasma cleaning approach to reduce the surface carbon contaminations. Plasma cleaning is a widely-applied and convenient method operated under mild conditions. An appropriate gas atmosphere

can be selected to apply to different materials. For example, oxygen plasma can be used for cleaning BWO-E and P25-E, while Ar plasma for cleaning CdS-E, since CdS-E can be oxidized by the reactive oxygen species under oxygen plasma. These plasma-cleaned samples are labeled as BWO-P, P25-P and CdS-P, respectively. As shown in **Figure S10d**, the plasma-cleaned samples yield the approximate amounts of products as the annealed samples, with CO and CH_4 as 19 and 5.2 μmol/g for BWO-P, 1.2 and 0.7 μmol/g for P25-P, and 1.8 and 0.6 μmol/g for CdS-P, respectively. These results show that plasma cleaning is another effective way to reduce carbon contaminations on nanomaterials. Raman spectra were also collected for the plasma-cleaned samples (**Figure S17)**. As can be seen, the carbon species-related Raman signals are notably reduced, indicating the apparent reduction of ethanol, CTAB and ethylenediamine on P25-P, BWO-P and CdS-P, respectively. Similarly, the *in situ* DRIFTS results also show that the surface carbon contaminants are greatly reduced compared with those on the ethanol- and water-washed samples (**Figure S18**). These results further confirm that the detected products are converted from the surface carbon contaminations introduced in the sample preparation and washing process. More importantly, the XRD patterns (**Figure S11**) show that the plasma cleaning did not apparently change the crystal structure and the FWHM value. As shown in **Figures S12-16** the morphology of plasma-cleaned samples did not change visibly during ethanol-washing. The above results show that the mild plasma cleaning does not apparently alter the crystal structures and morphology of nanomaterials. Therefore, we conclude that plasma cleaning is an effective and suitable approach to eliminate carbon contaminations on nanomaterials with appropriate plasma atmosphere, power and treatment time.

Experimental protocols. Based on the above results and discussion, we propose rigorous experimental protocols to remove all the carbon contaminations in photocatalytic CO_2 reduction (**Figure 3**). Firstly, the purity should be confirmed by taking into account two aspects: the out-system and the intrasystem contaminations. Different carbon contamination sources have been listed in Table S3. They can be identified by different blank experiments, Fourier-transform infrared spectroscopy (FTIR) and/or Raman spectroscopy. These contaminants can be removed by rigorous water/ethanol washing and/or high-temperature treatment or plasma cleaning. Proper blank experiments (Ar with photocatalyst and illumination, Ar with illumination, CO2 with photocatalysts and CO2 with illumination) are strongly recommended prior to the photocatalytic performance test. Furthermore, the performance test, reproducibility test and stability test are necessary to verify the reliability of the data. Especially, when the photocatalysts are carbon-based materials, photocatalysts

characterizations after the performance test not only indicate the stability of materials but also exclude the false-positive results originating from photocatalysts decomposition. Lastly, we recommend that the full protocols and data are reported in regards to the test of a new catalyst/reaction system to eliminate any carbon contamination sources.

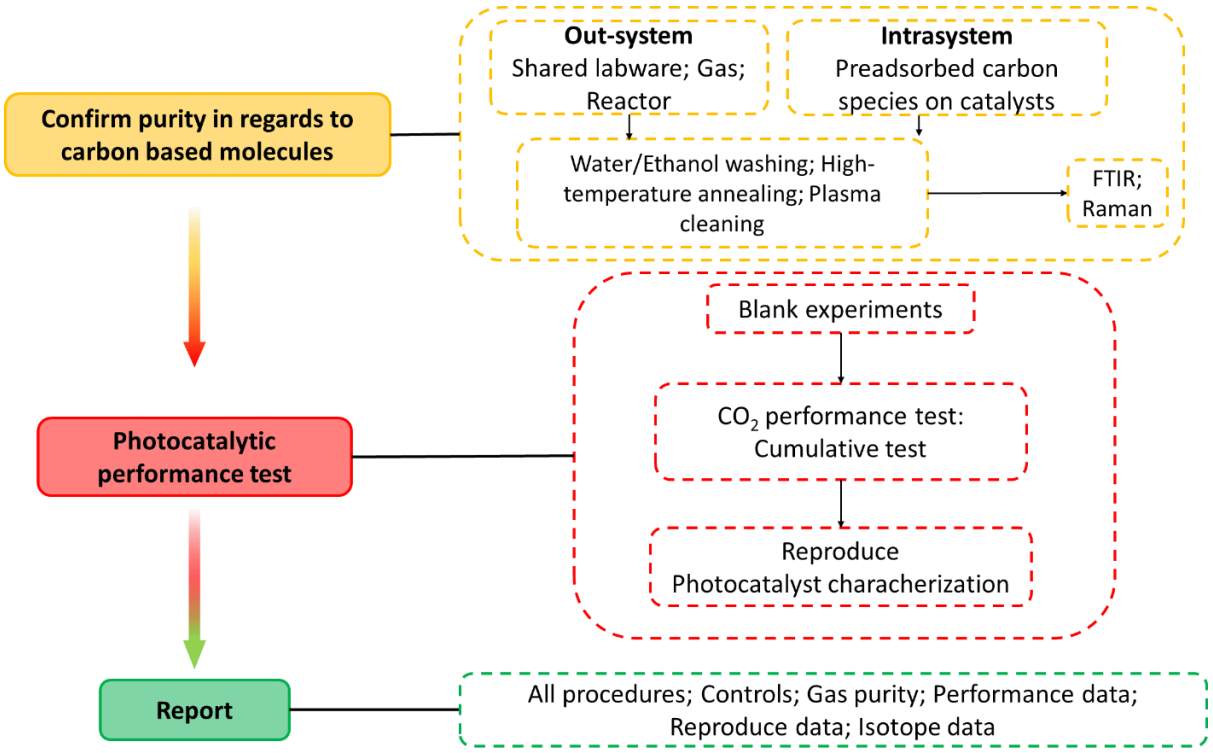

Figure 3. Photocatalytic CO_2 reduction experimental protocols.

In summary, we systematically identified possible carbon contaminations from the decomposition of carbon-based photocatalysts and preparation/washing of nanomaterials and proposed rigorous protocols to eliminate the carbon contaminations toward reliable photocatalytic CO_2 reduction study. We investigated the possible organic agents remaining on the photocatalysts surface, the amount of which can be greatly reduced by high-temperature annealing or plasma cleaning. In addition, researchers focusing on the carbon-based materials in photocatalytic CO_2 reduction should be extremely cautious when they exclude the falsely positive results from carbon contaminations and decomposition of photocatalysts. The identification/elimination of carbon contaminations and proposed experimental protocols can also provide new insights into the reliability of other photocatalytic systems, such as photocatalytic nitrogen reduction. Moreover, the elimination of carbon species under illumination can also provide some inspiration for the photocatalytic decomposition of organic pollutants, which is important in air purification. Nowadays, carbon neutrality becomes an

important target for the development of human society. Hence, a reliable breakthrough in photocatalytic research can lay a solid foundation for not only fundamental research but also industrial application.

ASSOCIATED CONTENT

Supporting Information

Supporting information is available free of charge on the ACS Publications website.

Experimental details, material characterization, determination of carbon contaminations, and supplementary figures showing TGA curve, *in situ* DRIFTS spectra, Raman spectra, TEM pictures, and XRD patterns.

AUTHOR INFORMATION

Corresponding Author

e-mail: s.qiao@adelaide.edu.au; jingrun.ran@adelaide.edu.au

ORCID

Yanzhao Zhang: 0000-0003-2894-4727

Dazhi Yao: 0000-0002-8019-0160

Bingquan Xia: 0000-0003-0909-7788

Mietek Jaroniec: 0000-0002-1178-5611

Jingrun Ran: 0000-0002-8840-862X

Shi-Zhang Qiao: 0000-0002-4568-8422

Notes

Views expressed in this Viewpoint are those of the authors and not necessarily the views of the ACS.

The authors declare no competing financial interest.

ACKNOWLEDGMENTS

This work is financially supported by the Australian Research Council (ARC) through the Discovery Project Programs (FL170100154, DP160104866, and DE200100629).

REFERENCES

(1) Zhang, Y.; Xia, B.; Ran, J.; Davey, K.; Qiao, S.-Z., Atomic-Level Reactive Sites for Semiconductor-Based Photocatalytic CO_2 Reduction. *Adv. Energy Mater.* **2020,** *10* (9), 1903879.

(2) Zhang, Y.; Yao, D.; Xia, B.; Xu, H.; Tang, Y.; Davey, K.; Ran, J.; Qiao, S.-Z., ReS_2 Nanosheets with *In Situ* Formed Sulfur Vacancies for Efficient and Highly Selective Photocatalytic CO_2 Reduction. *Small Sci.* **2021,** *1* (2), 2000052.

(3) Zhu, X.; Wang, Z.; Zhong, K.; Li, Q.; Ding, P.; Feng, Z.; Yang, J.; Du, Y.; Song, Y.; Hua, Y.; Yuan, J.; She, Y.; Li, H.; Xu, H., Mo-O-Bi Bonds as Interfacial Electron Transport Bridges to Fuel CO_2 Photoreduction via *In-situ* Reconstruction of Black Bi_2MoO_6/BiO_{2-x} Heterojunction. *Chem. Eng. Sci.* **2022,** *429*, 132204.

(4) Bi, W.; Hu, Y.; Jiang, H.; Zhang, L.; Li, C., Revealing the Sudden Alternation in Pt@h-BN Nanoreactors for Nearly 100% CO_2-to-CH_4 Photoreduction. *Adv. Funct. Mater.* **2021,** *31* (29), 2010780.

(5) Li, X.; Sun, Y.; Xu, J.; Shao, Y.; Wu, J.; Xu, X.; Pan, Y.; Ju, H.; Zhu, J.; Xie, Y., Selective Visible-Light-Driven Photocatalytic CO_2 Reduction to CH_4 Mediated by Atomically Thin $CuIn_5S_8$ layers. *Nat. Energy* **2019,** *4* (8), 690-699.

(6) Pang, H.; Meng, X.; Li, P.; Chang, K.; Zhou, W.; Wang, X.; Zhang, X.; Jevasuwan, W.; Fukata, N.; Wang, D.; Ye, J., Cation Vacancy-Initiated CO_2 Photoreduction over ZnS for Efficient Formate Production. *ACS Energy Lett.* **2019,** *4* (6), 1387-1393.

(7) Zhu, S.; Li, X.; Jiao, X.; Shao, W.; Li, L.; Zu, X.; Hu, J.; Zhu, J.; Yan, W.; Wang, C.; Sun, Y.; Xie, Y., Selective CO_2 Photoreduction into C_2 Product Enabled by Charge-Polarized Metal Pair Sites. *Nano Lett.* **2021,** *21* (5), 2324-2331.

(8) Williams, G.; Seger, B.; Kamat, P. V., TiO_2-Graphene Nanocomposites UV-Assisted Photocatalytic Reduction of Graphene Oxide. *ACS Nano* **2008**, *2* (7), 1487-1491.

(9) Das, R.; Chakraborty, S.; Peter, S. C., Systematic Assessment of Solvent Selection in Photocatalytic CO_2 Reduction. *ACS Energy Lett.* **2021**, *6* (9), 3270-3274.

(10) Kong, L.; Jiang, Z.; Wang, C.; Wan, F.; Li, Y.; Wu, L.; Zhi, J.-F.; Zhang, X.; Chen, S.; Liu, Y., Simple Ethanol Impregnation Treatment Can Enhance Photocatalytic Activity of TiO_2 Nanoparticles under Visible-Light Irradiation. *ACS Appl. Mater. Interfaces* **2015,** *7* (14), 7752-7758.

(11) Zhang, Y.; Wang, X.; Dong, P.; Huang, Z.; Nie, X.; Zhang, X., A Green Synthetic Approach for Self-Doped TiO_2 with Exposed Highly Reactive Facets Showing Efficient CO_2 Photoreduction under Simulated Solar Light. *Green Chem.* **2018,** *20* (9), 2084-2090.

(12) Zhang, Y.; Wang, X.; Dong, P.; Huang, Z.; Nie, X.; Zhang, X., TiO_2 Surfaces Self-Doped with Ag Nanoparticles Exhibit Efficient CO_2 Photoreduction under Visible Light. *RSC Adv.* **2018,** *8* (29), 15991-15998.

(13) Jiang, Y.; Chen, H.-Y.; Li, J.-Y.; Liao, J.-F.; Zhang, H.-H.; Wang, X.-D.; Kuang, D.-B., Z-Scheme 2D/2D Heterojunction of $CsPbBr_3/Bi_2WO_6$ for Improved Photocatalytic CO_2 Reduction. *Adv. Funct. Mater.* **2020,** *30* (50), 2004293.

(14) Cao, S.; Shen, B.; Tong, T.; Fu, J.; Yu, J., 2D/2D Heterojunction of Ultrathin MXene/Bi_2WO_6 Nanosheets for Improved Photocatalytic CO_2 Reduction. *Adv. Funct. Mater.***2018,** *28* (21), 1800136.

(15) Cho, K. M.; Kim, K. H.; Park, K.; Kim, C.; Kim, S.; Al-Saggaf, A.; Gereige, I.; Jung, H.-T., Amine-Functionalized Graphene/CdS Composite for Photocatalytic Reduction of CO_2. *ACS Catal.* **2017,** *7* (10), 7064-7069.

(16) Wang, J.; Wang, J.; Li, N.; Du, X.; Ma, J.; He, C.; Li, Z., Direct Z-Scheme 0D/2D Heterojunction of $CsPbBr_3$ Quantum Dots/Bi_2WO_6 Nanosheets for Efficient Photocatalytic CO_2 Reduction. *ACS Appl. Mater. Interfaces* **2020,** *12* (28), 31477-31485.

(17) Gong, D.; Subramaniam, V. P.; Highfield, J. G.; Tang, Y.; Lai, Y.; Chen, Z., *In Situ* Mechanistic Investigation at the Liquid/Solid Interface by Attenuated Total Reflectance FTIR: Ethanol Photo-Oxidation over Pristine and Platinized TiO_2 (P25). *ACS Catal.* **2011,** *1* (8), 864-871.

(18) Li, F.; Men, Z.; Li, S.; Wang, S.; Li, Z.; Sun, C., Study of Hydrogen Bonding in Ethanol-Water Binary Solutions by Raman Spectroscopy. *Spectrochim. Acta A Mol. Biomol. Spectrosc.* **2018,** *189*, 621-624.

(19) Jin, Z.; Chu, Q.; Xu, W.; Cai, H.; Ji, W.; Wang, G.; Lin, B.; Zhang, X., All-Fiber Raman Biosensor by Combining Reflection and Transmission Mode. *IEEE Photonics Technol. Lett.* **2018,** *30* (4), 387-390.

(20) Dendramis, A. L.; Schwinn, E. W.; Sperline, R. P., A Surface-Enhanced Raman Scattering Study of CTAB Adsorption on Copper. *Surf. Sci.* **1983,** *134* (3), 675-688.

(21) Krishnan, K.; Plane, R. A., Raman and Infrared Spectra of Complexes of Ethylenediamine with Zinc (II), Cadmium (II), and Mercury (II). *Inorg.* **1966,** *5* (5), 852-857.

(22) Deng, Z.-X.; Li, L.; Li, Y., Novel Inorganic- Organic-Layered Structures: Crystallographic Understanding of Both Phase and Morphology Formations of One-Dimensional CdE (E= S, Se, Te) Nanorods in Ethylenediamine. *Inorg.* **2003,** *42* (7), 2331-2341.

(23) Ma, Y.; Liu, Y.; Lan, L.; Wu, T.; Jiang, W.; Ong, C.; He, S., First Experimental Demonstration of an Isotropic Electromagnetic Cloak with Strict Conformal Mapping. *Sci. Rep.* **2013**, *3* (1), 2182.

(24) Das, R.; Sarkar, S.; Kumar, R.; D. Ramarao, S.; Cherevotan, A.; Jasil, M.; Vinod, C. P.; Singh, A. K.; Peter, S. C., Noble-Metal-Free Heterojunction Photocatalyst for Selective CO_2 Reduction to Methane upon Induced Strain Relaxation. *ACS Catal.* **2021**, *12* (1), 687-697.

(25) Zhang, R.; Wang, H.; Tang, S.; Liu, C.; Dong, F.; Yue, H.; Liang, B., Photocatalytic Oxidative Dehydrogenation of Ethane Using CO_2 as a Soft oxidant over Pd/TiO_2 Catalysts to C_2H_4 and Syngas. *ACS Catal.* **2018**, *8* (10), 9280-9286.

(26) Wilfong, W. C.; Srikanth, C. S.; Chuang, S. S., *In Situ* ATR and DRIFTS Studies of the Nature of Adsorbed CO_2 on Tetraethylenepentamine Films. *ACS Appl. Mater. Interfaces* **2014**, *6* (16), 13617-13626.

(27) Liu, Y.; Shen, D.; Zhang, Q.; Lin, Y.; Peng, F., Enhanced Photocatalytic CO_2 reduction in H_2O Vapor by Atomically Thin Bi_2WO_6 Nanosheets with Hydrophobic and Nonpolar Surface. *Appl. Catal. B.* **2021,** *283*, 119630.

(28) Gan, L.; Lu, Z.; Cao, D.; Chen, Z., Effects of Cetyltrimethylammonium Bromide on the Morphology of Green Synthesized Fe_3O_4 Nanoparticles Used to Remove Phosphate. *Mater. Sci. Eng. C* . **2018,** *82*, 41-45.

(29) Chankhanittha, T.; Somaudon, V.; Photiwat, T.; Hemavibool, K.; Nanan, S., Preparation, Characterization, and Photocatalytic Study of Solvothermally Grown CTAB-Capped Bi_2WO_6 Photocatalyst toward Photodegradation of Rhodamine B Dye. *Opt. Mater.* **2021,** *117*, 111183.

(30) Lima, M. C. F. S.; Zaida do Amparo, S.; Ribeiro, H.; Soares, A. L.; Viana, M. M.; Seara, L. M.; Paniago, R. M.; Silva, G. G.; Caliman, V., Aqueous Suspensions of Carbon Black with Ethylenediamine and Polyacrylamide-Modified Surfaces: Applications for Chemically Enhanced Oil Recovery. *Carbon* **2016,** *109*, 290-299.

(31) Liu, B. S.; Cheng, K.; Nie, S. C.; Zhao, X. J.; Yu, H. G.; Yu, J. G.; Fujishima, A.; Nakata, K., Ice-Water Quenching Induced Ti^{3+} Self-Doped TiO_2 with Surface Lattice Distortion and the Increased Photocatalytic Activity. *J. Phys. Chem. C.* **2017,** *121* (36), 19836-19848

Supporting Information for

Photocatalytic CO_2 Reduction: Identification and Elimination of False-Positive Results

Yanzhao Zhang,[†] Dazhi Yao,[†] Bingquan Xia,[†] Mietek Jaroniec,[§] Jingrun Ran[,†], and Shi-Zhang Qiao*[,†]*

[†]School of Chemical Engineering & Advanced Materials, The University of Adelaide, Adelaide, SA 5005, Australia.

[§]Department of Chemistry and Biochemistry & Advanced Materials and Liquid Crystal Institute, Kent State University, Kent, OH 44242, USA.

E-mail: s.qiao@adelaide.edu.au; jingrun.ran@adelaide.edu.au

Experiment Details

Chemicals and materials preparations

The following chemicals were used: titanium dioxide (P25, Sigma Aldrich), cadmium nitrate tetrahydrate ($Cd(NO_3)_2 \cdot 4H_2O$, Sigma Aldrich), thiourea (CH_4N_2S, Sigma Aldrich), ethylenediamine ($NH_2CH_2CH_2NH_2$, Sigma Aldrich), bismuth nitrate pentahydrate ($Bi(NO_3)_3 \cdot 5H_2O$, Sigma Aldrich), hexadecyltrimethylammonium bromide ($CH_3(CH_2)_{15}N(Br)(CH_3)_3$, CTAB, Sigma Aldrich), sodium tungstate dihydrate ($Na_2WO_4 \cdot 2H_2O$, Sigma Aldrich), ethanol (C_2H_5OH, ChemSupply), urea (CH_4N_2O, Sigma Aldrich). All of the chemicals are Analytical Reagent and used directly without any further purification. Ultrapure water used throughout all experiments was purified through an Adelab Millipore system. Ultra-high purity Ar (99.999%) was purchased from BOC Gas, Australia.

Synthesis of CdS nanorods: CdS nanorods were prepared by the solvothermal method. In the preparation, 5.4 mmol of $Cd(NO_3)_2 \cdot 4H_2O$ were dissolved in 108 mL of ethylenediamine under magnetic stirring for 30 min to obtain a uniform solution. After that, 10.8 mmol of thiourea were dropped into the solution and stirred for another 30 min, and then it was transferred to a 200 mL Teflon-lined autoclave. The autoclave was maintained at 180 ℃ for 12 h. The products were washed with water or ethanol. Firstly, the products were dispersed in the washing liquid (water or ethanol) then collected by centrifuge. Then, they were dispersed again in the liquid by sonication. This process was repeated three times. The resulting materials are denoted as CdS-W and CdS-E, respectively. Lastly, the products were dried in a vacuum oven at 60 ℃ for 10 h.

Synthesis of Bi_2WO_6 nanosheets: In the typical synthesis, the Bi_2WO_6 nanosheets were prepared under hydrothermal conditions. 50 mg of CTAB and 1 mmol of $Na_2WO_4 \cdot 2H_2O$ were dissolved in 70 mL water and sonicated for 30 min. After that, 2 mmol of $Bi(NO_3)_3 \cdot 5H_2O$ were added to the solution and sonicated for another 30 min to obtain a uniform solution, which was transferred to a 100 mL Teflon-lined autoclave. The autoclave was maintained at 120 ℃ for 24 h. The products were washed with water or ethanol (the washing process of Bi_2WO_6 nanosheets was the same as that of CdS nanorods). The resulting samples were labelled as BWO-W and BWO-E, respectively. Lastly, the products were dried in a vacuum oven at 60 ℃ for 10 h.

Synthesis of C_3N_4 nanosheets: In the typical synthesis, the C_3N_4 nanosheets were prepared by pyrolysis. 10g of urea were put in the crucible with a lid and then heated to 550 ℃ at the heating rate of 5 ℃/min in the Muffle furnace. The temperature was kept at 550 ℃ for four hours. After cooling down, the powder was ground. The resulting sample was labelled as CN.

Pretreatment of P25: P25 was performed with ethanol or water. In the preparation, 1 g of P25 was dispersed in 20 mL of ethanol or water under sonication for 5 min and then stirred for 1 hour. After that the P25 sample was collected by centrifuge and dried in a vacuum oven at 60 ℃ for 10 h. These two samples were labelled as P25-E and P25-W, respectively.

Characterization

X-ray diffraction: XRD data were collected on a powder X-ray diffractometer (Miniflex, Rigaku) using Cu Kα radiation. Raman spectroscopy data were collected using a confocal Raman microscope (Horiba LabRAM HR Evolution) with a 10X objective and a 532 nm laser in all experiments. Thermogravimetric analysis was conducted on the NETASCH STA 449 F5 Jupiter. Morphology observation was conducted on a Tecnai G2 *transmission electron microscopy (TEM).*

Plasma cleaning

Before illumination, the glass fibre filter loaded with photocatalysts was put into the plasma cleaner, which was vacuumed up to 150 mTorr and purged with oxygen or Argon (BOC). This process was repeated three times and until the cleaner was stable at 450 mTorr. Next, the plasma was turned on at high for 10 min. The BWO-E and P25-E samples were labelled as BWO-P and P25-P, respectively after the oxygen plasma cleaning and the CdS-E was labelled as CdS-P after the argon plasma cleaning.

Annealing treatment

A certain amount of photocatalysts was placed in a tube furnace, which was heated up to a certain degree under Argon or air atmosphere using 3 ℃/min heating rate. After maintaining for 4 hours, the furnace was cooled down naturally to room temperature. After annealing the samples CdS-E, BWO-E and P25-E were labelled as CdS-A, BWO-A and P25-A, respectively.

Photocatalytic test

The photocatalytic performance tests were conducted in a 287 mL home-made reactor sealed with silicone rubber septa at ambient conditions. A 300 W Xenon lamp was employed as the light source. In a typical test, 20 mg of photocatalysts were dispersed in water then loaded on the glass fibre filter and dried under infrared light. Before illumination, the reactor was purged

by ultrahigh purity Argon for 1 hour. The product was collected from the reactor per hour by the syringe and analysed by a gas chromatograph (GC, 7890B, Agilent). The GC is equipped with plot-Q and a 5 Å sieve column (Agilent) in series, TCD and methanizer/FID detectors and UHP Ar (BOC) as the carrier gas.

***In situ* DRIFTS for carbon contamination conversion**

All IR spectra were performed using a Nicolet iS20 spectrometer equipped with an HgCdTe (MCT) detector cooled with liquid nitrogen and a VeeMax III (PIKE technologies) accessory. The *in situ* DRIFTS studies were performed using a Praying Mantis DRIFTS accessory and a reactor (Harrick Scientific, HVC-DRP). A 300 W Xe lamp (ZhongJiaoJinYuan) connects a liquid light guide for irradiation. A 400 nm filter was used for CdS nanorods testing. No filter was used for BWO and P25 testing.

The sample in the reaction chamber was purged by Argon bubbling through deionized water for 30 min until the sample spectrum was stable. The background was collected and 5 min later the 0 min spectrum was recorded to ensure the sample and the reaction chamber are stable. Then, the illumination was started. Next, the FTIR spectra under irradiation conditions were recorded as a function of time to investigate the dynamics of surface carbon contamination.

Supplementary Figures

Figure S1. CO, CH_4 and C_2H_4 product yields of BWO in Argon under four-hour irradiation. The BWO sample was synthesized by hydrothermal reaction without any washing process and dried in a vacuum oven for 12 hours.

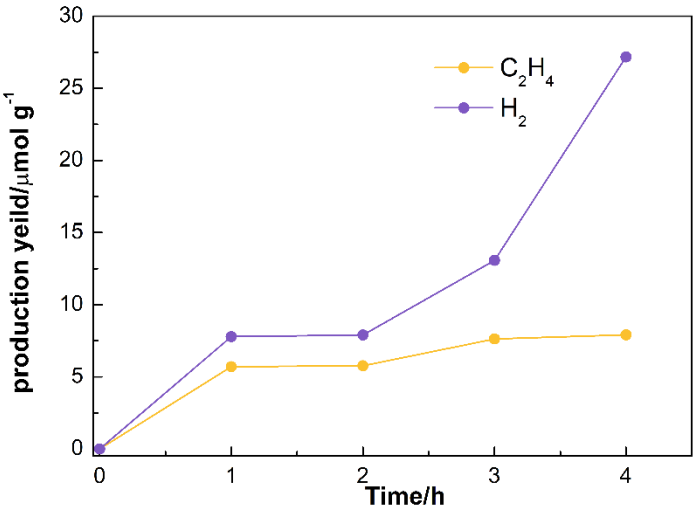

Figure S2. H_2 and C_2H_4 product yields of BWO-W in Argon under four-hour irradiation. The BWO was synthesized by hydrothermal reaction and washed by using deionized water three times and dried in a vacuum oven for 12 hours.

Figure S3. CO, CH_4 and H_2 product yields of CdS in Argon under four-hour irradiation. The CdS nanorods were synthesized by hydrothermal reaction without any washing process and dried in a vacuum oven for 12 hours.

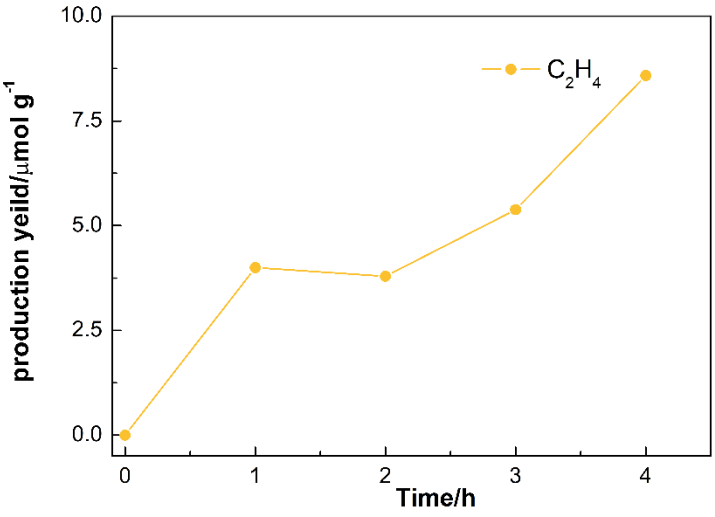

Figure S4. C_2H_4 product yield of BWO-E in Argon under four-hour irradiation. The BWO was synthesized by hydrothermal reaction and washed by using ethanol three times and dried in a vacuum oven for 12 hours.

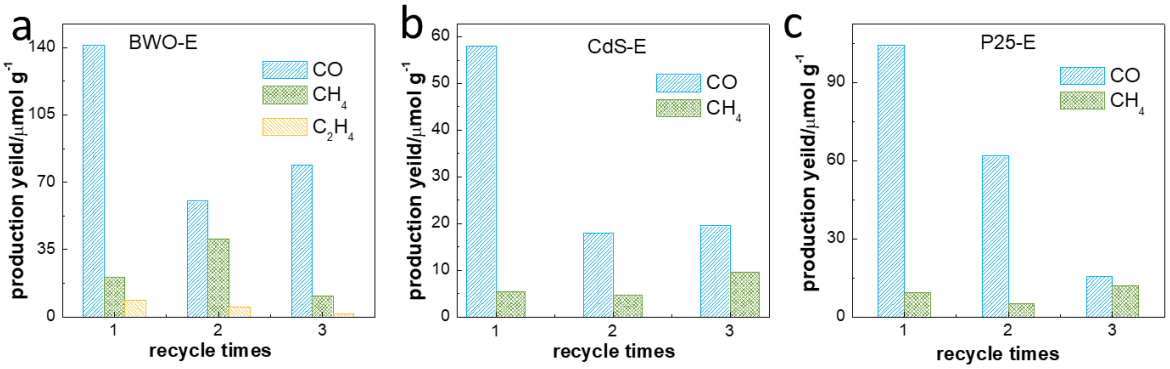

Figure S5. Repetition test in Argon for different samples. After the first cycle, the reactor is purged with Argon again to exclude the first-cycle products. Then the same process was repeated as the first time experiment. After four hours, the products were collected and analyzed. (a) BWO-E, (b) CdS-E and (c) P25-E.

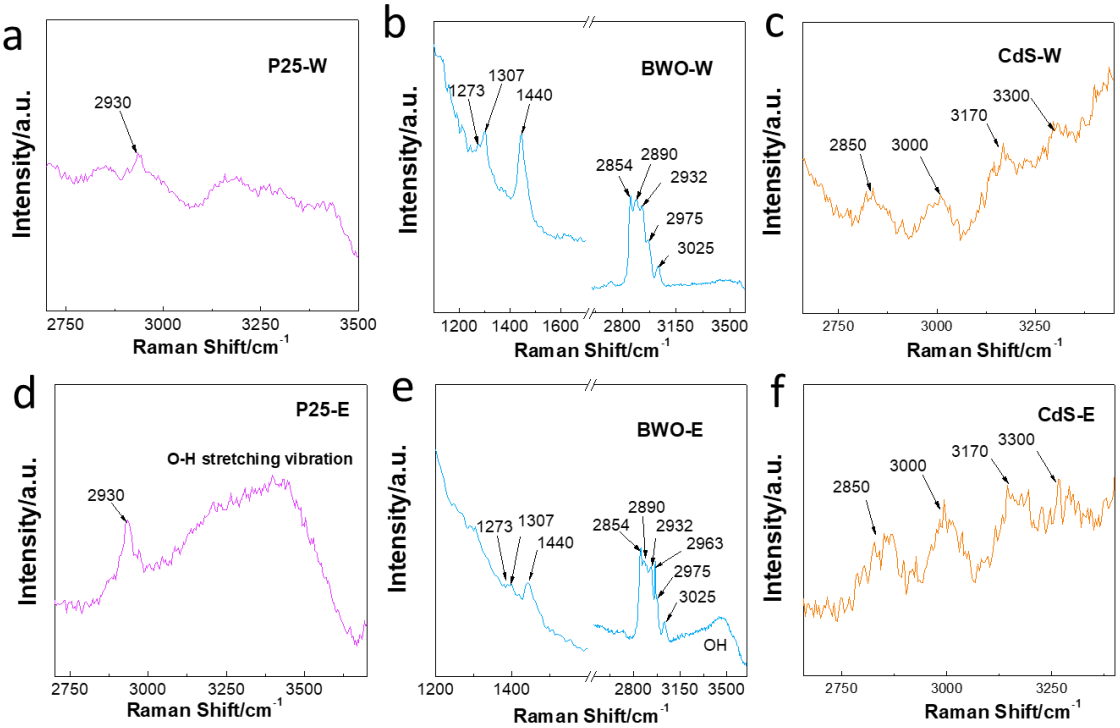

Figure S6. Raman spectra of various carbon contaminations on different samples. The Raman spectra were collected for the washed samples with water or ethanol: (a) P25-W (P25 after washing by using water), (b) BWO-W (BWO after washing by using water), (c) CdS-W (CdS after washing by using water), (d) P25-E (P25 after washing by using ethanol), (e) BWO-E (BWO after washing by using ethanol) and (f) CdS-E (CdS after washing by using ethanol).

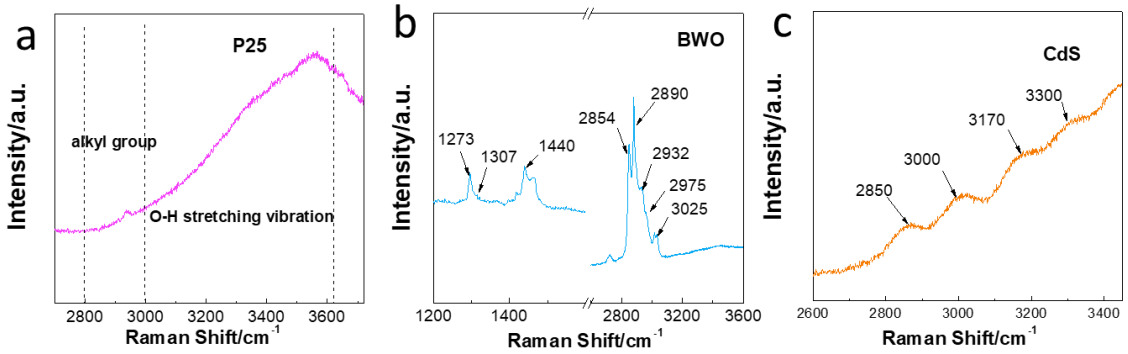

Figure S7. Raman spectra of various carbon contaminations on different samples. (a) P25 (commercial products without any treatment), (b) BWO (samples are characterized after hydrothermal reaction without any washing process) and (c) CdS (samples are characterized after hydrothermal reaction without any washing process).

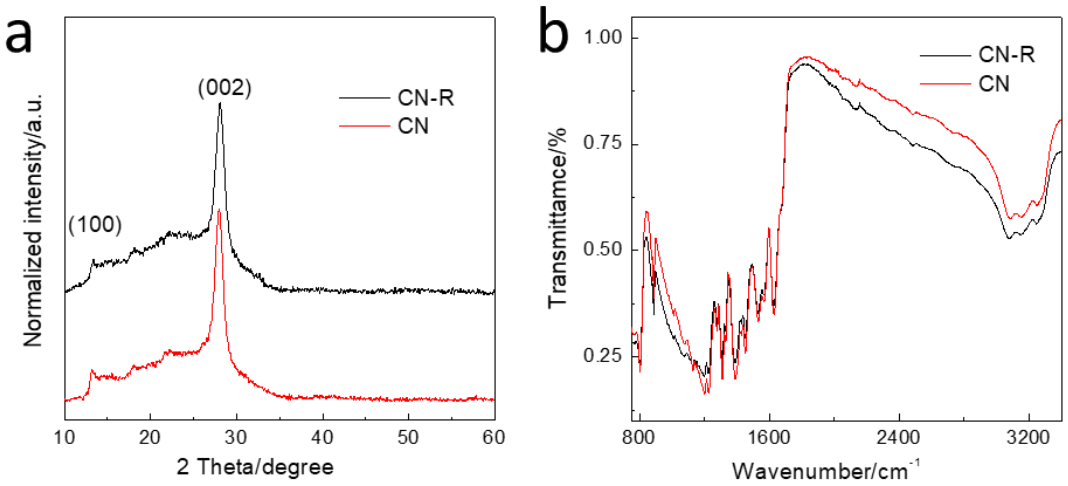

Figure S8. (a) XRD patterns and FTIR spectra of C_3N_4 nanosheets before (CN) and after (CN-R) illumination. Both the CN and CN-R spectra show clearly (100) and (002) peaks, which illustrate that the crystal structure is stable after the photocatalytic test. In FTIR spectra, peaks at about 802 cm^{-1} can be attributed to the individual breathing of triazine rings. The peaks between 1200 and 1640 cm^{-1} belong to the CN stretching in conjugation. The broad peak between 3000-3400 cm^{-1} originates from the stretching vibrational mode of NH groups and absorbed water. Similarly as the XRD patterns, the FTIR spectra confirm stability of the sample after photocatalytic testing.

Figure S9. TGA of CTAB powder in air. The powder started decomposing at 190 ℃ and finished the decomposition process at around 660 ℃. The heating rate was 5 ℃/min in air.

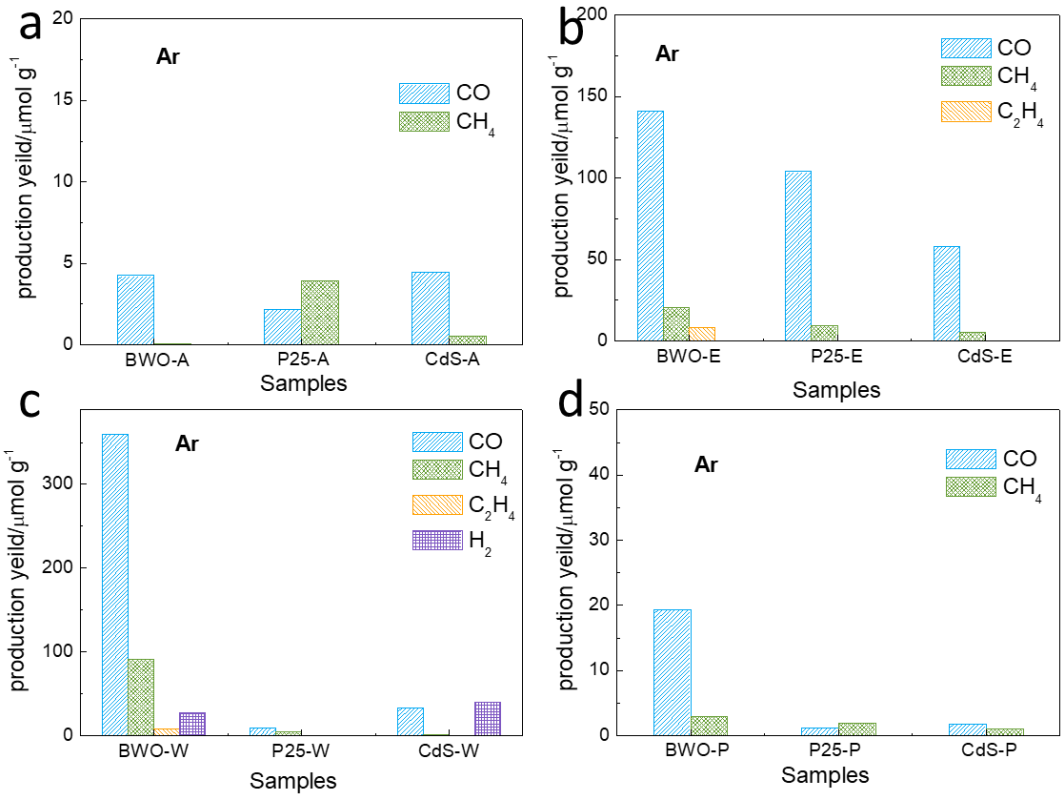

Figure S10. Products yield of different samples in Ar under four-hour irradiation (a) samples after high-temperature treatment, (b) samples after ethanol washing, (c) samples after water washing, (d) samples after plasma cleaning.

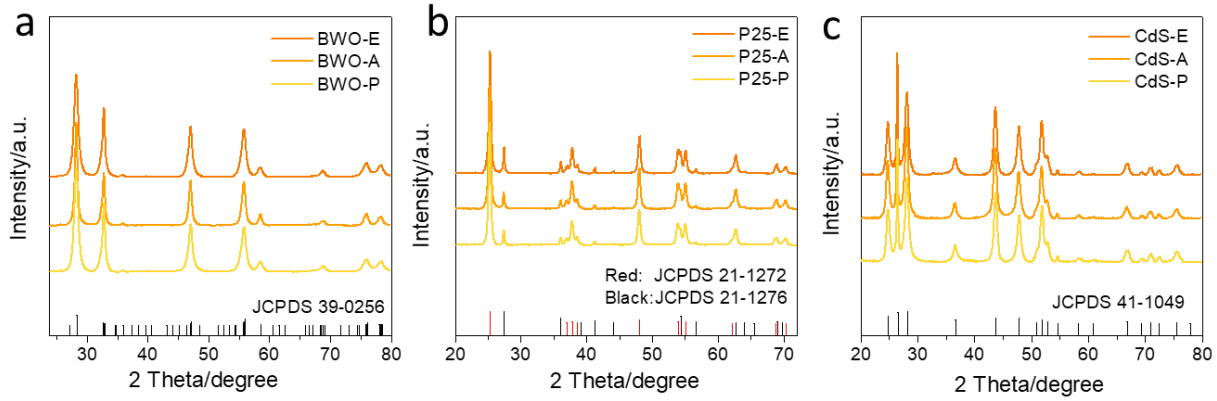

Figure S11. XRD patterns of (a) BWO-E (0.70°), BWO-A (0.49°) and BWO-P (0.70°), (b) P25-E (0.41°), P25-A (0.41°) and P25-P (0.41°) and (c) CdS-E (0.23°), CdS-A (0.23°) and CdS-P (0.23°). The value in brackets is the FWHM of the highest peak from each sample's XRD pattern.

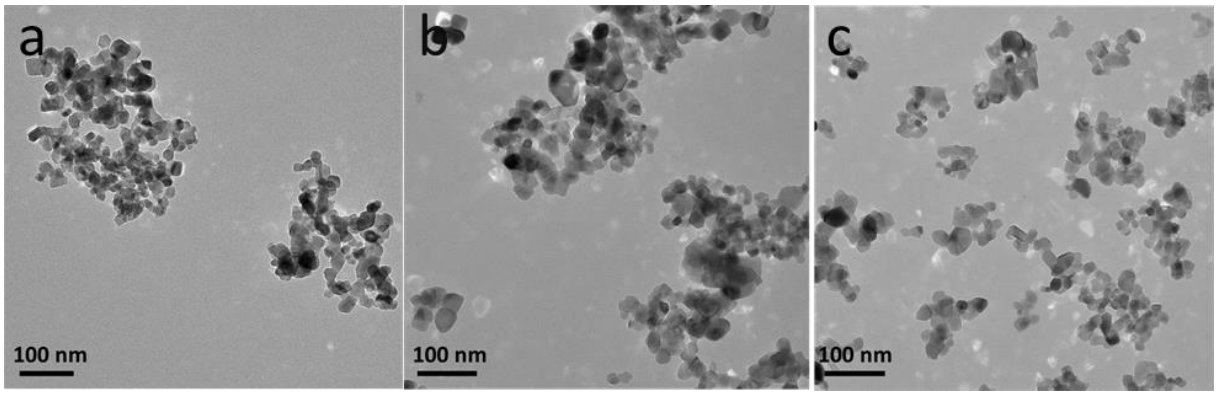

Figure S12. TEM pictures of different TiO_2 samples after different treatments. (a) P25-E (commercial P25 after ethanol washing), (b) P25-A (commercial P25 after high-temperature treatment) and (c) P25-P (commercial P25 after plasma cleaning).

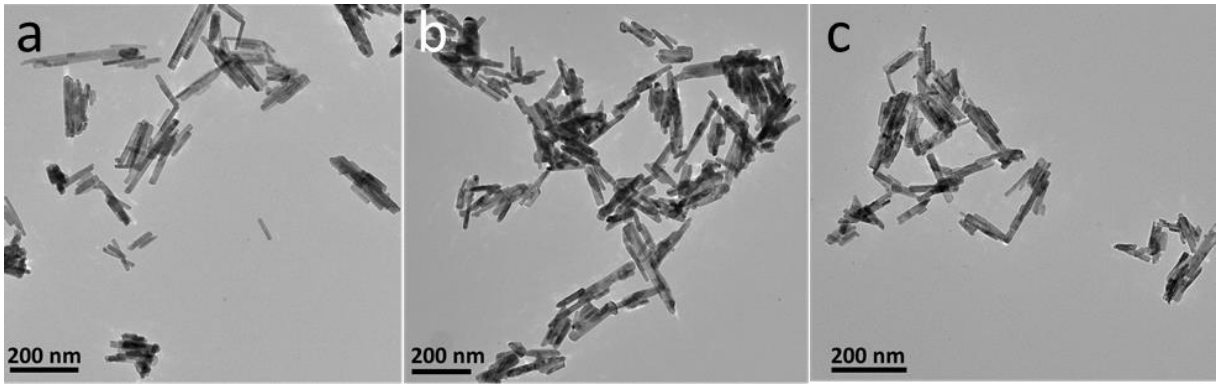

Figure S13. TEM pictures of different CdS samples after different treatments. (a) CdS-E (hydrothermal-reaction-synthesized CdS nanorods after ethanol washing), (b) CdS-A (hydrothermal-reaction-synthesized CdS nanorods after high-temperature treatment) and (c) CdS-P (hydrothermal-reaction-synthesized CdS nanorods after plasma cleaning).

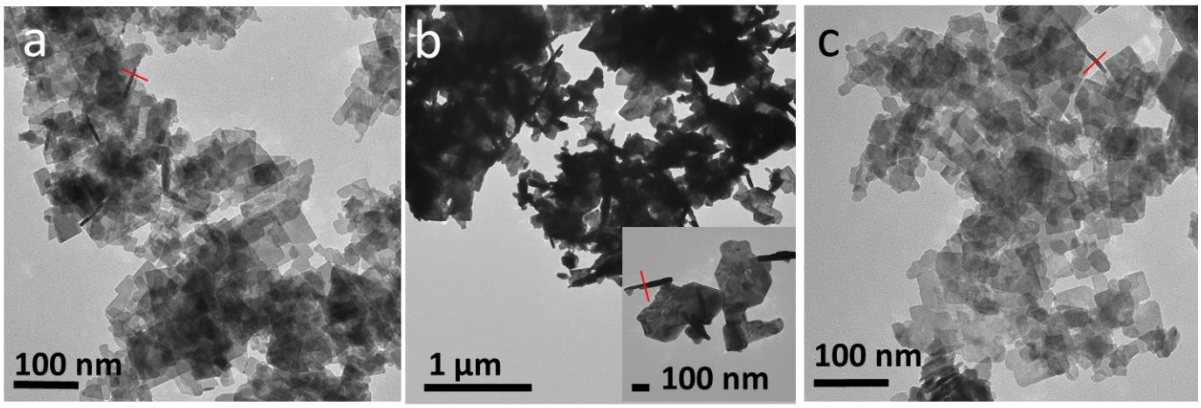

Figure S14. TEM pictures of different Bi_2WO_6 samples. (a) BWO-E, (b) BWO-A and (c) BWO-P. The red lines in pictures across the nanosheets measure its thickness and the results are shown in Figure S15.

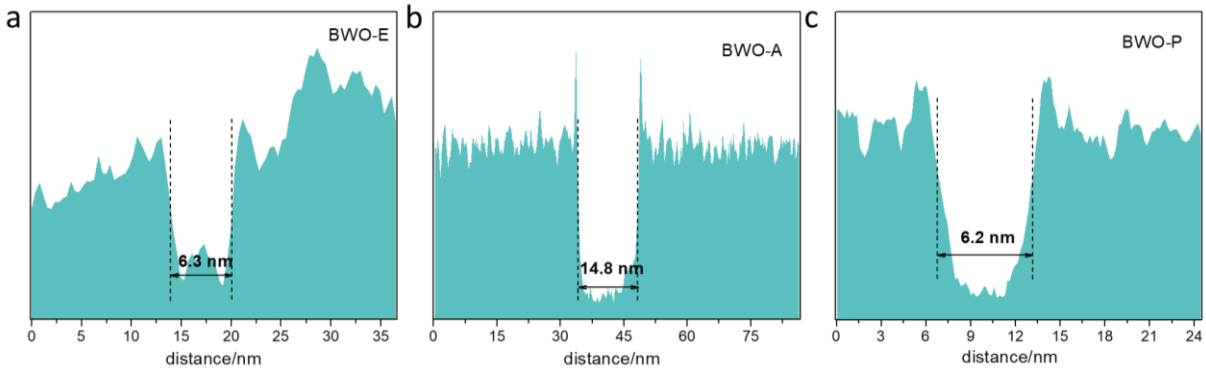

Figure S15. The thickness of different Bi_2WO_6 samples measured from TEM results in Figure S14. (a) BWO-E, (b) BWO-A and (c) BWO-P.

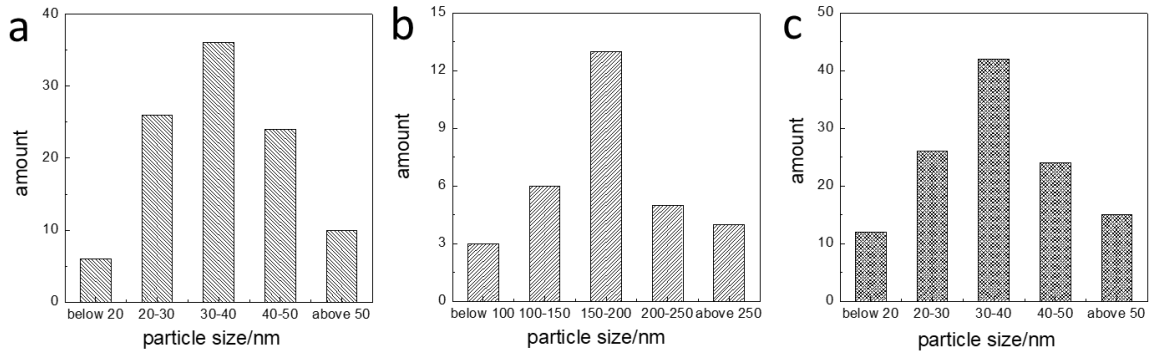

Figure S16. The lateral size distribution for different Bi_2WO_6 samples measured from TEM results in Figure S14. (a) BWO-E, (b) BWO-A and (c) BWO-P.

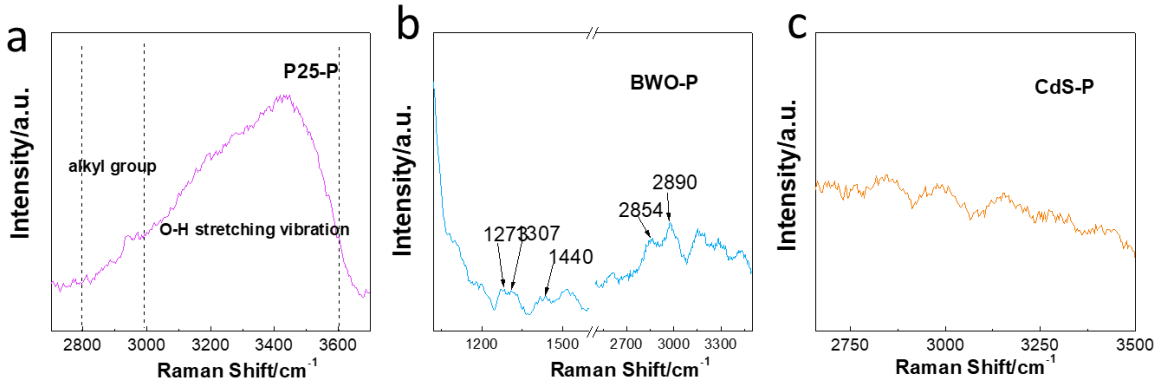

Figure S17. Raman spectra of carbon contaminations on different samples. (a) P25-P (commercial P25 after plasma cleaning), (b) BWO-P (BWO nanosheets after plasma cleaning) and (c) CdS-P (CdS nanorods after plasma cleaning).

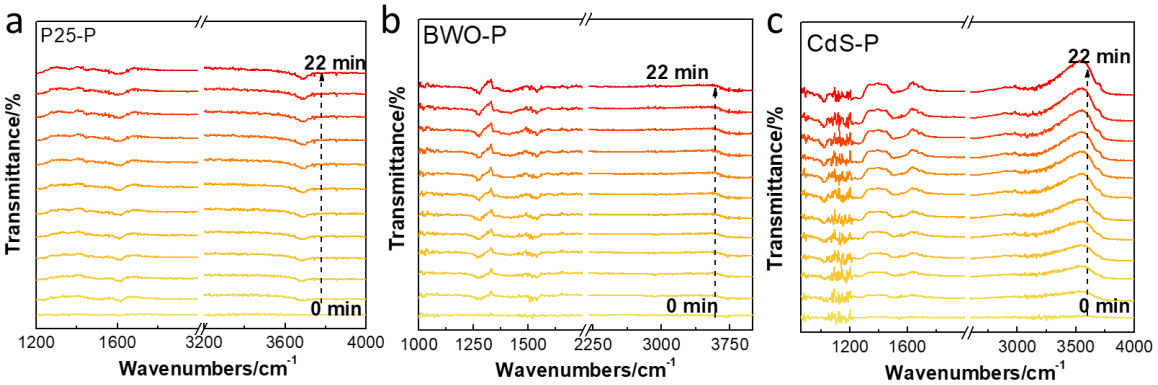

Figure S18. *In situ* DRIFTS of various carbon contaminations on different samples under illumination in Argon. 0 min spectrum was collected after background and the illumination started meantime. Then, the remaining spectra were collected every two minutes until 22 min. Argon was purging through the deionized water. (a) P25-P, (b) BWO-P and (c) CdS-P.

Table S1. Raman vibration peak wavenumbers of CTAB

Raman peak (cm^{-1})	Vibrational mode
1273	CH_2 wag
1307	CH_2 twist
1440	CH_2 scissors
2854	CH_2 sym. stretch
2890	CH_2 as. stretch
2932	Tern. CH_3 sym. stretch
2975	Headgroup CH_3 sym. stretch
3025	Headgroup CH_3 as. stretch

Table S2. *In situ* DRIFTS peaks of ethanol

peak (cm^{-1})	Vibrational mode
1387	CH_3 scissors
1440	CH_3 as. deformation
1476	CH_2 scissors
2940	CH_2 as. stretch
2980	CH_3 as. stretch

Table S3. Carbon contamination checklist for photocatalytic CO_2 reduction

category	source	identification	elimination
out-system	reactor	Ar+illumination+without catalysts	clean the reactor/use metalwares or glasswares
	gas	Ar or CO_2+dark+without catalysts	use ultra-high purity gas
	shared facilities	Ar+illumination+catalyst	exclusive use of facilities
	products analyser	Ultra-high purity gas	
intrasystem	preparation	FTIR or Raman spectroscopy	high-temperature treatment/plasma cleaning
	washing	FTIR or Raman spectroscopy	high-temperature treatment/plasma cleaning

Chapter 5

Facet-specific Active Surface Regulation of Bi_xMO_y (M= Mo, V, W) Nanosheets for Boosted Photocatalytic CO_2 reduction

5.1 Introduction and Significance

Active surface engineering of photocatalytic materials is widely used to improve catalytic performance. However, traditional approaches usually result in uncontrolled deviation from target active sites, and low catalytic performance. An improved understanding is needed therefore to better control processes for stable and well-defined surface chemistry and boosted photocatalytic performance. Here we report for the first time Bi-based semiconductors with active surface regulation via sonication-assisted etching.

1. A facile method for specific surface-regulated nanosheets. The (010) surface of nanosheets were actively regulated via oxygen vacancies. This facile method is applicable to Bi_2MoO_6, Bi_2WO_6 and $BiVO_4$. Experimental Raman, EELS and synchrotron-based XAS, confirmed a distorted crystal structure of these materials.

2. A highly active surface for CO_2 chemisorption/activation boosted CO_2 photoreduction. The surface-regulated Bi_2MoO_6 nanosheets exhibited a high activity of, respectively, 61.5 and 12.4 μmol g^{-1} for CO and CH_4, a selectivity > 83 % and stability > 20 h for the reaction for the Bi-based catalyst.

3. Active sites and reaction mechanism on Bi-based CRR photocatalysts. Combined theoretical computations, kinetics analyses and *in situ* infrared spectroscopy confirmed that surface unsaturated metal atoms formed as the active sites, and evidenced the hydrogenation of $*OCH_3$ for CH_4 formation as the rate-limiting step.

We conclude the method is generalizable to a wider range of materials to permit regulated surface chemistry for boosted photocatalytic performance. Findings will be of benefit and interest in the development of active surface engineering that is applicable to additional photocatalytic systems, including, hydrogen and oxygen evolution, and nitrogen reduction.

5.2 Facet-specific Active Surface Regulation of Bi_xMO_y (M= Mo, V, W) Nanosheets for Boosted Photocatalytic CO_2 reduction

This Chapter is presented as a submitted research paper by Yanzhao Zhang, Xing Zhi, Jeffrey R. Harmer, Haolan Xu, Kenneth Davey, Jingrun Ran and Shi-Zhang Qiao. Facet-specific Active Surface Regulation of Bi_xMO_y (M= Mo, V, W) Nanosheets for Boosted Photocatalytic CO_2 reduction, ***Angew. Chem. Int. Ed.*** 2022, e202212355.

Statement of Authorship

Title of Paper	Facet-specific Active Surface Regulation of BixMOy (M= Mo, V, W) Nanosheets for Boosted Photocatalytic CO2 reduction
Publication Status	☑ Published ☐ Accepted for Publication ☐ Submitted for Publication ☐ Unpublished and Unsubmitted w ork w ritten in manuscript style
Publication Details	Yanzhao Zhang, Xing Zhi, Jeffrey Harmer, Haolan Xu, Kenneth Davey, Jingrun Ran, Shizhang Qiao, Angewandte Chemie International Edition, 2022, e202212355

Principal Author

Name of Principal Author (Candidate)	Yanzhao Zhang		
Contribution to the Paper	Design and conducted the experiments, analysed the data, wrote the manuscript.		
Overall percentage (%)	70%		
Certification:	This paper reports on original research I conducted during the period of my Higher Degree by Research candidature and is not subject to any obligations or contractual agreements with a third party that would constrain its inclusion in this thesis. I am the primary author of this paper.		
Signature		Date	06/12/2022

Co-Author Contributions

By signing the Statement of Authorship, each author certifies that:

i. the candidate's stated contribution to the publication is accurate (as detailed above);

ii. permission is granted for the candidate in include the publication in the thesis; and

iii. the sum of all co-author contributions is equal to 100% less the candidate's stated contribution.

Name of Co-Author	Xing Zhi		
Contribution to the Paper	Guided the DFT calculations and data analysis. Discussion of manuscript		
Signature		Date	06/12/2022

Name of Co-Author	Jeffrey R. Harmer		
Contribution to the Paper	Conducted EPR tests and corresponding writing and discussion.		
Signature		Date	6/1/2023

Name of Co-Author	Haolan Xu		
Contribution to the Paper	Conducted XPS tests and data analysis		
Signature		Date	06/12/2022

Name of Co-Author	Kenneth Davey		
Contribution to the Paper	Discussion and revision of this manuscript		
Signature		Date	6/12/2022

Name of Co-Author	Jingrun Ran		
Contribution to the Paper	Manuscript evaluation and revision		
Signature		Date	25/11/2022

Name of Co-Author	Shi-Zhang Qiao		
Contribution to the Paper	Supervision of the work, discussion and conceptualization of this manuscript and manuscript evaluation and revision.		
Signature		Date	25/01/23

Facet-specific Active Surface Regulation of Bi_xMO_y (M=Mo, V, W) Nanosheets for Boosted Photocatalytic CO_2 reduction

Yanzhao Zhang,[†[a]] Xing Zhi,[†[a]] Jeffrey R. Harmer,[[b]] Haolan Xu,[[c]] Kenneth Davey,[[a]] Jingrun Ran[[a]] and Shi-Zhang Qiao*[[a]]*

[a] Y. Zhang, Dr. X. Zhi, A/Prof. K. Davey. Dr. J. Ran, Prof. S.Z. Qiao
Centre for Materials in Energy and Catalysis, School of Chemical Engineering and Advanced Materials, The University of Adelaide, Adelaide, SA 5005, Australia.
E-mail: s.qiao@adelaide.edu.au; jingrun.ran@adelaide.edu.au
[b] A/Prof. J. Harmer
Centre for Advanced Imaging, University of Queensland, Brisbane, 4072, Australia
[c] Prof. H. Xu
Future Industries Institute, University of South Australia, SA 5095, Australia.
These authors contributed equally to this work.

Abstract: Photocatalytic performance can be optimized via introduction of reactive sites. However, it is practically difficult to engineer these on specific photocatalyst surfaces, because of limited understanding of atomic-level structure-activity. Here we report a facile sonication-assisted chemical reduction for specific facets regulation *via* oxygen deprivation on Bi-based photocatalysts. The modified Bi_2MoO_6 nanosheets exhibit 61.5 and 12.4 μmol g^{-1} for CO and CH_4 production respectively, ~3 times greater than for pristine catalyst, together with excellent stability/reproducibility of ~20 h. By combining advanced characterizations and simulation, we confirm the reaction mechanism on surface-regulated photocatalysts, namely, induced defects on highly-active surface accelerate charge separation/transfer and lower the energy barrier for surface CO_2 adsorption/activation/reduction. Promisingly, this method appears generalizable to a wider range of materials.

Introduction

Photocatalytic carbon dioxide (CO_2) reduction *via* semiconductor-based catalysts is used for carbon fixation and green-energy production.[1] However, the thermodynamically stable CO_2 molecule and passivated photocatalyst surfaces result in a significant barrier for CO_2

adsorption/activation.[2] Surface modification including, surface defects,[3] single atoms[4] and functional groups[5] can boost CO_2 molecule chemisorption and activation in photocatalytic CO_2 reduction. These surface engineering changes can improve the active site and its coordination configuration on photocatalysts, boosting activity/selectivity for CO_2 conversion.[6] This is because, 1) the surface photogenerated charges are redistributed following surface regulated change, with electrons accumulating around active sites to facilitate reductive reactions[6-7] and 2) surface active sites with optimized coordination structure boost reactant chemisorption/activation and reduce the energy barrier for CO_2 reduction.[8]

Despite these advantages with surface engineering, it remains practically difficult to control surface defect concentration/distribution at high temperature and/or strong reducing conditions, because a bulk defect can readily be generated that will act as the recombination centre to reduce charge separation efficiency.[9] Additionally, the surface vacancy can be healed by oxygen atoms released from CO_2 molecules following the dissociation of C−O bonds.[10] These might lose affinity to CO_2 molecules, and reduce activity/stability of the photocatalyst.[11] The introduction of metal atoms, especially noble metals, is expensive and results in instability of photocatalysts. Moreover, it is complex to graft functional groups onto photocatalysts because introduced organic moieties are usually decomposed with illumination, and generate carbon contamination in CO_2 conversion.[5b, 12] Therefore, an improved understanding is needed to better control processes for stable and well-defined surface chemistry and boosted photocatalytic performance.

Active surface regulation of crystals can be rationally used to promote performance.[8a, 13] Controlled change can be made *via* formation of defects under strongly-reductive chemicals (hydrazine, sodium borohydride and hydrogen gas)[14] and high temperature/pressure.[15] However, these require toxic/expensive chemicals and high energy input, leading to high emissions. Sonication is an attractive alternative because it can be used with usual reductive chemicals under ambient condition to generate cavitation, resulting in local-area high temperature/pressure.[16] Reactions therefore that are difficult at room temperature/atmosphere pressure can be got using reductive chemicals with sonication treatment.

Here we report active surface regulation of the (010) facets oxygen vacancies on a series of nanostructured photocatalysts, including Bi_2MoO_6, $BiVO_4$ and $BiWO_4$ *via* sonication-assisted chemical reduction. The regulated surface is determined from combined advanced characterizations including X-ray photoelectron spectroscopy (XPS), synchrotron-based X-ray absorption near-edge structure (XANES) and extended X-ray absorption fine structure

(EXAFS) spectroscopy. Such proposed system exhibited three times photocatalytic CO_2 reduction performance together with excellent stability and reproducibility, compared with unmodified photocatalyst. Boosted performance originates from the modified surface that promotes chemisorption/activation of CO_2 molecules, reduced energy barrier in pathway and charge separation. The pathway for CO_2 reduction and rate-limiting steps are studied. The topmost surface of photocatalysts is impacted, whilst the crystal structure in the bulk is unaffected. This increases the electron-hole dissociation/transfer and CO_2 adsorption/activation on the surface, and reduces electron-hole recombination in the bulk, as was evidenced by *in situ* spectroscopy, photoluminescence spectroscopy and theoretical computations.

Results and Discussion

Bi_2MoO_6 nanosheet (BMO) was synthesized *via* hydrothermal reaction. The as-synthesized BMO was cleaned (see details in Supporting Information) to remove organic surfactant. Surface-regulated BMO (BMO-R) *via* controlled sonication-assisted chemical reduction in which BMO was dispersed in 80 mM Na_2SO_3 aqueous solution and subjected to sonication (Figure 1a). The sonication-induced cavitation with local-area high temperature/pressure, to significantly decrease the energy barrier to reduce BMO by Na_2SO_3 and significantly promote reduction of BMO by Na_2SO_3. This generates oxygen vacancies (V_O) on BMO (010) facets as is demonstrated in the following reaction:

$$Bi_2MoO_6 + xSO_3^{2-} \rightarrow Bi_2MoO_{6-x} + xSO_4^{2-} + xV_O \quad (1)$$

Oxygen vacancies in BMO-R were confirmed *via* electron paramagnetic resonance (EPR). As is shown in Figure S1, the stronger signal assigned to oxygen vacancy was observed from BMO-R, not BMO. This implies that the metal ions are slightly reduced because of oxygen depletion. XPS and XANES were conducted to determine electronic states for BMO-R. In Figure S2, the two peaks at 164.4 and 159.1 eV in XPS spectra are attributed to Bi 4f peaks of BMO. The two peaks at 235.5 and 232.4 eV are attributed to Mo 3d peaks of BMO.[17] Both Mo 3d and Bi 4f peaks for BMO-R exhibit a ~0.2 eV shift toward lower binding energy, compared with BMO because of the oxygen loss. The depletion of oxygen is also confirmed from O 1s XPS spectra (Figure S3).The peak at 531.6 eV is attributed to the change of oxygen caused by oxygen deprivation and lattice distortion.[18] BMO-R exhibited a significantly greater proportion of this peak than BMO, indicating massive oxygen vacancies formed in BMO-R. The adsorbed OH species is observed from 533.4 eV on BMO-R (nothing for BMO), evidencing boosted H_2O adsorption/activation on BMO-R.[19] The better affinity toward water

on BMO-R is favourable for water oxidation and proton generation for CO_2 reduction. Additionally, the XANES spectra (Figure S4) for the Mo L-edge for BMO-R exhibit a 'slight' reduction in the chemical state for Mo, compared with that for BMO. Such change in the chemical state of Mo is consistent with the findings in the XPS, confirming the formation of oxygen vacancies on BMO-R following active surface-regulated sonication. In contrast, where only sonication treatment or Na_2SO_3 aqueous solution is used, the reduction of BMO and generation of surface oxygen vacancy do not meaningfully occur. This was confirmed by high-resolution XPS (Figure S5 and S6) for BMO with only Na_2SO_3 aqueous solution treatment (BMO-Na_2SO_3), or sonication (BMO-sonication).

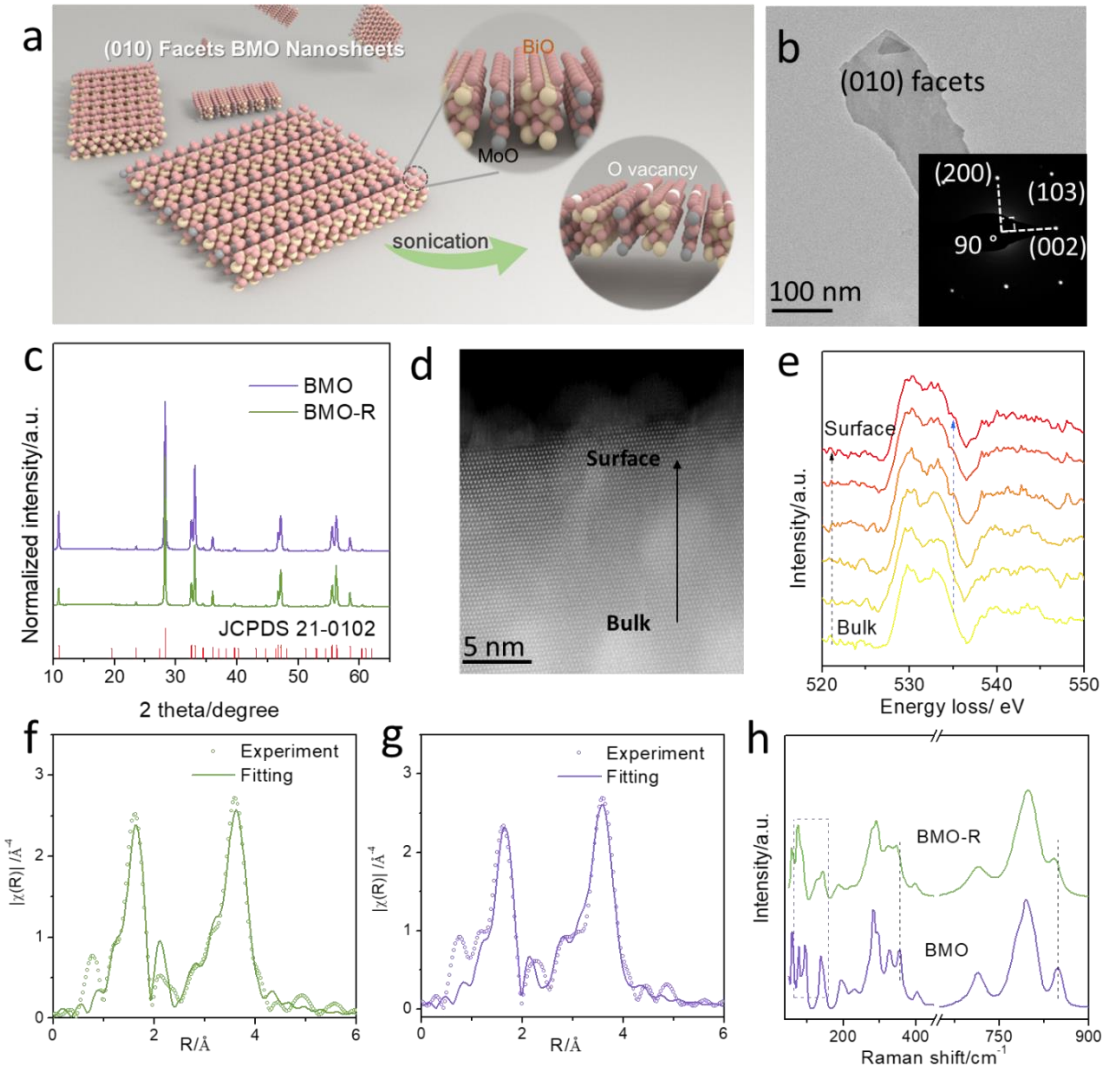

Figure 1. (a) Scheme for BMO nanosheet crystal structure. Bismuth, molybdenum, oxygen and oxygen vacancy are denoted as balls, respectively, yellow, grey, red and white; (b) TEM image and SAED, (c) XRD patterns for BMO and BMO-R; (d) STEM image and (e) series of O K-edge EELS spectra from bulk to surface of BMO-R; Bi L_3 edge XAS experiment and fitted data for (f) BMO-R and (g) BMO; (h) Raman spectra for BMO and BMO-R.

The existence of abundant oxygen vacancies on BMO-R surface induces relaxation and rearrangement of surface atoms to form a structure different to the bulk. Further, advanced characterizations, including atomic resolution high-angle annular dark field scanning transmission electron microscopy (HAADF-STEM), were employed to assess the surface chemical structure of BMO-R. As is shown in Figure 1b and Figure S7, these two samples exhibit similar, sheet-like shapes. The as-synthesized BMO nanosheets exhibited a mean thickness 10.9 nm (Figure S8). Following sonication-assisted chemical reduction, BMO-R exhibited reduced dimension with mean thickness 10.7 nm (Figure S9). These findings evidence that sonication did not significantly affect morphology of BMO. The crystal structure of BMO and BMO-R was determined *via* X-ray diffraction (XRD). As is seen in Figure 1c, all diffraction peaks for BMO and BMO-R are attributed to orthorhombic-structured Bi_2MoO_6 (JCPDS No. 21-0102), denoting that sonication-assisted chemical reduction did not meaningfully alter the crystal structure of BMO-R. The selected area electron diffraction (SAED) pattern for BMO-R is shown in Figure 1b inset. It can be indexed into diffraction spots along the [010] zone axis, confirming the single-crystal structure of BMO-R. Additionally, the atomic-resolution HAADF-STEM image of BMO-R (Figure S10) demonstrated two lattice spacing values of 0.28 nm, with an angle of 90°, that is attributed to, respectively, (200) and (002) facets. It is concluded therefore that the exposed surface is (010) facets of BMO. Energy dispersive X-ray (EDX) elemental mapping confirmed the elemental composition and distribution of the BMO-R (Figure S11).

To assess the top surface of BMO-R, combined atomic-resolution HAADF-STEM, local-area electron energy loss spectroscopy (EELS), synchrotron-based XANES/EXAFS and Raman spectroscopy were conducted. The atomic-resolution HAADF-STEM image of side-view of BMO-R (Figure 1d) evidences the regulated surface atoms on the topmost (010) facets. In contrast, the (010) facets for bulk BMO-R exhibit an ordered and aligned structure.

Additionally, EELS was collected to reveal the local oxidation state and coordination information. As the EELS area changed from the bulk to the surface of BMO (Figure 1e), the peak at ~ 534 eV for the O K edges shows an apparent increase, evidencing oxygen deprivation on the topmost (010) facets of BMO-R.[20] XANES and EXAFS spectra for BMO and BMO-R were determined to assess the chemical environment of BMO-R. As is presented in Figure S12, the Bi L_3-edge XANES spectra on the BMO-R and its corresponding derivative shift slightly to a lower direction compared with that for BMO, which confirms that the Bi oxidation state in BMO-R is reduced. The slight shift was affected by the transmission mode for data collection, for the information from bulk crystals. The well-coordinated lattice atoms reduce

sensitivity. Fourier transform (FT) EXAFS corroborated the valence change. Both samples exhibited the dominant peak at the same radial distance of 1.6 Å that is assigned to the Bi−O bond. However, the intensity of the peak for BMO-R weakens when compared with that for the pristine BMO, confirming the reduced Bi−O coordination number (Figure S13).[21] Additionally, quantitative least-squares EXAFS curve-fitting demonstrated that Bi−O and Bi−Bi are two backscattering paths involved in BMO and BMO-R. To get comparable results from two samples, the fitting analysis is based on the same backscattering paths. The coordination number for Bi−O decreased from 5.96 to 5.60 following sonication (Figures 1f, 1g, S14, and S15; Table S1). The reduced coordination number is attributed to the loss of lattice oxygen atoms. It is concluded these findings confirm the impact of active surface regulation. Raman spectroscopy was used to reveal the structure information and oxidation state of BMO-R. As is presented in Figure 1h, the stretching and deformation of the MoO_6 octahedral unit are seen in the transitions *ca.* 845 and 402 cm^{-1}, respectively. The redshift for these two bands in BMO-R evidences the distortion of the MoO_6 unit. The partial oxygen loss of Bi_2O_2 unit is demonstrated *via* the differences in Raman spectra range < 200 cm^{-1}.[22]

A similar surface regulation at (010) facets was apparent in the other Bi-based materials, $BiVO_4$ and Bi_2WO_6. This is because these have a similar, layered crystal structure and electronic transfer properties. Corresponding characterizations XRD, Raman and XPS were used to determine the partial reduction and surface transformation of these (Figures S16 and 17).

Compared with reported surface engineering, the as-synthesized BMO-R possesses a distinctive surface structure, distorted metal centre and coordination environment. The actively-regulated surface boosts activity in photocatalysis. Because CO_2 adsorption and activation on the surface is a prerequisite for photocatalytic CO_2 reduction, *in situ* diffuse reflectance infrared Fourier transform spectroscopy (DRIFTS) in dark was carried out on BMO-R, Figure 2a. Some intermediates are typical species for the products. The peaks *ca.* 1656 and 1607 cm^{-1} are attributed to $\cdot CO_2^-$, an important indicator for CH_4 generation.[23] The rising peaks at 1577, 1560, 1503 and 1307 cm^{-1} with increasing time are from the characteristic vibrations of monodentate carbonates (m-CO_3^{2-}). The formation of bidentate carbonate species (b-CO_3^{2-}) is evidenced by the peaks at 1540, 1376 and 1147 cm^{-1}. The adsorption of H_2O and CO_2 is inferred from HCO_3^{2-} (1437 and 1636 cm^{-1}) and H_2O vibrations (1619 cm^{-1}).[9b] The high concentration of protonation of carbonate species is significant as these are critical intermediates in CO production. Compared with the CO_2 adsorption spectrum for BMO-R, the detected intermediates are significantly less than on BMO (Figure 2b). The same peaks at 1650,

1637, 1617, 1576, 1558, 1542, 1437 and 1304 cm^{-1} are attributed to the intermediates, CO_2^-, HCO_3^{2-}, H_2O, m-CO_3^{2-} and b-CO_3^{2-}.[6, 14b] However, BMO mainly produces m-CO_3^{2-} rather than b-CO_3^{2-} which are the robust sites required for CO_2 adsorption. Therefore BMO-R exhibits significantly better CO_2 adsorption/activation ability in CO_2 photoreduction than BMO.

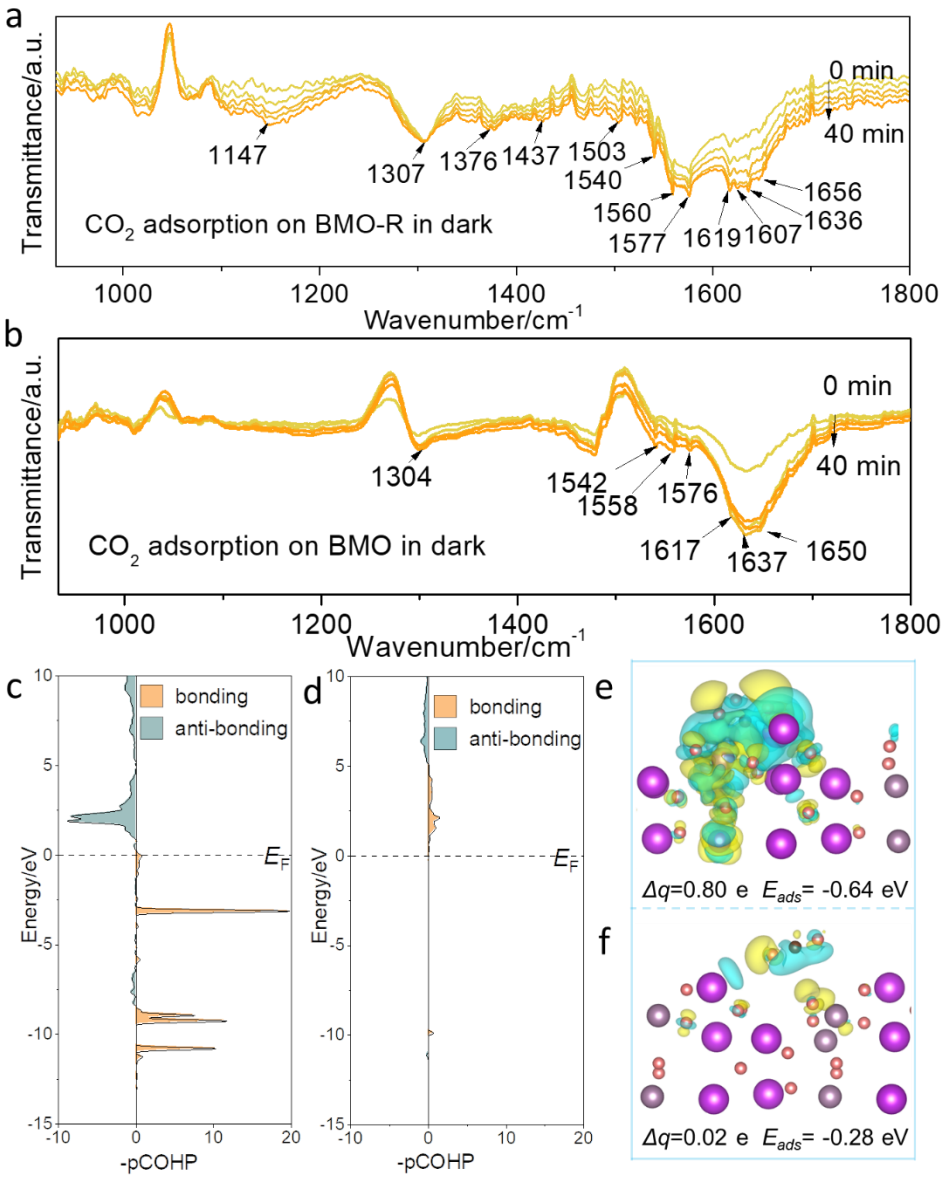

Figure 2. *In situ* DRIFTS test for CO_2 and H_2O interaction with (a) BMO-R and (b) BMO in dark; Projected crystal orbital Hamilton population (pCOHP) between carbon atom in CO_2 and Mo active site on (c) BMO-R and (d) BMO; Charge difference distributions for (e) BMO-R and (f) BMO following CO_2 adsorption (charge depletion is in yellow and accumulation in blue, positive values for Δq indicate electron accumulation on CO_2 E_{ads} is CO_2 adsorption energy on surface). Isosurfaces are 0.003 e $Å^{-3}$. Oxygen, carbon, bismuth and molybdenum atoms are denoted as balls, respectively red, brown, purple and grey.

Theoretical computations were used to determine the interaction between CO_2 and surface of BMO-R. It is seen in Figure 2c, the majority of valence band for BMO-R (below Fermi level, E_F) are on the bonding orbital, whilst the antibonding orbital population mainly distributes in the conduction band, above E_F. However, almost all the bonding orbital population (Figure 2d) for BMO distributes above E_F, which confirms the weak interaction between CO_2 and Mo active site. The integrated crystal orbital Hamilton population (ICOHP) for CO_2 adsorbed on BMO surface is –0.05, whilst that for BMO-R is –3.41. To determine CO_2 adsorption behaviour on different surfaces, the adsorption energy, charge difference and Bader charge analysis based on DFT computation for BMO and BMO-R were carried out (Figures 2e and f). The Mo atom around the distortion centre caused by the oxygen deprivation was assessed. The CO_2 adsorption energies on the two models exhibit a significant difference with, respectively, –0.64 and –0.28 eV on BMO-R and BMO. On the surface of BMO-R, the C−O−C bond was bent (134.5°) and elongated (1.27 and 1.25 Å) because of the electron (0.8 e) transfer from the surface to CO_2 molecule on the BMO-R (Figure S18). Additionally, the lower adsorption position on BMO-R evidences that the CO_2 molecule is more readily captured by the surface. For the BMO, the C−O−C bond was not bent significantly (178.6°) and elongated (1.17 and 1.17 Å). The Bader charge analysis confirmed that few electrons (0.02 e) transfer from surface to CO_2 molecule. It is concluded that these experimental and computational findings demonstrate the stronger adsorption of CO_2 on BMO-R than BMO.

As is shown in Figure 3a, BMO exhibited limited CO_2 photoreduction with CO and CH_4 production of, respectively, 17.7 and 3.3 μmol g^{-1}. In comparison, BMO-R exhibited CO and CH_4 generation of, respectively, 60.7 and 12 μmol g^{-1}, three times greater than for BMO. The performance for BVO-R and BWO-R were boosted following active surface regulation. The slight enhancement for BVO-R is due to the poor reduction capability of photogenerated electrons. Samples were cleaned following synthesis to eliminate carbon impurities[12b]. Compared with reported findings, BMO-R, BWO-R and BVO-R show excellent CO_2 photoreduction performance under similar conditions (Table S2).

Additionally, blank experiments were conducted under the same conditions and purged with ultra-high-purity Ar and not CO_2. When the Ar was purged instead of CO_2, negligible production was detected (Figure S19). Moreover, all the other blank experiments resulted in no products. This evidenced that CO and CH_4 were generated from photocatalytic CO_2 reduction. Stability was assessed with a three-time recycle test of 7 h per cycle. No apparent deterioration in performance was found (Figure 3b). The increased stability likely comes from

hindering healing oxygen vacancy by CO_2 and H_2O because of the distorted surface crystal and steric-hindrance. XPS, TEM, XRD and SAED data (Figures S20 and 21) for BMO-R following performance testing confirmed that the crystal structure and defects were stable, and therefore that the surface was not altered during CO_2 photoreduction.

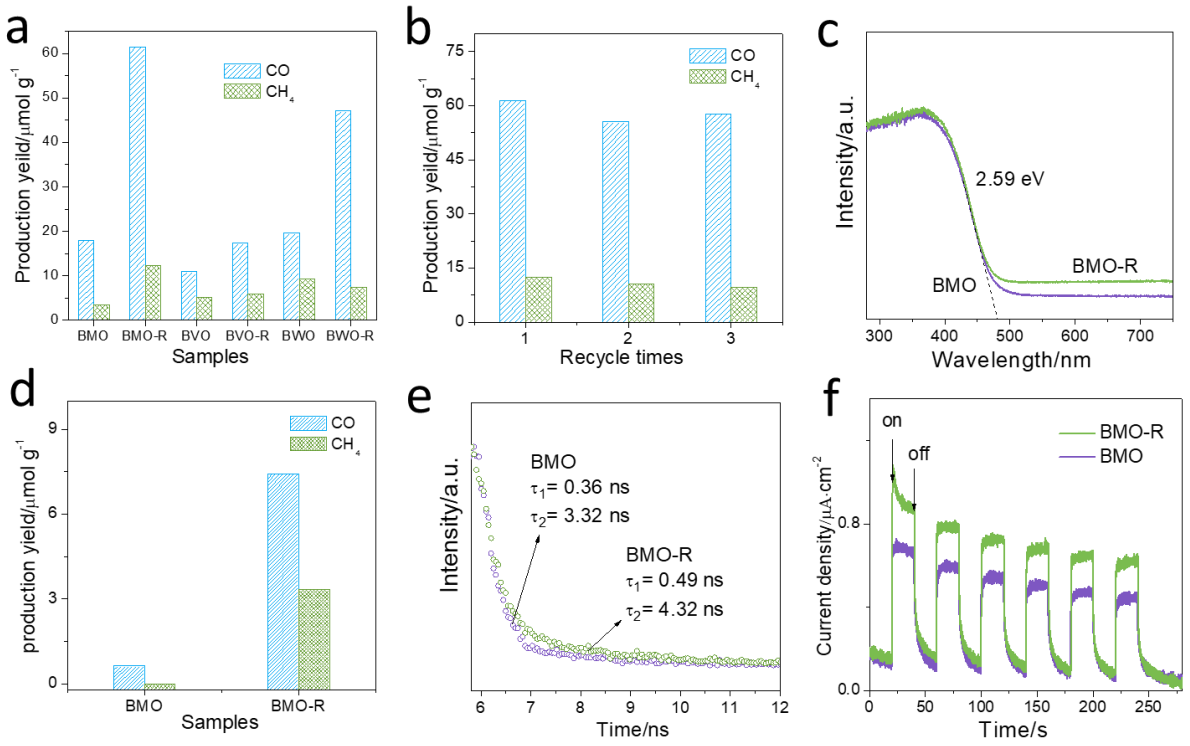

Figure 3. (a) Photocatalytic CO_2 reduction for BMO, BMO-R, BVO, BVO-R, BWO and BWO-R under Xenon lamp illumination; (b) Repeated photocatalytic CO_2 reduction test for BMO-R; (c) UV-vis diffuse reflectance spectroscopy and band gap for BMO and BMO-R; (d) CO_2 photoreduction for BMO and BMO-R under 540 nm LED illumination for 7 h; (e) TSPL spectra for BMO and BMO-R; (f) Transient photocurrent density for BMO and BMO-R in 0.5 M Na_2SO_4 aqueous solution.

To determine the origin of boosted activity and reaction mechanism for photocatalytic CO_2 reduction, UV-vis diffuse reflectance spectroscopy was obtained. As is shown in Figure 3c, increased absorption in the range 480 to 700 nm is attributed to oxygen deprivation on BMO-R (010) facets. However, compared with Figure S19, the performance enhancement is negligible (Figure 3d). However, no shift for the adsorption edge for BMO-R (479 nm) evidences that its bandgap (2.59 eV) is not changed. The positions of the valence band maximum (VBM) for BMO-R and BMO were detected *via* XPS valence spectra, respectively, as 2.06 and 2.56 eV, (Figure S22). From the VBM and bandgap, the conduction band minimum

(CBM) for BMO-R and BMO is estimated to be –0.53 and –0.03 eV. The CBM for BMO-R exhibits upshift, which results in a greater reduction ability of photogenerated electrons and therefore facilitates CO_2 photoreduction.

To determine photogenerated charge separation/transfer, steady-state photoluminescence (PL) spectroscopy, transient-state photoluminescence (TSPL) spectroscopy, transient photocurrent (TPC) density and electrochemical impedance spectroscopy (EIS) were obtained. The steady-state PL intensity for BMO-R is significantly less than that for BMO (Figure S23), evidencing that charge-carrier recombination is suppressed. Following fitting of the TSPL curves for Figure 3e, lifetimes of charge carriers of $\tau_1 = 0.49$ ns and $\tau_2 = 4.32$ ns, for BMO-R were greater in comparison with those for BMO of, respectively, 0.36 ns and 3.32 ns. BMO-R exhibited a greater TPC density than BMO (Figure 3f). Because TPC density is significantly affected by surface reaction efficiency and electron transfer resistance, TPC intensity is not correlated well the performance tests. This finding confirms the more efficient dissociation of light-induced excitons. The EIS spectra (Figure S24) exhibited a smaller-semicircle radius for the Nyquist plot, together with a decreased charge-transfer resistance of $R_{ct} = 3500\ \Omega$ for BMO-R in contrast with that for BMO of 6750 Ω, confirming a greater charge carrier transfer rate in BMO-R. The difference between the two evidences that the charge recombination was suppressed in BMO-R because MoO_{6-x} sites act as traps for photogenerated electrons, therefore facilitating charge separation.[24]

To determine the surface species on the surface of BMO and BMO-R under illumination, *in situ* DRIFTS were obtained (Figure 4a). The indicative intermediates in CO_2-to-CO conversion *COOH were detected at 1634 cm^{-1}.[25] Additionally, the intensity of carbonate species (1577, 1558 and 1304 cm^{-1}) was decreased with prolonged illumination time, confirming that the carbonate species is converted to *COOH. Additionally, there were new bands at 1067 cm^{-1} that is attributed to *OCH, and two new bands at 1110 and 1011 cm^{-1} attributed to *OCH_3.[9b, 24a] The intensity of these new bands increased highly significantly following illumination, confirming that the corresponding intermediate is accumulated on the surface of BMO-R. These species are important intermediates to generate CH_4.[26] However, a different spectrum was obtained for BMO. In Figure S25, the intensity of corresponding carbonate species was much less under illumination. *COOH was detected which confirms CO_2-to-CO.[27] However, there were no bands from *OCH or *OCH_3. Therefore, it is concluded that the reaction pathways on different samples are:

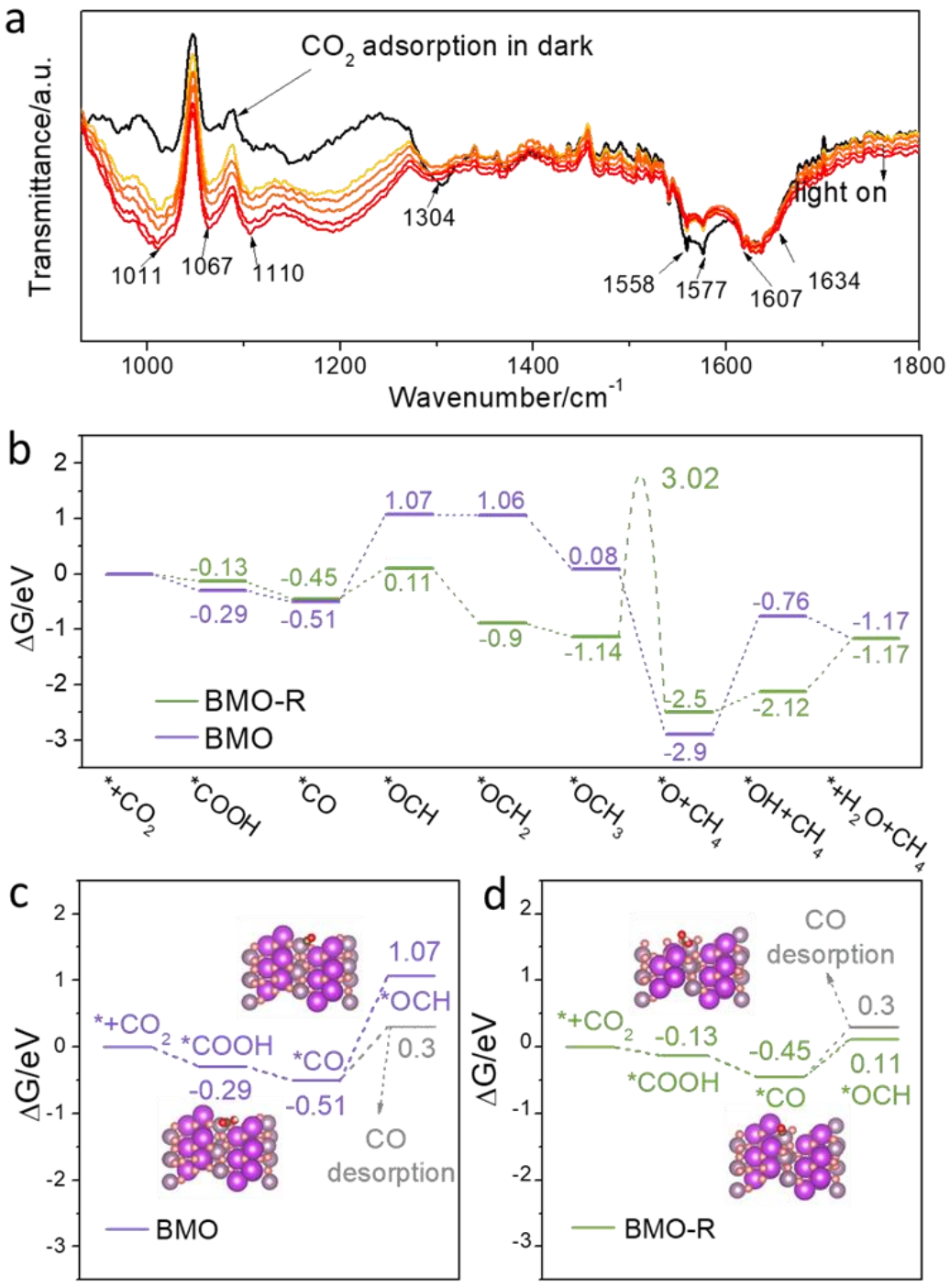

Figure 4. (a) *In situ* DRIFTS test for CO_2 and H_2O interaction with BMO-R under constant Xenon lamp illumination; (b) Computed Gibbs free energy for main reactions in photocatalytic CO_2 reduction to CH_4 for BMO and BMO-R; Key steps of CO_2 photoreduction to CH_4 for (c) BMO and (d) BMO-R, in which BMO-R convert the endoergic step to an exoergic reaction. Oxygen of absorbed intermediates, oxygen of BMO/BMO-R, carbon, bismuth and molybdenum atoms are denoted as balls, respectively red, pink, brown, purple and grey.

$*CO_2 \rightarrow CO_2^{-}/HCO_3^{2-}/CO_3^{2-} \rightarrow *COOH \rightarrow *CO$ for BMO

$*CO_2 \rightarrow CO_2^{-}/HCO_3^{2-}/CO_3^{2-} \rightarrow *COOH \rightarrow *CO \rightarrow *OCH \rightarrow *OCH_2 \rightarrow *OCH_3$ for BMO-R

The proposed CO_2 reduction pathway on both samples was assessed *via* computation of corresponding free energy changes (ΔG) for each reaction step, Figure 4b, Figures S26 and S27. The overall energy barrier for BMO-R is lower than that for BMO, evidencing that the surface condition of BMO-R significantly facilitates CO_2 photoreduction. The active site on the regulated surface was distorted, which is in favour of formation of some intermediates thereby reducing the energy barrier for these steps. Because the desorption of CO on BMO is more favourable compared with hydrogenation step, CO is therefore the main product of BMO (Figure 4c). On the contrary, BMO-R is prone to hydrogenation of *CO (Figure 4d), whereas the $*OCH_3$ protonation kinetics barrier is significantly high at 3.02 eV (Figure 4b and S28). The computed adsorption energy for $*OCH_3$ on BMO-R is –1.30 eV. It is speculated that the adsorptionconfiguration of $*OCH_3$ is highly stable. Additionally, the high kinetics barrier prevents further transformation, resulting in the significant accumulation of $*OCH_3$ on the surface of BMO-R, and therefore a strong band attributed to $*OCH_3$ species from the *in situ* DRIFTS of BMO-R.

Conclusion

A new, active surface-regulated Bi_2MoO_6 nanosheet exhibited high-performance production of, respectively, 61.5 and 12.4 μmol g^{-1} CO and CH_4, together with a stability of > 20 h of reaction in photocatalytic CO_2 reduction. The surface was regulated *via* chemical-assisted sonication within the nanosheet, and the structure and coordination environment of the surface were confirmed *via* HAADF-STEM and EXAFS at the atomic level. Distorted MoO_{6-x} is the highly reactive site for light absorption and charge separation. Additionally, this active site significantly promotes CO_2 activation during pre-adsorption and photoreduction as confirmed *via* theoretical computation and *in situ* spectroscopy. Importantly, hydrogenation of $*OCH_3$ for CH_4 formation was confirmed as the rate-limiting step. It is concluded the method is generalizable to a wider range of materials to permit regulated surface chemistry for boosted photocatalytic performance. Findings will be of benefit in development of active surface engineering that is applicable to additional photocatalytic systems, including, hydrogen and oxygen evolution, and nitrogen reduction.

Acknowledgments

This work was supported financially by the Australian Research Council (ARC) through the Discovery Project Program (DP220102596, FL170100154 and DE200100629). The authors thank Dr. Huimin Yu, University of South Australia, for XPS testing and Dr. Ashley Slattery, Adelaide Microscopy, The University of Adelaide for technical assistance. This research was undertaken on the X-ray absorption spectroscopy and soft X-ray spectroscopy beamlines at the Australian Synchrotron, part of ANSTO. DFT computations for this work were performed using supercomputing resources provided by the Phoenix HPC service at The University of Adelaide.

Conflict of Interest

The authors declare no conflict of interest.

Data Availability Statement

The data that support the findings of this study are available from the corresponding author upon reasonable request.

Keywords: Bi-based photocatalysts, specific surface regulation, photocatalytic CO_2 reduction, CO_2 chemisorption and activation, *in situ* spectroscopy

[1] a) H. Yu, F. Chen, X. Li, H. Huang, Q. Zhang, S. Su, K. Wang, E. Mao, B. Mei, G. Mul, T. Ma, Y. Zhang, *Nat. Commum.* **2021**, *12*, 4594; b) Y. Feng, C. Wang, P. Cui, C. Li, B. Zhang, L. Gan, S. Zhang, X. Zhang, X. Zhou, Z. Sun, K. Wang, Y. Duan, H. Li, K. Zhou, H. Huang, A. Li, C. Zhuang, L. Wang, Z. Zhang, X. Han, *Adv. Mater.* **2022**, *34*, 2109074.

[2] a) L. Chen, C. Tang, K. Davey, Y. Zheng, Y. Jiao, S.-Z. Qiao, *Chem. Sci.* **2021**, *12*, 8079-8087; b) W. A. Thompson, E. S. Fernandez, M. M. Maroto-Valer, *ACS Sustain. Chem. Eng.* **2020**, *8*, 4677-4692; c) X. Chang, T. Wang, J. Gong, *Energy Environ. Sci.* **2016**, *9*, 2177-2196.

[3] a) Y. Zhang, D. Yao, B. Xia, H. Xu, Y. Tang, K. Davey, J. Ran, S.-Z. Qiao, *Small Sci.* **2021**, *1*, 2000052; b) Y. Zhang, B. Xia, J. Ran, K. Davey, S. Z. Qiao, *Adv. Energy Mater.* **2020**, *10*, 1903879; c) Y. Zhang, X. Wang, P. Dong, Z. Huang, X. Nie, X. Zhang, *RSC Adv.* **2018**, *8*, 15991-15998; d) J. Di, C. Chen, C. Zhu, R. Long, H. Chen, X. Cao, J. Xiong, Y. Weng, L. Song, S. Li, H. Li, Y. Xiong, Z. Liu, *Adv. Energy Mater.* **2021**, *11*, 2102389.

[4] a) W. Bi, Y. Hu, H. Jiang, L. Zhang, C. Li, *Adv. Funct. Mater.* **2021**, *31*, 2010780; b) H. Zhang, Y. Wang, S. Zuo, W. Zhou, J. Zhang, X. W. D. Lou, *J. Am. Chem. Soc.* **2021**, *143*, 2173-2177; c) B. Xia, Y. Zhang, J. Ran, M. Jaroniec, S.-Z. Qiao, *ACS Cent. Sci.* **2021**, *7*,

39-54; d) J. Di, C. Chen, S.-Z. Yang, S. Chen, M. Duan, J. Xiong, C. Zhu, R. Long, W. Hao, Z. Chi, H. Chen, Y.-X. Weng, J. Xia, L. Song, S. Li, H. Li, Z. Liu, *Nat. Commun.* **2019**, *10*, 2840; e) L. Cheng, X. Yue, L. Wang, D. Zhang, P. Zhang, J. Fan, Q. Xiang, *Adv. Mater.* **2021**, *33*, 2105135.

[5] a) L. Pei, Y. Yuan, W. Bai, T. Li, H. Zhu, Z. Ma, J. Zhong, S. Yan, Z. Zou, *ACS Catal.* **2020**, *10*, 15083-15091; b) J.-C. Hu, M.-X. Gui, W. Xia, J. Wu, Y.-N. Zhou, N. Feng, J. Xiao, H. Liu, C.-H. Tung, L.-Z. Wu, F. Wang, *J. Mater. Chem. A* **2019**, *7*, 10475-10482; c) X. Zhu, G. Zhou, Z. Wang, K. Zhong, P. Ding, Y. Song, J. Yuan, Y. She, H. Li, H. Xu, *J. CO_2 Util.* **2021**, *54*, 101745.

[6] Y. Cao, L. Guo, M. Dan, D. E. Doronkin, C. Han, Z. Rao, Y. Liu, J. Meng, Z. Huang, K. Zheng, P. Chen, F. Dong, Y. Zhou, *Nat. Commun.* **2021**, *12*, 1675.

[7] a) W. Wang, C. Y. Deng, S. J. Xie, Y. F. Li, W. Y. Zhang, H. Sheng, C. C. Chen, J. C. Zhao, *J. Am. Chem. Soc.* **2021**, *143*, 2984-2993; b) S. Zhu, X. Li, X. Jiao, W. Shao, L. Li, X. Zu, J. Hu, J. Zhu, W. Yan, C. Wang, Y. Sun, Y. Xie, *Nano Lett.* **2021**, *21*, 2324-2331; c) S. Sun, M. Watanabe, J. Wu, Q. An, T. Ishihara, *J. Am. Chem. Soc.* **2018**, *140*, 6474-6482.

[8] a) D. Yao, C. Tang, L. Li, B. Xia, A. Vasileff, H. Jin, Y. Zhang, S.-Z. Qiao, *Adv. Energy Mater.* **2020**, *10*, 2001289; b) D. Yao, C. Tang, A. Vasileff, X. Zhi, Y. Jiao, S.-Z. Qiao, *Angew. Chem. Int. Ed.* **2021**, *60*, 18178-18184.

[9] a) Y. Zhang, X. Wang, P. Dong, Z. Huang, X. Nie, X. Zhang, *Green Chem.* **2018**, *20*, 2084-2090; b) X. Li, Y. Sun, J. Xu, Y. Shao, J. Wu, X. Xu, Y. Pan, H. Ju, J. Zhu, Y. Xie, *Nat. Energy* **2019**, *4*, 690-699.

[10] a) S. Luo, X. Li, M. Wang, X. Zhang, W. Gao, S. Su, G. Liu, M. Luo, *J. Mater. Chem. A* **2020**, *8*, 5647-5654; b) J. Lee, D. C. Sorescu, X. Deng, *J. Am. Chem. Soc.* **2011**, *133*, 10066-10069.

[11] a) B. Wang, X. Wang, L. Lu, C. Zhou, Z. Xin, J. Wang, X.-k. Ke, G. Sheng, S. Yan, Z. Zou, *ACS Catal.* **2018**, *8*, 516-525; b) X. Zu, Y. Zhao, X. Li, R. Chen, W. Shao, Z. Wang, J. Hu, J. Zhu, Y. Pan, Y. Sun, Y. Xie, *Angew. Chem. Int. Ed.* **2021**, *60*, 13840-13846.

[12] a) K. M. Cho, K. H. Kim, K. Park, C. Kim, S. Kim, A. Al-Saggaf, I. Gereige, H.-T. Jung, *ACS Catal.* **2017**, *7*, 7064-7069; b) Y. Zhang, D. Yao, B. Xia, M. Jaroniec, J. Ran, S.-Z. Qiao, *ACS Energy Lett.* **2022**, 7, 1611-1617.

[13] L. Zhang, J. Zhou, J. Li, G. Liu, X. Lin, B. Mao, R. Liu, S. Zhang, J.-Q. Wang, *J. Phys. Chem. C* **2014**, *118*, 13726-13732.

[14] a) X. Zhu, Z. Wang, K. Zhong, Q. Li, P. Ding, Z. Feng, J. Yang, Y. Du, Y. Song, Y. Hua, J. Yuan, Y. She, H. Li, H. Xu, *Chem. Eng. J.* **2022**, *429*, 132204; b) T. Di, J. Zhang, B. Cheng, J. Yu, J. Xu, *Sci. China Chem.* **2018**, *61*, 344-350.

[15] a) Y. Huang, Y. Yu, Y. Yu, B. Zhang, *Sol. RRL* **2020**, *4*, 2000037; b) C. Meng, M. Lin, X. Sun, X. Chen, X. Chen, X. Du, Y. Zhou, *Chem. Commun.* **2019**, *55*, 2904-2907.

[16] R. Feng, Y. Zhao, C. Zhu, T. J. Mason, *Ultrason. Sonochem.* **2002**, *9*, 231-236.

[17] Y. Huang, K. Li, S. Li, Y. Lin, H. Liu, Y. Tong, *ChemistrySelect* **2018**, *3*, 7423-7428.

[18] P. V. Shinde, N. M. Shinde, J. M. Yun, R. S. Mane, K. H. Kim, *ACS Omega* **2019**, *4*, 11093-11102.

[19] H. Liu, C. Du, H. Bai, Y. Su, D. Wei, Y. Wang, G. Liu, L. Yang, *J. Mater. Sci.* **2018**, *53*, 10743-10757.

[20] Y. Li, X. Chen, M. Zhang, Y. Zhu, W. Ren, Z. Mei, M. Gu, F. Pan, *Catal. Sci. Technol.* **2019**, *9*, 803-810.

[21] H. Jin, L. Li, X. Liu, C. Tang, W. Xu, S. Chen, L. Song, Y. Zheng, S.-Z. Qiao, *Adv. Mater.* **2019**, *31*, 1902709.

[22] a) C. Huang, S. Ma, Y. Zong, J. Gu, J. Xue, M. Wang, *Photochem. Photobiol. Sci.* **2020**, *19*, 1697-1706; b) J. H. Kim, A. Ma, H. Jung, H. Y. Kim, H. R. Choe, Y. H. Kim, K. M. Nam, *ACS Omega* **2019**, *4*, 17359-17365.

[23] J. Sheng, Y. He, M. Huang, C. Yuan, S. Wang, F. Dong, *ACS Catal.* **2022**, *12*, 2915-2926.

[24] a) X. Cao, Z. Chen, R. Lin, W.-C. Cheong, S. Liu, J. Zhang, Q. Peng, C. Chen, T. Han, X. Tong, Y. Wang, R. Shen, W. Zhu, D. Wang, Y. Li, *Nat. Catal.* **2018**, 1, 704-710; b) X. Yang, X. Xu, J. Wang, T. Chen, S. Wang, X. Ding, H. Chen, *Sol. RRL* **2021**, *5*, 2000442.

[25] G. Zhou, J. Yang, X. Zhu, Q. Li, Q. Yu, W. El-alami, C. Wang, Y. She, J. Qian, H. Xu, H. Li, *J. Energy Chem.* **2020**, *49*, 89-95.

[26] R. Das, K. Das, B. Ray, C. P. Vinod, S. C. Peter, *Energy Environ. Sci.* **2022**, *15*, 1967-1976.

[27] L. Chen, C. Tang, Y. Jiao, S.-Z. Qiao, *ChemSusChem* **2021**, *14*, 671-678.

Supporting Information

69451 Weinheim, Germany

Facet-specific Active Surface Regulation of Bi_xMO_y (M=Mo, V, W) Nanosheets for Boosted Photocatalytic CO_2 reduction

Yanzhao Zhang [+], Xing Zhi [+], Jeffrey R. Harmer, Haolan Xu, Kenneth Davey, Jingrun Ran * and Shi-Zhang Qiao *

Experimental Procedures

Chemicals and materials

Bismuth nitrate pentahydrate ($Bi(NO_3)_3 \cdot 5H_2O$, Sigma Aldrich), hexadecyltrimethylammonium bromide ($CH_3(CH_2)_{15}N(Br)(CH_3)_3$, CTAB, Sigma Aldrich), sodium molybdat dihydrate ($Na_2MoO_4 \cdot 2H_2O$, Sigma Aldrich), sodium tungstate dihydrate ($Na_2WO_4 \cdot 2H_2O$, Sigma Aldrich), sodium dodecyl benzene sulfonate ($C_{18}H_{29}NaO_3S$, SDBS, Sigma Aldrich), ammonium vanadate (NH_4VO_3, Sigma Aldrich), nitric acid (HNO_3, 70 % Sigma Aldrich), sodium hydroxide (NaOH, Sigma Aldrich), ethanol (C_2H_5OH, ChemSupply), sodium sulfite (Na_2SO_3, Sigma Aldrich). All of the chemicals were Analytical reagents (AR) and used directly without any further purification. Ultra-pure water used throughout all experiments was purified through an Adelab Millipore system. Ultra-high purity Ar (99.999 %) was purchased from BOC Gas, Australia.

Synthesis of Bi_2MoO_6 nanosheets

Bi_2MoO_6 nanosheets were prepared under hydrothermal conditions. 1 mmol of $Na_2MoO_4 \cdot 2H_2O$ and 0.3 g of CTAB were dissolved in 80 mL water and stirred for 30 min. 2 mmol of $Bi(NO_3)_3 \cdot 5H_2O$ was added to the solution and stirred for a further 30 min to obtain a uniform solution. The solution was transferred to a 100 mL Teflon-lined autoclave. The autoclave was transferred into an oven and maintained at 180 ℃ for 16 h. Products were collected and washed with water and ethanol three times. Following drying in a freeze-dryer, the sample was cleaned with plasma cleaner to remove carbon impurities on the surface. Plasma cleaning is detailed below. The resulting samples were labelled as BMO.

Synthesis of $BiVO_4$ nanosheets

$BiVO_4$ nanosheets were prepared by hydrothermal reactions. 2 mmol of $Bi(NO_3)_3 \cdot 5H_2O$ and 1.5 mmol SDBS were dissolved in 20 mL of 4 M HNO_3 solution to form Solution A. 2 mmol of NH_4VO_3 was dissolved in 20 mL of 2 M NaOH solution to form Solution B. B solution was dropped into Solution A and the solution stirred for 30 min. The solution was adjusted to pH ~ 2.5 by 2M NaOH solution and stirred for a further 30 min. It was transferred to 100 mL autoclave and heated under 160 ℃ for 2 h. Products were collected and washed with water and ethanol three times. Following drying in the freeze-dryer, the sample was cleaned with plasma cleaner to remove carbon impurities on the surface. Resulting samples were labelled as BVO.

Synthesis of Bi_2WO_6 nanosheets

Bi_2WO_6 nanosheets were prepared under hydrothermal conditions. 50 mg of CTAB and 1 mmol of $Na_2WO_4 \cdot 2H_2O$ were dissolved in 70 mL water and sonicated for 30 min. 2 mmol of $Bi(NO_3)_3 \cdot 5H_2O$ was added to the solution and sonicated for 30 min to obtain a uniform solution, which was transferred to a 100 mL Teflon-lined autoclave. The autoclave was maintained at 120 ℃ for 24 h. Products were washed with water or ethanol. The products were collected and washed with water and ethanol three times. Following drying in the freeze-dryer, the sample was cleaned with plasma cleaner to remove carbon impurities on the surface. Resulting samples were labelled as BWO.

Plasma cleaning

Following drying of the powders in the freeze-dryer, they were put in the plasma cleaner, vacuumed to 150 mTorr and purged with oxygen (BOC). This was repeated three times until the cleaner was stable at 450 mTorr. The plasma was conducted for 5 min. The powders were washed with water and dried in the freeze-dryer.

Sonication

Sonication was conducted under an ultra-sonic probe. Fifty (50) mg as-prepared samples were dispersed in 100 mL Na_2SO_3 solution (80 mM) for 2 h. The experiment is conducted at 0 ℃ in an ice-water mixture cooling system. The ultrasonic probe was operated for 2 s and stopped for 4 s. The samples were washed with water and dried in the freeze-dryer. Samples following sonication were labelled, respectively, BMO-R, BVO-R and BWO-R.

Material characterizations

X-ray diffraction, XRD data were determined on a powder X-ray diffractometer (Miniflex, Rigaku) using Cu Kα radiation. Raman spectroscopy data were determined using a confocal Raman microscope (Horiba LabRAM HR Evolution) with a 10X objective and a 532 nm laser. Morphology determination was conducted on a Tecnai G2 transmission electron microscopy (TEM). HRTEM, EDX mapping and EELS spectra were obtained on Transmission electron microscopy under STEM mode (FEI Titan Thermis, 200 kV). XPS measurement was on a VGESCALAB 210 XPS spectrometer with Mg Kα source. Binding energies were referenced to the C 1s peak at 284.6 eV. UV visible diffuse reflectance spectra were obtained on a UV-Vis spectrophotometer (UV2600, Shimadzu, Japan). An RF-5301PC spectrofluorophotometer (Shimadzu, Japan) was used to determine steady-state photoluminescence (PL) spectra at room temperature (25 ℃). Transient-state PL decay curves were determined on an FLS1000 fluorescence lifetime spectrophotometer (Edinburgh Instruments, UK). Continuous-wave (CW) X-band (*ca*. 9.385 GHz) electron paramagnetic resonance (EPR) spectra were recorded

on a Bruker Elexsys E500 spectrometer equipped with an ElexSys Super High Sensitivity Probehead and He cooling using a cryogen-free cryostat (Bruker waveguide Cryogen-free system with recirculator, WVGD SYS 5K F70H wRCRC 2). The magnetic field was calibrated with a Gauss meter and measurements were carried out using a modulation amplitude of 0.8 mT, a modulation frequency of 100 kHz and a microwave power of 0.5 mW (26 dB of 200 mW, non-saturating condition). Temperature was set to 20 K. Powder samples for EPR were weighted to 0.1 mg and packed in OD 4mm quartz EPR tubes. The height of these samples ranged from 5.9 to 13 mm because of available sample quantity. EPR signal intensity was calibrated by reference to frozen solutions of copper triflate in methanol and included data to cover the variable height of the samples. X-ray absorption was obtained from the XAS beamline of Australian Synchrotron (ANSTO, Melbourne). Data collection was conducted under the transmission mode. XAS raw data were background-substracted, normalized and Fourier-transformed with Athena.

Photocatalytic CO_2 reduction

Photocatalytic performance tests were conducted in a 287 mL reactor sealed with silicone-rubber septa at ambient conditions. A 300 W Xenon lamp was used as the light-source. No light filter was used for BMO, BMO-R, BWO and BWO-R whilst 420 nm filter was used for BVO and BVO-R. In a typical test, 20 mg of photocatalyst was dispersed in 5 mL water and sonicated for 5 min then loaded on a glass-fibre filter to reduced the stack effect and dried under infrared light. Prior to illumination, the reactor was purged with laser-grade CO_2 for 1 h. Product was collected from the reactor h^{-1} *via* syringe and analysed *via* gas chromatograph (GC, 7890B, Agilent). GC was equipped with plot-Q and a 5 Å sieve column (Agilent) in series, TCD and methanizer/FID detectors and UHP Ar (BOC) as carrier-gas. Each test was conducted in triplicate. Blank experiments were conducted under conditions, namely, photocatalysts in ultra-high purity Ar under illumination, photocatalysts in laser-grade CO_2 without illumination, and laser-grade CO_2 under illumination without photocatalysts. Trace/no products were apparent. Importantly, these blank experiments confirmed there were no carbon impurities in the experimental system.

Electrochemical and photoelectrochemical testing

Testing was conducted in a standard, three-electrode system with the as-prepared samples as the working electrode, a Pt wire as the counter electrode, and Ag/AgCl (saturated KCl) as reference electrode. In the identical three-electrode system, EIS measurement was carried out in the range 1 to 2×10^5 Hz with an AC amplitude of 20 mV. 0.5 M Na_2SO_4 was used as

electrolyte. Polarization curves were obtained in the three-electrode system. The bias sweep range was –1.5 to –0.8 V *vs.* Ag/AgCl with a step size of 5 mV. 0.5 M Na_2SO_4 was the electrolyte. In the same three-electrode system the TPC response measurement was carried out. A 300 W Xenon light was used as the light source. 0.5 M Na_2SO_4 aqueous solution was the electrolyte. Working electrodes were prepared as follows: 5 mg sample, 960 μL of mixed solvent ($V_{isoproponal}$: V_{water} = 1: 2) with the addition of 40 μL of 5% Nafion. The dispersion was vigorously sonicated for 6 h to form a homogenous ink. A doctor-blade method was used to coat the slurry onto a 2 × 1.5 cm FTO glass electrode.

In situ diffuse reflectance infrared spectroscopy (DRIFTS)

All IR spectra were determined using a Nicolet iS20 spectrometer equipped with an HgCdTe (MCT) detector cooled with liquid nitrogen and a VeeMax III (PIKE technologies) accessory. The *in situ* DRIFTS were determined using a Praying Mantis DRIFTS accessory and a reactor (Harrick Scientific, HVC-DRP). A 300 W Xe lamp (ZhongJiaoJinYuan) is connected to a liquid light guide for irradiation.

Samples were purged with wet CO_2 for 40 min until the sample spectrum was stable. CO_2 adsorption in dark was recorded until it was stable. Spectra under irradiation were recorded as a function of time to determine the dynamics of surface carbon contamination.

Theoretical computation

DFT computations were performed with the Vienna *Ab Initio* Simulation Package (VASP) code.[1] The Perdew-Burke-Ernzerhof (PBE) functional was employed for electron exchange-correlation within the generalized gradient approximation.[2] The projector-augmented wave (PAW) method was used to describe the ionic cores.[3] Geometry optimizations were performed with a 400 eV cut-off energy for plane wave expansion. Ionic relaxations were conducted until all forces were < 0.01 $eV \cdot Å^{-1}$. A Gaussian smearing was used with 0.2 eV width and a (2 × 2 × 1) Monkhorst-Pack k-point grid was applied. The Tkatchenko-Scheffler method was employed to describe long-range van der Waals interactions.[4]

Kinetic barriers were computed *via* climbing-image nudged elastic band (CI-NEB).[5] Four images were interpolated between initial (IS) and the final state (FS) to determine minimum energy path, and geometry of the transition state (TS). TS was confirmed through frequency analysis to ensure only one imaginary frequency existed, assigned to the unstable mode of minimum energy path.

BMO and BMO-R (010) surfaces were optimized in a 1 × 2 × 1 supercell. A vacuum space of 20 Å was applied to separate the interactions between neighbouring slabs. The

computational hydrogen electrode (CHE) model was employed for free energy computations.[6] Free energies for intermediates were obtained from, $G = E + ZPE - TS$. The zero-point energy (*ZPE*) and entropy correction (*TS*) were computed from vibration analysis and used to convert electronic energy (*E*) into free energy (*G*) at 298.15 K.

Supplementary Figures

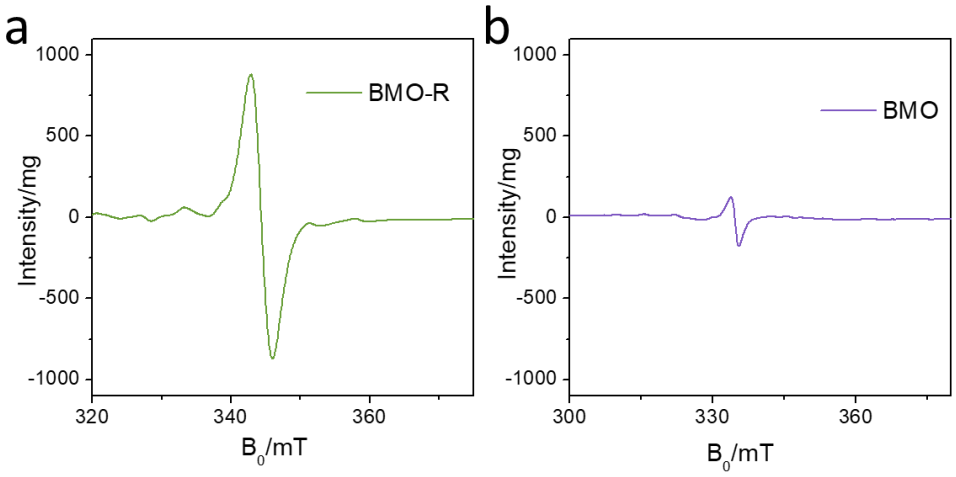

Figure S1. X-band CW EPR spectra for (a) BMO-R and (b) BMO. Double integration of EPR signal gives the number of radicals: 7.5 × 10^{16} spin/mgram (BMO-R) and 0.05 × 10^{16} spin/mgram (BMO).

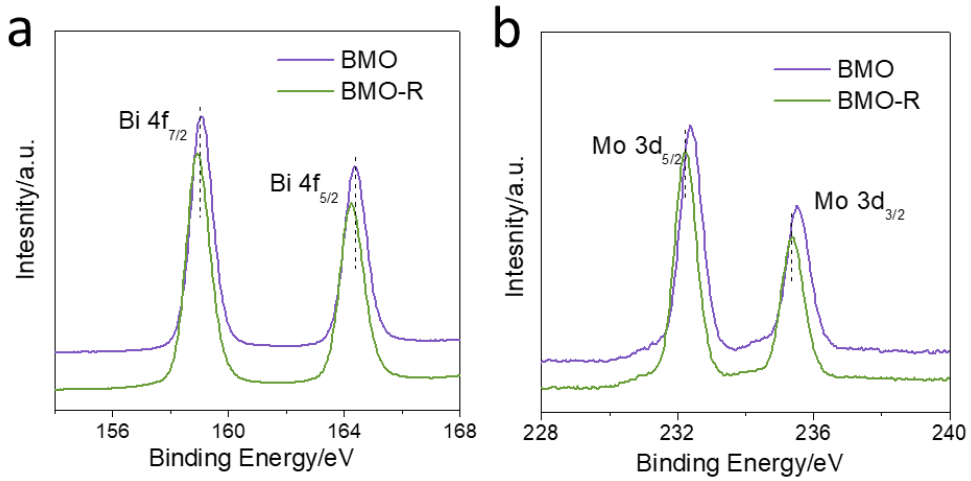

Figure S2. (a) High-resolution XPS spectra for Bi 4f for BMO and BMO-R. (b) High-resolution XPS spectra of Mo 3d for BMO and BMO-R.

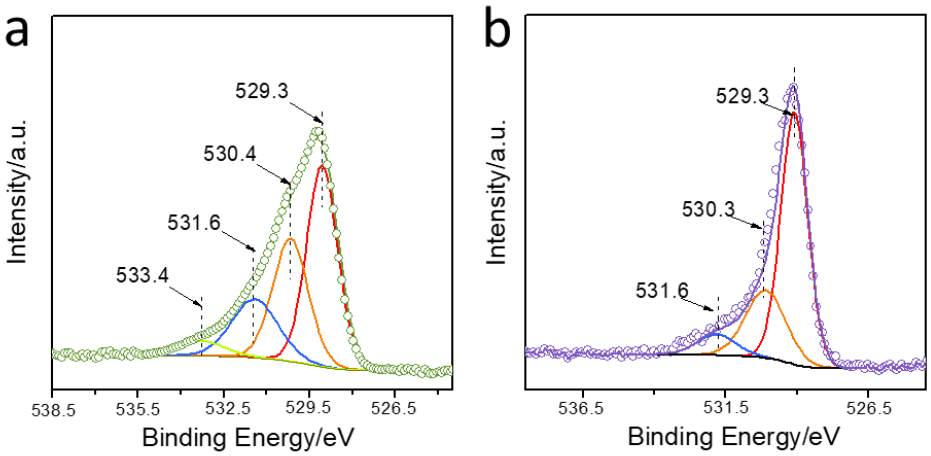

Figure S3. High-resolution XPS spectra for O 1s for (a) BMO-R and (b) BMO. The 529.3 and 530.3 eV peaks are attributed to, respectively, Bi-O and Mo-O bonds.[7] 531.6 eV peak is assigned to oxygen atoms changed by the oxygen vacancy. 533.4 eV peak is from the surface absorbed OH species on BMO-R. It evidences that the regulated surface is more efficient in activating water molecules.

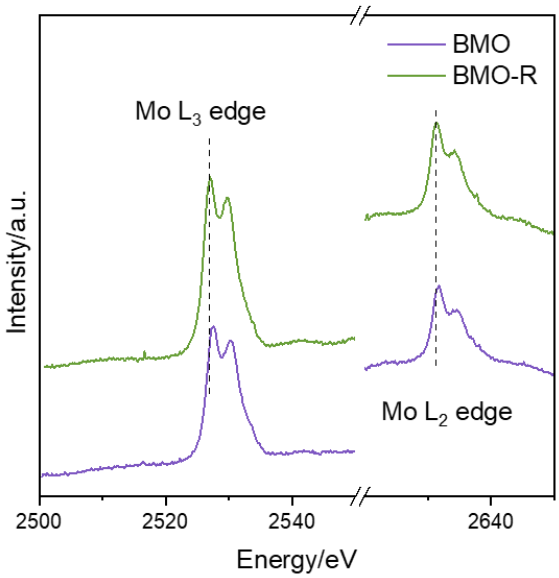

Figure S4. XANES spectra for Mo L edge for BMO and BMO-R.

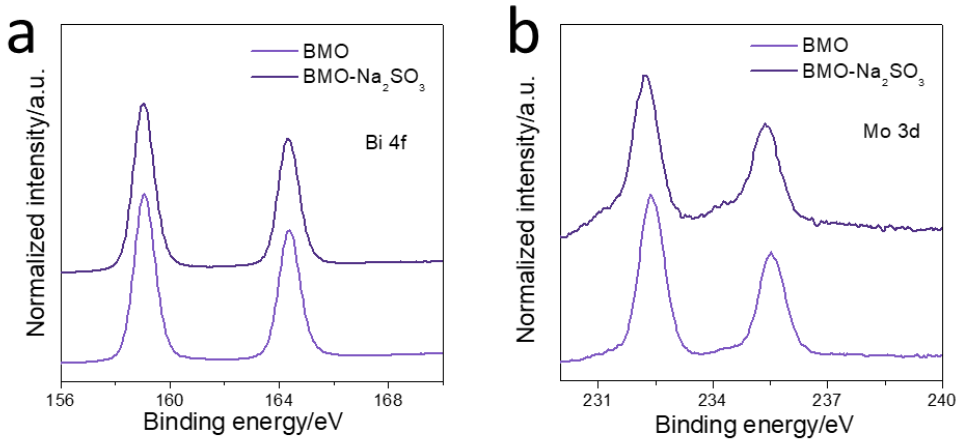

Figure S5. (a) High-resolution XPS spectra for Bi 4f and (b) Mo 3d for BMO and BMO-Na_2SO_3. BMO-Na_2SO_3 was prepared by dispersing BMO in 100 mL Na_2SO_3 solution (80 mM) without sonication for 2 h. It was washed and dried *via* the same procedure as for BMO-R.

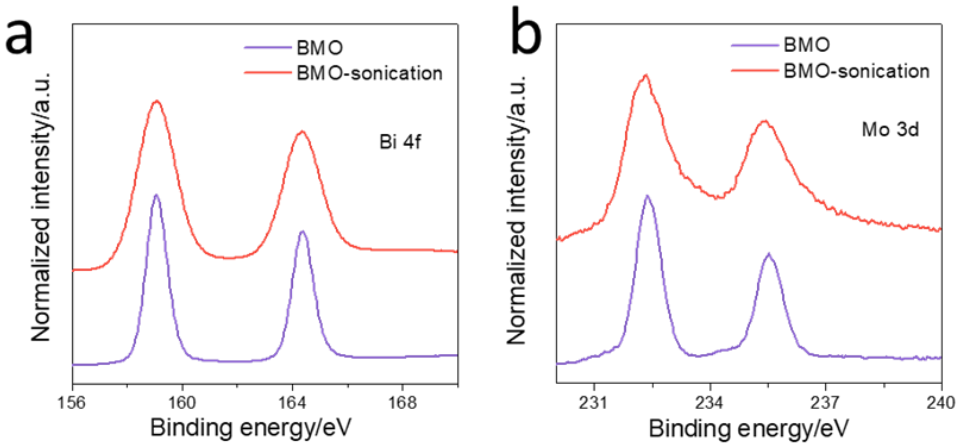

Figure S6. (a) High-resolution XPS spectra for Bi 4f and (b) Mo 3d for BMO, and BMO-sonication. BMO-sonication was in 100 mL of deionized water for 2 h. It was washed and dried *via* the same procedure as for BMO-R.

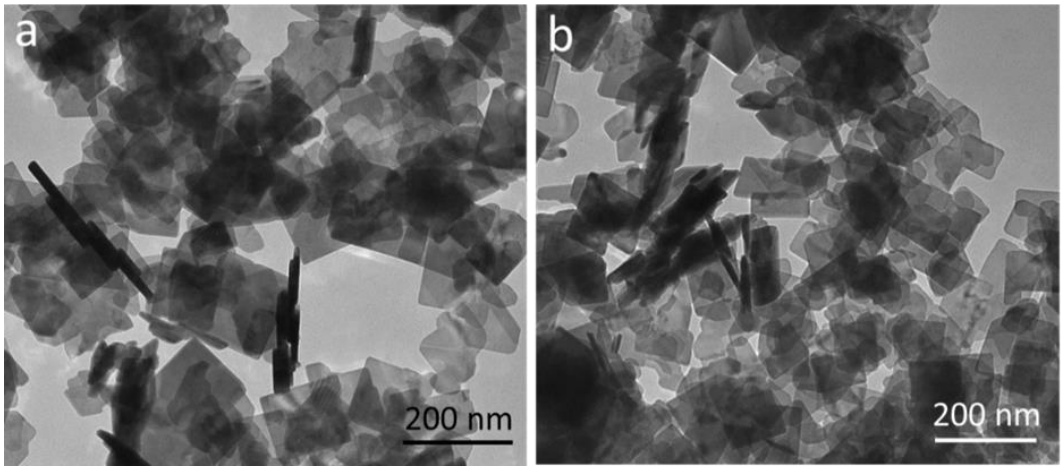

Figure S7. TEM images of (a) BMO and (b) BMO-R.

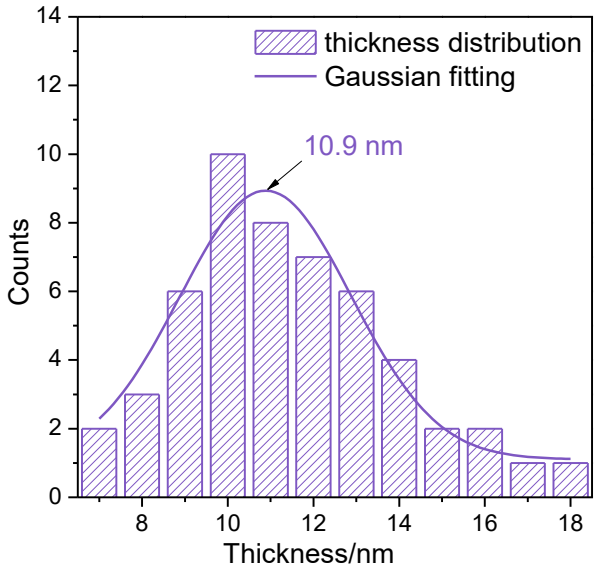

Figure S8. Thickness distribution with Gaussian fitting for BMO.

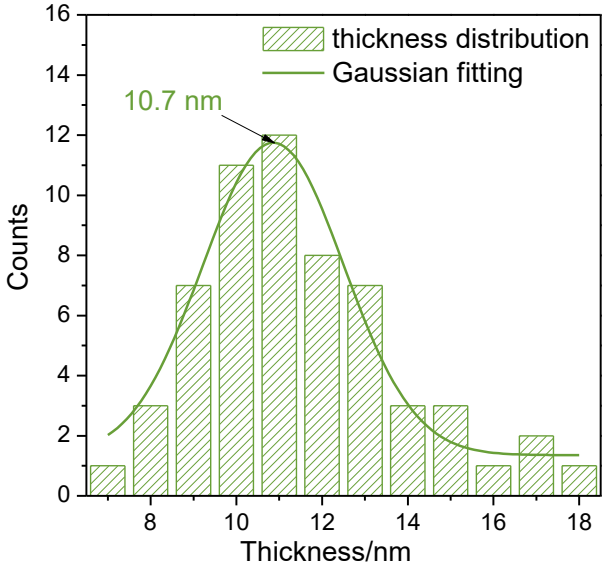

Figure S9. Thickness distribution with Gaussian fitting for BMO-R.

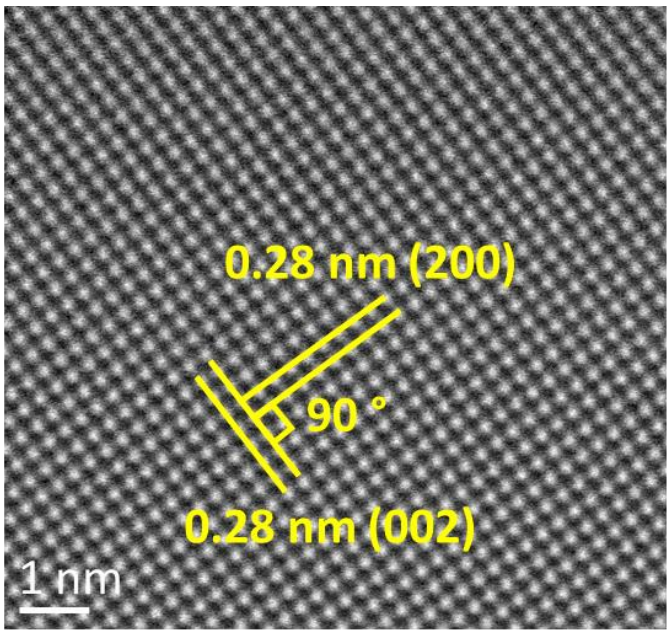

Figure S10. HAADF-STEM images of BMO-R.

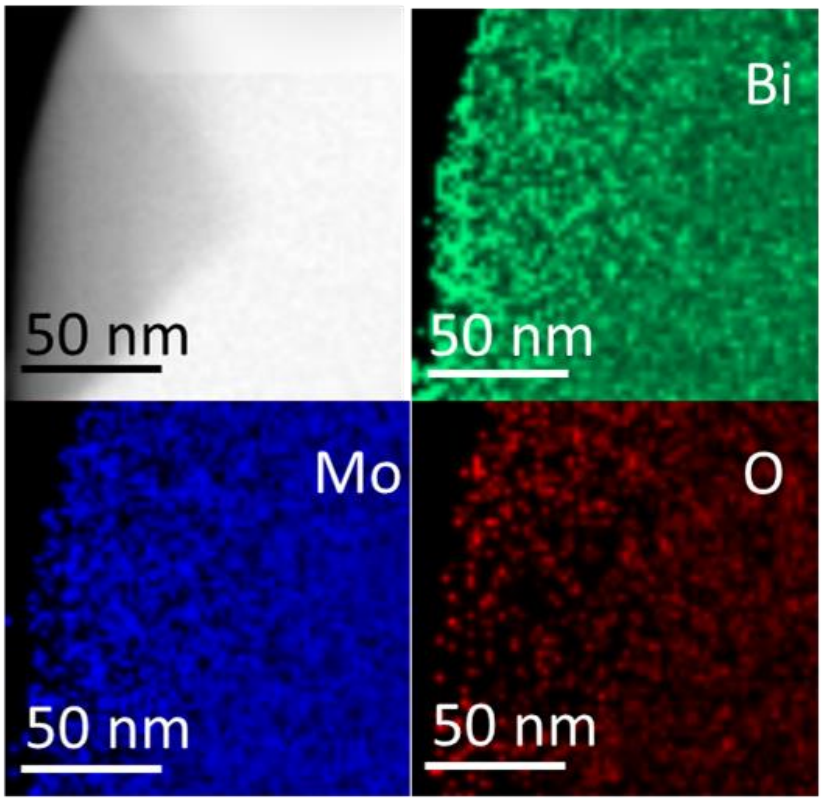

Figure S11. EDX elemental mapping for BMO-R.

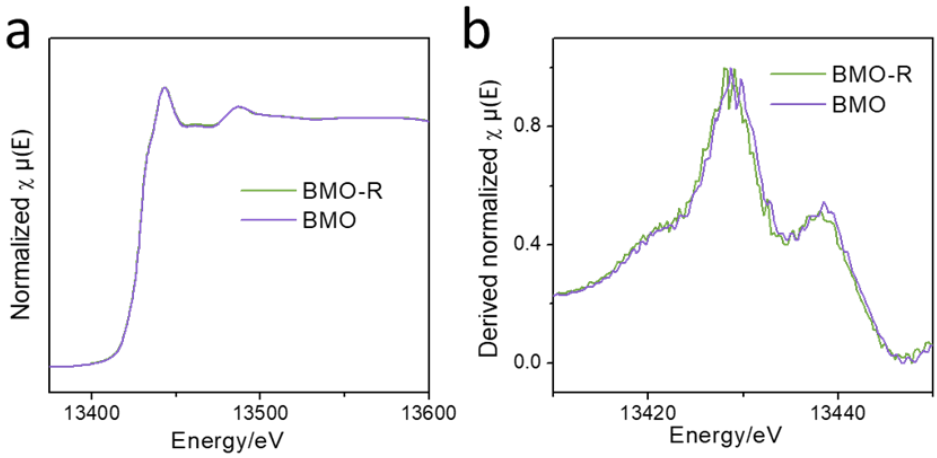

Figure S12. (a) XANES and b) first derivative spectra for Bi L_3 edge for BMO and BMO-R. Peaks in (b) evidence the edge position in (a). There is a slight shift toward lower binding energy for BMO-R, compared with that for BMO, confirming change in chemical state.

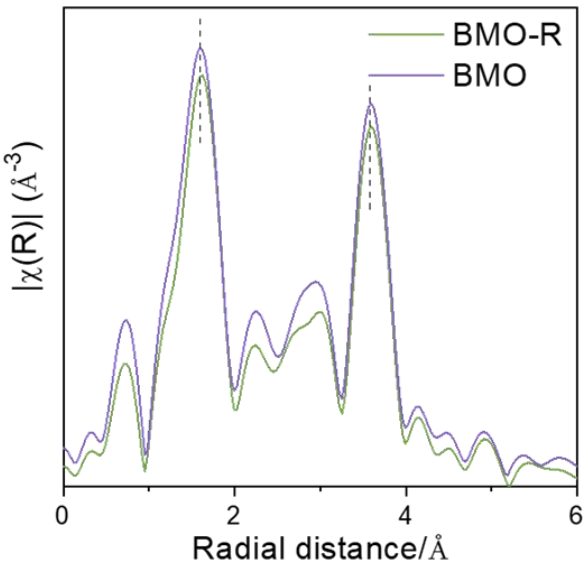

Figure S13. Bi L_3 edge FT-EXAFS for BMO and BMO-R.

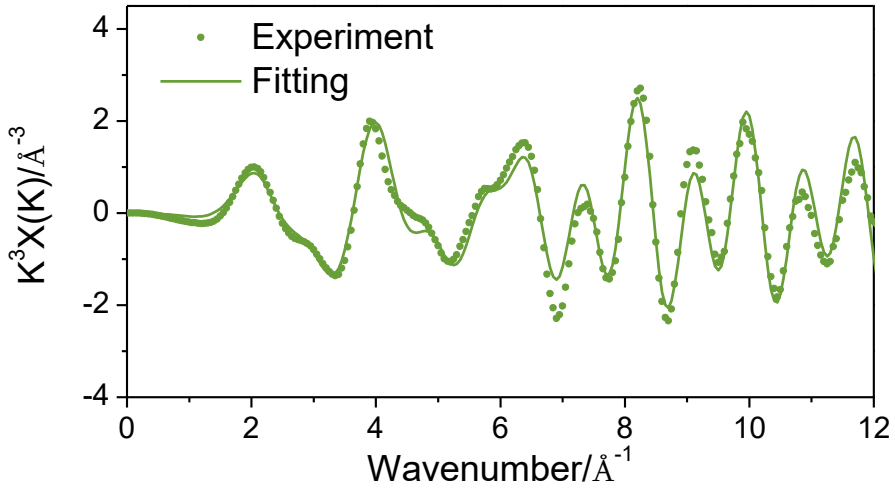

Figure S14. EXAFS fitted curves in k-space for Bi L_3 edge for BMO-R. The dotted line is experimental findings, solid line is fitted spectra.

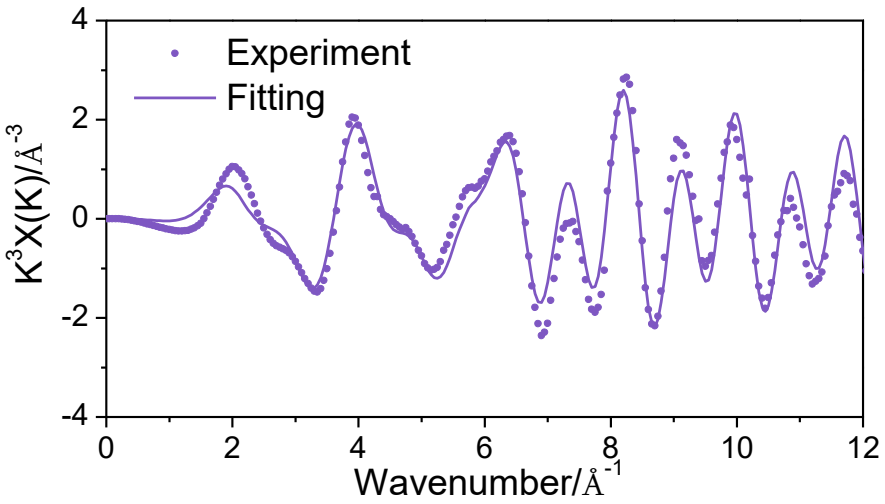

Figure S15. EXAFS fitted curves in k-space for Bi L_3 edge for BMO. The dotted line is experimental findings, solid line is fitted spectra.

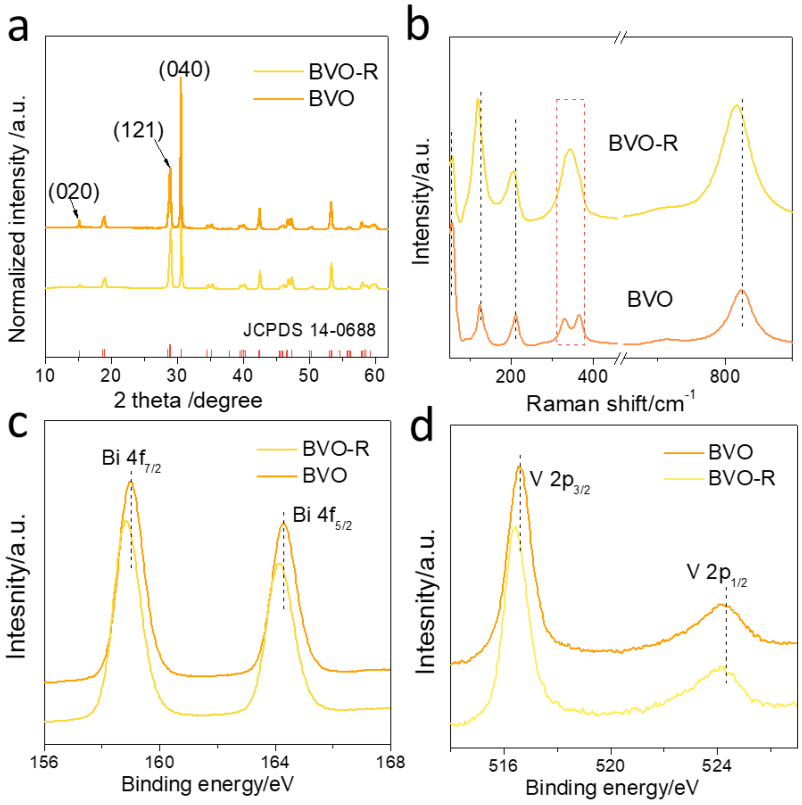

Figure S16. (a) XRD patterns for BVO and BVO-R. All peaks are assigned to JCPDS 14-0688. (b) Raman shift for BVO and BVO-R. High-resolution XPS spectra for (c) Bi 4f and (d) V 2p for BVO and BVO-R.

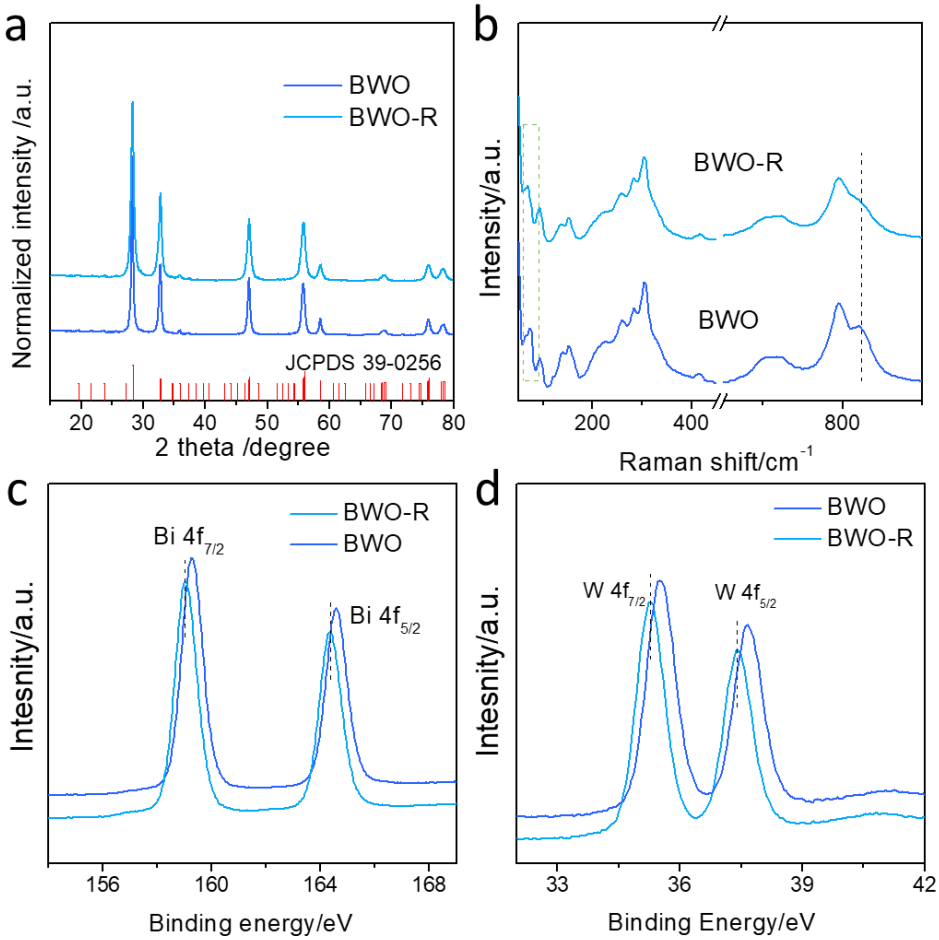

Figure S17. (a) XRD patterns for BWO and BWO-R. All peaks are assigned to JCPDS 39-0256. (b) Raman shift for BWO and BWO-R. High-resolution XPS spectra for (c) Bi 4f and (d) W 4f for BWO and BWO-R.

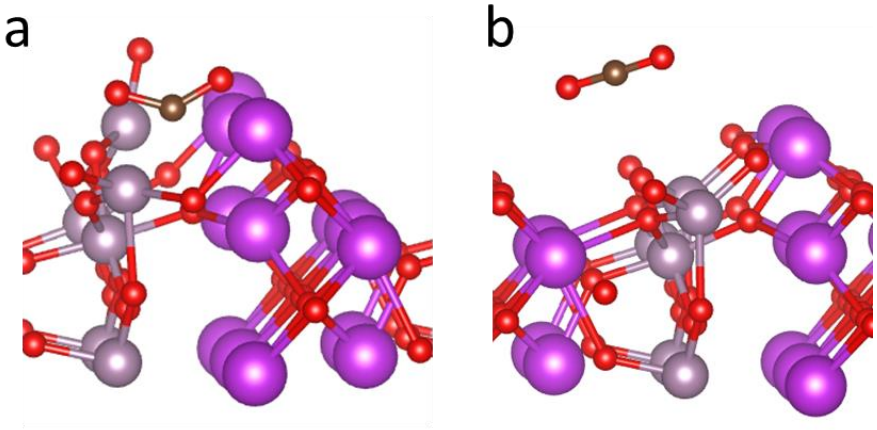

Figure S18. CO_2 adsorption configuration on (a) BMO-R and (b) BMO surface.

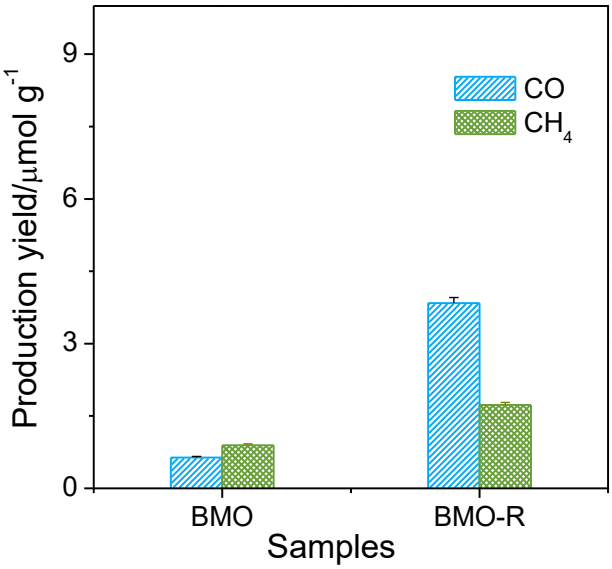

Figure S19. Blank photocatalytic CO_2 reduction test for BMO-R and BMO under illumination with ultra-high-purity Ar for 7 h. No products were detected in other blank experiments.

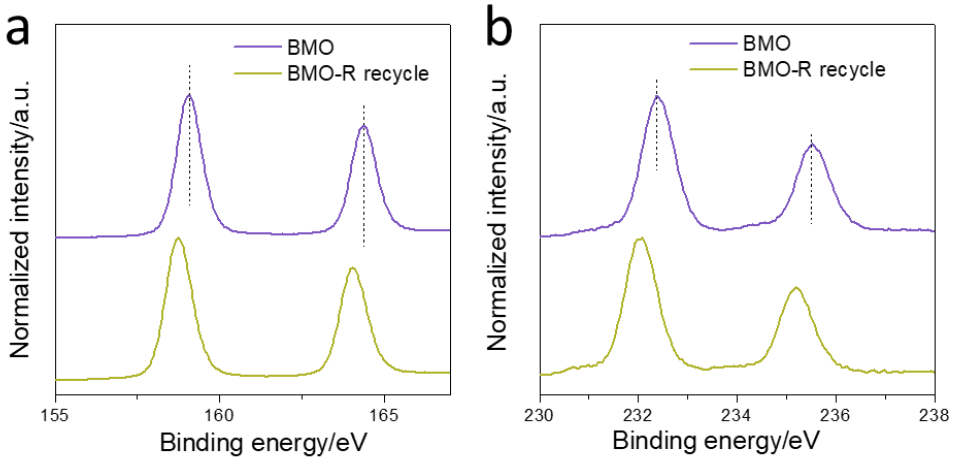

Figure S20. (a) Bi 4f and (b) Mo 3d XPS spectra prior to and following photocatalytic CO_2 reduction. Binding energy shifts remain stable evidencing that the modified surface remains stable during photocatalytic CO_2 reduction testing.

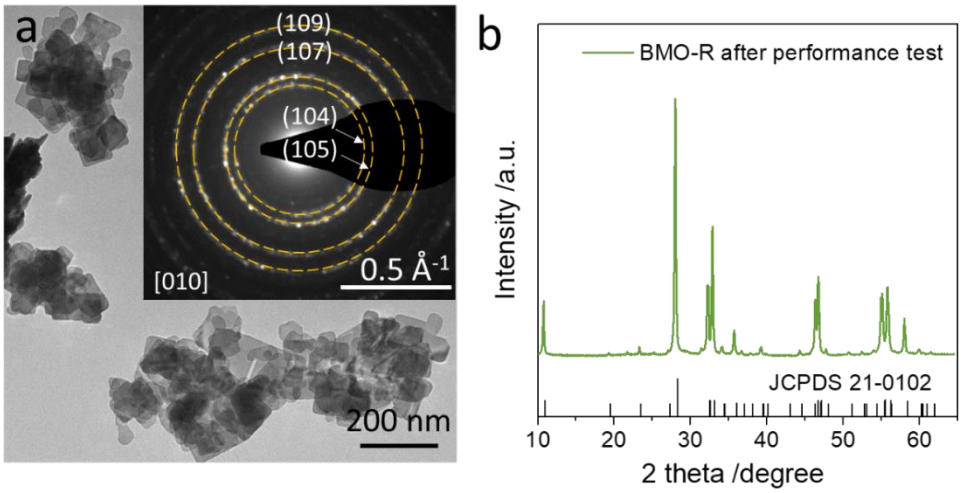

Figure S21. (a) TEM image of BMO-R following photocatalytic CO_2 reduction. Inset is corresponding SAED. The labelled pattern confirms that (010) facets are the dominant exposure facet; (b) XRD patterns for BMO-R following photocatalytic CO_2 reduction performance testing.

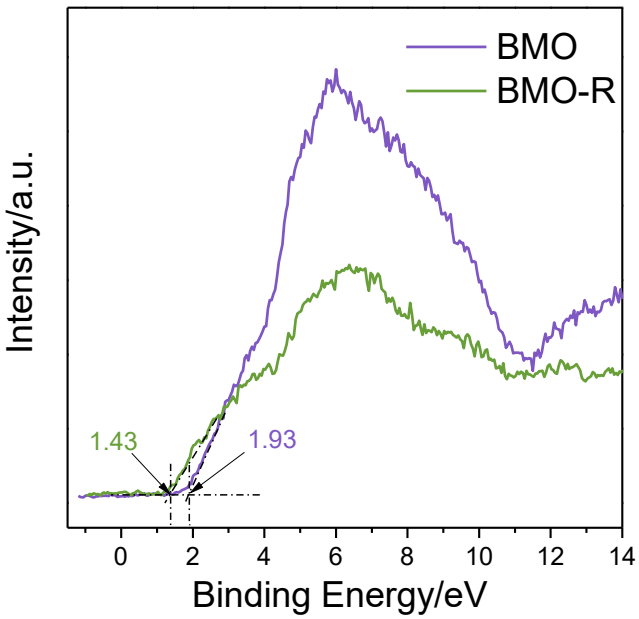

Figure S22. Valence band spectra for BMO and BMO-R samples.

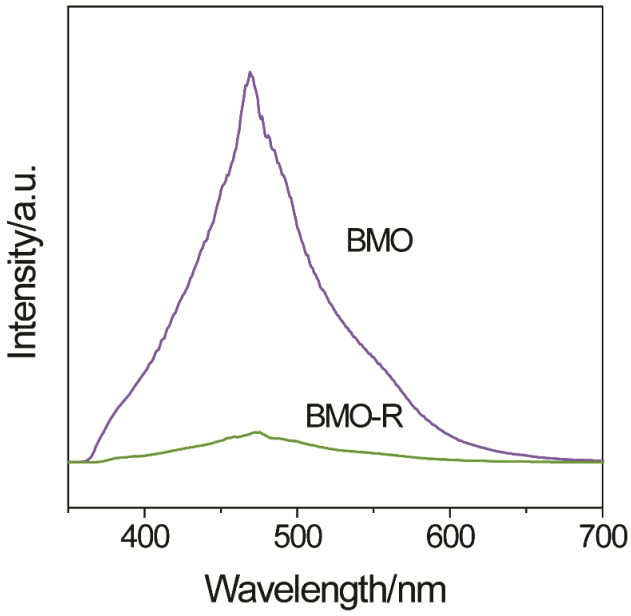

Figure S23. PL spectra for BMO and BMO-R.

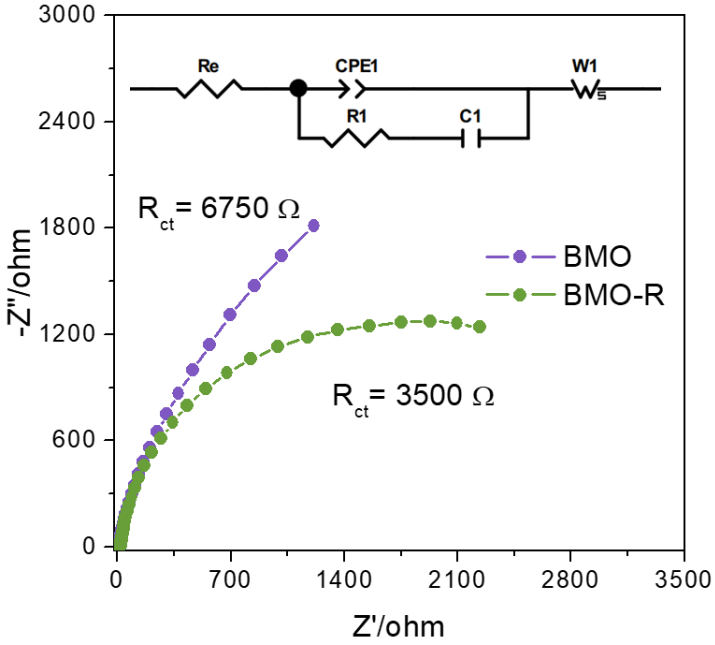

Figure S24. EIS spectra for BMO and BMO-R. Inset is the fitted circuit.

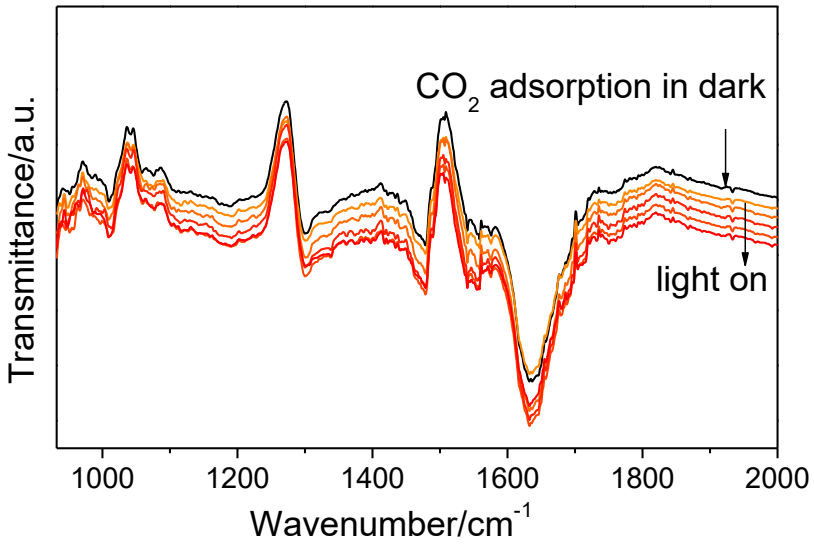

Figure S25. *In situ* DRIFTS for CO_2 photoreduction on BMO. Black-colour line is CO_2 adsorption in dark.

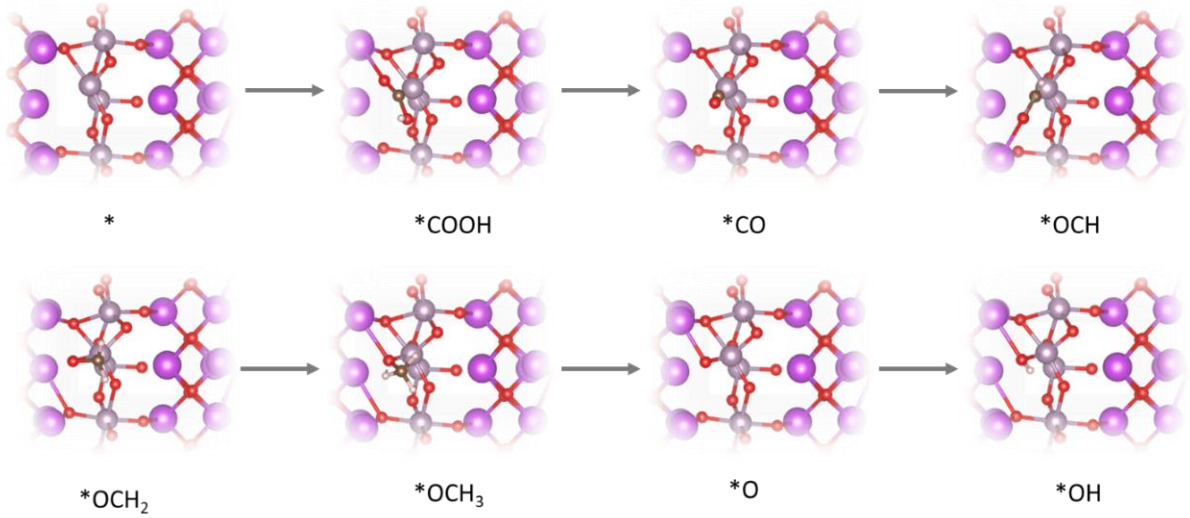

Figure S26. Intermediate configurations for BMO-R along CH_4 pathway. Oxygen, carbon, bismuth, hydrogen and molybdenum atoms are denoted as balls, respectively, red-colour, brown, purple, white and grey.

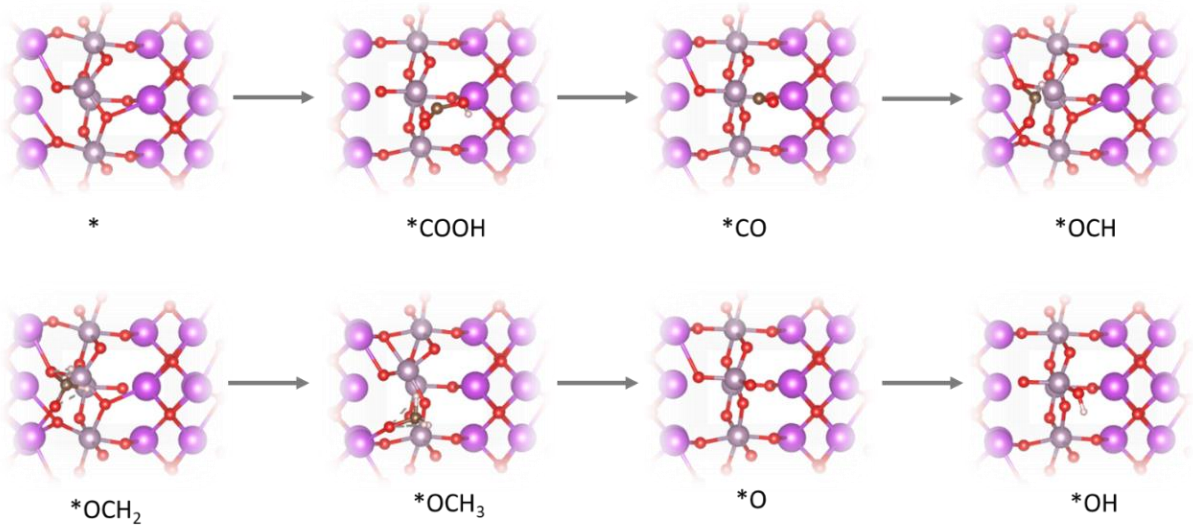

Figure S27. Intermediate configurations for BMO along CH_4 pathway. Oxygen, carbon, bismuth, hydrogen and molybdenum atoms are denoted as balls, respectively, red-colour, brown, purple, white and grey.

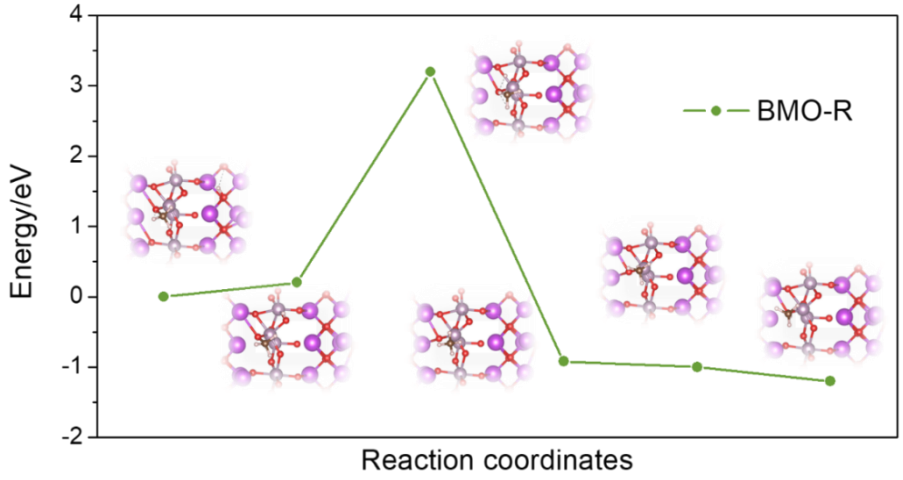

Figure S28. Minimum energy path for BMO-R involved in $*OCH_3 + H \rightarrow *O + CH_4$. Insets are optimized geometry structures for initial, transition and final states. Oxygen, carbon, bismuth, hydrogen and molybdenum atoms are denoted as balls, respectively, red-colour, brown, purple, white and grey.

Supplementary Tables

Table S1. Fitted results for Bi L_3-edge EXAFS data for BMO and BMO-R.

Sample	Path		N (Coordination Number)	R (Å)	ΔE_0 (eV)	σ^2 (A^2)	R-factor
BMO-R	Bi–O	$Bi–O_1$	5.60	1.94	2.226	3.2435	0.0072	0.03185
		$Bi–O_2$		1.46	2.295			
		$Bi–O_3$		1.99	2.501			
		$Bi–O_4$		0.21	3.657			
	Bi-Bi		6		3.778			
BMO	Bi–O	$Bi–O_1$	5.96	1.87	2.226	5.7059	0.0071	0.02928
		$Bi–O_2$		1.43	2.295			
		$Bi–O_3$		1.37	2.501			
		$Bi–O_4$		1.29	3.657			
	Bi-Bi		6		3.778			

R = the length of Bi–O and Bi–Bi path, N = coordination number of Bi atoms corresponding to Bi–O or Bi–Bi path, σ^2 = Debye-Waller factor, and ΔE_0 = inner potential correction.

Table S2. Summary comparison of CO_2 photoreduction performance on Bi-based photocatalysts.

Catalyst	Reaction medium	Light source	Product(s)	Production yield μmol g^{-1} h^{-1}	Ref
Bi_2MoO_6-R	H_2O vapor	Xe lamp	CO, CH_4	8.7, 1.7	This work
Bi_2WO_6-R	H_2O vapor	Xe lamp	CO, CH_4	7.3, 1.02	This work
$BiVO_4$-R	H_2O vapor	Xe lamp	CO, CH_4	2.4, 0.76	This work
Bi_2MoO_6	H_2O	Xe lamp	CO	3.62	[8]
BiOCl-Ov	H_2O	Xe lamp	CO, CH_4	1.01, 0.15	[9]
BiOBr (001)	H_2O vapor	Xe lamp	CO	4.45	[10]
$BiOIO_3$	H_2O vapor	Xe lamp	CO	5.42	[11]
$Bi_4O_5Br_2$	H_2O vapor	Visible light	CO, CH_4	2.73, 2.04	[12]

3D Bi_2MoO_6	H_2O	Xe lamp	CO	41.5	[13]
$ZnFe_2O_4/Bi_2MoO_6$	H_2O	Xe lamp	CO, CH_4	6.5, 2.9	[14]
Ru/Bi_2MoO_6	H_2O	Xe lamp	CO	23.8	[15]
Bi_2WO_6	H_2O vapor	Visible light	CH_4	1.1	[16]
Bi_2WO_6/CODs	H_2O vapor	Visible light	CH_4	0.89	[17]
Bi_2WO_6-V	H_2O vapor	Xe lamp	CO, CH_4	7.7, 0.37	[18]
Bi_2WO_6-C	H_2O vapor	Xe lamp	CO, CH_4	7.12, 0.63	[19]
$CdS/BiVO_4$	H_2O vapor	Xe lamp	CO, CH_4	1.75, 0.39	[20]
$BiVO_4$/EF	H_2O vapor	Visible light	CO, CH_4	1.37, 2.41 μmol cm^{-2} h^{-1}	[21]
$Cu/Bi/BiVO_4$	H_2O vapor	Xe lamp	CO	11.15	[22]

Supporting References

[1] G. Kresse, J. Furthmuller, *Phys. Rev. B: Condens. Matter Mater. Phys.* **1996**, *54*, 11169-11186.

[2] J.P. Perdew, K. Burke, M. Ernzerhof, *Phys. Rev. Lett.* **1996**, *77*, 3865-3868.

[3] G. Kresse, D. Joubert, *Phys. Rev. B: Condens. Matter Mater. Phys.* **1999**, *59*, 1758-1775.

[4] A. Tkatchenko, M. Scheffler, *Phys. Rev. Lett.* **2009**, *102*, 073005.

[5] G. Henkelman, H. Jonsson, *J. Chem. Phys.* **2000**, *113*, 9978–9985.

[6] J.K. Nørskov, J. Rossmeisl, A. Logadottir, L. Lindqvist, J.R. Kitchin, T. Bligaard, H. Jonsson, *J. Phys. Chem. B* **2004**, *108*, 17886-17892.

[7] P.V. Shinde, N.M. Shinde, J.M. Yun, R.S. Mane, K.H. Kim, *ACS Omega* **2019**, *4*, 11093-11102.

[8] J. Di, X. Zhao, C. Lian, M. Ji, J. Xia, J. Xiong, W. Zhou, X. Gao, Y. She, H. Liu, K. P. Loh, S. J. Pennycook, H. Li, Z. Liu, *Nano Energy* **2019**, *61*, 54-59.

[9] L. Zhang, W. Wang, D. Jiang, E. Gao, S. Sun, *Nano Research* **2015**, *3*, 821-831.

[10] D. Wu, L. Ye, H. Y. Yip, P. K. Wong, *Catal. Sci. Technol.*, **2017**, *7*, 265.

[11] F. Chen, H. Huang, L. Ye, T. Zhang Y. Zhang, X. Han, T. Ma, *Adv. Funct. Mater.* **2018**, *28*, 1804284.

[12] L. Ye, X. Jin, C. Liu, C. Ding, H. Xie, K. H. Chu, P. K. Wong, *Appl. Catal. B* **2016**, *187*, 281-290.

[13] X. Zhang, G. Ren, C. Zhang, R. Li, Q. Zhao, C. Fan, *Catal. Lett.* **2020**, *150*, 2510-2516.

[14] Y. Zhou, W. Jiao, Y. Xie, F. He, Y. Ling, Q. Yang, J. Zhao, H. Ye, Y. Hou, *J. Colloid Interface Sci.* **2022**, *608*, 2213-2223.

[15] G. Ren, S. Liu, Z. Li, H. Bai, X. Hu, X. Meng, *Sol. RRL* **2022**, *6*, 2200154.

[16] Y. Zhou, Z. Tian, Z. Zhao, Q. Liu, J. Kou, X. Chen, J. Gao, S. Yan, Z. Zou, *ACS Appl. Mater. Interfaces* **2011**, *3*, 3594–3601.

[17] X. Y. Kong, W. L. Tan, B.-J. Ng, S.-P. Chai, A. R. Mohamed, *Nano Research* **2017**, *5*, 1720-1731.

[18] C. Lu, X. Li, Q. Wu, J. Li, L. Wen, Y. Dai, B. Huang, B. Li, Z. Lou, *ACS Nano* **2021**, *15*, 3529−3539.

[19] Y. Liu, D. Shen, Q. Zhang, Y. Lin, F. Peng, *Appl. Catal. B* **2021**, *283*, 119630.

[20]Z.-H. Wei, Y.-F. Wang, Y.-Y. Li, L. Zhang, H.-C. Yao, Z.-J. Li, *J. CO_2 Util.* **2018**, *28*, 15–25.

[21] S. Yue, L. Chen, M. Zhang, Z. Liu, T. Chen, M. Xie, Z. Cao, W. Han, *Nano-Micro Lett.* **2021**, *14*, 1.

[22] L. Huang, Z. Duan, Y. Song, Q. Li, L. Chen, *ACS Appl. Nano Mater.* **2021**, *4*, 3576–3585.

Author Contributions

Shi-Zhang Qiao conceived the concept and supervised whole project. Yanzhao Zhang is the lead of contribution and charges the methodology, data curation and analysis and writing of original draft. Xing Zhi conducts DFT computation and relative parts writing and reviewing. Jeffrey R. Harmer supports this job in EPR data curation and analysis and relative parts writing and reviewing. Haolan Xu supports the XPS data curation. Kenneth Davey corrects and edits the paper. Shi-Zhang Qiao and Jingrun Ran undertake funding acquisition, supervision, as well as correct and edit the whole paper.

Chapter 6

Reversed Electron Transfer in Dual-Single-Atom Promotes CO_2 Photoreduction

6.1 Introduction and Significance

The transfer and distribution of photogenerated electrons on the surface of photocatalysts play an important role in photocatalytic CO_2 reduction. There are many reports about charge separation and transfer between two composites in heterojunction. However, single atoms play a different role in semiconductor-based photocatalysts. They may act as electrons acceptor or donors in different systems. Moreover, the modulation of charge transfer and distribution between dual single atoms lacks reports. Here we report for the first time that the dual single atoms can modulate the different charge transfer mechanisms.

1. A new photogenerated electron transfer mechanism in a dual-single-atom system. Photogenerated electrons can be accumulated around Au/Co single atoms on CdS nanoparticles. However, DFT simulation, combined with the *in situ* XPS, reveals that the electrons transfer direction and accumulation was modulated in Au and Co single atoms on CdS.

2. The accumulated electrons around Co single atom boost CO_2 photoreduction. The electrons can be accumulated around Co single atoms in Co and Au dual-single-atom system thus boosting the CO_2 adsorption, activation and reduction. The modulated surface electron density exhibited a high activity of, respectively, 64.1 and 7.7 μmol g^{-1} for CO and CH_4, a selectivity > 89 % and stability > 20 h for the reaction for dual single atoms.

3. Active sites and reaction mechanism dual single atoms CRR photocatalysts. Combined theoretical computations and *in situ* spectroscopy confirmed that single Co atoms formed as active sites and Au acted as the electrons donor surface unsaturated metal atoms, and evidenced the activation of CO_2 as the rate-limiting step.

We conclude the charge transfer and accumulation on the surface of catalysts are critical for surface redox reactions. A dual-single-atom system can modulate this process and change the transfer direction. Findings will be of benefit and interest in the development of a charge transfer process that is applicable to additional catalytic reactions and single-atom catalysts.

6.2 Reversed Electron Transfer in Dual-Single-Atom Promotes CO_2 Photoreduction

This Chapter is presented as a manuscript format for a research paper by Yanzhao Zhang, Yan Jiao, Jingrun Ran and Shi-Zhang Qiao. Reversed Electron Transfer in Dual-Single-Atom Promotes CO_2 Photoreduction, In preparation.

Statement of Authorship

Title of Paper	Reversed Electron Transfer in Dual-Single-Atom Promotes CO2 Photoreduction
Publication Status	☐ Published ☐ Accepted for Publication ☐ Submitted for Publication ☑ Unpublished and Unsubmitted w ork w ritten in manuscript style
Publication Details	Yanzhao Zhang, Yan Jiao, Jingrun Ran, Shi-Zhang Qiao, In preparation

Principal Author

Name of Principal Author (Candidate)	Yanzhao Zhang		
Contribution to the Paper	Design and conducted the experiments, analysed the data, wrote the manuscript.		
Overall percentage (%)	70%		
Certification:	This paper reports on original research I conducted during the period of my Higher Degree by Research candidature and is not subject to any obligations or contractual agreements with a third party that would constrain its inclusion in this thesis. I am the primary author of this paper.		
Signature		Date	06/12/2022

Co-Author Contributions

By signing the Statement of Authorship, each author certifies that:

i. the candidate's stated contribution to the publication is accurate (as detailed above);

ii. permission is granted for the candidate in include the publication in the thesis; and

iii. the sum of all co-author contributions is equal to 100% less the candidate's stated contribution.

Name of Co-Author	Yan Jiao		
Contribution to the Paper	Supervision of the simulation part of this work		
Signature		Date	25/01/2023

Name of Co-Author	Jingrun Ran		
Contribution to the Paper	Discussion and revision of manuscript		
Signature		Date	23/1/2023

Name of Co-Author	Shi-Zhang Qiao		
Contribution to the Paper	Supervision of the work, discussion and conceptualization of this manuscript and manuscript evaluation and revision.		
Signature		Date	25/01/2023

Reversed Electron Transfer in Dual-Single-Atom Promotes CO_2 Photoreduction

Yanzhao Zhang, Yan Jiao, Jingrun Ran and Shi-Zhang Qiao**

Y. Zhang, Dr. Y. Jiao, Dr. J. Ran, Prof. S.Z. Qiao

School of Chemical Engineering & Advanced Materials, The University of Adelaide, Adelaide, SA 5005, Australia.

E-mail: s.qiao@adelaide.edu.au; jingrun.ran@adelaide.edu.au

Abstract

The photogenerated electron transfer and distribution on the surface significantly affect the photocatalytic performance. However, the mechanism of charge transfer and accumulation is still unclear in dual-single-atom systems. Herein, we propose a different strategy for the modulation of surface electron transfer by taking CdS nanoparticles as an example. Isolated single Au or Co atoms anchored, respectively, on CdS nanoparticles can accumulate photogenerated electrons while electrons are localized around Co atoms when Co and Au are loaded simultaneously. Detailed spectroscopic investigation unravels that this surface electron redistribution facilitates the interaction of CO_2 with semiconductor photocatalysts, thus promoting the photocatalytic performance, showing at least 28-fold enhancement compared with CdS nanoparticles on production yield. This report broadens our understanding of the new mechanism of charge transfer in single-atom material and CO_2 photoreduction.

Introduction

Photocatalytic carbon dioxide (CO_2) reduction reaction is highly attractive for achieving solar energy utilization and carbon neutrality.[1-5] However, it is not yet satisfactory for the current conversion and yield rate on photocatalytic CO_2 reduction because of the following two aspects.[1] First, the inertness of CO_2 molecules, due to their non-electric dipoles and stubborn C=O double bonds, hurdles its adsorption and activation.[6,7] Second, the intrinsic multi-electron process also requires more effective electron distribution and utilization.[8] In recent studies, it has been demonstrated that surface electron redistribution creates a locally polarized

microenvironment to boost CO_2 activation by facilitating the electron adoption, electronic and geometric structure asymmetry of linear CO_2 and CO_2 chemisorption.[8,9]

Surface modification strategies, including the introduction of surface defects[10-16], grafted groups[17,18] and heterogeneous metal atoms[19-24], have been validated to effectively achieve the redistribution of electrons and to activate CO_2 molecules. Among them, metal sites are always attracting attention because their surface electron distribution can be flexibly adjusted via phase/size engineering.[8, 25-28] For instance, Pd nanoparticles can accept electrons from TiO_2 nanosheets, where metal nanoparticles can act as a reservoir of electrons facilitating the charge separation and transfer.[29] However, with the decrease in the size of metal nanoparticles to the single-atom level, the impact of metal sites and the mechanism of electron transfer and distribution become complicated.[30,31] Similar to Pd nanoparticles, Pt single atom can attract electrons from the hosting C_3N_4 and accumulate electrons for redox reaction.[32] Contrastively, single Pd atoms reversed the electron migration direction and donated the electron to the supporting TiO_2 nanosheets.[29] Similarly, surface electron density and transfer direction on $Cd_{1-x}S$ can be modulated *via* the induction of a single Au atom.[8] These findings reveal that different metal sites and matrixes can induce opposite electron flows, resulting in different regions where electrons can be localized.[33] Therefore, is it possible to utilize the specific and contrastive electron flow to modulate the surface electron distribution towards favorable reactions, for instance, CO_2 photoreduction?

The development of dual-single-atom catalysts provides a potential platform to establish flexible electron configurations to tune the charge transfer and accumulations.[34-36] Under this circumstance, on a specific hosting matrix, one kind of single-atom active site can accept electrons and reduce CO_2 molecules, while the other could lose electrons and become partially positively charged at the localized regions. Such a system can play the role of electron acceptor and donor at different sites, thus promoting the activation and conversion of CO_2. Therefore, for this purpose, we designed and developed the Co/Au dual-single-atom catalyst supported on CdS nanoparticles and studied the mechanism for surface photogenerated charges migration and accumulation for CO_2 conversion. By comparing to the isolated single-atom Au and Co, Au and Co atoms in the dual-single-atom system play as the electron donor and acceptor, respectively. Affected by superior electron transfer mechanism and higher surface electron density, CO_2 could be more easily activated and dissociated on Co atoms in dual sites system instead of physical adsorption promoting the photocatalytic CO_2 performance.

Results and Discussion

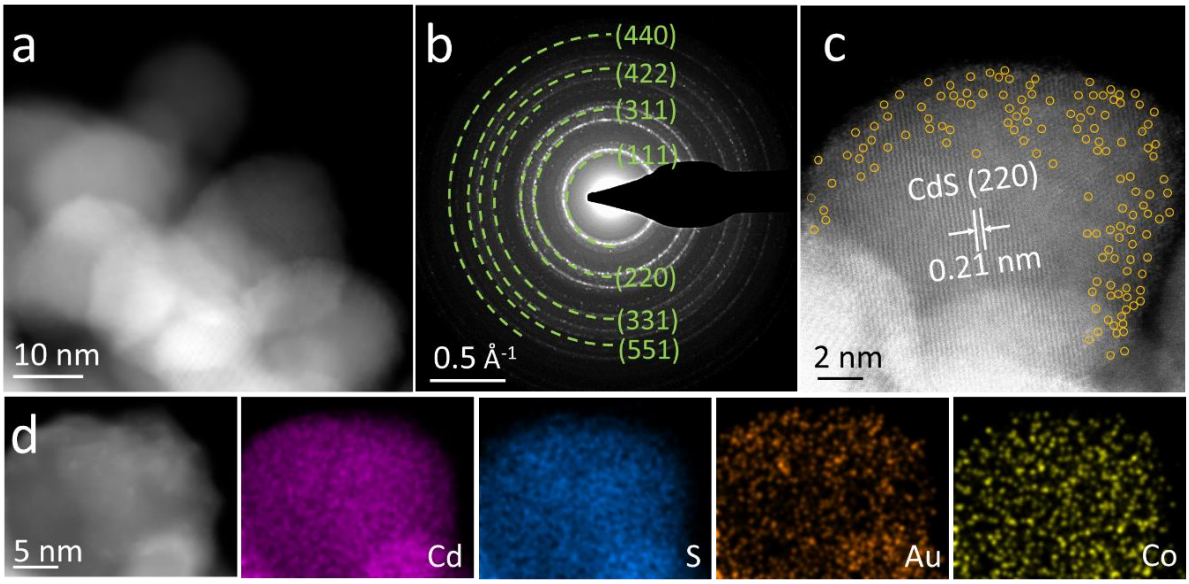

Figure 1. a) TEM image and b) corresponding selected area electron diffraction (SAED) pattern of CAC2; c) HAADF-STEM images of CAC2; d) EDS mapping of CAC2.

We selected CdS as the matrix material due to its simple synthesis and excellent photocatalytic performance. Co or Au single atoms are the loaded metal sites on CdS nanoparticles, respectively, are denoted as CC1, CC2 and CA1, CA2, according to different loading amount, (see details in Supporting Information). Moreover, CdS nanoparticles loaded by two single atoms are labeled as CAC1, CAC2, CAC3 and CAC4 (see details in Supporting Information). CdS nanoparticles with single atoms are prepared by hydrothermal reaction and chemical adsorption/impregnation methods. X-ray diffraction (XRD) pattern, transmission electron microscopy (TEM), selected area electron diffraction (SAED) and aberration-corrected high-angle annular dark field scanning transmission electron microscopy (HAADF-STEM) of the prepared samples were performed to investigate the single atoms. No diffraction peaks from impurity crystals in XRD patterns (cubic CdS, JCPDS 10-0454) were detected which indicated that there were no Co or Au particles (Figure S1). The synthesized samples displayed cubic CdS nanoparticles with the size of 19.7 nm (Figure S2). Moreover, the HAADF-STEM image exhibits the 0.34 nm crystal lattice assigned to the (111) facets of cubic CdS (Figure S2b). After the Co and Au were loaded on the nanoparticle, the morphology and crystal structure were also investigated. In Figures 1a and b, CAC2 exhibits the same morphology and crystal structure as that of CdS nanoparticles. However, single atoms were observed under HAADF-STEM and labeled by yellow circles (Figure 1c). These are most probably Au single atoms since the cobalt is too light in contrast to be observed on CdS. The

crystal lattice shows the distance as 0.21 nm, attributed to the cubic CdS (220). To study the elemental distribution, energy dispersive X-ray (EDX) elemental mapping was conducted. In Figure 1d, both Au and Co were observed and in agreement with the HADDF-STEM image, which indicates single atoms were successfully loaded on CdS nanoparticles. Furthermore, the CA2 and CC2 samples were also studied and the corresponding XRD, EDX and HAADF-STEM show that Au or Co single atoms are loaded on CdS nanoparticles, respectively (Figure S1, S3 and S4). The formation of metal–sulfur bonds was studied by Raman spectroscopy. In Figure S5, the Co–S at around 660 cm^{-1} can be observed at both CC2 and CAC2. The peak around 400 cm^{-1} is from Au–S in CA2 and CAC2.[37-39] All of above results verify that the single Au and Co are loaded on CdS nanoparticles successfully.

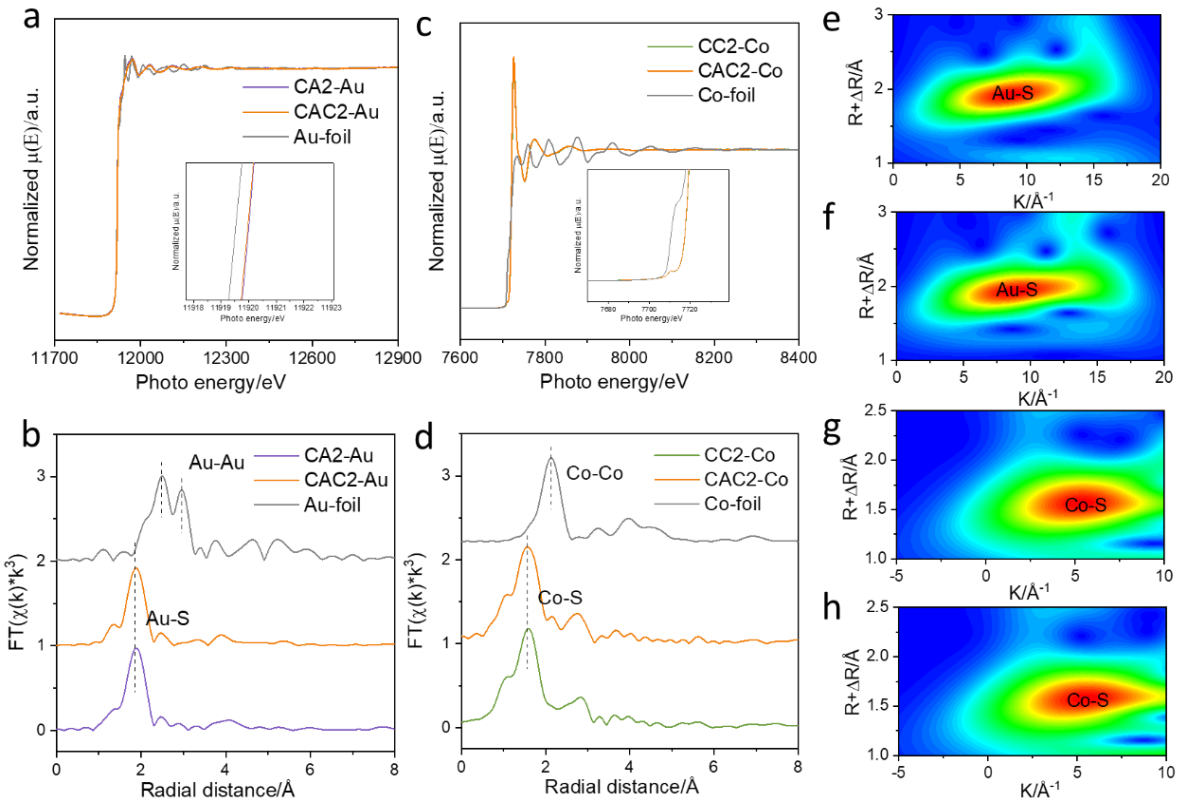

Figure 2. a) XANES and b) corresponding EXAFS spectra of Au L_3-edge for CAC2, CA2 and Au foil; c) XANES and d) corresponding EXAFS spectra of Co K-edge for CAC2, CC2 and Co foil; WT for the K^3-weighted EXAFS signal at Au L_3-edge for e) CA2 and f) CAC2; WT for the K^3-weighted EXAFS signal at Co K-edge for g) CAC2 and h) CC2.

To investigate the coordination environment of Au and Co single atoms in different samples, Au L_3-edge X-ray absorption near edge structure (XANES) and extended X-ray absorption fine structure (EXAFS) spectra of CAC2, CA2 and CC2 were investigated (Figure 2). Compared to the XANES spectra of Au foil, Au presents a similar oxidation state in CA1

and CAC2 ($Au^{\delta+}$, $0 < \delta < 3$) (Figure 2a). In Figure 2b, EXFAS spectra of CA2 and CAC2 show that the Au exhibits a peak near 1.8 Å, attributed to Au–S bonds. Also the absence of Au–Au bonds between 2 and 4 Å further confirms the atomic dispersion of Au in CA1 and CAC2 samples. Similarly, results from the XANES of Co K-edge in CC2, CAC2 and Co foil, Co presents as Co^{2+} (Figure 2c). The absence of Co–Co (2.2 Å) coordination shown in Figure 2d implies that the isolated Co atoms (1.5 Å) in CC2 and CAC2. Correspondingly, to more clearly discriminate coordinated information, EXAFS wavelet transform (WT) of different samples and referenced metal foil was carried out. The maximum intensity of Au L_3-edge spectra in Figures 2e and f is at 8.5 $Å^{-1}$ for CA2 and CAC2, which is attributed to Au–S. Similarly, the Co–S in CC2 and CAC2 in Figures 2g and h shows maximum intensity of Co K-edge spectra is at 5 $Å^{-1}$. All of these single atom samples show different profiles with those of metal foil (Figure S6) with intensity maximum at 10 and 7.5 $Å^{-1}$ for Co–Co and Au–Au, respectively.

The CdS nanoparticles loaded with single atoms were studied for CO_2 photoreduction. As shown in Figure 3a, CdS shows limited CO_2 photoreduction performance with CO and CH_4 production of 2.3 and 1.12 μmol g^{-1}, respectively. After loading Au single atoms, the production yields of CO and CH_4 were significantly enhanced with 24.3 and 2.6 μmol g^{-1}, respectively, while the CA2 shows a little decrease in performance. Similarly, the CC1 (CO and CH_4 with 11.4 and 1.9 μmol g^{-1}) exhibits more excellent performance than CC2 (CO and CH_4 with 8.8 and 5.1 μmol g^{-1}). Note that the CH_4 production was enhanced greatly which may indicate cobalt are favorable for methane generation. Moreover, loading dual-single-atom can promote performance prominently. CAC2 shows the best performance as CO and CH_4 with 64.1 and 7.7 μmol g^{-1}. The decreasing efficiency (CAC3 and CAC4) with increasing cobalt may be due to the shelter effect from the loading of single atoms. In addition, the different types of single atoms were also studied. In Figure 3b, dual-single-atom such as Au/Ni, Au/In and Pt/Co, denoted as CAN2, CAI2, CPC2 (see details in Supporting Information), exhibit different performances while CAC2 shows the best activity and selectivity. It is noted that methane is the main final product with poor activity for CPC2 because of the strong absorption of CO on Pt.[40] The stability and reproducibility of CAC2 were also studied. After four-time recycles (28 h), production yields keep around 80% (Figure 3c). The XRD, X-ray photoelectron spectroscopy (XPS) and TEM (Figure S7-11) of CC2, CA2 and CAC2 after the performance test demonstrated that crystal structure and loaded single atoms are stable. To exclude the effect of possible carbon impurities, blank experiments under the same conditions but purged with the ultra-high-purity argon instead of CO_2, without/with illumination and photocatalysts,

negligible products in blank experiments were detected suggesting that these products were from the conversion of CO_2 photoreduction (Figure S12).

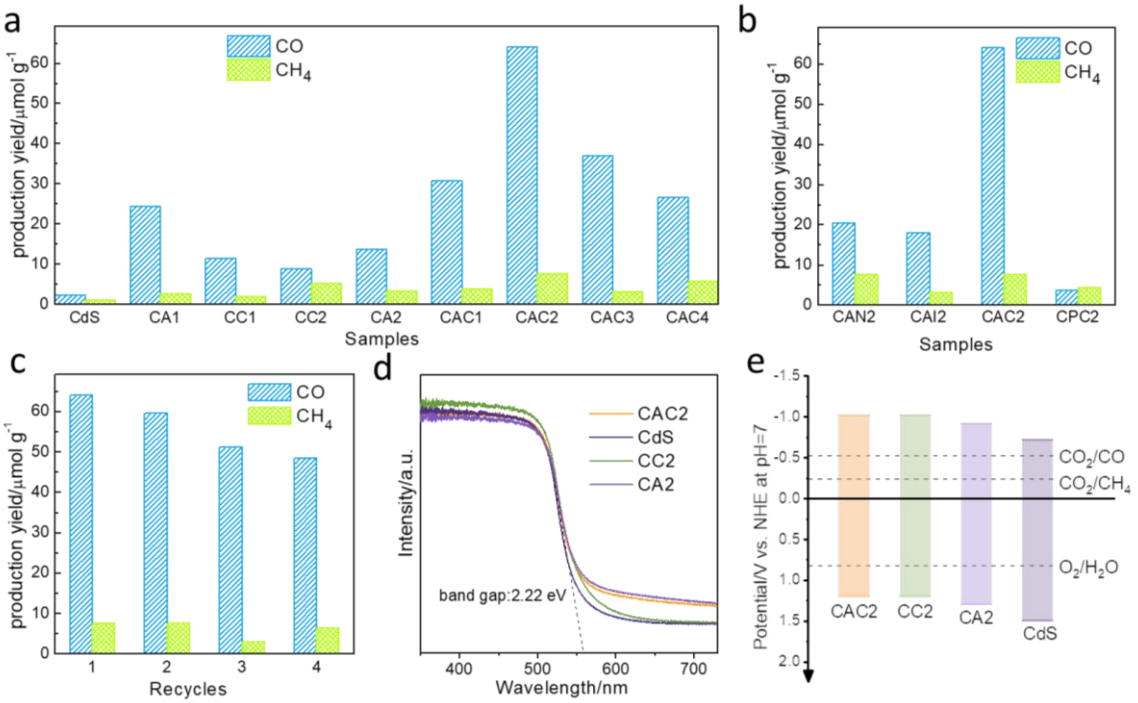

Figure 3. a) Photocatalytic CO_2 reduction performance of CdS, CA1, CC1, CC2, CA2, CAC1, CAC2, CAC3 and CAC4 under visible light illumination ($\lambda \geq 400$ nm); b) Photocatalytic CO_2 reduction performance of CAN2, CAI2, CAC2, CPC2 under visible light illumination ($\lambda \geq 400$ nm); c) Stability test of CAC2 under visible light illumination ($\lambda \geq 400$ nm). Each test lasts for 7 hours; d) UV-Vis spectra of CdS, CA2, CC2 and CAC2; e) Schematic illustration of the electronic band structures for different reactions.

For the photocatalytic CO_2 reduction, light absorption, photogenerated charges immigration and surface redox reactions are three important factors to the performance. To investigate the origin of boosted activity and reaction mechanism for photocatalytic CO_2 reduction, UV-Vis diffuse reflectance spectroscopy was conducted. As shown in Figure 3d, the absorption edge of these catalysts keeps the same at 558 nm, suggesting the band gap is 2.22 eV. Note that the light adsorption of decorated samples in the range of longer than 600 nm was also enhanced. To study the impacts, CO_2 photoreduction testing under 630 nm LED light was performed. Figure S13 shows that the dual-single-atom system shows a minor increase in the performance test, indicating that the increased absorption in visible light contributes to the CO_2 conversion. To study the band structure, the positions of valence band maximum (VBM) for CdS, CA2, CC2 and CAC2 were detected as 1.5, 1.3, 1.2 and 1.2 eV, respectively by XPS valence band spectra (Figure S14). From the VBM and band gap, the conduction band

minimum (CBM) of CdS, CA2, CC2 and CAC2 was estimated to be –0.72, –0.92, –1.02 and –1.02 eV. In Figure 3e, compared to pristine CdS, the CBM and VBM of these single-atom catalysts show upshift, indicating more reducing ability of the photogenerated electrons, facilitating the CO_2 photoreduction.

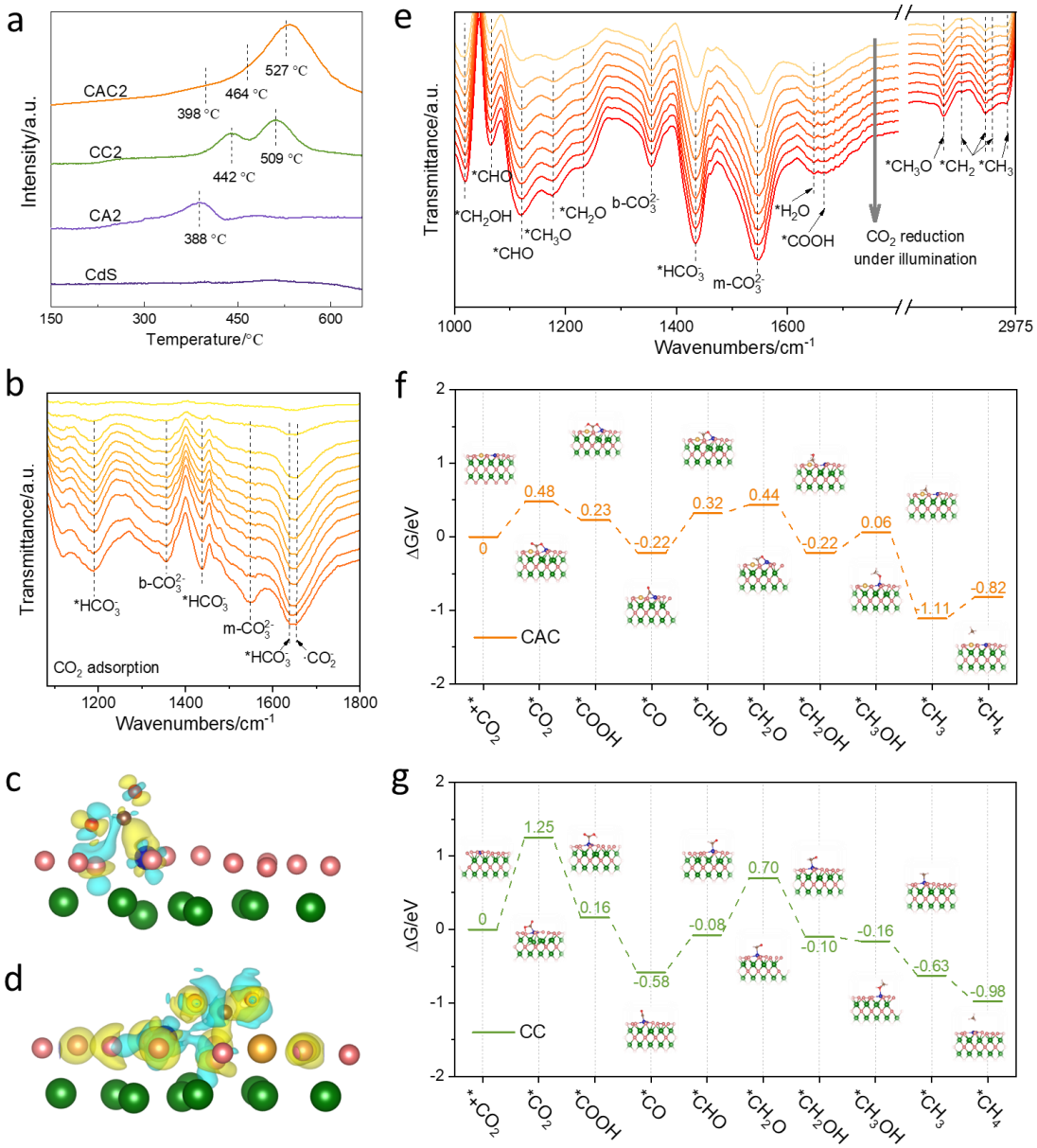

Figure 4. a) CO_2-TPD spectra of CdS, CC2, CA2 and CAC2; b) *In situ* DRIFTS for CO_2 adsorption of CAC2; the charge difference distributions of c) CA2 and d) CAC2 after CO_2 adsorption. The isosurfaces are 0.003 e $Å^{-3}$. Charge depletion and accumulation are labeled in cyan and yellow, respectively. Cadmium, sulfur, oxygen, carbon, cobalt and gold are denoted as green, pink, red, brown, blue and yellow balls, respectively; e) *In situ* DRIFTS of CO_2 photoreduction for CAC2; Computed Gibbs free energy and corresponding configurations for main reactions in photocatalytic CO_2 reduction to CH_4 for f) CAC and g) CC.

To study the photogenerated charge transfer process, transient-state photoluminescence (TSPL) spectroscopy, electrochemical impedance spectroscopy (EIS), and transient photocurrent (TPC) density measurement were executed. After fitting the TSPL curves in Figure S15 and Table S1, the average lifetimes of photogenerated electrons are decreased from 3.87 (CdS) to 3.37, 3.18 and 2.73 ns for CA2 and CC2 and CAC2. It indicates that the synergistic effect of Au and Co single atoms prominently accelerates the electron transfer to the surface under illumination.[8] Additionally, single-atom samples show a much greater intensity of TPC compared to CdS and CAC exhibits the highest intensity (Figure S16). It also confirms dual-single-atom significantly promotes the surface photogenerated electrons density. EIS spectra exhibit a decreased charge transfer resistance R_{ct} = 197 Ω for CAC2, compared to CdS (R_{ct} = 4300 Ω), CA2 (R_{ct} = 2600 Ω) and CC2 (R_{ct} = 3050 Ω), confirming the boosted electron transfer in dual-single-atom photocatalyst (Figure S17). These findings confirm that the dual-single-atom loaded CdS show a faster charge transfer process and higher surface electron density, favoring the photocatalytic process.

Reactant absorbed on the catalyst is the prerequisite for surface redox reactions. To investigate the affinity of catalysts for CO_2 molecules, CO_2-Temperature programmed desorption (TPD) and *in situ* diffuse reflectance infrared Fourier transform spectroscopy (DRIFTS) for these four samples were conducted. In Figure 4a, CdS shows no obvious CO_2 desorption peak. While metal-loaded CdS nanoparticles show much stronger desorption peaks due to more alkaline sites compared to that on pristine CdS. Because of the similar chemisorption sites, single atoms show similar CO_2 chemisorption peak locations. But the dual-single-atom shows a much stronger peak strength, suggesting the synergistic effect on this process. It is speculated that the increased chemisorption originates from the charge transfer process between multiple single atoms.

To further investigate the chemisorbed species, *in situ* DRIFTS was conducted in CO_2 atmosphere. As is shown in Figure 4b, there are several different intermediates for CO_2 chemisorption and some important intermediates are typical species for the products. The peaks at 1355 and 1547 cm^{-1} are attributed to bidentate carbonate (b-CO_3^{2-}) and monodentate carbonates (m-CO_3^{2-}).[41] The formation of HCO_3^- via the coadsorption of water and CO_2 is evidenced by the peaks at 1637, 1438 and 1190 cm^{-1}.[42] The rising peak at 1650 cm^{-1} with increasing time is from the vibration of $\cdot CO_2^-$, an important indicator towards CH_4.[9] The high concentration of surface chemisorption species shows dual-single-atom is more affinity to CO_2 molecules, which is critical for the following CO_2 photoreduction. As a comparison, in Figure

S18-20, CdS shows much weaker vibration peaks due to its less adsorbed surface moieties. Compared with the CAC2, CC2 shows similar CO_2 adsorption peaks with much-reduced strength, especially for the m-CO_3^{2-}. Moreover, b-CO_3^{2-} was reduced significantly in the spectra of CA2. These results are consistent with the abovementioned TPD-CO_2. To further reveal the CO_2 chemisorption process, simulation based on density functional theory (DFT) was conducted. Figure 4c and d show that more electrons were transferred from CAC to CO_2 compared to that from CC to CO_2, elucidating the efficient CO_2 activation on dual-single-atom system. To clarify the difference in the surface catalytic behavior of these four samples, we investigated the surface catalysis of these samples in the 0.5 M Na_2SO_4 via linear scan voltammogram (LSV) testing. As shown in Figure S21, all samples show higher current density in the CO_2-saturated 0.5 M Na_2SO_4 compared to that in the Ar-saturated electrolyte, denoting that these samples have obvious activity for the CO_2 reduction reaction. Notably, different CdS-based samples exhibit contrasted LSV responses in the CO_2-saturated 0.5 M Na_2SO_4. Figure S22 reveals that the cathodic current density of the CAC2 increases significantly below –1.0 V vs RHE and reaches –1.5 mA cm^{-2} at –1.55 V vs RHE. Also, CAC2 shows the lower onset potential for –0.97 vs RHE at j=10 mA cm^{-2} in Table S2 and the largest current density among these samples, implying its superior catalytic performance to other counterparts for CO_2 reduction. To determine the surface redox reaction under illumination, *in situ* DRIFTS were carried out. In Figure 4e, the critical indicator for CO_2-to-CO, i.e.,*COOH, was detected at 1667 cm^{-1}. The intensity of carbonate species (HCO_3^{2-}/CO_3^{2-}) was greatly increased with prolonged illumination time, confirming that the CO_2 can be more easily activated under illumination and provide enough intermediates for the following conversion. Additionally, there were some new bands, for example, CHO, CH_2O CH_3OH and CH_3, which are important intermediates to CH_4 generation.[9, 43] Therefore, it is concluded that the reaction pathways on catalysts are:

$*CO_2 \rightarrow HCO_3^{2-}/CO_3^{2-} \rightarrow *COOH \rightarrow *CO \rightarrow *CHO \rightarrow *CH_2O \rightarrow *CH_3OH \rightarrow *CH_3 \rightarrow *CH_4$

The proposed reaction pathway on these samples was studied via computation of corresponding free energy changes (ΔG) for each reaction step (Figure 4f and g; Figure S23). The overall energy barrier for CAC is lower than the others, convincing that the dual-single-atom catalyst prominently boosts the CO_2 photoreduction. Note that the rate-limited step is the chemisorption of CO_2 molecules with the largest energy barrier at 1.25 eV for CC. It is reduced to 0.48 eV for CAC, confirming that the dual-single-atom favors CO_2 photoreduction. The reason can be

attributed to the surface charge transfer change illustrated in Figure 4 c and d. More electron transfer occurs between catalysts and CO_2 molecules, resulting in easier activation of the reactant on dual-single-atom. Compared to CC and CAC, the CO_2 chemisorption is more difficult on CA and CdS. As evidenced in the Figure S24, there is very trace electron transfer between CO_2 and CA or CdS surface. Additionally, the bond angle (180°) and bond length (1.17 Å) for absorbed CO_2 molecules are not changed. Moreover, the largest energy barrier step for CAC is the hydrogenation of *CO, which indicates that CO is the main final product.

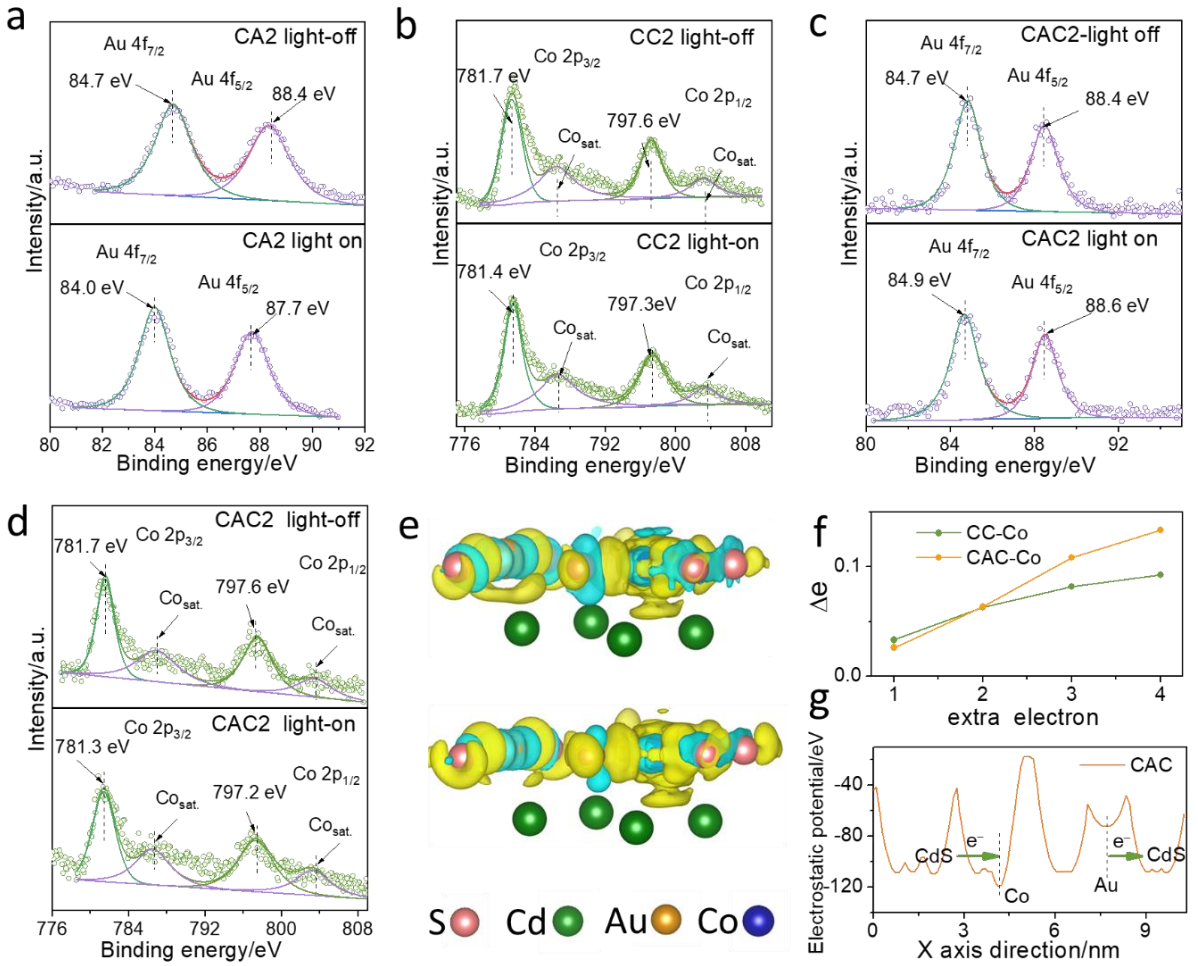

Figure 5. Quasi *in situ* Au 4f XPS spectra of a) CA2 in dark and under illumination; Co 2p XPS spectra of b) CC2 in dark and under illumination; Au 4f XPS spectra of c) CAC2 in dark and under illumination; Co 2p XPS spectra of d) CAC2 in dark and under illumination; electron density distribution of e) CAC2 (top-side) and CAC2 after introducing extra electrons in the model (bottom-side). The isosurface value is 0.0045e $Å^{-3}$. Charge depletion and accumulation are labeled in cyan and yellow, respectively; f) The increasing value of valence electrons of Co atom in CAC model after introducing different extra electrons; g) Electrostatic potential energy along the X-axis for CAC model.

To identify the charge population of CdS after loading single Au and Co atoms, quasi *in situ* XPS spectra were presented. For CA2 sample (Figure 5a), the peaks indexed to Au 4f have a shift to lower binding energy (0.7 eV) after the illumination is on, indicating that the photogenerated electrons transfer from CdS to Au single atoms on CA2. Similarly, the photogenerated electrons also transfer from CdS to Co single atoms in CC2 samples after the light is on (Figure 5b). While for CAC2 system, the peaks corresponding to Au 4f show a shift of around 0.2 eV to higher binding energy (Figure 5c), suggesting Au single atoms lose electrons after illumination is on. This is inverse to the photogenerated electron transfer direction in CA2 sample. Meantime, the Co 2p peaks have a shift of 0.4 eV (Figure 5d) to lower binding energy, demonstrating Co can accumulate photogenerated electrons. Hence, it is observed that electrons are localized around single Au or Co atoms in CA2 or CC2 system. After the dual-single-atom is loaded simultaneously, single Au atoms will delocalize electrons, which will accumulate around single Co atoms. To study the electron redistribution process and mechanism, DFT computation was performed. From Figure 5e, consistent results were also observed from the computation. After extra electrons were introduced into the model, the charge density difference presented that electrons around Au were delocalized and transferred to Co atoms.[44-45] The increasing electrons around Co atom were analyzed by Bader charge. As Figure 5f shows, Co in CAC system can accumulate more electrons than that of Co in CC system, indicating that loading dual-single-atom promotes electron redistribution. The integrated PDOS areas (Figure S25) of uncaptured single atoms electrons above the Fermi (F_E) level in CC, CA and CAC are calculated and shown in Table S3. The more uncaptured electrons indicate the relative electron deficient property of catalysts, confirming the weaker ability for capturing electrons from the matrix CdS nanoparticles.[33, 46] Au atoms in CA is 0.4 which is much less than that in CAC (1.1). However, Co atoms in CC is 1.8 much more than that in CAC (1.2). Therefore, Au in CA and Co in CAC show a much stronger ability for capturing electrons from CdS than Au in CAC and Co in CC respectively. To identify the internal factors affecting electron redistribution, the potential profile was studied. In Figure 5g and S26, the potential energy of CdS is higher than that of Co atom while much lower than that of Au atom. Therefore, a driving force promotes electron transfer from Au to CdS and CdS to Co. On the contrary, for CC and CA models, both Co and Au show lower potential energy than CdS (Figure S27 and S28), resulting in electron accumulation around a metal single atom (Au/Co). Hence, electrons are localized around Au/Co single atoms on CdS nanoparticles while a new transfer channel from Au to CdS then Co is built after dual-single-atom is loaded on CdS.

Conclusion

In conclusion, with a new charge transfer channel formed, the electron transfer direction can be modulated via loading Au and Co single atoms on CdS nanoparticles simultaneously. The photogenerated charge separation and migration and the adsorption and activation of CO_2 molecules are both significantly improved by the dual-single-atom system. By combining advanced characterizations, a driving force between single atoms and CdS crystal because of the different electrostatic potential energy reverses the electron transfer direction. This new type of dual-single-atom loading CdS exhibited 28-fold production yields than that of pristine CdS, together with a stability of more than 28 h of CO_2 photoreduction reaction. Researchers who concentrate on photocatalysis and single atoms will benefit from developing dual-single-atom catalysts and understanding the mechanism for charge transfer process in this system.

Acknowledgments

This work was supported financially by the Australian Research Council (ARC) through the Discovery Project Program (DP160104866, FL170100154 and DE200100629). The authors thank Dr. Huimin Yu, University of South Australia, for the XPS testing, Mr. Zhenpu Lu, Tianjin University for the TPD-CO_2 test and Dr. Ashley Slattery, Adelaide Microscopy, The University of Adelaide for technical assistance. Y.Z. acknowledges financial support from the Australian Government Research Training Program Scholarship (RTP). This research was undertaken on the X-ray absorption spectroscopy beamline at the Australian Synchrotron, part of ANSTO.

Keywords

photocatalytic CO_2 reduction, electron localization, dual-single-atom, charge transfer modulation, *in situ* spectroscopy

References

(1) Zhang, Y.; Xia, B.; Ran, J.; Davey, K.; Qiao, S.-Z., Atomic-Level Reactive Sites for Semiconductor-Based Photocatalytic CO_2 Reduction. *Adv. Energy Mater.* **2020**, *10*, 1903879.
(2) Albero, J.; Peng, Y.; Garcia, H., Photocatalytic CO_2 Reduction to C_{2+} Products. *ACS Catal.* **2020**, *10*, 5734-5749.
(3) Fu, J.; Jiang, K.; Qiu, X.; Yu, J.; Liu, M., Product Selectivity of Photocatalytic CO_2 Reduction Reactions. *Mater. Today* **2020**, *32*, 222-243.

(4) Zhang, Y.; Yao, D.; Xia, B.; Jaroniec, M.; Ran, J.; Qiao, S.-Z., Photocatalytic CO_2 Reduction: Identification and Elimination of False-Positive Results. *ACS Energy Lett.* **2022**, *7*, 1611-1617.

(5) Ji, S.; Qu, Y.; Wang, T.; Chen, Y.; Wang, G.; Li, X.; Dong, J.; Chen, Q.; Zhang, W.; Zhang, Z.; Liang, S.; Yu, R.; Wang, Y.; Wang, D.; Li, Y., Rare-Earth Single Erbium Atoms for Enhanced Photocatalytic CO_2 Reduction. *Angew. Chem. Int. Ed.* **2020**, *59*, 10651-10657.

(6) Zhu, S.; Li, X.; Jiao, X.; Shao, W.; Li, L.; Zu, X.; Hu, J.; Zhu, J.; Yan, W.; Wang, C.; Sun, Y.; Xie, Y., Selective CO_2 Photoreduction into C_2 Product Enabled by Charge-Polarized Metal Pair Sites. *Nano Lett.* **2021**, *21*, 2324-2331.

(7) Zhang, Y.; Zhi, X.; Harmer, J.; Xu, H.; Davey, K.; Ran, J.; Qiao, S.-Z., Facet-Specific Active Surface Regulation of Bi_xMO_y (M=Mo, V, W) Nanosheets for Boosted Photocatalytic CO_2 reduction. *Angew. Chem. Int. Ed.* **2022**, *61*, e202212355.

(8) Cao, Y.; Guo, L.; Dan, M.; Doronkin, D. E.; Han, C.; Rao, Z.; Liu, Y.; Meng, J.; Huang, Z.; Zheng, K.; Chen, P.; Dong, F.; Zhou, Y., Modulating Electron Density of Vacancy Site by Single Au Atom for Effective CO_2 Photoreduction. *Nat. Commun.* **2021**, *12*, 1675.

(9) Sheng, J.; He, Y.; Huang, M.; Yuan, C.; Wang, S.; Dong, F., Frustrated Lewis Pair Sites Boosting CO_2 Photoreduction on Cs_2CuBr_4 Perovskite Quantum Dots. *ACS Catal.* **2022**, *12*, 2915-2926.

(10) Zhang, Y.; Yao, D.; Xia, B.; Xu, H.; Tang, Y.; Davey, K.; Ran, J.; Qiao, S.-Z., ReS_2 Nanosheets with *In Situ* Formed Sulfur Vacancies for Efficient and Highly Selective Photocatalytic CO_2 Reduction. *Small Sci.* **2021**, *1*, 2000052.

(11) Zhang, Y.; Wang, X.; Dong, P.; Huang, Z.; Nie, X.; Zhang, X., A Green Synthetic Approach for Self-Doped TiO_2 with Exposed Highly Reactive Facets Showing Efficient CO_2 Photoreduction under Simulated Solar Light. *Green Chem.* **2018**, *20*, 2084-2090.

(12) Yu, H.; Chen, F.; Li, X.; Huang, H.; Zhang, Q.; Su, S.; Wang, K.; Mao, E.; Mei, B.; Mul, G.; Ma, T.; Zhang, Y., Synergy of Ferroelectric Polarization and Oxygen Vacancy to Promote CO_2 Photoreduction. *Nat. Commun.* **2021**, *12*, 4594.

(13) Di, J.; Zhu, C.; Ji, M.; Duan, M.; Long, R.; Yan, C.; Gu, K.; Xiong, J.; She, Y.; Xia, J.; Li, H.; Liu, Z., Defect-Rich $Bi_{12}O_{17}Cl_2$ Nanotubes Self-Accelerating Charge Separation for Boosting Photocatalytic CO_2 Reduction. *Angew. Chem. Int. Ed.* **2018**, *57*, 14847-14851.

(14) Hao, L.; Huang, H.; Zhang, Y.; Ma, T., Oxygen Vacant Semiconductor Photocatalysts. *Adv. Funct. Mater.* **2021**, *31*, 2100919.

(15) He, Y.; Rao, H.; Song, K.; Li, J.; Yu, Y.; Lou, Y.; Li, C.; Han, Y.; Shi, Z.; Feng, S., 3D Hierarchical $ZnIn_2S_4$ Nanosheets with Rich Zn Vacancies Boosting Photocatalytic CO_2 Reduction. *Adv. Funct. Mater.* **2019**, *29*, 1905153.

(16) Di, J.; Zhao, X.; Lian, C.; Ji, M.; Xia, J.; Xiong, J.; Zhou, W.; Cao, X.; She, Y.; Liu, H.; Loh, K. P.; Pennycook, S. J.; Li, H.; Liu, Z., Atomically-Thin Bi_2MoO_6 Nanosheets with Vacancy Pairs for Improved Photocatalytic CO_2 reduction. *Nano Energy* **2019**, *61*, 54-59.

(17) Liu, L.; Wang, S.; Huang, H.; Zhang, Y.; Ma, T., Surface Sites Engineering on Semiconductors to Boost Photocatalytic CO_2 Reduction. *Nano Energy* **2020**, *75*, 104959.

(18) Cho, K. M.; Kim, K. H.; Park, K.; Kim, C.; Kim, S.; Al-Saggaf, A.; Gereige, I.; Jung, H.-T., Amine-Functionalized Graphene/CdS Composite for Photocatalytic Reduction of CO_2. *ACS Catal.* **2017**, *7*, 7064-7069.

(19) Zhang, Y.; Wang, X.; Dong, P.; Huang, Z.; Nie, X.; Zhang, X., TiO_2 Surfaces Self-Doped with Ag Nanoparticles Exhibit Efficient CO_2 Photoreduction under Visible Light. *RSC Adv.* **2018**, *8*, 15991-15998.

(20) Xiong, X.; Mao, C.; Yang, Z.; Zhang, Q.; Waterhouse, G. I. N.; Gu, L.; Zhang, T., Photocatalytic CO_2 Reduction to CO over Ni Single Atoms Supported on Defect-Rich Zirconia. *Adv. Energy Mater.* **2020**, *10*, 2002928.

(21) Dong, X.-Y.; Si, Y.-N.; Wang, Q.-Y.; Wang, S.; Zang, S.-Q., Integrating Single Atoms with Different Microenvironments into One Porous Organic Polymer for Efficient Photocatalytic CO_2 Reduction. *Adv. Mater.* **2021**, *33*, 2101568.

(22) Yu, Y.; Dong, X.; Chen, P.; Geng, Q.; Wang, H.; Li, J.; Zhou, Y.; Dong, F., Synergistic Effect of Cu Single Atoms and Au–Cu Alloy Nanoparticles on TiO_2 for Efficient CO_2 Photoreduction. *ACS Nano* **2021**, *15*, 14453-14464.

(23) Shi, H.; Wang, H.; Zhou, Y.; Li, J.; Zhai, P.; Li, X.; Gurzadyan, G. G.; Hou, J.; Yang, H.; Guo, X., Atomically Dispersed Indium-Copper Dual-Metal Active Sites Promoting C-C Coupling for CO_2 Photoreduction to Ethanol. *Angew. Chem. Int. Ed.* **2022**, *61*, e202208904.

(24) Li, Y.; Li, B.; Zhang, D.; Cheng, L.; Xiang, Q., Crystalline Carbon Nitride Supported Copper Single Atoms for Photocatalytic CO_2 Reduction with Nearly 100% CO Selectivity. *ACS Nano* **2020**, *14*, 10552-10561.

(25) Jia, G.; Sun, M.; Wang, Y.; Shi, Y.; Zhang, L.; Cui, X.; Huang, B.; Yu, J. C., Asymmetric Coupled Dual-Atom Sites for Selective Photoreduction of Carbon Dioxide to Acetic Acid. *Adv. Funct. Mater.* **2022**, *32*, 2206817.

(26) Luo, Z.; Ye, X.; Zhang, S.; Xue, S.; Yang, C.; Hou, Y.; Xing, W.; Yu, R.; Sun, J.; Yu, Z.; Wang, X., Unveiling the Charge Transfer Dynamics Steered by Built-in Electric Fields in BiOBr Photocatalysts. *Nat. Commun.* **2022**, *13*, 2230.

(27) Xia, B.; He, B.; Zhang, J.; Li, L.; Zhang, Y.; Yu, J.; Ran, J.; Qiao, S.-Z., TiO_2/$FePS_3$ S-Scheme Heterojunction for Greatly Raised Photocatalytic Hydrogen Evolution. *Adv. Energy Mater.* **2022**, *12*, 2201449.

(28) Zhang, L.; Mohamed, H. H.; Dillert, R.; Bahnemann, D., Kinetics and Mechanisms of Charge Transfer Process in Photocatalystic Systems: A Reivew. *J. Photochem. Photobiol.* **2012**, *13*, 263-276.

(29) Zhang, W.; Fu, C.; Low, J.; Duan, D.; Ma, J.; Jiang, W.; Chen, Y.; Liu, H.; Qi, Z.; Long, R.; Yao, Y.; Li, X.; Zhang, H.; Liu, Z.; Yang, J.; Zou, Z.; Xiong, Y., High-Performance Photocatalytic Nonoxidative Conversion of Methane to Ethane and Hydrogen by Heteroatoms-Engineered TiO_2. *Nat. Commun.* **2022**, *13*, 2806.

(30) Liu, Y.; Yang, W.; Chen, Q.; Cullen, D.A.; Xie, Z.; Lian, T., Pt Particle Size Affects Both the Charge Separation and Water Reduction Efficiencies of CdS-Pt Nanorod Photocatalysts for Light Driven H_2 Generation. *J. Am. Chem. Soc.* **2022**, *144*, 2705-2715.

(31) Peng, H.; Yang, T.; Lin, H.; Xu, Y.; Wang, Z.; Zhang, Q.; Liu, S.; Geng, H.; Gu, L.; Wang, C.; Fan, X.; Chen, W.; Huang, X., Ru/In Dual-Single Atoms Modulated Charge Separation for Significantly Accelerated Photocatalytic H_2 Evolution in Pure Water. *Adv. Energy Mater.* **2022**, *12*, 2201688.

(32) Zhang, L.; Long, R.; Zhang, Y.; Duan, D.; Xiong, Y.; Zhang, Y.; Bi, Y., Direct Observation of Dynamic Bond Evolution in Single-Atom Pt/C_3N_4 Catalysts. *Angew. Chem. Int. Ed.* **2020**, *59*, 6224-6229.

(33) Zhou, P.; Chen, H.; Chao, Y.; Zhang, Q.; Zhang, W.; Lv, F.; Gu, L.; Zhao, Q.; Wang, N.; Wang, J.; Guo, S., Single-Atom Pt-I_3 Sites on All-Inorganic Cs_2SnI_6 Perovskite for Efficient Photocatalytic Hydrogen Production. *Nat. Commun.* **2021**, *12*, 4412.

(34) Wang, C.; Wang, K.; Feng, Y. B.; Li, C.; Zhou, X. Y.; Gan, L. Y.; Feng, Y. J.; Zhou, H. J.; Zhang, B.; Qu, X. L.; Li, H.; Li, J. Y.; Li, A.; Sun, Y. Y.; Zhang, S. B.; Yang, G.; Guo, Y.; Yang, S. Z.; Zhou, T. H.; Dong, F.; Zheng, K.; Wang, L. H.; Huang, J.; Zhang, Z.; Han, X. D., Co and Pt Dual-Single-Atoms with Oxygen-Coordinated Co-O-Pt Dimer Sites for Ultrahigh Photocatalytic Hydrogen Evolution Efficiency. *Adv. Mater.* **2021**, *33*, 2003327.

(35) Cheng, L.; Yue, X.; Wang, L.; Zhang, D.; Zhang, P.; Fan, J.; Xiang, Q., Dual-Single-Atom Tailoring with Bifunctional Integration for High-Performance CO_2 Photoreduction. *Adv. Mater.* **2021**, *33*, 2105135.

(36) Zhao, X.; Wang, F.; Kong, X.-P.; Fang, R.; Li, Y., Dual-Metal Hetero-Single-Atoms with Different Coordination for Efficient Synergistic Catalysis. *J. Am. Chem. Soc.* **2021**, *143*, 16068-16077.

(37) Tiwari, M.; Gupta, S.; Prakash, R., One Pot Synthesis of Coordination Polymer 2,5-Dimercapto-1,3,4-Thiadiazole-Gold and Its Application in Voltametric Sensing of Resorinol. *RSC Adv.* **2014**, *4*, 25675-25682.

(38) Shen, M.; Yin, W.; Li, J.; Zhang, H.; Chen, L., One-Step Facile Hydrothermal Synthetic Route to Prepare CoS Nanoplates as Counter Electrode Material for Fiber-Shaped Dye-Sensitized Solar Cells. *J. Mater. Sci. Mater.* **2018**, *29*, 13709-13714.

(39) Li, J.; Liu, Y.; Tang, X.; Xu, L.; Min, L.; Xue, Y.; Hu, X.; Yang, Z., Multiwalled Carbon Nanotubes Coated with Cobalt(II) Sulfide Nanoparticles for Electrochemical Sensing of Glucose via Direct Electron Transfer to Glucose Oxidase. *Microchim. Acta* **2020**, *187*, 80.

(40) Chung, D. Y.; Kim, H.-I.; Chung, Y.-H.; Lee, M. J.; Yoo, S. J.; Bokare, A. D.; Choi, W.; Sung, Y.-E., Inhibition of CO Poisoning on Pt Catalyst Coupled with the Reduction of Toxic Hexavalent Chromium in a Dual-Functional Fuel Cell. *Sci. Rep.* **2014**, *4*, 7450.

(41) Di, T.; Zhu, B.; Cheng, B.; Yu, J.; Xu, J., A Direct Z-Scheme g-C_3N_4/SnS_2 Photocatalyst with Superior Visible-Light CO_2 Reduction Performance. *J. Catal.* **2017**, *352*, 532-541.

(42) Yang, Y.; Chai, Z.; Qin, X.; Zhang, Z.; Muhetaer, A.; Wang, C.; Huang, H.; Yang, C.; Ma, D.; Li, Q.; Xu, D., Light-Induced Redox Looping of a Rhodium/Ce_xWO_3 Photocatalyst for Highly Active and Robust Dry Reforming of Methane. *Angew. Chem. Int. Ed.* **2022**, *61*, e202200567.

(43) Liu, P.; Huang, Z.; Gao, X.; Hong, X.; Zhu, J.; Wang, G.; Wu, Y.; Zeng, J.; Zheng, X., Synergy between Palladium Single Atoms and Nanoparticles *via* Hydrogen Spillover for Enhancing CO_2 Photoreduction to CH_4. *Adv. Mater.* **2022**, *34*, 2200057.

(44) Zhao, Q.; Liu, L.; Li, S.; Liu, R., Built-In Electric Field-Assisted Charge Separation over Carbon Dots-Modified Bi_2WO_6 Nanoplates for Photodegradation. *Appl. Surf. Sci.* **2019**, *465*, 164-171.

(45) Zhang, Y.; Zhao, J.; Wang, H.; Xiao, B.; Zhang, W.; Zhao, X.; Lv, T.; Thangamuthu, M.; Zhang, J.; Guo, Y.; Ma, J.; Lin, L.; Tang, J.; Huang, R.; Liu, Q., Single-atom Cu Anchored Catalysts for Photocatalytic Renewable H_2 Production with a Quantum Efficiency of 56%. *Nat. Commun.* **2022**, *13*, 58.

(46) Zhou, P.; Lv, F.; Li, N.; Zhang, Y.; Mu, Z.; Tang, Y.; Lai, J.; Chao, Y.; Luo, M.; Lin, F.; Zhou, J.; Su, D.; Guo, S., Strengthening Reactive Metal-Support Interaction to Stabilize High-

Density Pt Single Atoms on Electron-Deficient g-C_3N_4 for Boosting Photocatalytic H_2 Production. *Nano Energy* **2019**, *56*, 127-137.

Table of contents

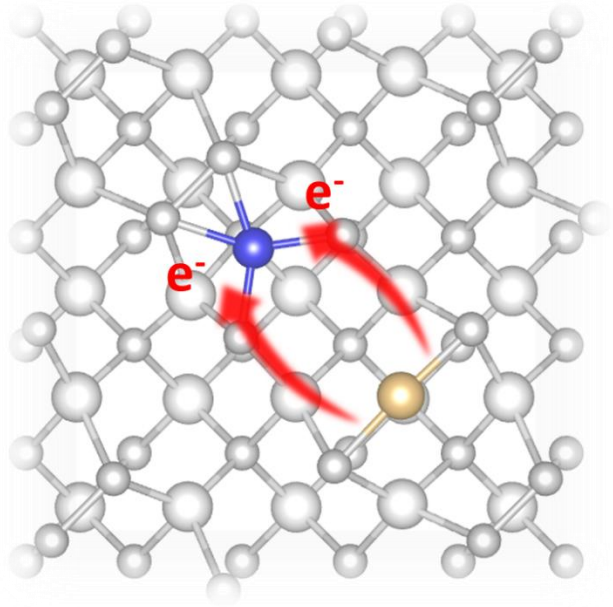

This work reports CdS nanoparticles decorated with Co and Au single atoms. This new dual-single-atom system shows modulated photogenerated electrons transfer and separation mechanism. Localized electrons around Co single atoms boost the photocatalytic CO_2 reduction performance.

Supporting information

Reversed Electron Transfer in Dual-Single-Atom Promotes CO_2 Photoreduction

Yanzhao Zhang, Yan Jiao, Jingrun Ran and Shi-Zhang Qiao**

Y. Zhang, Dr. Y. Jiao, Dr. J. Ran, Prof. S.Z. Qiao
School of Chemical Engineering & Advanced Materials, The University of Adelaide, Adelaide, SA 5005, Australia.
E-mail: s.qiao@adelaide.edu.au; jingrun.ran@adelaide.edu.au

Chemicals and Material Synthesis

Chemicals: Cadium nitrate pentahydrate ($Cd(NO_3)_2 \cdot 4H_2O$, Sigma Aldrich), sodium sulfide nonahydrate ($Na_2S \cdot 9H_2O$, Sigma Aldrich), gold(III) chloride trihydrate ($HAuCl_4 \cdot 3H_2O$, Sigma Aldrich), cobalt(II) chloride hexahydrate ($CoCl_2 \cdot 6H_2O$, Sigma Aldrich), nickel(II) chloride hexahydrate ($NiCl_2 \cdot 6H_2O$, Sigma Aldrich), indium(III) chloride tetrahydrate($InCl_3 \cdot 4H_2O$, Sigma Aldrich), chloroplatinic acid hexahydrate ($H_2PtCl_6 \cdot 6H_2O$, Sigma Aldrich), sodium borohydride ($NaBH_4$, Sigma Aldrich). All of the chemicals are Analytical reagents and used directly without any further purification. Ultrapure water used throughout all experiments was purified through an Adelab Millipore system. Ultra-high purity Ar (99.999%) was purchased from BOC Gas, Australia.

Synthesis of CdS nanoparticles: in the typical synthesis, CdS nanoparticles were prepared by a precipitation-hydrothermal method. 3.424g $Cd(NO_3)_2 \cdot 4H_2O$ was added into 87 mL deionized water followed by stirring for 60 min. Subsequently, 20 mL 0.9 M Na_2S aqueous solution was added dropwise into the solution, followed by stirring for 1 h. The suspension was transferred to a 200 mL Teflon-lined autoclave and kept at 180 °C for 12 h. The products were collected and washed with water three times. After being dried in the frozen dryer, the sample was collected. The resulting sample was labelled as CdS.

Synthesis of Co single atom loaded CdS nanoparticles: in the typical synthesis, 100 mg CdS nanoparticles were dispersed in the deionized water. A certain amount (0.3 and 0.6 mL) of $Co(NO_3)_2$ solution (20 mM) was dropped into the former solution under stirring followed by sonication for 20 min. Then, 2 mL $NaBH_4$ solution (20 mM) was dropped into the above solution under stirring. After 12 hours the products were collected and washed with water three times and dried in the frozen dryer. The different loading amount samples were denoted as CC1 and CC2.

Synthesis of Au single atom loaded CdS nanoparticles: in the typical synthesis, 100 mg CdS nanoparticles were dispersed in deionized water. Then, a certain amount of $HAuCl_4$ solution (20 mM) was dropped into the former solution under stirring. The reaction was kept at 70 ℃ for 6 hours. Lastly, the products were collected and washed with water three times and dried in the frozen dryer. The samples were denoted as CA1 and CA2, respectively, according to the added $HAuCl_4$ solution as 0.3 and 0.6 mL.

Synthesis of Au and Co single atom loaded CdS nanoparticles: The preparation process is similar with CC. CC was prepared first, then Au single atom was loaded as the same method

with CA1. The samples were denoted as CAC1, CAC2, CAC3 and CAC4, respectively, according to the added $CoCl_2$ solution as 0.15, 0.3, 0.45 and 0.6 mL.

Synthesis of Au/Ni, Au/In and Pt/Co single atom loaded CdS nanoparticles: the preparation process is similar with CAC2 by $HAuCl_4$, $NiCl_2$, $InCl_3$ and H_2PtCl_6 solutions as the precursors. These samples were denoted as CAN2, CAI2 and CPC2, respectively.

Materials Characterization

X-ray diffraction: XRD data were collected on a powder X-ray diffractometer (Miniflex, Rigaku) using Cu Kα radiation. Raman spectroscopy data were collected using a confocal Raman microscope (Horiba LabRAM HR Evolution) with a 10X objective and a 532 nm laser in all experiments. Morphology observation and EDS spectra were conducted on a Tecnai G2 transmission electron microscopy (TEM). Transmission electron microscopy under STEM mode (FEI Titan Thermis, 200 kV) was utilized to obtain HRTEM and EDS mapping. Valance band XPS spectra measurement was performed on a VGESCALAB 210 XPS spectrometer with Mg Kα source. The binding energies were referenced to the C 1s peak at 284.8 eV. UV Visible diffuse reflectance spectra were obtained on a UV-Vis spectrophotometer (UV2600, Shimadzu, Japan). The transient-state PL decay curves were obtained on an FLS1000 fluorescence lifetime spectrophotometer (Edinburgh Instruments, UK). The X-ray absorption was obtained from XAS beamline of Australian Synchrotron (ANSTO, Melbourne). The XAS raw data were background-substracted, normalized and Fourier-transformed with Athena. CO_2-TPD was carried out with a Micromeritics AutoChem2920 apparatus.

Photocatalytic Tests and Electrochemical Measurements

Photocatalytic CO_2 reduction: the photocatalytic performance tests were conducted in a 287 mL home-made reactor sealed with silicone rubber septa at ambient conditions. A 300 W Xenon lamp with 400 nm filter was employed as the visible light source. In a typical test, 20 mg of photocatalysts were dispersed in water then loaded on the glass fibre filter (Whatman) and dried under infrared light. Before illumination, the reactor was purged by laser-grade purity CO_2 for 1 hour. The product was collected from the reactor per hour by the syringe and analysed by a gas chromatograph (GC, 7890B, Agilent). The GC is equipped with plot-Q and a 5 Å sieve column (Agilent) in series, TCD and methanizer/FID detectors and UHP Ar (BOC) as the carrier gas.

Electrochemical and photoelectrochemical test: Mott-Schottky plots were obtained on an electrochemical analyser (CHI760D instruments) using 0.5 M Na_2SO_4 aqueous solution. The

test was conducted in a standard, three-electrode system with the as-fabricated samples as the working electrode, a Pt wire as the counter electrode, and Ag/AgCl (saturated KCl) as a reference electrode. The alternating current (AC) frequency applied was 1200 Hz. In the identical three-electrode system the EIS measurement was carried out in the range from 1 to 2 x 10^5 Hz with an AC amplitude of 20 mV. 0.5 M Na_2SO_4 was employed as the electrolyte. The polarization curves were acquired in the three-electrode system. The bias sweep range was -1.5 to -0.8 V *vs.* Ag/AgCl with a step size of 5 mV. 0.5 M Na_2SO_4 was applied as the electrolyte. In the same three-electrode system the TPC response measurement was carried out. A 300 W Xenon light was utilized as the light source. 0.5 M Na_2SO_4 aqueous solution was applied as the electrolyte. The working electrodes were prepared as follows: 5 mg sample, 960 μL of mixed solvent ($V_{isoproponal}$: V_{water} = 1 : 2) with the addition of 40 μL of 5% Nafion. The dispersion was vigorously sonicated for 6 h to form a homogenous ink. A doctor-blade method was used to coat the slurry onto a 2 x 1.5, cm FTO glass electrode.

***In situ* diffuse reflectance infrared spectroscopy (DRIFTS)**

All IR spectra were performed using a Nicolet iS20 spectrometer equipped with an HgCdTe (MCT) detector cooled with liquid nitrogen and a VeeMax III (PIKE technologies) accessory. The *in situ* DRIFTS studies were performed using a Praying Mantis DRIFTS accessory and a reactor (Harrick Scientific, HVC-DRP). A 300 W Xe lamp (ZhongJiaoJinYuan) connects a liquid light guide for irradiation.

The sample was purged with wet CO_2 for 40 min until the sample spectrum was stable. The CO_2 adsorption process in dark was recorded until it is stable. Next, the spectra under irradiation conditions were recorded as a function of time to investigate the dynamics of surface carbon contamination.

Quasi *in situ* XPS test

Quasi *in situ* XPS measurements were performed on an ultrahigh vaccum system using monochromatized Al Kα irradiation (hν = 1486.6 eV) and an Omicron Sphera II hemispherical electron energy analyser. All of the XPS spectra were collected in dark firstly. Then, the quasi *in situ* XPS were conducted after the samples were illumintated for 3 min. The binding energies were referenced to the C 1s peak at 284.8 eV.

Computational Methods

All DFT calculations were performed with the Vienna Ab Initio Simulation Package (VASP) code.[1] The Perdew-Burke-Ernzerhof (PBE) functional was employed for electron exchange-correlation within the generalized gradient approximation.[2] The projector-augmented wave (PAW) method was used to describe the ionic cores.[3] The geometry optimizations were performed with a 520 eV cut-off energy for plane wave expansion. The ionic relaxations were conducted until all the forces were smaller than 0.02 $eV \cdot Å^{-1}$. A Gaussian smearing was used with 0.2 eV width and a (2 × 2 × 1) Gamma k-point grid was applied. The Tkatchenko-Scheffler method was employed to describe long-range van der Waals interactions.[4]

The CdS was optimized in a 2 × 2 × 1 supercell. A vacuum space of 15 Å was applied to separate the interactions between neighbouring slabs. Co, Au and Co/Au single atom models were built based on the optimized CdS model and were denoted as CC, CA and CAC, respectively. The computational hydrogen electrode (CHE) model was employed for free energy calculations.[5] The free energies of intermediates were obtained by $G = E + ZPE - TS$. The zero-point energy (ZPE) and entropy correction (TS) were calculated from vibration analysis and used to convert electronic energy (E) into free energy (G) at 298.15 K.

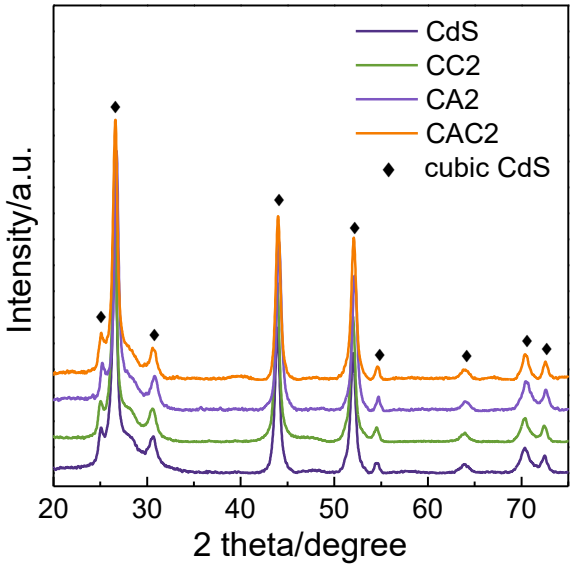

Figure S1. X-ray diffraction patterns of synthesised samples. All of the diffraction peaks can be attributed to the cubic CdS (JCPDS #10-0454).

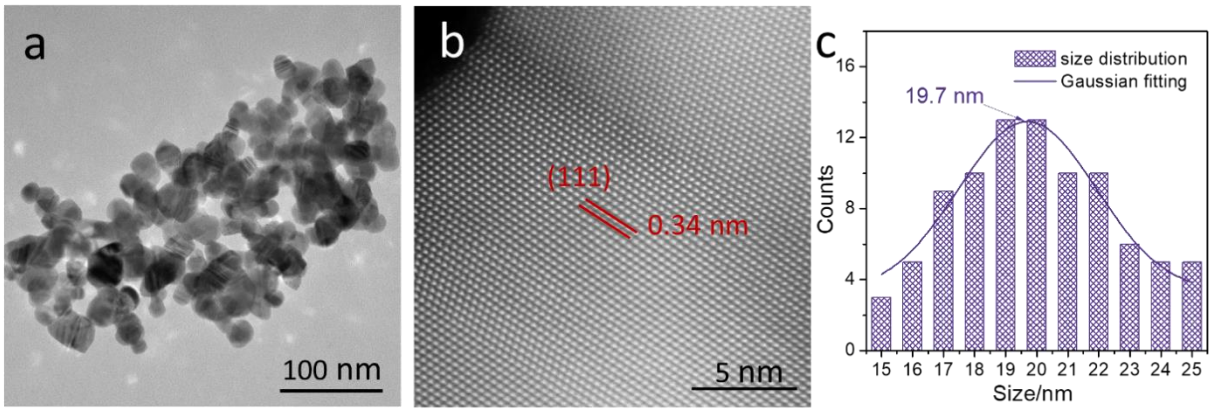

Figure S2. a) TEM image and b) HAADF-STEM images of CdS nanoparticles, c) distribution and Gaussian fitting of CdS nanoparticles.

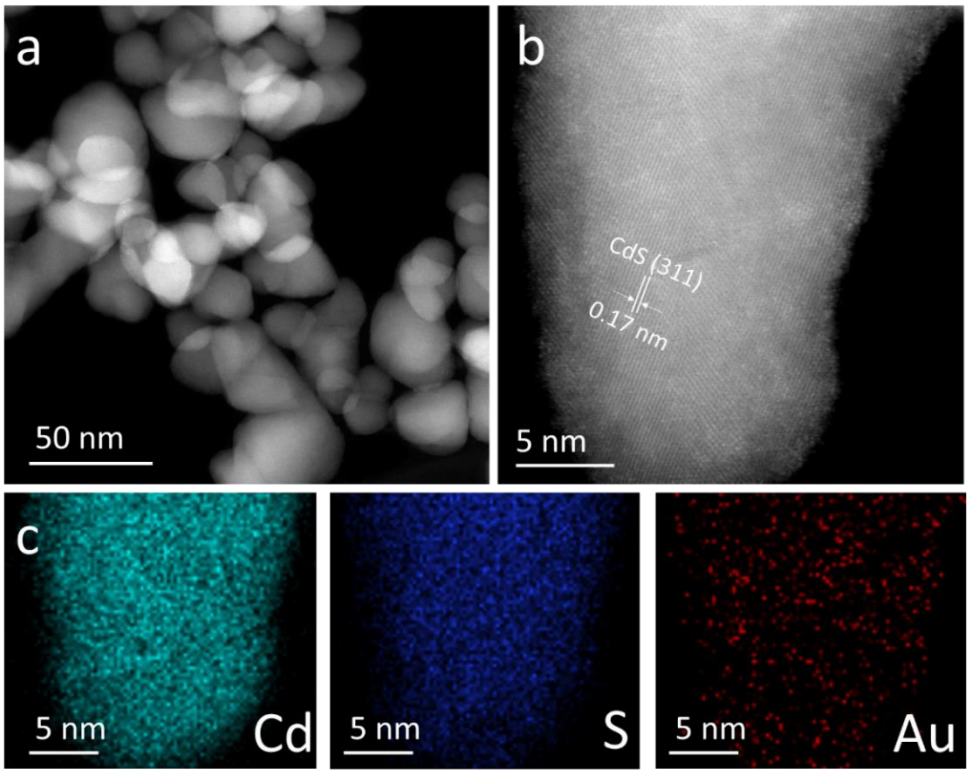

Figure S3. a) TEM image and b) HAADF-STEM of CA2. c) EDS mapping of CA2.

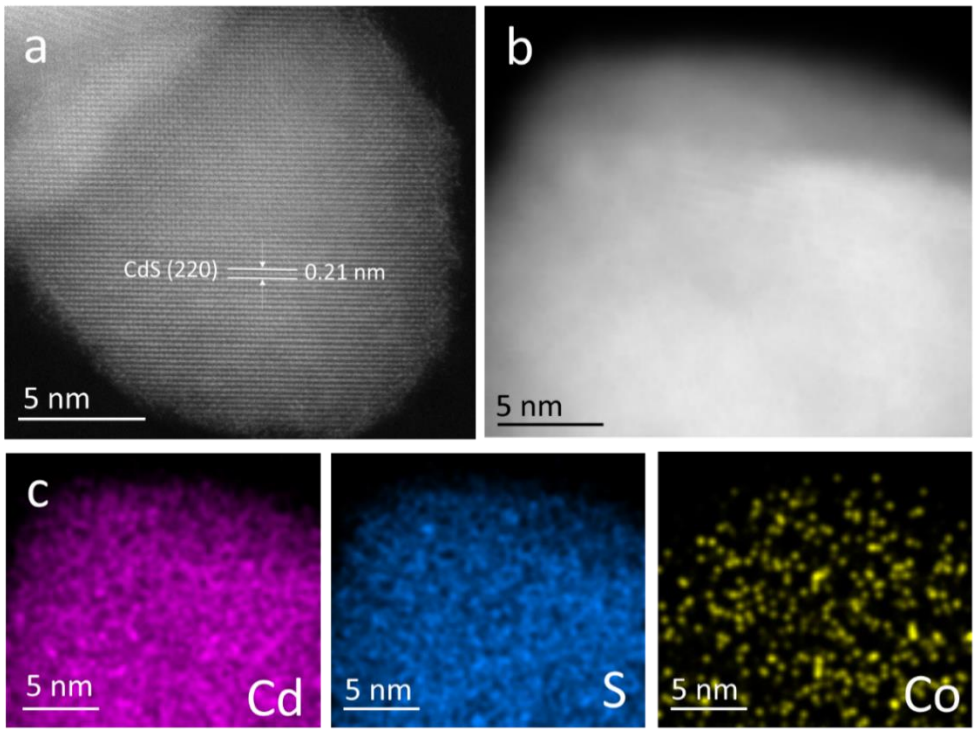

Figure S4. a) HAADF-STEM, b) morphology and c) EDS mapping of CC2.

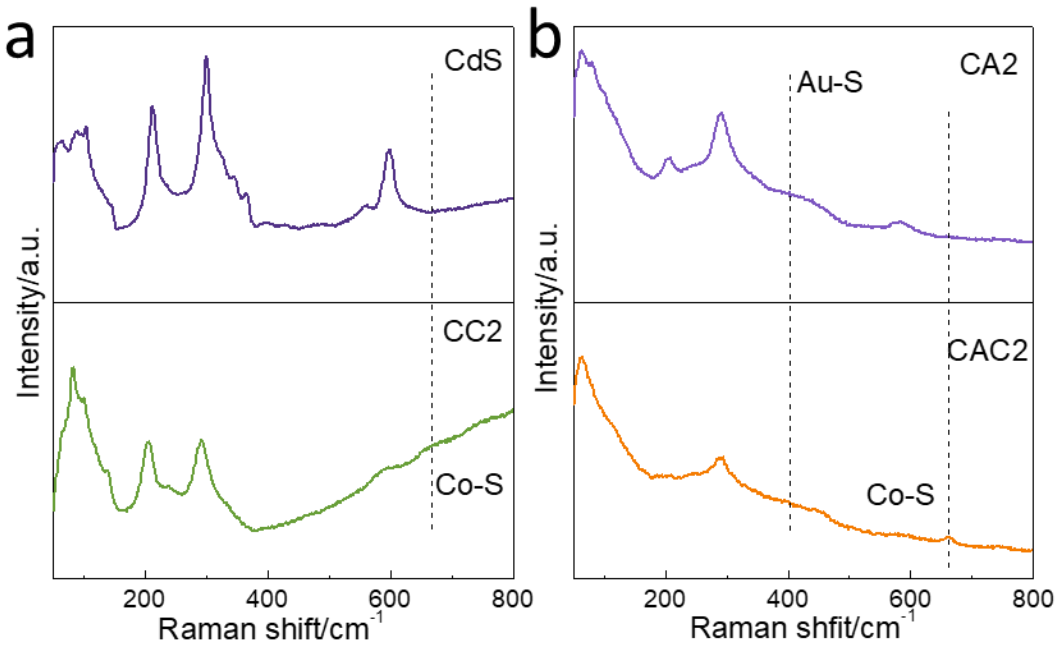

Figure S5. Raman spectra of a) CdS, CC2 and b) CA2, CAC2.

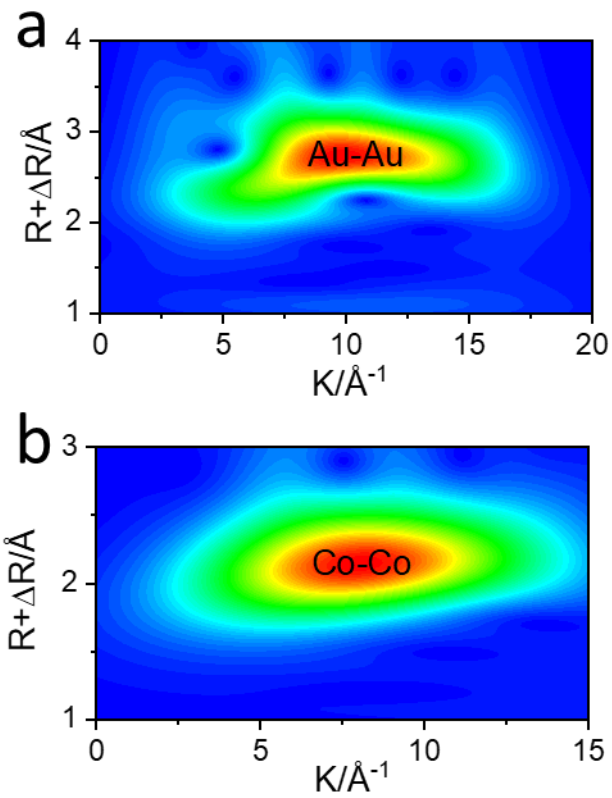

Figure S6. WT for the K^3-weighted EXAFS signal at a) Co K-edge for Co foil and b) Au L_3-edge for Au foil.

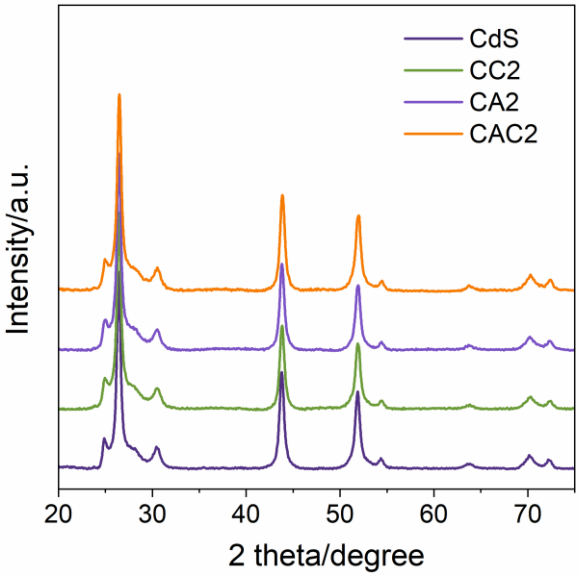

Figure S7. X-ray diffraction patterns of synthesised samples. All of the diffraction peaks can be attributed to the cubic CdS (JCPDS #10-0454).

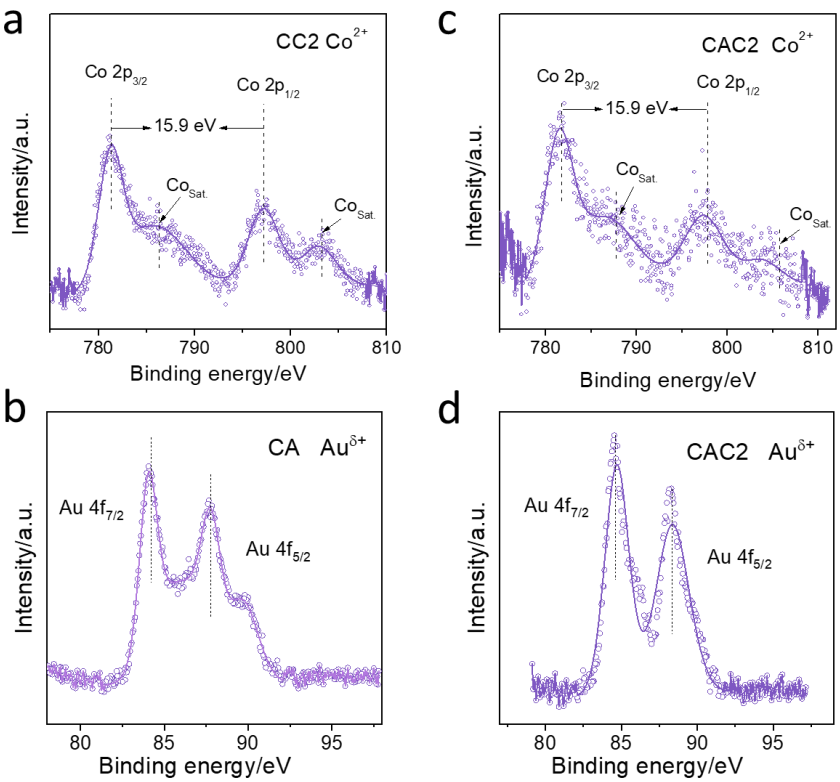

Figure S8. XPS spectra for post-catalysis of samples. a) Co in CC2, b) Au in CA2, c) Co and d) Au in CAC2.

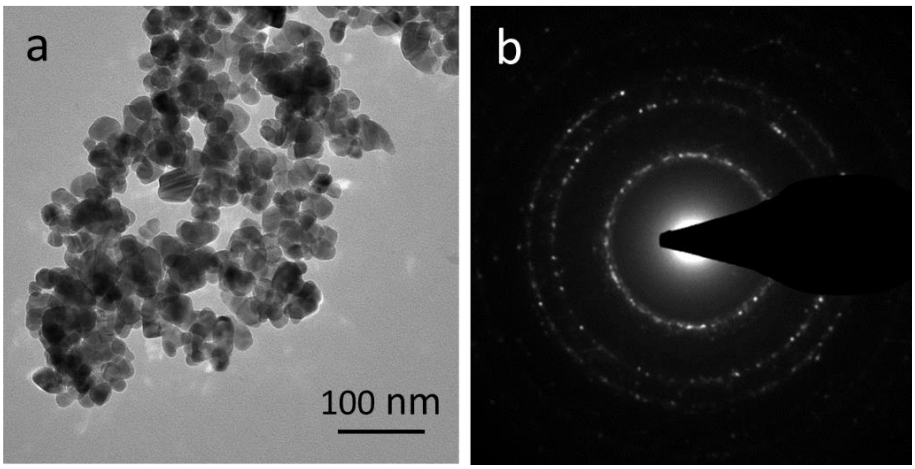

Figure S9. a) TEM image and b) corresponding SAED pattern of CC2.

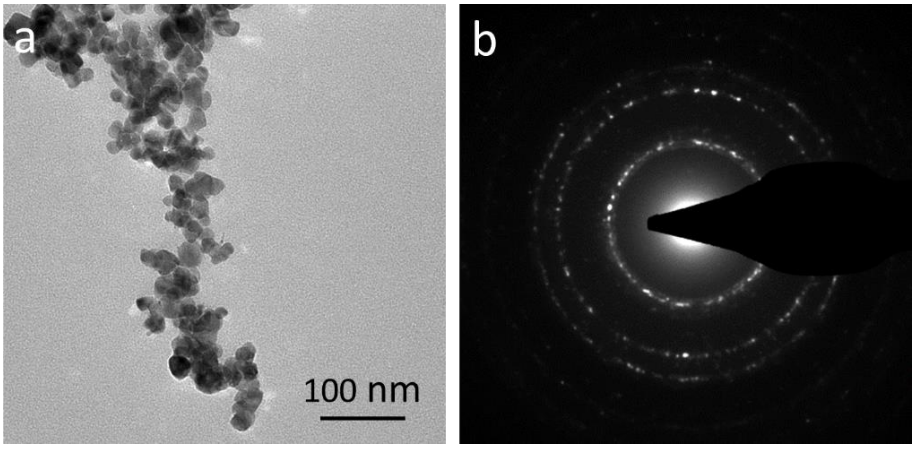

Figure S10. a) TEM image and b) corresponding SAED pattern of CA2.

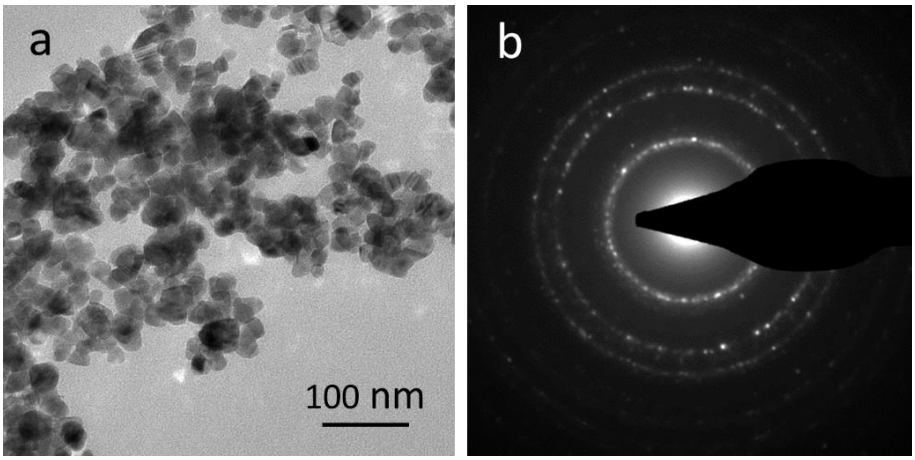

Figure S11. a) TEM image and b) corresponding SAEDpattern of CAC2.

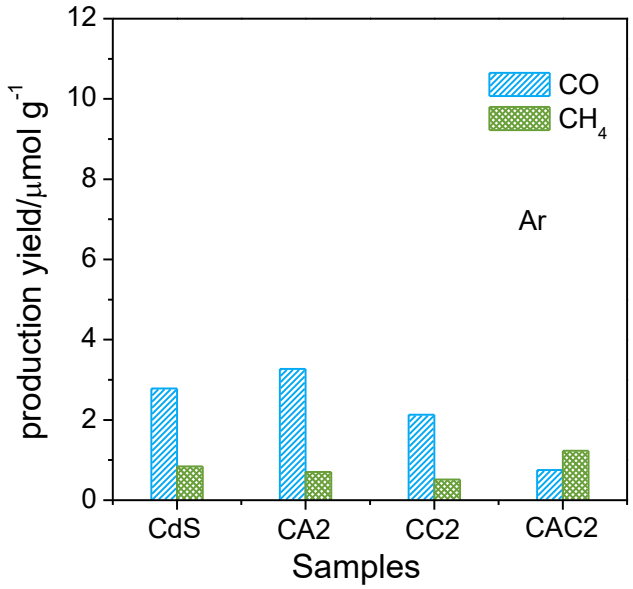

Figrue S12. Blank experiments for photocatalytic performance test in ultrahigh purity Ar of CdS, CA2, CC2 and CAC2 under visible light illumination ($\lambda \geq 400$ nm) for 7 hours.

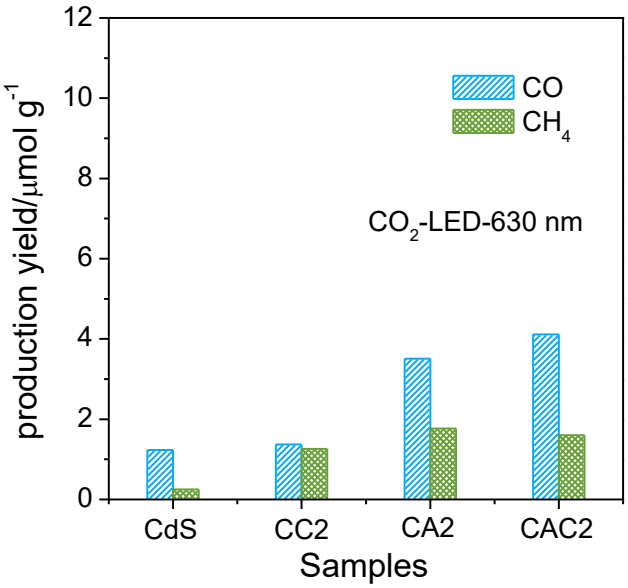

Figrue S13. Photocatalytic CO_2 reduction performance of CdS, CC2, CA2 and CAC2 under 630 nm LED light illumination for 7 hours.

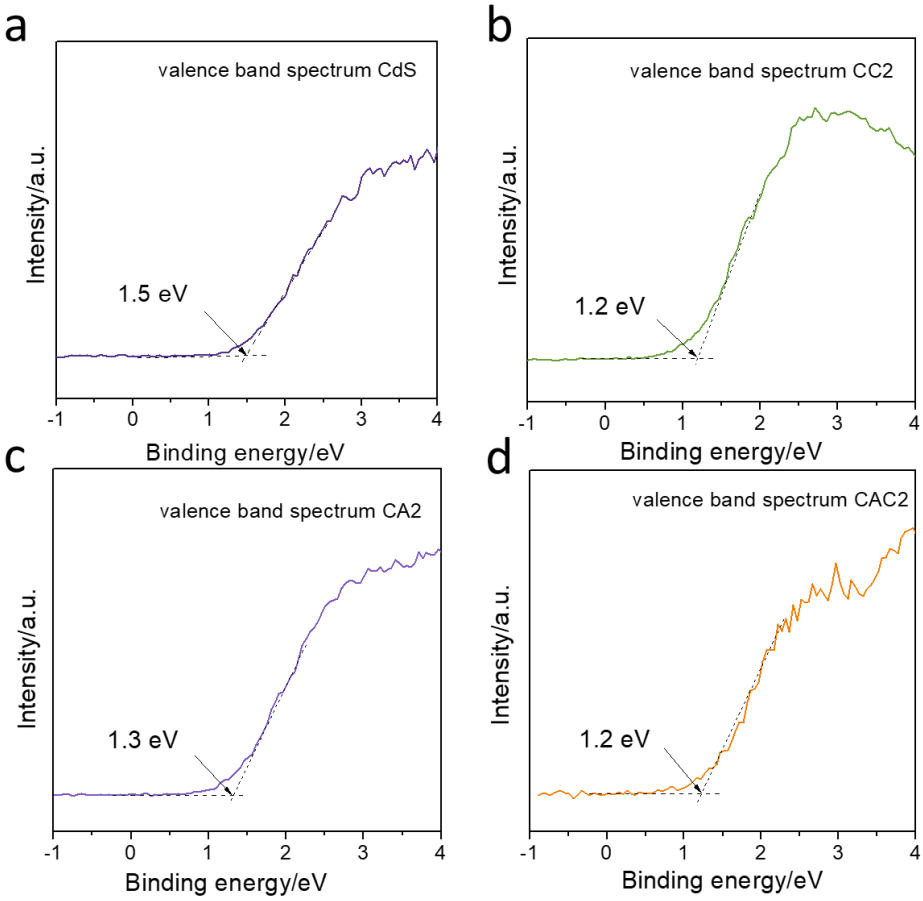

Figure S14. Valence band spectra of a) CdS, b) CC2, c) CA2 and d) CAC2.

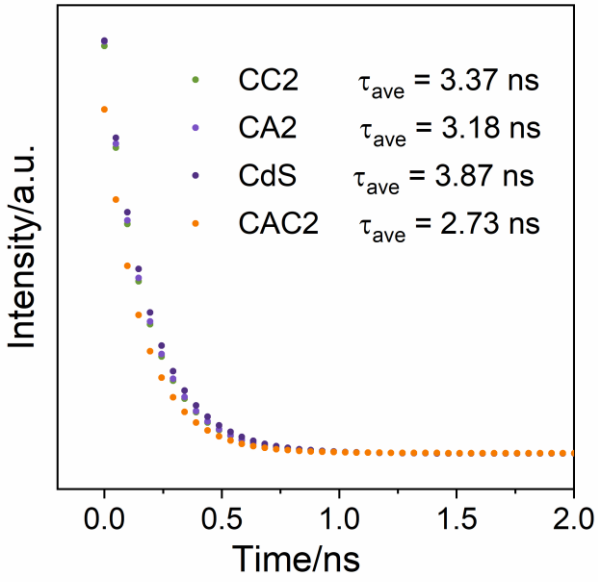

Figure S15. TSPL spectra for CdS, CC2, CA2 and CAC2.

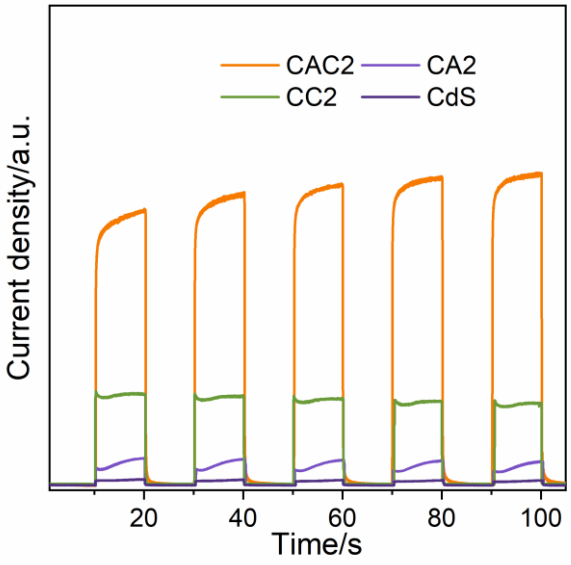

Figure S16. Transient photocurrent density for CdS, CC2, CA2 and CAC2 in 0.5 M Na_2SO_4 aqueous solution.

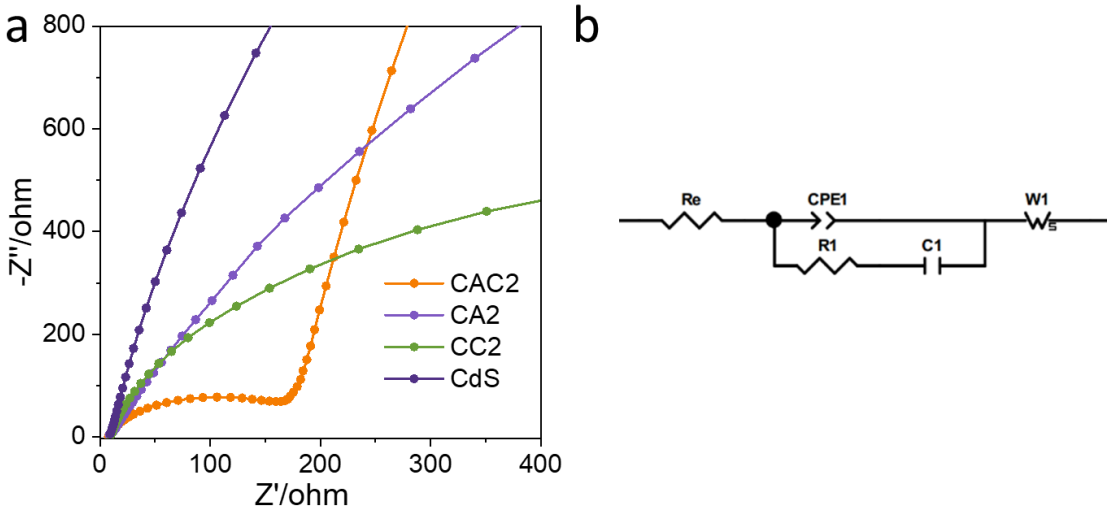

Figure S17. a) EIS spectra for CdS, CC2, CA2 and CAC2 and b) corresponding fitted circuit.

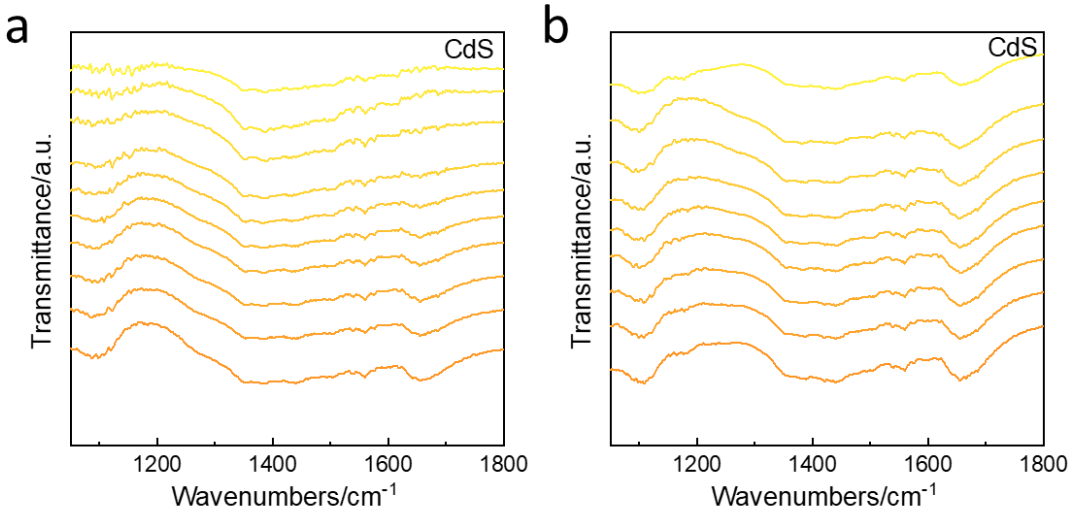

Figure S18. a) *In situ* DRIFTS for CO_2 adsorption of CdS; b) *In situ* DRIFTS of CO_2 photoreduction for CdS.

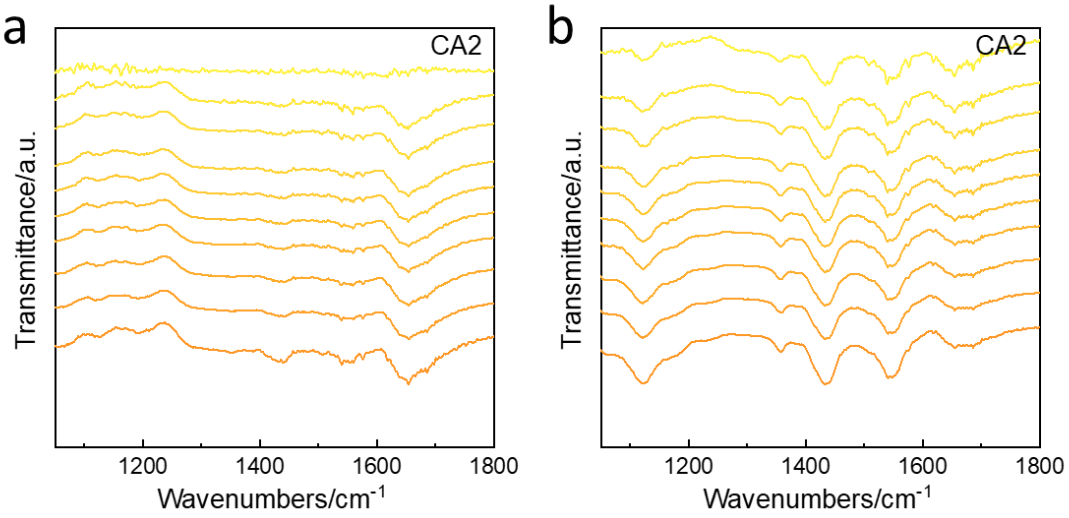

Figure S19. a) *In situ* DRIFTS for CO_2 adsorption of CA2; b) *In situ* DRIFTS of CO_2 photoreduction for CA2.

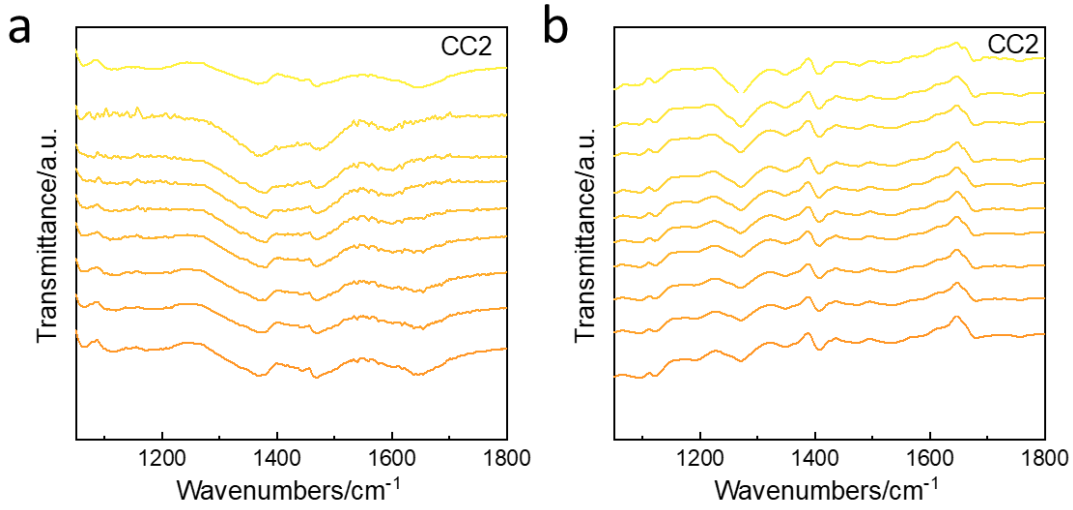

Figure S20. a) *In situ* DRIFTS for CO_2 adsorption of CC2; b) *In situ* DRIFTS of CO_2 photoreduction for CC2.

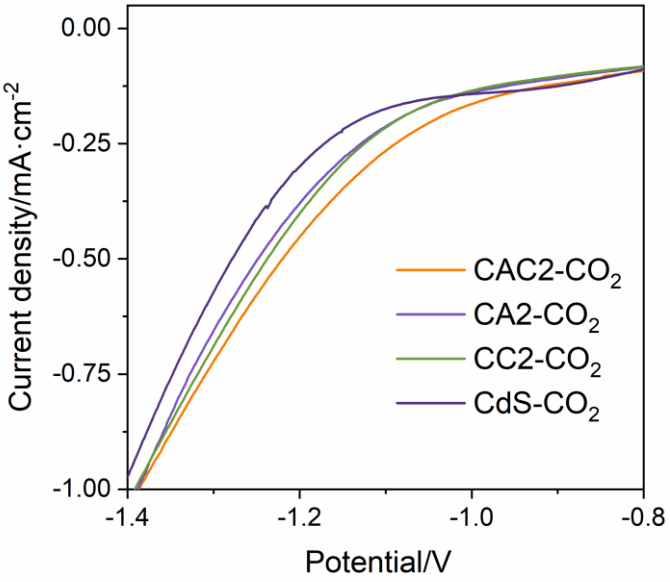

Figure S21. a) LSV for CdS, CC2, CA2 and CAC2 in 0.5 M Na_2SO_4 aqueous solution in CO_2 atmosphere.

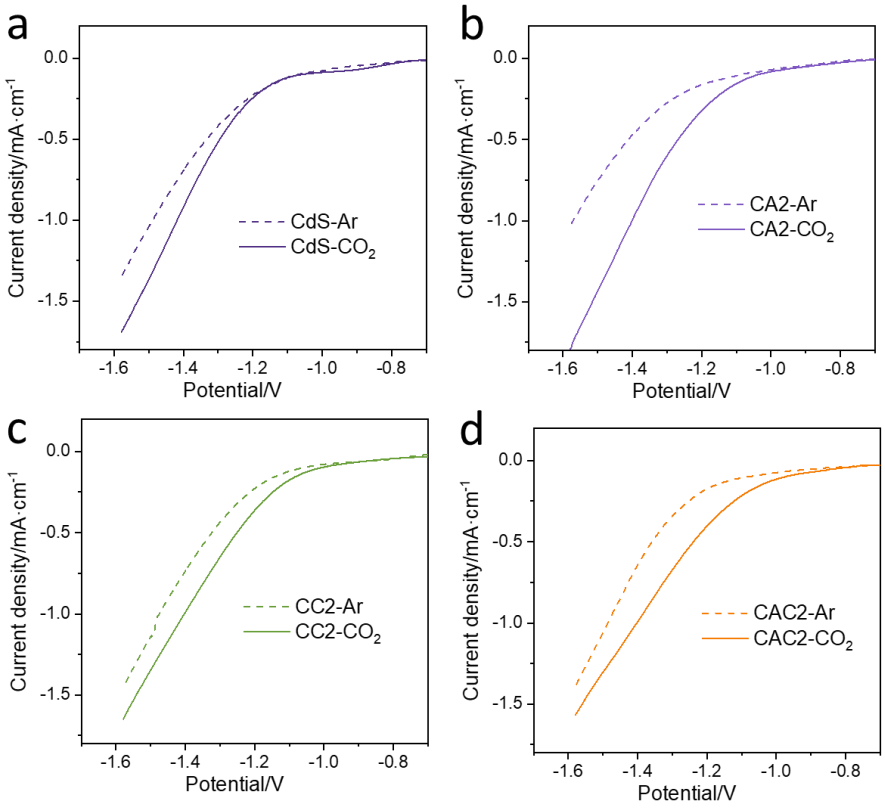

Figure S22. LSV for a) CdS, b) CC2, c) CA2 and d) CAC2 in 0.5 M Na_2SO_4 aqueous solution in Ar/CO_2 atmosphere.

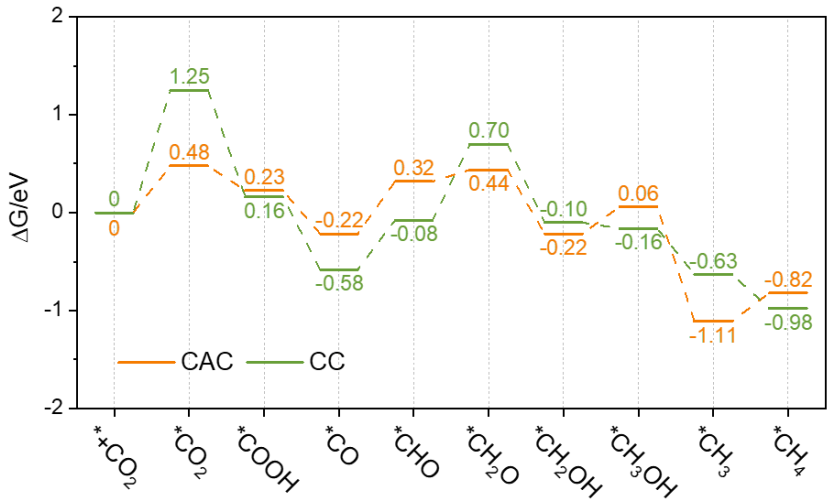

Figure S23. Computed Gibbs free energy and corresponding configurations for main reactions in photocatalytic CO_2 reduction to CH_4 for CAC and CC.

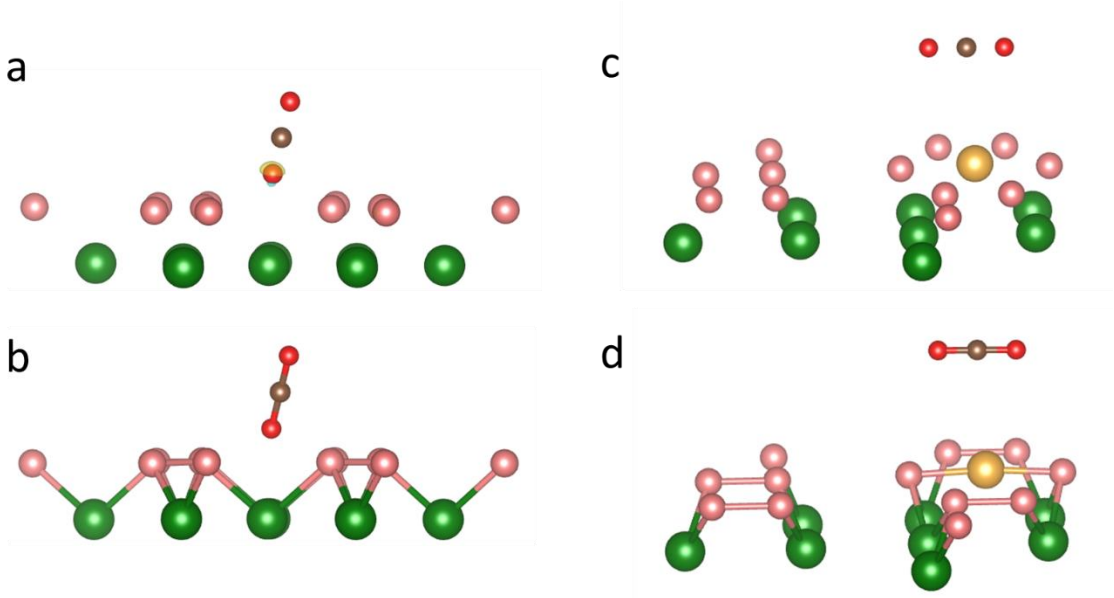

Figure S24. The charge difference distributions of a) CdS and c) CA after CO_2 adsorption and corresponding configuartions of b) CdS and d) CA. The isosurfaces are 0.003 e $Å^{-3}$. Cadmium, sulfur, oxygen, carbon and gold are denoted as green, pink, red, brown and yellow balls. Charge depletion and accumulation are labeled in cyan and yellow, respectively.

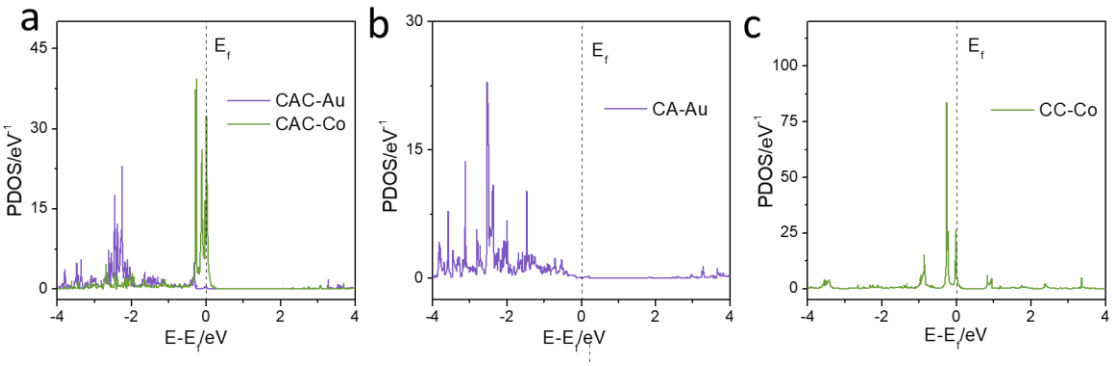

Figure S25. PDOS of a) CAC-Au/Co, b) CA-Au and c) CC-Co.

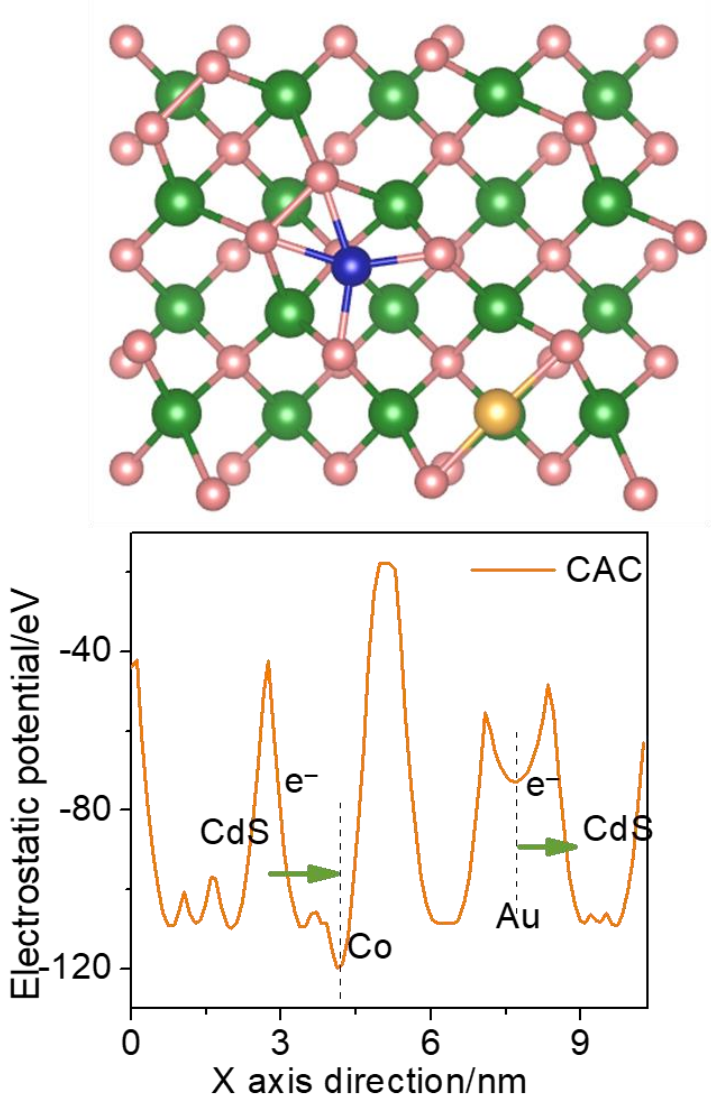

Figure S26. CAC model and corresponding electrostatic potential energy along X-axis.

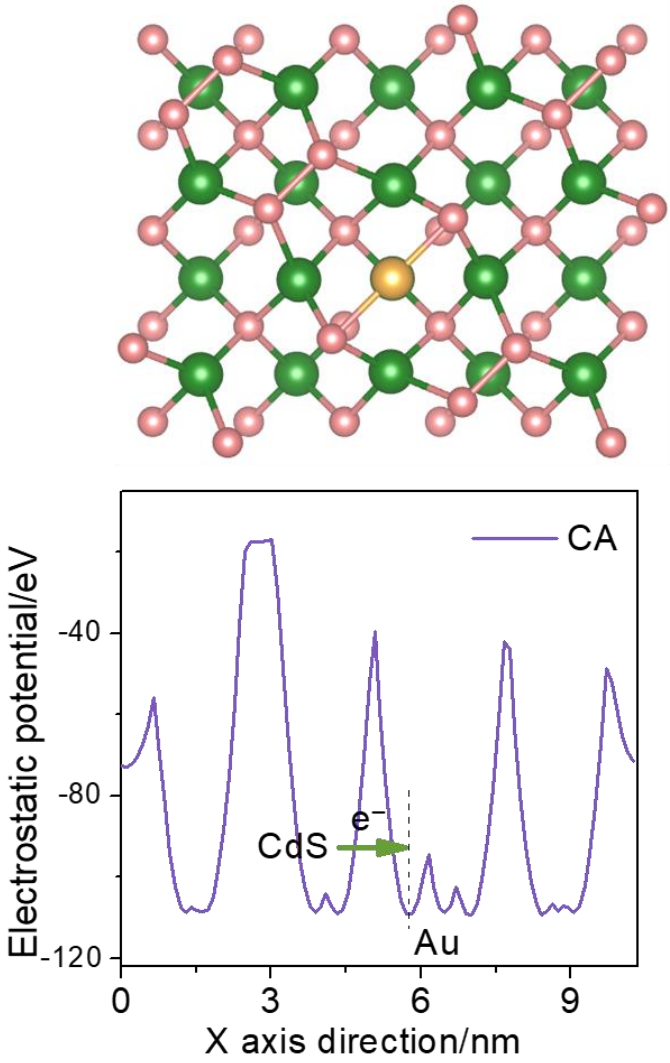

Figure S27. CA model and corresponding electrostatic potential energy along X-axis.

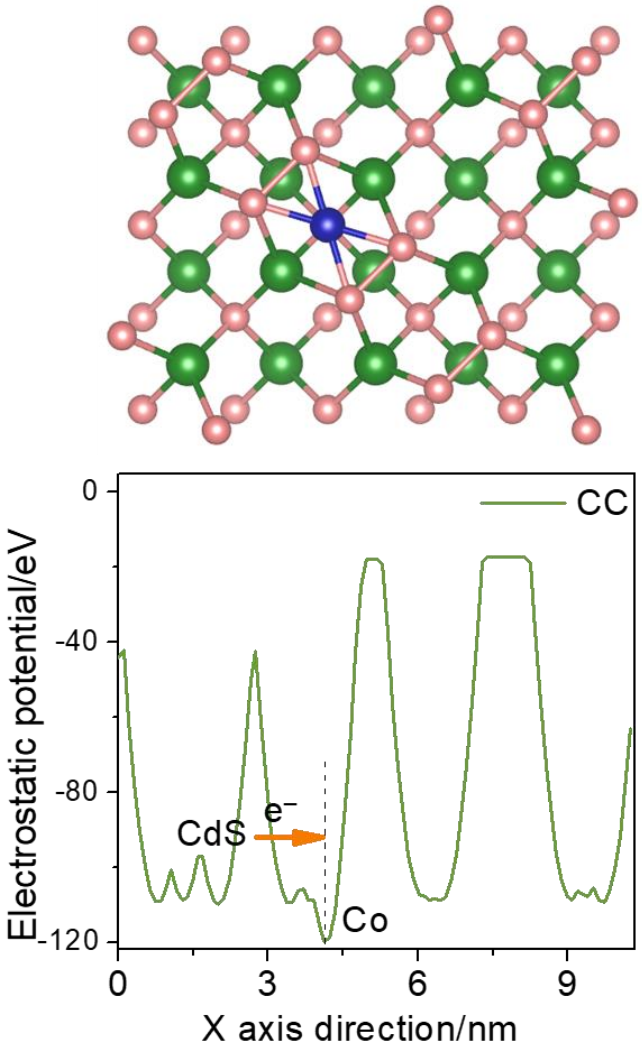

Figure S28. CC model and corresponding electrostatic potential energy along X-axis.

Table S1 TRPL fitting results of pristine CdS, CA2, CC2 and CAC2

samples	τ_{ave}/ns	τ_1/ns (Rel%)	τ_2/ns (Rel%)
CdS	3.87	1.816 (95.89%)	51.71 (4.11%)
CA2	3.18	1.714 (95.92%)	37.54 (4.08%)
CC2	3.37	1.794 (91.12%)	19.54 (8.88%)
CAC2	2.73	1.518 (95.46%)	28.21 (4.54%)

Table S2. The onset potential of different CdS-based samples determined at j = 10 mA cm^{-2}

	Onset Potential (V vs RHE) determined at j = 10 mA cm^{-2}
CdS	–1.06
CC2	–1.02
CA2	–1.04
CAC2	–0.97

Table S3. The uncaptured electrons above the Fermi level in different modes

	Uncaptured electrons in Co	Uncaptured electrons in Au
CC	1.8	–
CA	–	0.4
CAC	1.2	1.1

References

(1) Kresse, G.; Furthmuller, J., *Phys. Rev. B: Condens. Matter Mater. Phys.*, **1996**, *54*, 11169-11186.

(2) Perdew, J.P.; Burke, K.; Ernzerhof, M., *Phys. Rev. Lett.*, **1996**, *77*, 3865-3868.

(3) Kresse, G.; Joubert, D., *Phys. Rev. B: Condens. Matter Mater. Phys.*, **1999**, *59*, 1758-1775.

(4) Tkatchenko, A.; Scheffler, M., *Phys. Rev. Lett.*, **2009**, *102*, 073005.

(5) Nørskov, J.K.; Rossmeisl, J.; Logadottir, A.; Lindqvist, L.; Kitchin, J.R.; Bligaard T.; Jonsson, H., *J. Phys. Chem. B*, **2004**, *108*, 17886-17892.

(6) Shinde, P.V.; Shinde, N.M.; Yun, J.M.; Mane, R.S.; Kim, K.H., *ACS Omega* **2019**, *4*, 11093-11102.

Chapter 7

Conclusions and Outlook

7.1 Conclusions

This Thesis developed strategies for design and synthesis of nanomaterials and development of experimental protocols for photocatalytic CO_2 reduction. Mechanistic investigations of photocatalysis including surface-active sites, reaction thermodynamics and kinetics and photogenerated charge transfer. Combining advanced characterizations and boosted the understanding of fundamentals, the following conclusions can be drawn:

1. Ultrathin ReS_2 nanosheets were synthesized *via* sonication exfoliation and based on this new type of TMDs material and CdS nanoparticles, a heterojunction was synthesized in which fabricated. photogenerated charge transfer and separation were promoted resulting in boosted CO_2 photoreduction. Surface sulfur vacancies were formed on-site during photocatalysis as reactive sites for CO_2 chemisorption and activation.

2. Carbon contaminations in the experimental system can significantly affect performance evaluation and assessment. Carbon impurities were classified and discussed separately. Based on judicious cleaning approaches, plasma cleaning and high-temperature annealing, a rigorous experimental protocol was established to obviate carbon impurities and false-positive results. These developments can be reliably used in evaluation of CO_2 photoreduction and application for pollution conversions.

3. A facile, green and apparent universal method was developed to synthesize surface defects on Bi-based metal oxide nanosheets. Bi_2MoO_6, Bi_2WO_6 and $BiVO_4$ nanosheets synthesized *via* hydrothermal reaction and sonication-assisted chemical etching were found to induce oxygen vacancy on specific facets, exposing unsaturated-coordinated metal atoms. Combined, advanced characterizations and theoretical simulation (DFT) confirmed promoted charge separation, improved light absorption and nominally optimized free energy barriers for photocatalytic CO_2 reduction.

4. A new photogenerated electron transfer mechanism was proposed for dual-single atoms systems. Photogenerated electrons accumulate around Au/Co single atoms on CdS nanoparticles and electron transfer direction and accumulation is modulated in Au and Co single atoms on CdS in which accumulated electrons around Co single atoms boost CO_2 photoreduction. Electrons accumulated around Co single atoms in Co and Au dual single-atom system boosting CO_2 adsorption, activation and reduction. The modulated surface electron density exhibited a high activity of, respectively, 64.1 and 1.9 μmol g^{-1} for CO and CH_4, a selectivity > 97 % and stability > 20 h for the reaction for dual single atoms.

Combined theoretical computations and *in situ* spectroscopy confirmed that single Co atoms formed as active sites and Au acted as the electrons donor surface unsaturated metal atoms, and evidenced the activation of CO_2 as the rate-limiting step.

7.2 Outlook

Future research to improve structure and performance will need to address the following:

1. Nanostructured materials together with targeted surface modification strategies using existing materials might be developed as new and imporved catalysts for CO_2 photoreduction. To explore promising photocatalytic materials, atomic level understanding of the photocatalytic process, especially the "structure-performance" relations, more advanced characterizations should be developed, for instance, the *in situ*/operando spectroscopies and microscopies. Monitoring the change of catalysts and the key intermediates on the catalysts' surface is critical for understanding the thermodynamics and kinetics of surface photocatalysis. The reconstruction may occur by illumination or special chemical conditions during photocatalysis.
2. Advanced synthetic approaches should be developed to achieve the precise control of physicochemical properties and modified surface of photocatalysts. For instance, homonuclear single atoms attracted much attentions, however, the precise synthesis of two or more heteronuclear metal sites is still a challenge.
3. Improved simulation will permit exploration of mechanisms in photocatalysis. *In situ* computations based on simulated conditions including solution, illumination and different physical fields, togther with machine learning will enable better investigation for understanding to improve design of new photocatalysts.
4. New nanomaterials based on high performance, low cost, durable and environmental friendly should be developed for future application. Titania-based materials are still the most promising material. Different modifications can be applied to further enhance their performance.
5. The reaction system including reactor design, light illumination and reaction environment might be optimized. The reaction system should be improved to fit for the scale-up industrial applications. For instance, the reactor can be optimized for accepting more solar illumination under field conditions and products separation can be further a significant issue after photocatalysis. More efforts should be put in for studying these problems.

Appendix: Publications During Ph.D. Candidature

[1] **Y. Zhang**, X. Zhi, J. R. Harmer, H. Xu, K. Davey, J. Ran, S.Z. Qiao, Active Surface Regulation of Bi_xMO_y (M=Mo, V, W) for Boosted Photocatalytic Activity. ***Angew. Chem. Int. Ed.*** 2022, e202212355.

[2] **Y. Zhang**, D. Yao, B. Xia, M. Jaroniec, J. Ran, S.Z. Qiao, Photocatalytic CO_2 Reduction: Identification and Elimination of False-Positive Results. ***ACS Energy Lett.*** 2022, 7, 1611-1617.

[3] **Y. Zhang**, D. Yao, B. Xia, H. Xu, Y. Tang, K. Davey, J. Ran, S. Z. Qiao, ReS_2 Nanosheets with *In Situ* Formed Sulfur Vacancies for Efficient and Highly Selective Photocatalytic CO_2 Reduction. ***Small Sci.*** 2021, 1, 2000052.

[4] **Y. Zhang**, B. Xia, J. Ran, K. Davey, S.Z. Qiao, Atomic-Level Reactive Sites for Semiconductor-Based Photocatalytic CO_2 Reduction. ***Adv. Energy Mater.*** 2020, 10, 1903879.

[5] **Y. Zhang**, J. Ran, S.Z. Qiao, Reversed Electron Transfer in Dual-Single-Atom Promotes CO_2 Photoreduction. In preparation.

[6] **Y. Zhang**, J. Ran, S.Z Qiao, Synergistic Effect of Cu Single Atom and Clusters for CO_2 photoreduction. In preparation.

[7] B. Xia, **Y. Zhang**, J. Ran, M. Jaroniec, S. Z. Qiao, Single-Atom Photocatalysts for Emerging Reactions, ***ACS Cent. Sci.*** 2021, 7, 39.

[8] B. Xia, **Y. Zhang**, B. Shi, J. Ran, K. Davey, S. Z. Qiao, Photocatalysts for Hydrogen Evolution Coupled with Production of Value-Added Chemicals, ***Small Methods*** 2020, 4, 2000063.

[9] B. Xia, Yi Yang, **Y. Zhang**, Y. Xia, M. Jaroniec, J. Yu, J. Ran, S. Z. Qiao, Metal–Organic Framework with Atomically Dispersed $Ni–N_4$ Sites for Greatly-Raised Visible-Light Photocatalytic H_2 Production, ***Chem. Eng. J.*** 2022, 431, 133944.

[10] J. Ran, B. Xia, **Y. Zhang**, S. Z. Qiao, Two-dimensional Building Blocks for Photocatalytic Ammonia Production, ***J. Mater. Chem. A*** 2021, 9, 18733.

[11] B. Xia, B. He, J. Zhang, L. Li, **Y. Zhang**, J. Yu, J. Ran, S. Z. Qiao, $TiO_2/FePS_3$-Scheme Heterojunction for Greatly Raised Photocatalytic Hydrogen Evolution, ***Adv. Energy Mater.*** 2022, 2201449.

[12] D. Yao, C. Tang, L. Li, B. Xia, A. Vasileff, H. Jin, **Y. Zhang**, S. Z. Qiao, *In Situ* Fragmented Bismuth Nanoparticles for Electrocatalytic Nitrogen Reduction, ***Adv. Energy Mater.*** 2020, 10, 2001289.